

Identification of processing parameters for the  
preparation of dECM-based resins for 3D  
(bio)printing

Inaugural-Dissertation  
to obtain the academic degree  
Doctor rerum naturalium (Dr. rer. nat.)

submitted to the Department of Biology, Chemistry, Pharmacy  
of Freie Universität Berlin

by  
M.Sc. Ahed Almalla  
2024

This work was conducted from July 2019 to July 2024 under the supervision of Prof. Dr. Marie Weinhart and Prof. Dr. Rainer Haag at the Institute of Chemistry and Biochemistry of Freie Universität Berlin.

1<sup>st</sup> reviewer: Prof. Dr. Marie Weinhart

2<sup>nd</sup> reviewer: Prof. Dr. Rainer Haag

Date of defense: 11.10.2024

## ACKNOWLEDGMENT

First and foremost, I would like to express my deepest appreciation to my supervisor, Prof. Marie Weinhart for providing me with the opportunity to conduct this thesis under her supervision and for welcoming me into her research family and introducing me to an amazing research topic. I also want to express my gratitude to my second supervisor, Prof. Rainer Haag and his group members for their great support during the period of conducting this dissertation and for being part of this journey. I am profoundly grateful to Dr. Laura Elomaa, for her long-term support, guidance, encouragement, and motivational words, which not only shaped my thesis but also helped me grow both academically and personally.

Many thanks to Helmholtz Graduate School Macromolecular Bioscience and SFB 1449 for their financial support. This thesis evolved through collaborations with several research groups, and I sincerely appreciate their significant contributions, particularly Prof. Britta Siegmund and Prof. Igor M. Sauer and their groups at Charité – Universitätsmedizin Berlin, as well as Prof. Sebastian Seiffert at Johannes Gutenberg University Mainz.

I want to express my gratitude to all my students – your input, whether direct or indirect, has made a real impact on this work. Special thanks to the present and past members of the Weinhart group, who I consider my second family. Thanks for the fantastic scientific discussions, fun activities, and all the laughs and tears. You have always had my back whenever I needed you.

My deepest appreciation goes to my friends and family, including my siblings and parents. Papa and Mama, the seeds of curiosity you planted in my childhood have blossomed into a thriving forest, guiding me through this incredible PhD journey.

A big thank you to my husband, **Laith**, my midnight tech support hero. From fixing printer jams at the most inconvenient times, always changing the ink right when I needed it, to answering my endless tech questions – you were my personal IT savior. Thank you for pretending to be interested in my thesis topic, even though you had no clue what it was about and always forgot. And thanks for managing the household chaos like a pro while I was lost in my research bubble.

Lastly, to my wonderful daughter, thank you for putting up with my 'working mood' and for your patience when I was mentally checked out during your school stories. Your silly jokes were the perfect antidote to my serious research mode. Thanks for all the emotional talks, hugs, and cries – they were better than any stress relief therapy. And a big thanks for understanding that Mama is working and for letting her do it (most of the time). Thank you for being my inspiration and my greatest cheerleader. This thesis is dedicated to you, **Janna**.

## **Declaration of authorship**

I hereby declare that I alone am responsible for the content of my doctoral dissertation and that I have only used the sources or references cited in the dissertation.

Berlin, July 2024

Ahed Almala

# Table of Contents

<b>1. INTRODUCTION</b> .....	1
<b>2. THEORETICAL BACKGROUND</b> .....	4
2.1. Composition and function of ECM.....	4
2.2. Three dimensional (3D) bioprinting of dECM-based materials.....	6
2.3. Decellularization of native tissue ECM: an overview.....	9
2.4. Application of dECM in regenerative medicine .....	11
2.5. Enzymatic digestion for solubilization of dECM and its physical crosslinking .....	13
2.6. Chemical covalent crosslinking and chemical modifications of dECM into photocrosslinkable biomaterial resins .....	16
2.6.1. Chemical covalent crosslinking of unmodified dECM.....	17
2.6.2. Photoinitiators and photo-induced covalent crosslinking of unmodified and chemically modified dECM for vat photopolymerization .....	18
2.7. Characterization of dECM biomaterial resins and 3D bioprinted structures .....	22
2.8. Adjusting bioresin properties and bioprinting parameters: ideal bioresin and bioprinting window .....	31
2.9. dECM-based 3D tissue constructs and in vitro tissue models: liver and intestine.....	32
<b>3. OBJECTIVES</b> .....	37
<b>4. PUBLICATIONS AND MANUSCRIPTS</b> .....	39
<b>4.1. Papain-Based Solubilization of Decellularized Extracellular Matrix for the Preparation of Bioactive, Thermosensitive Pre-Gels</b> .....	39
<b>4.2. Chemistry Matters: A Side-by-Side Comparison of Two Chemically Distinct Methacryloylated dECM Bioresins for Vat Photopolymerization</b> .....	66
<b>4.3. Hydrogel-Integrated Millifluidic Systems: Advancing the Fabrication of Mucus-producing Human Intestinal Models</b> .....	99
<b>5. SHORT SUMMARY</b> .....	149
<b>6. KURZZUSAMMENFASSUNG</b> .....	151
<b>7. OUTLOOK</b> .....	154
<b>8. LIST OF PUBLICATIONS AND CONFERENCE CONTRIBUTIONS</b> .....	156
<b>9. References</b> .....	157

# 1. INTRODUCTION

Development of in vitro tissue models is a critical frontier in biomedical research, offering transformative potential for disease modeling, drug discovery, and regenerative medicine [1]. Efforts to replicate the extracellular matrix (ECM) for in vitro 3D cell culture and tissue engineering scaffolds have led to the creation of various innovative biofabrication methods and a large group of new synthetic and natural biomaterials. Three-dimensional (3D) printing as a biofabrication technique has evolved significantly from a core technology in additive manufacturing (AM) to a revolutionary approach in bioprinting, catalyzing advancements in both tissue engineering and regenerative medicine [2]. This technology offers precise control over structural design and optimizes material utilization, making it ideal for creating complex, customized biological structures tailored for personalized medicine [3]. Despite these advancements, engineered 3D constructs often lack the intricate microenvironment and essential ECM components that are crucial for optimal cell viability, functionality, tissue maturation and regeneration [4]. Reproducing the complex microenvironment of native tissues remains challenging, particularly in mimicking in vivo cellular interactions and functionalities. For that, decellularized extracellular matrix (dECM) biomaterials have emerged as a promising solution due to their ability to closely mimic the natural ECM environment.

dECM has the potential to stimulate tissue regeneration by providing a native-like milieu with crucial bioinstructive cues that guide cellular behavior and development, making them ideal candidate materials for 3D bioprinting [4]. The decellularization process removes all cellular content and immunogenic molecules from donor tissues, preserving a complex network of bioactive molecules such as growth factors, cytokines, and extracellular matrix proteins and proteoglycans. These components are crucial as they coordinate cell fate and support intercellular communication [5]. For over 20 years, dECM-derived products in 2D sheets and powder forms from various animal and human tissues have been available for 'off-the-shelf' use. These products have numerous clinical applications, including wound healing, surgical reinforcement, and tissue reconstruction for large defects, and have been implanted in millions of patients [6-8].

Following decellularization, the dECM is enzymatically solubilized to create a versatile pre-gel that preserves the natural properties of the extracellular matrix. This pre-gel has the remarkable

ability to self-assemble into hydrogels through physical non-covalent crosslinking when temperature and pH are adjusted [9]. Excitingly, dECM hydrogels derived from porcine myocardium have advanced to clinical applications, successfully passing phase I clinical trials and demonstrating their safety for injection via catheter into patients [10]. Additionally, dECM hydrogels derived from porcine colon and small intestine have been effectively used as an alternative to Matrigel™ for growing human organoids, significantly expanding the potential applications of these innovative materials [11,12].

The versatility of dECM hydrogels doesn't stop there. These hydrogels can be seamlessly integrated into bioprinting technologies, opening new frontiers in tissue engineering and regenerative medicine. dECM hydrogels can be bioprinted using two main techniques: extrusion bioprinting, which involves extruding the dECM bioink through a bioprinter, layer by layer, to create cell-laden tissue constructs. This method allows for precise placement of cells within the bioink, closely mimicking the microenvironment of native tissues. On the other hand, vat photopolymerization offers a different approach by using light to cure layers of photocrosslinkable dECM biomaterial resin or bioresin in a vat. This technique achieves higher resolution but offers less control over the spatial distribution of cells compared to extrusion methods [13]. For this, the thermo-gelling dECM pre-gel can be mixed with crosslinking agents and photocatalysts to induce an additional covalent crosslinking or can be chemically modified to introduce photocrosslinkable groups to improve printability and mechanical properties of the formed hydrogel making it suitable for use as biomaterial resins or bioresin in vat photopolymerization processes [14,15].

This thesis delves deep into the formulation of both thermo-gelling solubilized dECM and photocrosslinkable dECM biomaterial resins and bioresins. This includes the step-by-step production, processing, characterization, and standardization of dECM biomaterials, culminating in their final biotesting. The overarching aim of this thesis is to explore and expand the potential applications of dECM in tissue engineering and regenerative medicine through a trilogy of interrelated studies, each addressing distinct but complementary facets of dECM utilization. The workflow for dECM bioprinting starting from tissue isolation and decellularization, through material solubilization and formulation, to the final bioprinting of tissue constructs is illustrated in **Figure 1**.

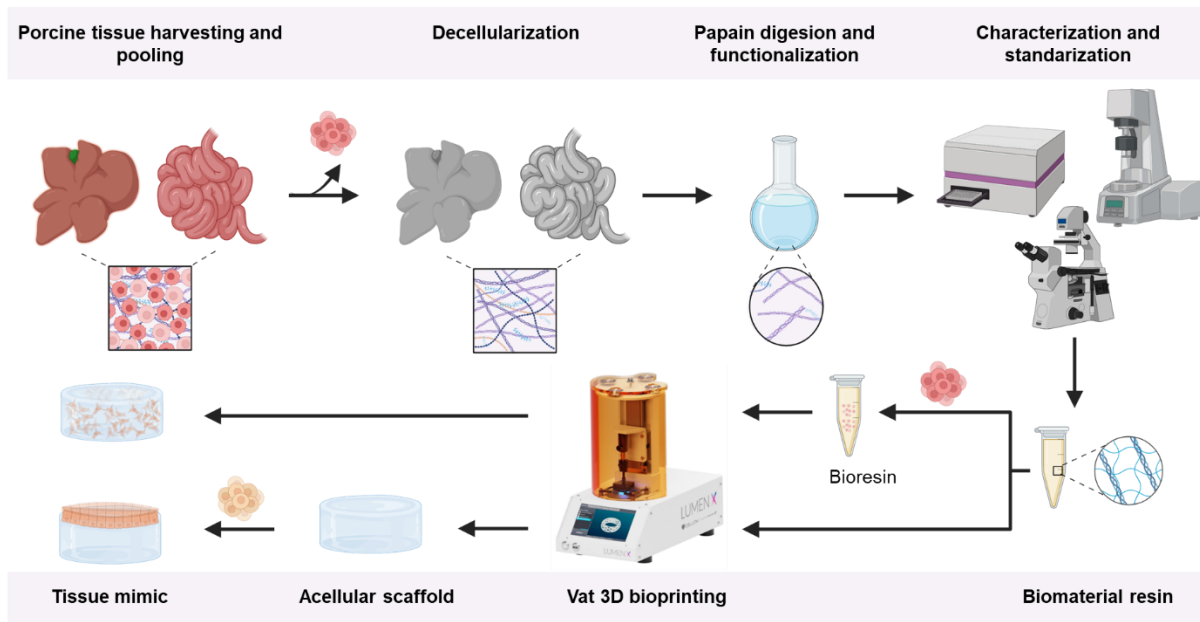


**Figure 1.** The workflow for (bio)printing dECM-based tissue constructs, encompassing the isolation of tissue from human or animal sources, followed by its decellularization, solubilization, and subsequent formulation into a printable material, ultimately leading to 3D (bio)printing. The figure created using BioRender.com and the vat 3D bioprinter image is courtesy of CELLINK.



## 2. THEORETICAL BACKGROUND

### 2.1. Composition and function of ECM

The ECM is a highly organized and dynamic 3D network composed of macromolecules like proteins, glycoproteins, and proteoglycans, which are crucial for providing structural and mechanical support to cells within tissues and organs. Additionally, the ECM acts as a reservoir for growth factors and other bioactive molecules that regulate key cellular functions such as adhesion, migration, proliferation, differentiation, and apoptosis [5]. These processes are essential for tissue and organ development, as well as for maintaining the integrity and function of cells and tissues. Among the components of the ECM, collagens stand out as the most abundant proteins, pivotal in providing tensile strength and structural integrity due to their unique triple helical structure [16]. They form fibrillar networks essential for mechanical resistance and elasticity in connective tissues. Among the over 28 types of collagens, types I, II, III, and IV are the most common. Types I, II, and III create fibrillar structures vital in skin, bone, and muscle, while type II is primarily found in cartilage and type IV forms sheet-like structures in basement membranes [17]. These collagens, featuring repeating glycine-rich tripeptides (Gly-X-Y) where "Gly" stands for glycine, and "X" and "Y" can be any amino acid, though proline and hydroxyproline (or less frequently, hydroxylysine) are most common in these positions, are crucial for their helical structure, self-assembly, and crosslinking. Fiber-forming collagens have three  $\alpha$ -chains which twist around each other to form a helical configuration (triple helix) extending approximately 300 nm, leading to microfibril then fiber formation. This structure is stabilized by hydrogen bonds, with the helix's rigidity enhanced by proline and hydroxyproline. The collagen precursor, procollagen, undergoes enzymatic trimming to form tropocollagen units, initiating fibrillogenesis where telopeptides contribute to covalent crosslinking. These triple helices aggregate into microfibrils and eventually into collagen fibers and bundles, further stabilized by crosslinking through oxidized lysine or hydroxylysine residues, facilitating strong fibril packing. Collagen V plays a regulatory role in the assembly of collagens I, II, and III, highlighting its importance in the structural integrity and assembly of collagen fibrils [16].

Elastin, on the other hand, significantly enhances tissue functionality by imparting elasticity, enabling tissues such as blood vessels, lungs, and skin to resume their shape post expansion or

contraction. This protein's abundance in tissues subject to frequent stretching underscores its importance in maintaining tissue resilience and flexibility [18]. Proteoglycans, which consist of a core protein linked to one or more glycosaminoglycan (GAG) chains, are pivotal in the ECM for maintaining hydration and ensuring a gel-like consistency. These GAG chains have a net negative charge and may be either sulfated—like chondroitin sulfate, dermatan sulfate, heparan sulfate, keratan sulfate, and heparin—or non-sulfated, such as hyaluronan. Their presence supports tissue resilience and shock absorption, enhances cell signaling, and regulates cell growth and differentiation, underscoring the multifaceted role of proteoglycans in the ECM. Furthermore, proteoglycans may also help to trap and store growth factors within the ECM. Glycoproteins, including fibronectin, laminin, and vitronectin, are indispensable for cell adhesion, migration, and signaling processes. Fibronectin, for instance, creates bridges between cells and collagen fibers, facilitating wound healing and cell migration. Laminin, a fundamental component of basement membranes, supports cell adhesion and influences differentiation, while vitronectin engages with integrins to modulate cell adhesion and survival [19]. Together, these components exemplify the ECM's complexity and its critical role in maintaining tissue structure and facilitating cellular functions essential for overall organism health and development (**Figure 2**).

Furthermore, cell-ECM interactions are mediated by integrins, transmembrane receptors that relay external cues to the cell, influencing a range of cellular functions. The RGD domain—(Arg-Gyl-Asp)—found in collagen and fibronectin, is a crucial integrin-binding motif that enhances cell attachment to biomaterial surfaces [5]. Additionally, the ECM is accessible to matrix metalloproteinases (MMPs) enzymes which actively remodel the ECM, adjusting its physical properties to meet developmental and repair needs [20].

An essential function of the ECM in tissue development and homeostasis is providing a niche for stem cells, where it supports the establishment and maintenance of their phenotype and differentiation [21]. It also plays a key role in several processes, including wound healing and regeneration [22]. Yet, the specific mechanisms in which ECM scaffolds support constructive remodeling, integral to tissue development and homeostasis, remain not fully understood.

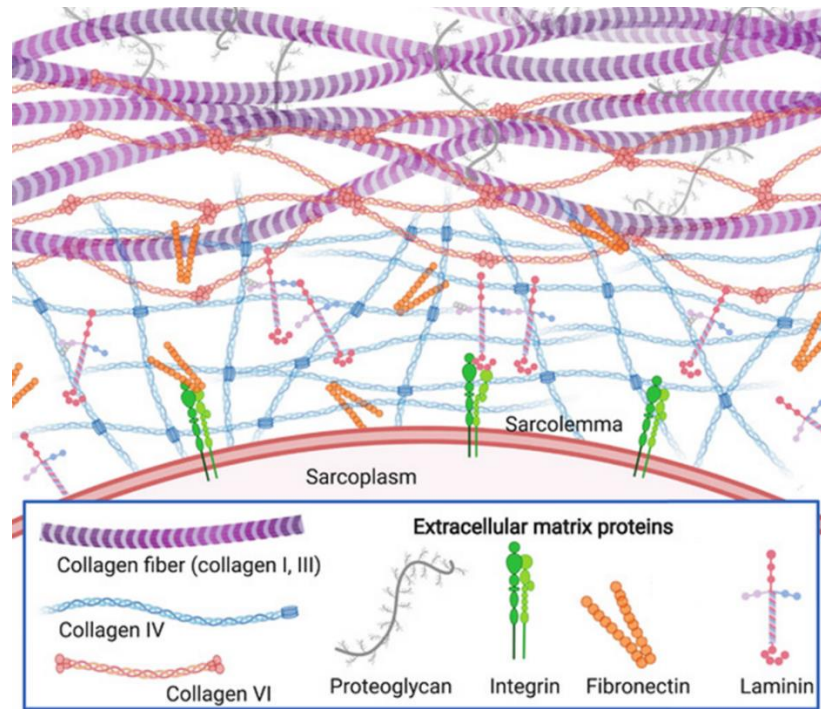


**Figure 2.** Schematic representation of the composition of ECM. Adapted from [23] and licensed under CC BY 4.0.

## 2.2. Three dimensional (3D) bioprinting of dECM-based materials

3D printing, also known as additive manufacturing, originated with the invention of the first stereolithography (SLA) printer by Chuck Hull in 1984 [24,25]. Fundamentally, this technology constructs objects layer by layer, guided by precise digital blueprints from computer-aided designs (CAD) [24]. 3D bioprinting emerged as a specialized application of 3D printing, adapting this core principle and extending others to accommodate living materials [26]. Nearly 20 years after the invention of SLA, a notable development occurred in early 2003 when Wilson *et al.* made the first attempt to print cells using a modified inkjet printer, marking a significant milestone in the adaptation of 3D printing for biological applications [27]. Since then, various printing techniques such as material jetting (inkjet, microvalve, laser-assisted and acoustic), material extrusion (mechanical/pneumatic) and light-based vat photopolymerization (laser-based SLA, digital light processing (DLP), and liquid crystal display (LCD), and two-photon polymerization (2PP)) been applied to a large variety of biomaterial inks and cell-laden bioinks that aim to recapitulate the natural properties and function of ECM [26]. Recently, there has been an increasing focus on

bioinks that are either solely based on solubilized dECM or mixed with it. This trend is primarily observed with extrusion bioprinters, although reports of their use in vat bioprinters are also growing [5].

In bioprinting, meticulously designed structures are crafted using either cell-laden or cell-free dECM materials. These materials undergo a series of processes, including digestion, solubilization, and functionalization with photocrosslinkable groups, to meet the specific requirements of various printers. The detailed steps of processing, crosslinking mechanisms, and formulations of dECM bioinks will be thoroughly explored in the following sections.

Notably, the term 'bio' in bioink and bioresin signifies the mandatory inclusion of cells. According to the classification by Groll *et al.*, biomaterials that are 3D printed and contain only cell-free bioactive components are categorized as biomaterial inks or resins, rather than bioinks or bioresins [28]. The distinction between "ink" and "resin" relates to the type of 3D printing technology used: bioresins are bioinks specifically engineered for light-based bioprinting methods such as vat photopolymerization, whereas bioinks are typically used with non-light-based printers like extrusion-based systems (**Figure 3**) [29]. While numerous bioinks and biomaterial inks have been developed for extrusion-based bioprinting, vat photopolymerization bioprinting lags behind significantly in terms of available printable bioresins and biomaterial resins for tissue engineering. This gap arises from the intricate nature of the vat polymerization process and the demanding material properties required to withstand it (see ideal bioresins in section 2.6), which pose significant challenges to the advancement of this technology [26,30]. However, due to the method's numerous advantages, there has been a recent surge in the development of photocrosslinkable biomaterial resins and bioresins, heralding what is now recognized as the "3D bioprinting era"[6,31].

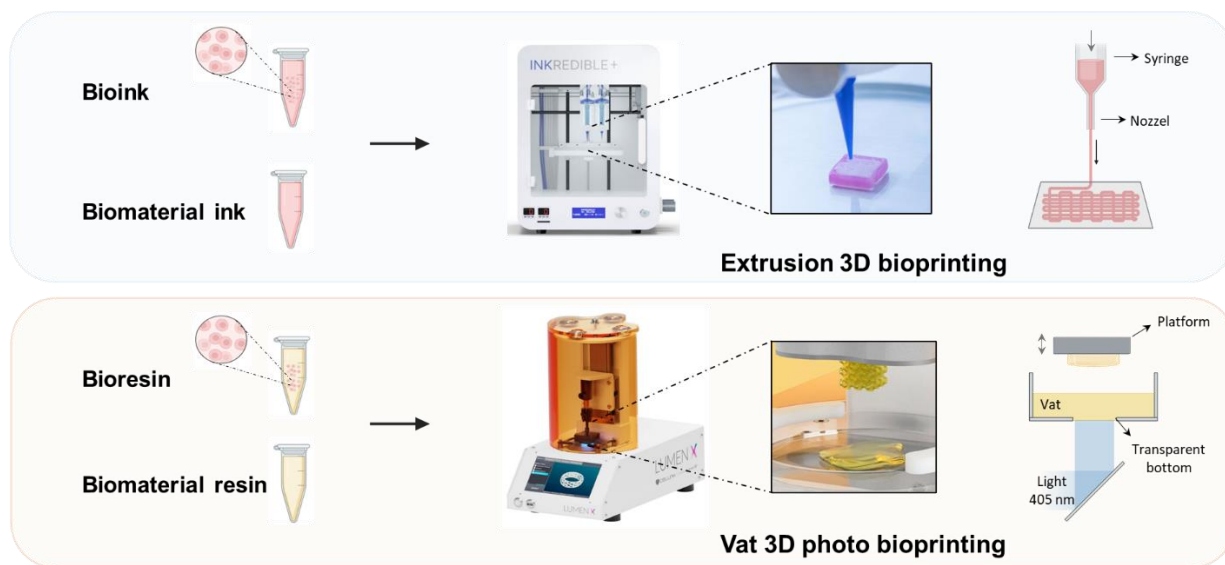


**Figure 3.** Bioinks, bioresins, and biomaterial inks and resins developed for extrusion and vat 3D photobioprinting. The figure created using BioRender.com and the 3D bioprinter images are courtesy of CELLINK.

Extrusion 3D printing has emerged as a dominant technique in the bioprinting of dECM biomaterials due to its simplicity, precision control and adaptability to various bioinks. This method effectively utilizes the viscous nature, shear-thinning properties, and suitable thermal gelation time of dECM hydrogels, which are necessary properties for ideal bioinks [5,32]. In this method, a syringe-like cartridge moves horizontally to deposit the bioink according to a CAD model, while the build platform adjusts vertically between layers. The viscous dECM bioink is extruded through a nozzle onto the platform or a supporting medium, where it is solidified using thermal crosslinking. When additional materials like alginate or photocrosslinkable materials such as methacrylate gelatin (GelMA) are included, ionic or light-induced crosslinking methods are employed. Solubilized unmodified dECM derived from different sources like cartilage [33], heart [34], adipose [35], and skin [36] tissue or chemically modified dECM such as cartilage [33,37], kidney [38], bone [39] and skeletal muscle [40] tissues are utilized in extrusion-based bioprinting to create various tissue engineering hydrogels. Despite its advantages, extrusion 3D printing faces challenges like the difficulty of extruding small volumes through narrow nozzles without high shear stress and the inability to achieve high-resolution, complex structures that closely mimic native tissue microenvironments [41].

Vat photopolymerization, a cutting-edge technique based on photocrosslinking, fabricates 3D constructs by solidifying a liquid resin containing a photoinitiator into precise geometries guided by a CAD file and using UV or visible light. This method offers higher resolution and avoids the shear stresses typical of material extrusion [26]. Solubilized unmodified or chemically functionalized dECM from liver [42,43], intestine [15], heart and cornea [44] tissues has been successfully used in vat bioprinting to create various tissue engineering hydrogels. Crosslinking in this technique occurs either through naturally present amino acids in the dECM, typically phenolic groups activated by a photocatalyst, or through the chemical functionalization of the ECM with photocrosslinkable groups in the presence of photoinitiator (see section 2.5) [45].

In both extrusion and vat photopolymerization methods, depending on how the dECM pre-gels are used—whether solely or mixed with other components, and whether they are functionalized or not—various types of crosslinking, including non-covalent physical and covalent chemical, can occur. In this thesis, the focus will be solely on vat 3D (bio)printing, where light-activated dECM bioresins and biomaterial resins are used for the printing. Consequently, extrusion-based printing methods are not covered in this thesis.

### 2.3. Decellularization of native tissue ECM: an overview

Optimal decellularization of ECM aims at complete removal of cellular components while meticulously preserving the ECM's structure, composition, and biochemical and mechanical properties [6]. The lack of universally accepted protocols is due to variations in species, age, anatomical location, and size of the source tissue. Because of these differences, various protocols incorporating physical, chemical, and enzymatic treatments—often in combination—have been developed [46]. Efficacy criteria for decellularization include less than 50 ng of double-stranded DNA (dsDNA) per mg dry weight and/or DNA fragments under 200 base pairs, and/or the absence of visible nuclear material in hematoxylin and eosin (H&E) or 4',6-diamidino-2-phenylindole (DAPI) staining [47]. **Figure 4** summarizes the physical decellularization techniques, along with the chemical and enzymatic reagents used in decellularization processes.

*Physical Methods [48-51]* : Physical decellularization techniques include freeze-thaw cycles that rupture cell membranes, perfusion that flushes out cells while maintaining the ECM, and scraping that mechanically removes tissue surfaces. Sonication and electroporation disrupt membranes to

enhance cell removal, while pressure gradients and immersion with agitation improve solution diffusion and ensure comprehensive cell clearance. Additionally, apoptosis-assisted decellularization selectively eliminates cells, and supercritical fluids along with vacuum-assistance facilitate thorough penetration of decellularization agents. While physical approaches effectively preserve ECM structures, they may not efficiently remove cellular debris. Therefore, physical methods should be complemented by enzymatic or chemical treatments to ensure the complete elimination of cellular material by aiding the diffusion of decellularizing agents.

*Enzymatic methods [5,49,52]:* Enzymatic decellularization involves using specific enzymes, each with unique considerations. Nucleases require controlled conditions to digest nucleic acids without harming the ECM collagens. Trypsin is effective for broad protein digestion but must be quickly inactivated to protect ECM integrity. Dispase, milder than trypsin, cleaves fibronectin and collagen and needs regulated treatment times. Lipase, targeting membrane lipids, requires precise pH and temperature settings for effectiveness. Collagenase helps open the ECM but risks degrading structural collagen if not carefully applied.  $\alpha$ -Galactosidase, focusing on glycoconjugates, must be finely balanced to preserve ECM components. Optimizing these enzymatic activities is essential for successful decellularization while maintaining ECM function and structure.

*Chemical Methods[47,49,51,52]:* Chemical decellularization techniques involve a range of agents, each requiring precise application to ensure effectiveness while minimizing ECM damage. Ionic detergents like SDS disrupt cell membranes and solubilize proteins, demanding careful control of concentration and exposure to prevent ECM degradation. Non-ionic detergents such as Triton X-100 gently remove membrane lipids, requiring meticulous monitoring to avoid residual effects on cell reseeding. Acids and bases break down nucleic acids, with pH levels critically adjusted to dissolve cellular debris without harming the ECM's properties. Hypertonic and hypotonic solutions induce cellular lysis through osmotic pressure, needing exact osmolarity adjustments to balance cell removal and ECM preservation. Organic solvents, including ethanol and acetone, dehydrate and denature proteins to remove lipids, controlled to avoid excessive protein denaturation. Chelators like EDTA and EGTA, which disrupt cell-matrix interactions by binding divalent cations, must be used with precise timing and concentration to maintain ECM integrity.

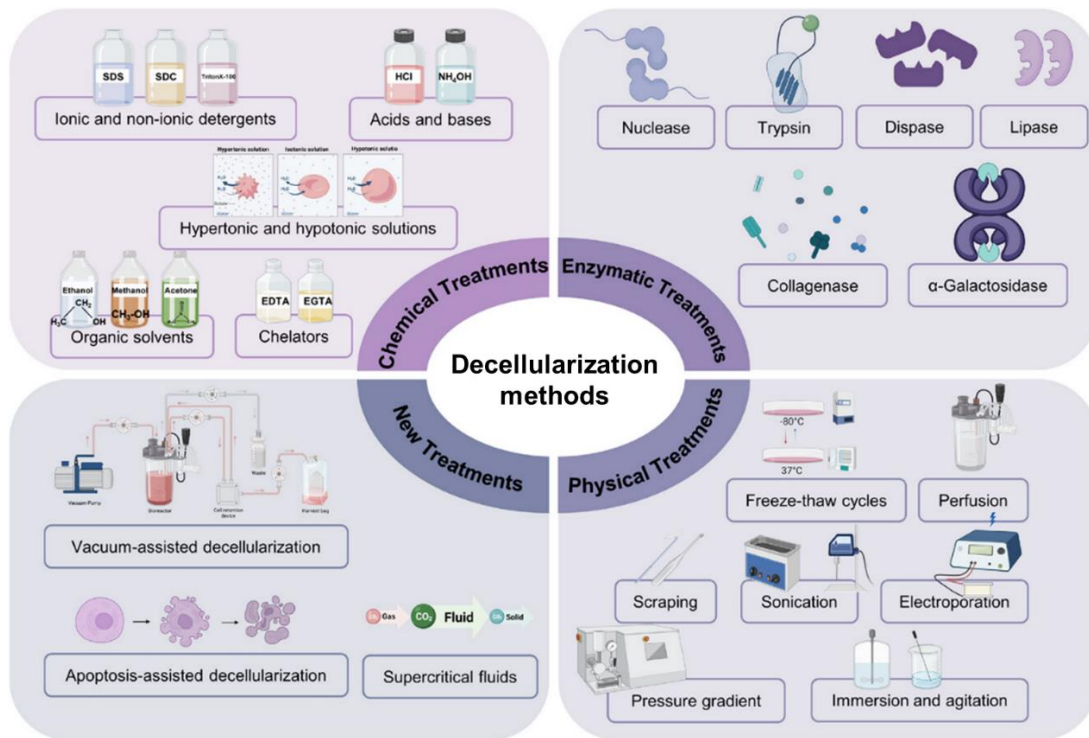


**Figure 4.** An overview of the various preparation methods for decellularized ECM (dECM). Adapted from [49] and licensed under CC BY 4.0.

After decellularization, thoroughly rinsing with water or PBS is crucial to remove cellular remnants and toxic residual chemicals or enzymes that could inhibit the subsequent cell proliferation [6]. This step is typically followed by sterilization to eliminate antigenic and microbial components, thereby reducing immunogenic responses in the dECM [6]. Widely used sterilization methods include gamma-ray or electron beam irradiation, ethylene oxide and supercritical carbon dioxide, which, despite their effectiveness, are costly and require specialized equipment and safety measures, limiting accessibility [53,54]. A cost-effective alternative is peracetic acid (0.1 - 0.5 v/v%), which sterilizes effectively through oxidation, is simple to use, and easy to rinse, thus minimizing residual toxicity [53,55]. However, it's essential to consider that all sterilization methods can affect the dECM's structural and mechanical integrity. Therefore, selecting a method that ensures sterility while preserving the dECM's functional properties is essential.

#### 2.4. Application of dECM in regenerative medicine

Solid dECM materials are utilized in various forms for regenerative medicine applications (**Figure 5**) [14]. They are directly used as whole organ for recellularization or as bulk scaffolds [56], shaped



into batches or sheets [57] to fit specific anatomical requirements or processed where they can be lyophilized and pulverized into microparticles and powders [58,59]. These finer forms can be either suspended alone in a liquid phase to create a slurry or a paste or mixed with other materials to enhance biocompatibility and are particularly useful in injectable therapies or as drug delivery carriers [59]. Most commonly, dECM materials are digested and solubilized and neutralized to form hydrogel networks, which can be used for ECM-gel injections, 3D construction, or as 2D coatings for cell culture substrates [60,61].

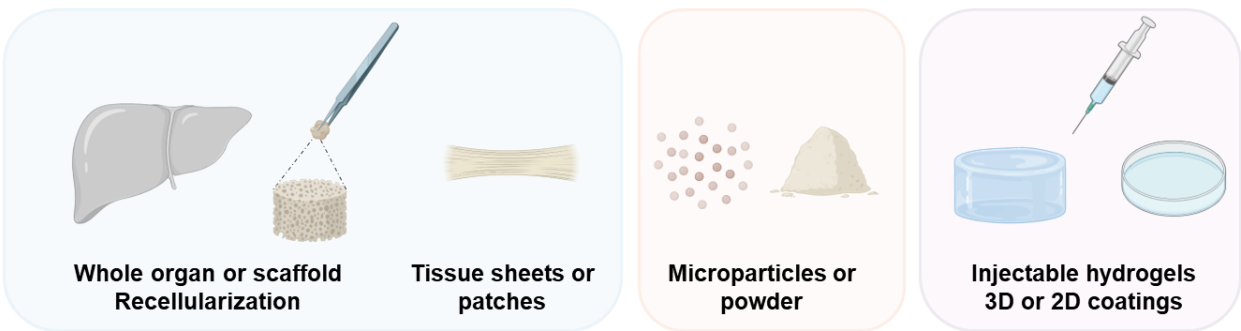


**Figure 5.** Various forms of solid and processed dECM are utilized for specific applications. Figure created by BioRender.com.

Porcine tissues and organs are a primary source for dECM bioinks due to their abundant availability and high breeding capabilities, which provide tissues in larger quantities. However, using them for clinical applications faces challenges such as the risk of infectious disease transmission and potential immune reactions to animal-derived dECM [62,63]. These issues can be mitigated by breeding pigs in controlled environments and using gene editing techniques to produce antigen gene-knockout animals, which result in dECM bioinks that do not trigger immune responses [5]. To minimize these risks from animals, human tissue is the most common source for deriving human-sourced dECM bioinks [64].

Unlike whole organ decellularization and recellularization aimed at maintaining tissue architecture, dECM-based bioprinting requires the ECM to be fully solubilized; thus, the tissue can be randomly sectioned into small pieces to facilitate decellularization. This is often achieved by immersing and agitating the tissue fragments in chemical or/and enzymatic decellularization agents. The most common chemical agents for ECM decellularization are ionic and non-ionic detergents (SDS/Triton X100) [45]. For bioprinting, the dECM must be converted into a liquid or semi-liquid

pre-gel, which involves enzymatic digestion followed by solubilization in an acidic medium to form gel-like substance ready for bioprinting applications.

## 2.5. Enzymatic digestion for solubilization of dECM and its physical crosslinking

The dECM suspensions of paste and slurries are not typically used in 3D bioprinting due to their inhomogeneity (coarse micrometer sized particles  $>250\ \mu\text{m}$ ) [65,66]. Generally, the dECM needs to be first digested into smaller components to make it soluble in aqueous media. The thermo-gelling properties of dECM bioprinting materials rely on the self-assembly of collagen, regulated by the presence of GAGs, proteoglycans, and other ECM proteins, necessitating a careful solubilization protocol to maintain gelling potential [7]. The preparation process involves first lyophilizing the dECM, then cryo-grinding it to increase surface area and facilitate effective enzymatic digestion. Proteolytic pepsin, the most commonly used enzyme for this purpose as first reported by Voytik-Harbin *et al* [67], is particularly effective in a strong acidic environment (pH 1-5 in HCl or AcOH) [68], where it cleaves peptide bonds, at the N-terminal, adjacent to phenylalanine, leucine, tyrosine and tryptophan (hydrophobic and aromatic residues) [69]. This process removes non-helical telopeptide regions from tropocollagen, separating crosslinks between units without harming the collagen's triple helical structure [70]. For complete solubilization, dECM is mixed with a pepsin solution (typically 1 mg/mL at a 1:10 enzyme-to-dECM ratio), stirred and homogenized until fully dissolved and no visible particles are left. If digestion is incomplete, additional filtration or centrifugation may be required to achieve homogeneity. The enzyme is then irreversibly deactivated by raising the pH above 6 [68]. Digestion times can vary from 24 to 96 hours, depending on the tissue type and specific application [7]. After digestion, the dECM undergoes purification via dialysis against water or diluted acids, is lyophilized, sterilized or disinfected and stored at  $-20^{\circ}\text{C}$  or  $-80^{\circ}\text{C}$  for long periods. This processed dECM is then ready for formulation into biomaterial ink or resins, as depicted in **Figure 6** [45].

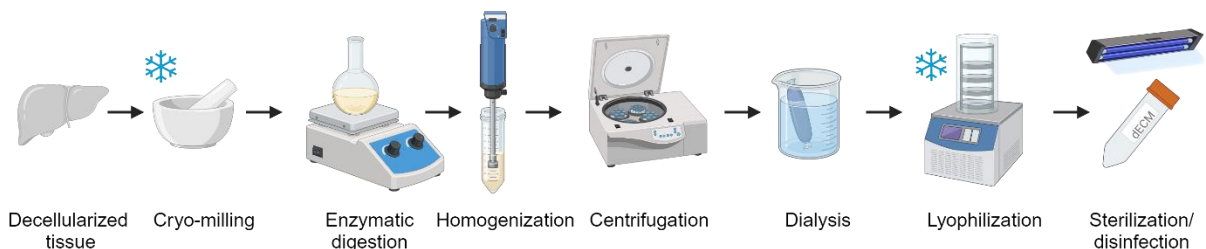


**Figure 6.** *A schematic diagram illustrating the typical steps involved in the digestion of dECM to prepare the materials for use in bioink and bioresin formulations. Adapted from [45] and licensed under CC BY-NC-ND 4.0.*

The dry digested dECM, when solubilized in diluted acid (pre-gel), and subsequently neutralized to physiological conditions—temperature (37 °C), salt (1 x PBS), and pH (7.4)—induces the free collagen alpha-chains in the dECM to self-assemble into a 3D hydrogel network (**Figure 7A**) [71]. This assembly is entropy driven by chain entanglements and thermal condensation due to the loss of surface-bound solvent molecules, facilitated by non-covalent hydrophobic interactions [72,73]. These interactions further promote  $\beta$ -sheet crosslinking within the pre-gel, while the resultant macromer structure is stabilized through a network of electrostatic ionic interactions, hydrogen bonds, and van der Waals forces (**Figure 7B**) [14]. Such self-assembly enhances the viscosity and mechanical properties of the material, rendering it ideal for preparing bioinks and biomaterial inks, especially suited for extrusion-based 3D bioprinters.

Pepsin digestion of dECM has been successfully applied to various types of tissues and organs, including liver [74], intestine [75], stomach [76], lung [60], heart and cornea [44], adipose [64], skeletal muscle[40], pancreas[77] brain and spinal cord [75], and placenta tissues [78]. Most dECM pre-gels are designed for 2D coatings or 3D cell culture, with only a few adapted for 3D bioprinting, due to challenges in adjusting viscosity and printability.

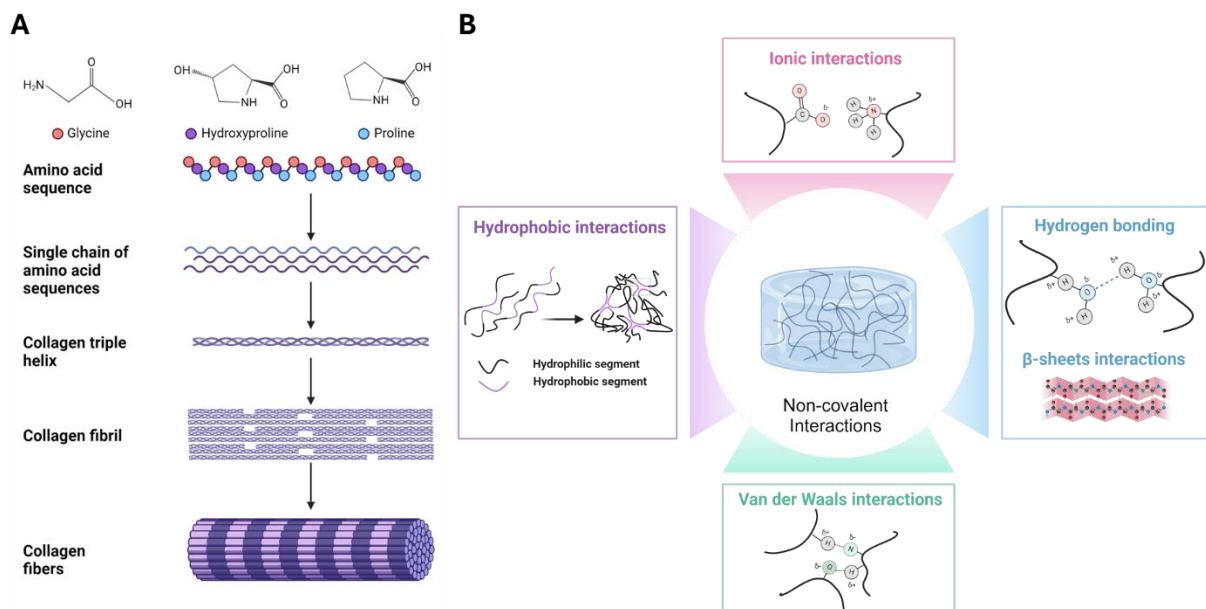


**Figure 7.** (A) Schematic depiction of the collagen fiber self-assembly process beginning with individual amino acids. (B) Various physical non-covalent crosslinking mechanisms involved in transforming dECM pre-gels into hydrogels. The figure was created using BioRender.com.

While pepsin is widely employed to produce pre-gels that can self-assemble into hydrogels, not all enzymatic digestions of dECM yield similar results. The ability to form a self-assembling pre-gel largely depends on the specific interactions between the enzyme's characteristics, the source of the dECM, and the processing conditions. Enzymes such as trypsin, collagenase, proteinase K, papain, and the glycolytic  $\alpha$ -amylase have also been used in various contexts for dECM digestion. Each enzyme has distinct effects based on its specific proteolytic or glycolytic activity, targeting different ECM components or peptide bonds and resulting in varied digestion outcomes. **Trypsin**, a serine protease from bovine or porcine pancreas, is extensively used in biotechnology and medicine, particularly for proteomic analysis, tissue dissociation and preparing cell cultures, due to its ability to cleave peptide bonds at the carboxyl side of lysine and arginine, aiding in cell detachment from culture vessels [79]. It is also postulated that it tends to cleave before proline, leading to increased susceptibility to digestion, disruption of the collagen alpha-helix, and thus, inability to form hydrogels [78]. **Collagenase**, derived from *Clostridium histolyticum*, disrupts the collagen triple helix by targeting bonds between glycine and a preceding amino acid like proline,

preventing hydrogel formation due to lost structural integrity [69]. This enzyme is highly valuable for tissue dissociation, wound debridement, and cell culture preparations [79]. **Proteinase K**, a fungal enzyme with its broad specificity, cleaves near aliphatic and aromatic amino acids, resulting in extensive protein degradation [69]. It is particularly effective in nucleic acid extractions from ECM as it can degrade most proteins under denaturing conditions. Derived from papaya seeds, the proteolytic enzyme **papain** solubilizes dECM by cleaving terminal non-helical telopeptides in the collagen  $\alpha 1$  chain similarly to pepsin, and differently in the  $\alpha 2$  chain [80]. It targets peptide bonds at the C-terminal of basic and aromatic residues like arginine, lysine, or phenylalanine [69]. Depending on digestion conditions, papain can partially preserve the helical structure, allowing potential hydrogel formation. It is primarily used to digest the dECM in biochemical analyses, particularly for assessing sGAGs content [69]. Conversely, the glycolytic enzyme  **$\alpha$ -amylase**, cleaves carbohydrate groups instead of peptide bonds, facilitating the solubilization of intact collagen fibrils in dilute acid and enabling subsequent hydrogel self-assembly [81]. Research has demonstrated that  $\alpha$ -amylase can effectively solubilize human decellularized adipose tissues [82,83], porcine dermal tissue [84] and decellularized porcine left ventricle [85] for applications such as surface coatings, tissue foams, and microcarriers. However, it should be noted that these studies do not provide conclusive evidence of hydrogel formation via self-assembly mechanisms; instead, they suggest that the formation of these dECM-gels primarily results from processes of dehydration and subsequent rehydration.

Although dECM hydrogels offer broad applicability, they lack the adaptable matrix mechanics compared to native tissue, exhibit long gelation times (approximately 15-60 minutes, varying by dECM concentration [86]) and are susceptible to rapid biodegradation by resident or seeded cells, further compromising their mechanical stability [87]. For applications like 3D bioprinting that require improved mechanical stability, a commonly adopted approach is to implement additional covalent crosslinking. This method strengthens the dECM hydrogels' mechanical properties, effectively balancing enhanced durability with the preservation of their biological qualities.

## 2.6. Chemical covalent crosslinking and chemical modifications of dECM into photocrosslinkable biomaterial resins

Advancing the mechanical properties of decellularized extracellular matrix (dECM) materials often involves covalent chemical crosslinking. This section will explore two main approaches: chemical

covalent crosslinking of unmodified dECM and the light activation or integration of photocrosslinkable groups to create biomaterial resins suitable for vat photopolymerization.

### 2.6.1. Chemical covalent crosslinking of unmodified dECM

The solubilized, unmodified dECM pre-gel can also transition into a hydrogel through a two-step process, initially undergoing thermo-physical non-covalent crosslinking followed by covalent chemical crosslinking. This method involves the integration of functional crosslinking monomers that react with the natural functional groups present in dECM proteins, facilitating the coupling of dECM polymer chains. These reactions create strong and durable covalent bonds that significantly enhance the mechanical properties of the hydrogels and therefore their stability. Various synthetic, natural, and enzymatic crosslinkers are employed for this purpose, each with distinct mechanisms, advantages, and disadvantages.

Synthetic crosslinkers like carbodiimide (EDC), often combined with N-hydroxysuccinimide (NHS), create covalent bonds in a three-step process by activating carboxyl groups to form unstable intermediates that react with amino groups [88,89]. Glutaraldehyde (GA) [90] and epoxy [91] components also induce crosslinking via lysine residues. Epoxy-treated ECM materials are more flexible and softer than GA-treated ones [91]. However, synthetic crosslinkers can be cytotoxic if not fully purified and may not be completely biocompatible or biodegradable [92]. Natural crosslinkers, such as Genipin [89] and Procyanidins [93], offer less toxic alternatives. Genipin does this through Schiff base formation and cyclization into heterocyclic structures, while Procyanidins involve oxidative processes and the formation of reactive quinone intermediates, enhancing mechanical strength and biocompatibility. Enzymatic crosslinkers, including transglutaminase [94] and tyrosinase [9], catalyze covalent bonds in collagen, improving mechanical properties and cell viability in hydrogels. Transglutaminase forms bonds between glutamine and lysine residues, while tyrosinase oxidizes phenols to react with amino groups.

Despite notable advancements, each crosslinker has distinct advantages and limitations and has been sparingly used to induce covalent crosslinking or fixate dECM sheets and scaffolds, enhancing mechanical properties to near-natural levels. However, their application in 3D (bio)printing remains largely unexplored. As research progresses, these crosslinkers are likely to become pivotal for chemically crosslinked hydrogels in extrusion-based 3D bioprinting, where light-activated processes are not involved.

## 2.6.2. Photoinitiators and photo-induced covalent crosslinking of unmodified and chemically modified dECM for vat photopolymerization

To further enhance the mechanical and chemical properties of dECM for 3D (bio)printing, particularly in vat photopolymerization, photoinitiators and photo-induced covalent crosslinking offer promising avenues. Photocrosslinking is initiated by photons, which provide the energy needed to activate a photosensitive additive called a photoinitiator (PI). This activation generates reactive species, such as cations or radicals, which trigger a chain reaction that polymerizes the liquid resin in a process known as photopolymerization [95]. Depending on the type of reactive species in the dECM soluble resins and the process conditions, photopolymerization typically proceeds via three types of mechanisms: free radical chain-growth, step-growth of thiol-ene groups, and redox polymerization.

When selecting a PI for biomedical applications, it must meet several fundamental criteria: water solubility, low cytotoxicity, high efficiency, and biocompatibility. To date, a number of PIs absorbing photons from the UV to visible light region have been investigated for dECM photopolymerization (**Figure 8**). Irgacure 2959 (1-[4-(2-hydroxyethoxy)-phenyl]-2-hydroxy-2-methyl-1-propane-1-one); [38] and LAP (lithium phenyl-2,4,6-trimethylbenzoyl-phosphinate) [15,43,96,97] are commonly applied type I PIs which undergo photocleavage to create free radicals. Riboflavin (RF; vitaradical ions, Eosin Y (EY) [98] and tris(2,2-bipyridyl) dichlororuthenium(II) hexahydrate ( $[\text{Ru}(\text{bpy})_3]^{2+}$ ) [11,44,99] are type II PIs where the excited initiator molecule reacts with the appropriate co-initiator such as an electron donor or acceptor or a hydrogen donor in order to produce radicals or radical-ions.

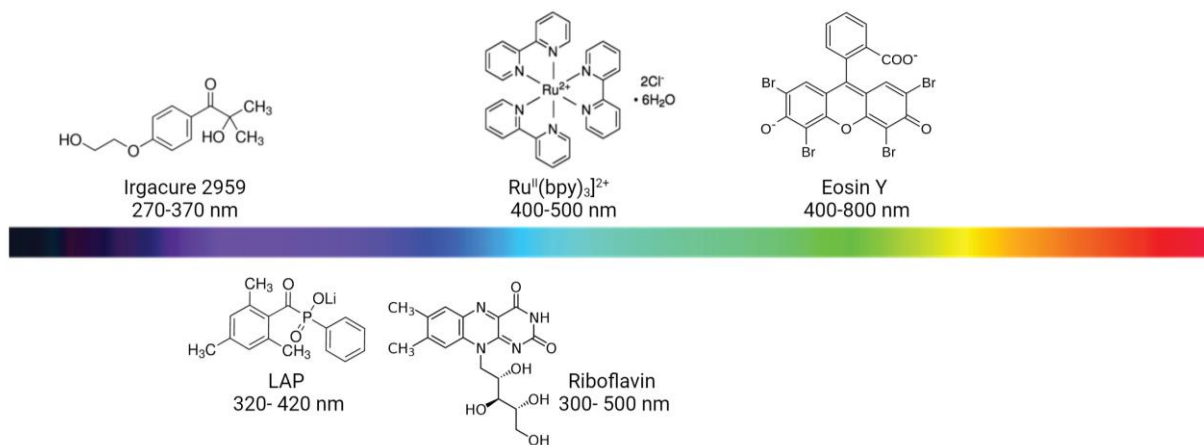


**Figure 8.** Photoinitiators absorbing light from the UV to visible spectrum have been utilized for dECM photopolymerization. Adapted from [30] and licensed under CC BY 4.0.

Irgacure 2959 (276–365 nm) and LAP (320–420 nm) absorb light in the UVB-UVA range and they are colorless, odorless, and require no co-initiator [100,101]. This is because they can generate reactive species through an efficient unimolecular process, utilizing the sufficient photon energy available in this range. In biological applications, LAP is often preferred over Irgacure 2959 due to its higher water solubility and absorbance in the visible light spectrum. This characteristic is particularly advantageous as it reduces the risks of genotoxicity and cell membrane damage commonly associated with UV light exposure [100,101]. Upon photolysis, LAP produces phosphinoyl and phenyl radicals, whereas Irgacure 2959 generates benzoyl and alkyl radicals. These reactive radicals initiate the polymerization process by reacting with carbon-carbon double bonds in resin monomers, forming new radicals and propagating the chain reaction. Finally, the radicals react with each other, terminating the polymerization and forming the final crosslinked polymer. These stages constitute free-radical chain growth photopolymerization [100,102].

Despite the efficiency of free-radical chain polymerization in rapidly crosslinking polymeric materials, oxygen inhibition can cause incomplete photocrosslinking, hindering shape fidelity post-bioprinting and limiting the printing of complex tissue structures [102]. Chemical additives, such as higher concentrations of photoinitiators, singlet oxygen generators, scavengers, and hydrogen donors, can reduce oxygen inhibition [102]. Chemically modified methacryloylated dECM, such as dECM-MA (via methacrylic anhydride; MA) [15,43,96,97] and dECM-GMA (via glycidyl methacrylate; GMA) [37], are typically used in this photopolymerization process.

To further mitigate oxygen inhibition, thiol-ene photoactivated chemistry can be employed. Thiol-ene photoresins possess rapid reaction kinetics, generating fewer harmful radicals and requiring significantly lower polymer content, resulting in a better accommodating cellular matrix [102]. In the presence of thiol compounds, typically thiolated polyethylene glycol (PEG-SH), methacryloylated dECM can be crosslinked by kinetic chain propagation and also form crosslinks in a step-growth manner, resulting in mixed-mode photopolymerization and complex polymer network [102,103].



When functionalizing dECM with carbic anhydride (CA) to produce norbornene-functionalized dECM (dECM-NB), the thiol-ene reaction proceeds exclusively via step-growth, forming a more uniform polymer network [104]. This can lead to different mechanical properties and network homogeneity compared to methacryloylated dECM. Additionally, dECM has been functionalized with thiol groups using Traut's reagent (2-Iminothiolane to produce dECM-SH) and crosslinked with double-bond functional PEG (PEG-ene) in a step-growth mechanism [105,106]. The inclusion of synthetic PEG in thiol-ene systems compromises material biocompatibility, emphasizing the need for a more natural solution. Investigating the integrated orthogonal bioconjugation crosslinking of dECM-NB and dECM-SH, similar to other gelatinous systems [107], could significantly enhance the biocompatibility and functionality of dECM resins, offering improved performance for biomedical applications.

In the context of photoinitiators, RF (300-500 nm) and EY (400-800 nm) require an electron donor co-initiator, typically triethylamine (TEA). Upon light exposure, these PIs reach a triplet state, transferring energy to molecular oxygen to produce reactive oxygen species (ROS) such as singlet oxygen and superoxide radicals. Concurrently, the PIs triplet-state accepts an electron from TEA, forming radical anions of RF/EY and radical cations of TEA. Subsequent proton transfer from the TEA radical cation generates neutral radicals, which initiate polymerization by creating additional radicals from the monomer or co-initiator molecules [108,109]. Similarly,  $[\text{Ru}(\text{bpy})_3]^{2+}$  (400-500 nm) absorbs light, becomes excited, and transfers an electron to an electron acceptor co-initiator, typically sodium persulfate (SPS), together shortly abbreviated Ru/SPS, forming  $[\text{Ru}(\text{bpy})_3]^{2+}$  and highly reactive sulfate anion radicals that can abstract hydrogen atoms from the surrounding molecules, generating secondary radicals that initiate polymerization.

Building on this, type II PIs oxidize reactive crosslinking sites in unmodified dECM, typically targeting tyrosine residues, through ROS or highly reactive radicals, resulting in the formation of dityrosine bonds [109]. This method is advantageous due to its mild reaction conditions and the ability to achieve dual crosslinking (both physical and chemical). However, it may be limited by the availability of redox-active sites in the ECM. RF has been used to prepare porcine heart dECM for cardiac repair [98,110], while EY combined with TEA and *N*-vinyl pyrrolidone (as co-monomer) has been used to prepare a bioink from caprine esophagus dECM [98]. Both bioinks have undergone dual crosslinking through extrusion-based printing but have not yet been studied for vat

photopolymerization. Additionally, Ru/SPS has been employed to prepare a light-activated porcine colon dECM bioink to fabricate a perfusable tubular model [11] and to create bioinks and resins from porcine heart and bovine cornea for fabricating centimeter-scale tissue constructs using both extrusion and vat 3D bioprinters [44].

Photoinitiators operating in the visible range offer benefits for cell viability; however, they face challenges due to lower photon energy, making efficient initiators difficult to find. This necessitates the use of bimolecular systems often requiring co-initiators. Consequently, these processes are slower and less efficient due to competitive reactions involving the monomer, co-initiator, and atmospheric oxygen, compared to type I PIs [95]. Additionally, RF, EY, and  $[\text{Ru}(\text{bpy})_3]^{2+}$  can leave a yellow stain on tissues post-fabrication, raising concerns for aesthetic applications and necessitating further assessment for long-term in vivo use [95].

In 3D vat bioprinting, while some bioprinters use the full visible light spectrum or 365 nm wavelength, most bioprinters use blue light at 405 nm. Unlike other PIs that absorb light around 405 nm, Irgacure 2959 and EY do not, resulting in compromised reaction efficiency due to insufficient energy absorption. This inefficiency requires higher light intensity, longer irradiation times, or increased PI concentrations, which can increase cytotoxicity. Therefore, it is crucial to choose a printer with a wavelength that matches the absorbance peak of the PI used. Balancing light wavelength, intensity, PI concentration, and cytotoxicity is essential to achieve effective crosslinking while preserving cell viability.

Photocrosslinking enables rapid network formation under mild conditions with tunable mechanical properties. It allows precise selection of reaction sites, creating materials with specific properties and structures [111]. Chemical crosslinking methods generally provide enhanced mechanical properties, stability under physiological conditions, and tunable degradation behavior compared to physical crosslinking. Although they may sometimes reduce biocompatibility due to added chemical agents, these methods are particularly useful for applications requiring high stiffness and stability, such as scaffolds for cartilage and bone, disease models like fibrosis and drug delivery systems, where controlled degradation and release rates are essential. Balancing mechanical properties, stability, degradation behavior, and biocompatibility is crucial for advancing bioprinting

processes. **Figure 9** provides an overview of the various chemical covalent crosslinking methods used for both unmodified and chemically modified dECM.

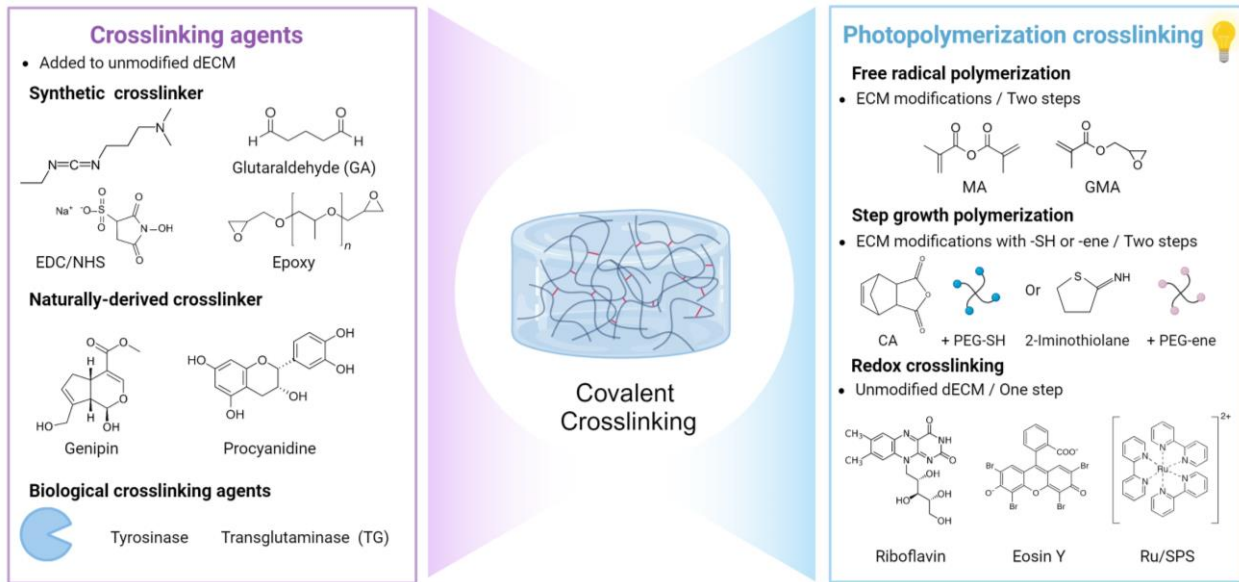


**Figure 9.** Various chemical covalent crosslinking agents and photocrosslinking mechanisms for dECM crosslinking. The figure was created using BioRender.com.

## 2.7. Characterization of dECM biomaterial resins and 3D bioprinted structures

Bioprinting dECM-based tissue constructs involves multiple steps, from decellularization to obtaining the printing biomaterial and finally fabricating 3D printed hydrogel constructs. Addressing the biological variability of ECM before decellularization is critical, as batch-to-batch variations can affect the consistency of dECM-derived biomaterials. To mitigate this issue, pooling tissues and organs before decellularization is recommended to ensure the reproducible performance of dECM biomaterial resins and bioresins, thereby enhancing the consistency of the printed tissue constructs [112]. Numerous analytical techniques are essential for monitoring and standardizing the steps from decellularization to the final 3D constructs. Established compositional, structural, and biomechanical analysis methods, traditionally used for ECM and dECM scaffolds, can also be applied to unmodified, chemically modified, and digested dECM printing biomaterials, as well as 3D printed dECM hydrogels. These techniques are crucial for studying the retention of ECM's characteristic composition throughout processing and evaluating any modifications to the final

printing biomaterials. The following sections will detail these characterization methods, as summarized in **Figure 10**.

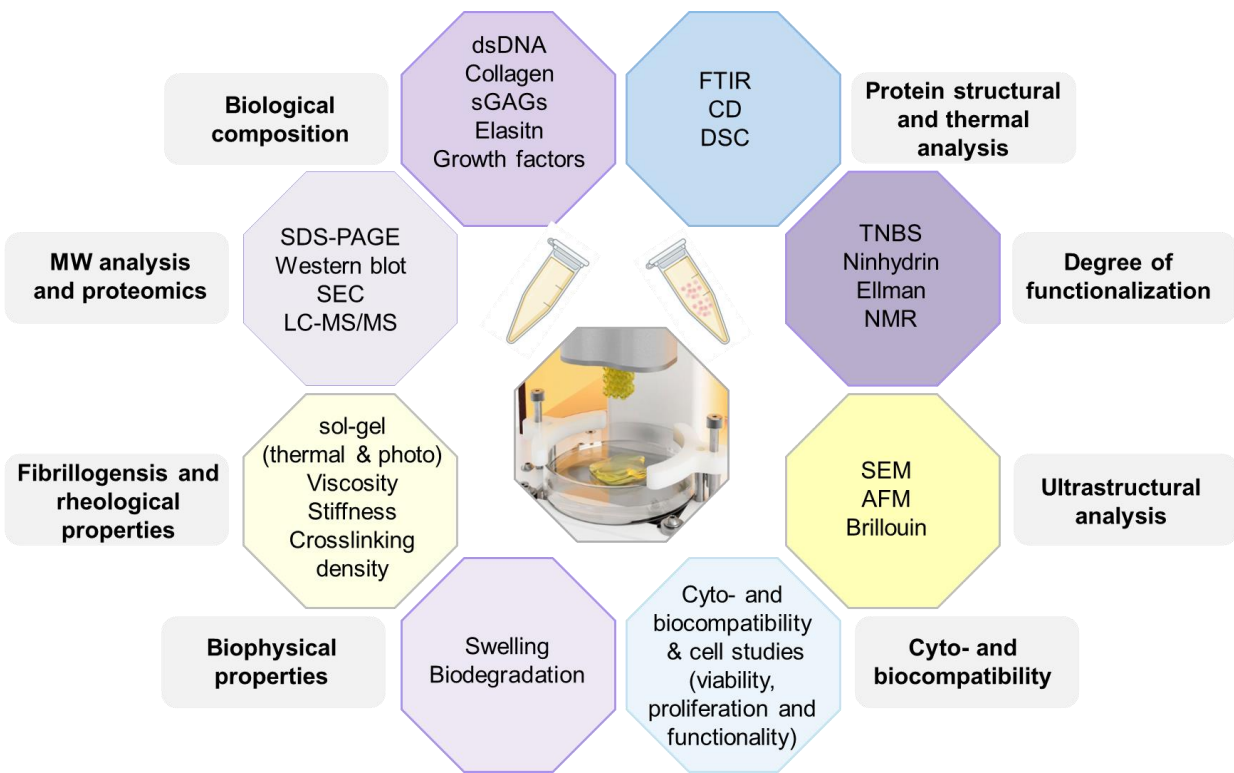


**Figure 10.** Characterization methods used for evaluation of dECM biomaterial resins and resulting 3D (bio)printed hydrogels. 3D bioprinter image is courtesy of CELLINK.

### 2.7.1. Biological composition, structural, and thermal characterization of dECM biomaterial resins

Evaluating the success of decellularization and the quality of dECM-based biomaterial resins involves several key biochemical assays to ensure consistency, bioactivity, and functionality. The first step is to confirm successful decellularization by measuring residual dsDNA, commonly using commercial assays such as AccuBlue™ [15] and Quant-iT™ PicoGreen™ [39] dsDNA assays. AccuBlue™ is a colorimetric assay that quantifies dsDNA based on dye binding, resulting in a measurable color change. PicoGreen™ is a fluorescent assay that binds selectively to dsDNA, significantly increasing fluorescence for the detection of low DNA concentrations with high sensitivity. These assays ensure dsDNA content is below recommended thresholds, confirming effective decellularization. Matrix proteins and glycoproteins, such as collagen, elastin, and

sulfated GAGs, are crucial for the resilience and hydration of the ECM. Their presence can be qualitatively detected using customized or commercial assays. For collagen, the chloramine-T [113] and Sircol™ Soluble Collagen assay [39] estimate collagen content. The chloramine-T assay measures hydroxyproline, which is directly related to the total collagen amount in digested dECM. The Fastin™ Elastin Assay Kit [39] detects elastin and the dimethylmethylene blue (DMMB) [9] and Blyscan™ GAGs Assay Kit [39] detect sGAGs. Preserving these key components through processing steps is vital for maintaining ECM characteristics. Additionally, matrix proteins and glycoproteins can be qualitatively assessed through staining techniques [36]. To address bioactivity, residual growth factors and cytokines in digested dECM solutions are detected using commercial ELISA-based growth factor arrays [38,114]

Protein fragments in digested dECM can be qualitatively assessed using SDS-polyacrylamide gel electrophoresis (SDS-PAGE), which separates denatured proteins by size [60]. Specific proteins can then be identified with Western blot analysis using monoclonal antibodies [60]. Size exclusion chromatography (SEC) can complement SDS-PAGE by analyzing molar mass distribution, although it has been primarily applied to acid-soluble collagen and gelatin rather than digested dECM [115]. For extensive protein fragmentation and analysis, proteomics via liquid chromatography coupled with tandem mass spectrometry (LC-MS/MS) can be employed. This technique determines the components of digested dECM by comparing the generated protein fragments to a protein database. Proteomic analysis has revealed that while dECM bioinks from cornea, heart, liver, and skin tissues share a similar protein composition, each tissue also possesses a unique set of tissue-specific components [116].

Fourier-transform infrared (FTIR) spectroscopy, circular dichroism (CD) spectroscopy, and differential scanning calorimetry (DSC) are key techniques for assessing the structural and thermal properties of dECM biomaterials. These methods provide a comprehensive understanding of the biochemical composition, secondary structure, and thermal stability of dECM, crucial for developing consistent and functional biomaterial resins for 3D bioprinting. FTIR and CD spectroscopy are employed to study the collagen secondary structure in dECM materials. FTIR can assess the integrity of the collagen triple helix by analyzing the amide I, II and II bands, where changes in these bands can indicate cross-linking or denaturation [98,104]. CD spectroscopy detects  $\alpha$ -helices,  $\beta$ -sheets, and coils, and monitors conformational changes during dECM processing to ensure no denaturation in the final biomaterial resins [104]. DSC measures the thermal stability and

denaturation properties of proteins in dECM by recording heat flow associated with protein denaturation as the temperature increases [117,118]. This reveals thermal transitions and stability of ECM components, critical for understanding the impact of different decellularization protocols on dECM structural integrity [117,118].

### 2.7.2. *Methods for confirming the chemical modifications in dECM biomaterial resins*

Confirming the success of the modification process in photocrosslinkable dECM biomaterial resins is crucial. Reagents like methacrylic anhydride (MA), glycidyl methacrylate (GMA), carbic anhydride (CA), and Traut's reagent have been used to functionalize dECM biomaterials, primarily reacting with the amine groups of lysine residues and, in the case of GMA, potentially with hydroxyl groups [37]. Given the complex protein composition of dECM, the exact functionalization mechanisms and reaction sites are not fully understood. Chromogenic analytical assays such as TNBS (2,4,6-Trinitrobenzene sulfonic acid), ninhydrin, and Ellman's are employed to detect and confirm these chemical modifications. TNBS and ninhydrin assays quantify free primary amines by producing a chromogenic yellow or purple product, respectively, measurable by spectrophotometry. These assays provide an indirect measure of the degree of functionalization (DOF) by indicating the reduction in free amine groups after modification compared to unmodified controls [105,119]. Ellman's assay quantifies free sulfhydryl groups introduced by reagents such as Traut's reagent. Ellman's reagent, known as DTNB (5,5'-dithiobis-(2-nitrobenzoic acid)), reacts with these free sulfhydryl groups to produce a yellow-colored product measurable by spectrophotometry. This assay directly measures thiol-functionalization by detecting increases in thiol groups content in the dECM [105,106]. To ensure accurate results, it is essential to compare with unmodified dECM, as naturally present thiol groups in the dECM from cysteine residues could affect the results.

Nuclear Magnetic Resonance (NMR) spectroscopy can directly identify and quantify the photo-sensitive functional groups introduced during chemical modification [98]. NMR detects magnetic properties of atomic nuclei, providing detailed structural information. By integrating peaks of the introduced functional groups and comparing them to unmodified dECM controls and an internal standard like 3-(trimethylsilyl)propionic acid-d<sub>4</sub> sodium salt (TMSP), NMR allows precise measurement of their content. Kiyotake *et al.* found that when functionalizing cartridge dECM with MA and GMA, assays like TNBS quantify the functionalized amine groups

(methacrylamides), neglecting the functionalized hydroxyl groups (methacrylates) [37]. NMR differentiates between these chemical groups, as methacrylamides and methacrylates exhibit distinct chemical shifts due to their different electronic environments and structures, providing detailed insights into the functionalization process.

### 2.7.3. Gelation kinetics and rheological properties of dECM biomaterial resins and hydrogels

Turbidimetric gelation kinetics measures the turbidity of collagen-rich dECM solutions as they transition from sol to gel, indicating collagen self-assembly, through light scattering by the developing network [86]. Variations in gelation kinetics among different dECM pre-gels are due to differences in protein composition, with specific ratios and types of proteins such as collagen, elastin, and glycoproteins significantly influencing the self-assembly process and the structural properties of the resulting physically crosslinked gels [35]. For example, the time required to reach 95% of the final turbidity was longer for porcine urinary bladder matrix hydrogels (~21 min) compared to brain (~15 min) and spinal cord ECM hydrogels (~12 min) under the same conditions [75].

By studying gelation kinetics under various conditions, such as pH, temperature, and macromer and salt concentrations, optimal gelation parameters can be determined, thereby enhancing the consistency and functionality of dECM-based biomaterials. The impact of enzymatic or chemical modifications on the gelation properties of dECM has significant effects on the pre-gel viscosity, and therefore, stiffness of the physically crosslinked gel. Excessive or longer enzymatic digestion times produce shorter protein fragments, resulting in lower viscosity and reduced stiffness, while insufficient or shorter digestion times maintain longer fragments, increasing these properties. Pouliot *et al.* demonstrated that pepsin digestion of lung dECM is time-dependent, significantly affecting protein concentration, fragment size, turbidity, viscosity, gelation potential, Young's modulus, as well as cell viability and metabolic activity [60]. Chemical modifications can alter molecular weight, add/shield charges, and change hydrophobicity/ hydrophilicity, impacting self-assembly and viscosity of the dECM resins. For photosensitive vat 3D (bio)printing, low-viscosity biomaterial resins (0.25–10 Pa.s) are preferred as they enhance curing rates, reduce construction time, and facilitate cleaning [26]. Shear viscosity, which is influenced by molecular weight, concentration, and fiber chain entanglements, is a crucial parameter to assess [120]. While increased

viscosity from physical crosslinking is essential for extrusion bioprinting due to the shear-thinning behavior of dECM biomaterial resins, which decreases viscosity under high shear stress, this is not necessary for vat photopolymerization [32]. However, dual crosslinking (physical and light induced) of unmodified dECM has been proposed to improve shape fidelity, cell viability, and functionality in vat 3D printing [44,98].

Besides turbidimetric gelation kinetics measurements, the thermal sol-gel transition of unmodified dECM pre-gels can be tracked in real-time using a rheometer by increasing the temperature from approximately 4°C to 37°C under physiological conditions (salt concentration and pH) [32,35]. Similarly, the light-induced sol-gel transition in both unmodified and chemically modified, photo-sensitive dECM biomaterial resins can be monitored using an in-situ photorheometer, which studies photocrosslinking kinetics [15]. Measuring the bulk stiffness of acellular hydrogel scaffolds after physical or light-induced gelation is essential, especially for those intended for cell encapsulation [35]. This ensures that the constructs maintain the desired stiffness range for specific organ/tissue or cells. These techniques allow for precise optimization of gelation and crosslinking conditions, enhancing the reliability, performance, consistency, and functionality of dECM-based biomaterials. Turbidimetric gelation kinetics combined with detailed rheological analysis, such as pre-gel viscosity, real time physical and photo induced gelation as well as the bulk stiffness of physically or chemically crosslinked hydrogels, serve as quality control measures for dECM biomaterials to ensure reproducibility. Establishing baseline gelation kinetics and rheological properties for a specific dECM type allows for detection of deviations in future batches, with consistent profiles indicating stable processing and composition, while significant variations may suggest preparation issues or changes in source material. By meticulously analyzing the gelation behavior and mechanical properties, researchers can enhance the reliability and functionality of these materials, paving the way for their successful implementation in various therapeutic and regenerative contexts.

#### *2.7.4. Ultrastructural characterization, surface morphology, and local micromechanical properties of dECM hydrogels*

For bioprinting with encapsulated cells, the presence of pores in 3D bioprinted hydrogels is crucial. Porosity significantly influences cell viability, proliferation, migration, and nutrient exchange.



Pores allow nutrients and oxygen to diffuse to the encapsulated cells while enabling the removal of waste products, essential for maintaining cell health and function within the dense hydrogel matrix [15,104,118]. Adequate porosity also facilitates cell migration and organization, which are critical for tissue formation and regeneration. Additionally, pores affect the hydrogel's mechanical properties, influencing its suitability for mimicking natural tissue environments. Scanning electron microscopy (SEM) is commonly used to visualize the internal and surface structures of hydrogels, providing high-resolution images to analyze pore size, distribution, and connectivity [121]. Nevertheless, SEM is inherently flawed because it requires extensive sample preparation, including fixation, dehydration, and sputtering, which can create artifacts from collapsed gel structures and potentially result in inaccurate assessments of microstructure and porosity [45].

Atomic force microscopy (AFM) is ideal for evaluating the surface morphology and roughness of dECM hydrogels in their natural wet state without any prior sample preparations [122,123]. In AFM, a sharp fine tip on a cantilever, controlled by piezoelectric motors, gently touches the hydrogel surface, enabling nanometer-scale scanning without damage. This makes it perfect for analyzing surface fibers and pores, especially for hydrogel surfaces prepared for cell seeding. However, AFM is limited to surface analysis and cannot access bulk microstructure. AFM also provides detailed information about the local mechanical properties, such as stiffness and viscoelasticity, useful for assessing the heterogeneity of the hydrogel surface [124]. Similarly, but more advanced, Brillouin spectroscopy analyzes the frequency shift of light scattered by sound waves in a material in a non-invasive and non-contact manner, providing information about surface and bulk characteristics of hydrogels, including mechanical properties and mesh size throughout the sample [125]. This technique is particularly useful for studying soft materials like hydrogels and biological tissues.

In conclusion, while the SEM is widely used for characterizing dECM hydrogels, there is limited use of AFM and no reported applications of Brillouin spectroscopy in this context. This highlights an opportunity for further exploration of these advanced techniques to enhance our understanding of dECM hydrogels

#### *2.7.5. Swelling, crosslinking density, degradation, and matrix remodeling of dECM hydrogels*

The hydrogel's bulk stiffness and mesh size (type and distribution) are interconnected factors that influence its water content. Hydrogels with lower crosslinking density typically have larger mesh sizes, which allow them to retain more water and facilitate efficient nutrient transport and cellular

activities, crucial for tissue constructs [15,126]. The water content or swelling properties of dECM 3D printed hydrogels are measured by the swelling ratio, defined as the weight of the hydrogel in its swollen state divided by its dry weight [15]. This water absorption capability is also significantly influenced by the components of the dECM. A higher concentration of GAGs (including hyaluronic acid and heparan sulfate) increases the hydrogel's water content and swelling capacity, whereas a dense collagen network may limit swelling to preserve structural integrity. Additionally, incorporating functional groups such as carboxyl or hydroxyl can enhance the solubility of collagen polymer chains in aqueous solutions, thereby improving the hydrogel's swelling properties [127].

The crosslinking density of 3D printed dECM resins, which determines the mesh size, is influenced by factors such as the polymer DOF, light intensity and exposure time, and the kinetics of crosslinking, including polymer and photoinitiator concentrations [45]. It can be assessed indirectly through swelling ratio, elastic modulus ( $G'$ ), or spectrophotometrically using chemical reagents like potassium permanganate to detect double bond moieties in polymers [126,128]. Despite its importance, crosslinking density is often overlooked in dECM biofabrication studies. More research is needed to develop accurate methods for measuring and considering the crosslinking density of bioprinted dECM hydrogels.

Biodegradability is crucial for hydrogels in tissue engineering as it influences cell interactions and simulates natural tissue environments. Hydrogels degrade through hydrolytic or enzymatic mechanisms. Hydrolysis occurs via hydrolytically unstable bonds throughout the hydrogel, while enzymatic degradation is localized, driven by cell-mediated proteases like matrix metalloproteinases (MMPs). The degradation rate can be tuned by the crosslinking density and the nature of the crosslinked bonds (non-covalent or covalent) in the hydrogel network [126]. For acellular dECM 3D printed hydrogels, enzymatic degradation assays using enzymes like collagenase are used to evaluate degradability. This involves measuring the weight of degraded proteins or the remaining hydrogel by elapsing time [129]. Notably, methacrylation and photocrosslinking do not impede enzymatic degradation [15,129]. In cellular hydrogels, dECM hydrogels are rich in MMP-degradable proteins, offering numerous sites for enzymatic activity that remodels the matrix by degrading and reassembling its components [126].

#### *2.7.6. Sterilization and cytocompatibility of dECM Derived Hydrogels*

To prepare biomaterial resins, processed and freeze-dried dECM materials are initially solubilized in either basic or acidic solutions. Reliable and effective sterilization of acellular hydrogel 3D printed scaffolds can be performed at the final step before storage or cell seeding for ease of handling. If sterilization is not performed last, all processing steps until 3D printing must be conducted under sterile conditions, which is especially challenging for large-scale experiments. For cellular hydrogels, effective sterilization must occur on the biomaterial resins before cell encapsulation and 3D bioprinting, preferably on the freeze dried dECM before solubilization. The sterilization process must sanitize the hydrogels or biomaterial resins while minimizing destructive effects such as protein crosslinking, chain scission, and denaturation, which could compromise the bioactivity and gelation ability of dECM-based materials [53].

Various inexpensive and lab-accessible sterilization methods include filtration, steam (autoclaving), UV irradiation, and chemical reagents such as peracetic acid and ethanol, each with its own pros and cons [53]. Filtration is ideal for preserving the properties of liquid proteins but is unsuitable for viscous forms like dECM formulations [130]. Steam sterilization is highly effective but significantly alters dECM properties, causing protein denaturation, making it unsuitable for dECM resins or hydrogels [131]. UV irradiation offers a less destructive alternative but is not yet approved for clinical use and is considered more of a disinfection method [132]. Chemical sterilization with peracetic acid and ethanol is widely used, separate or in combination, but has limitations due to potential corrosive effects and/or incomplete sterilization [53,97,133]. In conclusion, selecting the appropriate sterilization method is crucial for maintaining the functional integrity of dECM and preparing it for cell seeding in successful bioprinting applications.

Cytocompatibility studies of dECM hydrogels are crucial for confirming the absence of cytotoxicity and indirectly assessing the quality of dECM resins, including their sterilization process, bioactivity, and structural integrity. These tests can be conducted in vitro cultures by seeding cells onto 2D acellular hydrogel scaffolds after 3D printing, where cells grow as monolayers, or by encapsulating cells within bioresins and bioprint 3D cellular hydrogels, allowing cells to grow inside the 3D bioprinted construct, or by directly applying dECM resins in vivo [15,129]. For both 2D and 3D hydrogel forms, cellular responses such as viability, proliferation, and functionality are assessed to ensure the material is free from cytotoxicity. Beyond in vitro cultures, in vivo studies provide a more comprehensive evaluation of the biocompatibility of dECM hydrogels [134]. By implanting the material into animals, researchers can observe the complete

biological response, including immune reactions, integration with surrounding tissues, and potential long-term effects such as scar formation or fibrosis [32,45].

## 2.8. Adjusting bioresin properties and bioprinting parameters: ideal bioresin and bioprinting window

To effectively formulate biomaterial resins and bioresins for vat 3D bioprinting, it is crucial to meet specific criteria in three categories: functionality, printability, and biocompatibility. These elements together define the optimal characteristics of an “ideal bioresin” (**Figure. 11A**) [134]. The dECM biomaterial, which contains photoactive groups, is inherently bioactive, non-immunogenic, non-toxic, and water-soluble. Once appropriately sterilized, solubilized and neutralized, it is ready for immediate mixing with the PI solution and cell suspensions. The PI must also be water-soluble, non-toxic, and sterile when introduced to bioresin.

In bioprinting, when living cells are involved, the ideal bioresin balances high cell viability with excellent printing fidelity, forming the “biofabrication window” (**Figure 11B**) [135]. This requires careful control of viscosity, cell density, and crosslinking density. dECM biomaterial resin must flow freely before photocrosslinking to prevent excess material and over-crosslinking. When neutralized, dECM materials can physically crosslink at 37°C, but due to slow gelation kinetics, the viscosity does not change drastically; however, the bioprinting temperature still needs to be considered in vat bioprinting.

When mixing with cell suspensions, the cell-laden bioresin must be used immediately to avoid cell sedimentation and inhomogeneous cell distribution especially if the resin's viscosity is too low (see section 2.7.3) [26]. Cell densities in dECM formulations typically range from 1 to 50 million cells/mL, affecting the bioresin's physicochemical properties such as rheological and crosslinking properties, as cells occupy volume and hinder polymer chains crosslinking [45]. As a result, high cell densities can lead to several issues, including rapid nutrient depletion, toxic waste accumulation, physical crowding, and increased resin viscosity, which compromise printability and tissue structure. Conversely, low cell densities can result in poor tissue formation, reduced cellular communication, and slower maturation, all of which impact tissue functionality [136,137].

The crosslinking density must be optimized, involving precise management of the light source, intensity, exposure time, and resin and photoinitiator concentrations to ensure rapid solidification without harming cells [45]. This tuning aims to produce materials with desired mechanical

properties, such as stiffness, elasticity and appropriate degradation rates for biological functions and tissue integration. Achieving a balance between high cell viability and high printing fidelity is challenging. Generally, stiffer hydrogels with higher crosslinking density offer good mechanical properties and shape fidelity but are not ideal for cell housing. Conversely, soft hydrogels that create a tissue-like environment for living cell protection often lack the physical characteristics needed for printability and stability [134]. In conclusion, achieving the ideal bioresin for vat 3D bioprinting involves balancing multiple requirements to optimize cell viability and print fidelity, ensuring the creation of functional and structurally sound tissue constructs

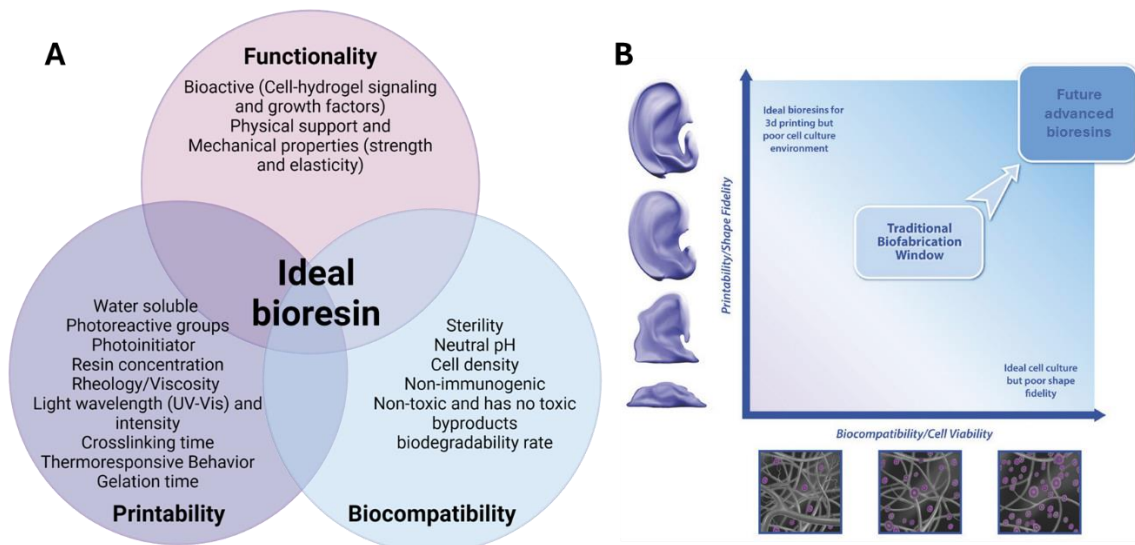


**Figure 11.** (A) specific criteria in three categories: functionality, printability, and biocompatibility. These elements together define the optimal characteristics of an ideal bioresin. (B) The biofabrication window describes the formulation of the traditional bioresins, which compromises the properties between structural fidelity and cell viability. A created using BioRender.com and B adapted from [138] with permission. Copyright © 2017 John Wiley and Sons.

## 2.9. dECM-based 3D tissue constructs and in vitro tissue models: liver and intestine

The evolution of in vitro tissue models spans a spectrum from basic 2D cell cultures to advanced systems like organ-on-a-chip and animal models. **Figure 12** showcases this progression, emphasizing the balance between throughput and physiological relevance. This thesis focuses on

3D bioprinted liver hydrogels and intestinal scaffolds, integrating the latter with intestinal organoids and fluidic systems. These innovative approaches offer a compelling combination of enhanced physiological relevance over 2D cell cultures and greater throughput compared to in vivo animal models.

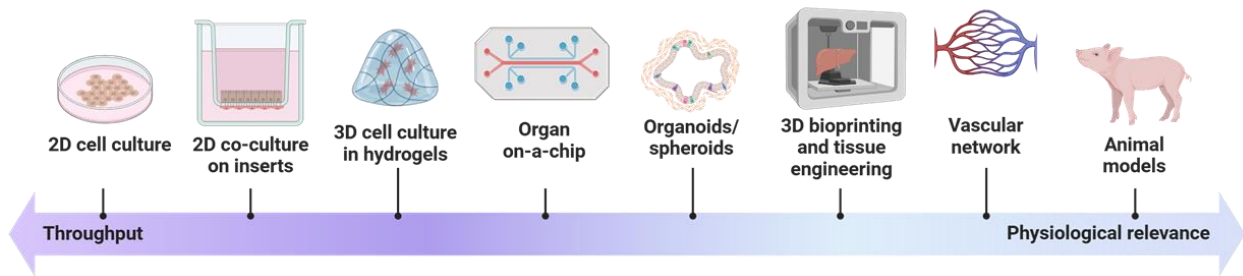


**Figure 12.** The evolution of in vitro tissue models, ranging from 2D cell cultures to advanced organ-on-chip systems and animal models, illustrating the trade-off between throughput and physiological relevance. Adapted from [139] and licensed under CC BY.

Bioprinted dECM-based in vitro models of liver and intestinal tissues are particularly important due to their roles in metabolism, absorption, and detoxification, which are challenging to replicate. The liver is central to detoxification and protein synthesis, while the intestine is crucial for nutrient absorption and immune responses [119,140]. Functional in vitro models of these two organs are essential for understanding their functions under normal and pathological conditions and are invaluable for developing therapeutic interventions [32]. To achieve this, constructing these models requires integrating complex geometries, varied mechanical properties, multiple cell types, and functional capabilities that mirror natural organs. Biofabrication provides the tools to build accurate and functional in vitro models of the intestine and liver, advancing our ability to study their functions, interactions, and responses to treatments in a controlled setting [32].

For instance, several liver tissue constructs have been 3D bioprinted using dECM-based bioresins, either by mixing unmodified dECM in the photocrosslinkable bioink and crosslinking with light in the presence of LAP, where the dECM is not part of the covalently crosslinked hydrogel network, or by chemically modifying the dECM to be incorporated into the covalently crosslinked network. One example is Ma *et al.* who employed a UV-based DLP printer to bioprint unmodified porcine liver dECM/GelMA bioresin, modulating stiffness through light exposure, and found that encapsulated HepG2 cells within the hydrogel showed varying responses depending on the

stiffness, emphasizing the importance of mechanical properties [97]. Similarly, Mao *et al.* bioprinted thicker constructs with porcine liver dECM and GelMA, enhancing printing resolution and promoting hepatocyte growth and function [96]. In another study, methacrylated rat liver dECM and PCL methacrylate were used with a visible light DLP printer to create a hybrid network, forming soft yet highly crosslinked multilayered acellular hydrogels [141]. Moreover, Rezaei *et al.* modified porcine liver dECM to create dECM-GMA/GelMA bioresin, which was seeded with HepG2 cells and used for SLA bioprinting in the presence of EY as PI, resulting in enhanced cell proliferation and liver functionality [129].

In contrast, the development of 3D bioprinted intestinal constructs using vat technology and dECM resins, whether from the small intestine or colon, is still in its early stages. Recently, a dSIS-NB/4-arm thiolated PEG bioresin was developed and crosslinked using a DLP 3D bioprinter with LAP as PI. The resulting 3D bioprinted dSIS-NB hydrogels supported a highly interconnected microvascular network with human umbilical vein endothelial cells (HUVECs) after just three days of *in vitro* culture [104]. Additionally, a bioresin based solely on dSIS-MA from porcine small intestinal submucosa was synthesized and crosslinked using DLP 3D printing in the presence of LAP to form acellular 2D and 3D villi-shaped hydrogel scaffolds that supported the growth of both Caco-2/HT29-MTX and terminal-ileum organoid-derived primary intestinal stem cells (ISCs) monolayers from human biopsy [15]. Despite the current scarcity, these studies introduce a new level of natural complexity, physiological relevance and *in vivo* mimicry by integrating angiogenesis or organoid-derived human ISCs with biofabrication [142]. However, these *in vitro* models currently operate under static culture conditions and do not fully replicate the dynamic mechanical forces that cells encounter in the body, which are crucial for promoting accurate cellular responses and tissue organization.

To address these limitations, advancements in the organ-on-chip (OoC) technology that integrates organoids and microfluidic systems can significantly enhance the physiological relevance of *in vitro* tissue models for both the intestine and liver [143]. This revolutionary tool creates reliable *in vitro* models with relatively high throughput of functional human organ units by using microfluidic devices to impart organ functions to human cells, allowing culture under physiologically relevant conditions, such as fluid shear stress, a mechanical force generated by fluid flow [140]. While both liver and gut on-chip are important, this thesis focuses on the gut, particularly the terminal ileum in the small intestine.

Biopsy-derived intestinal organoids, which are 3D miniaturized versions of organs with stem cell potential, can be grown in Matrigel™. These organoids can then be subsequently opened and seeded onto 2D or 3D surfaces to form tight epithelial barriers that more accurately mimic the natural architecture and function of human intestinal tissues, including mucus production, providing a precise and personalized approach [144,145]. Notably, shear stress has been identified as essential for the development of crypt-villus architecture in gut-on-a-chip devices [139]. Nevertheless, the field of gut-on-chip research has primarily concentrated on the colon and other parts of the intestines, with comparatively less attention given to the small intestine, especially the terminal ileum, and its mucus-related functions [144-151].

A significant limitation in current gut-on-chip models is the absence of bioactive hydrogels that precisely represent the native small intestinal submucosa (SIS). Typically, semi permeable polydimethylsiloxane (PDMS) membranes in these microfluidic devices are coated with a thin layer of either collagen or Matrigel™, rather than a thicker hydrogel ( $\geq 1$  mm) that mimics the in vivo ECM [139,144-151]. Although hydrogel-integrated microfluidic systems have been developed for various stem cell types, there is a distinct lack of systems designed specifically for intestinal ISCs [150,151]. Additionally, these systems generally operate at a microscale, which does not precisely represent the true size and scale of tissues or organs, thereby limiting the use of thicker hydrogels and large cell complexes. For example, human midbrain-specific organoids (hMOs) [152] range from 0.5 to 2 mm to exhibit physiologically scaled metabolism, and cumulus-oocyte complexes (COCs) [153] can grow and mature to dimensions measured in centimeters in diameter during the preovulatory maturation phase. Both of these studies have been conducted in millifluidic devices that better replicate the physiological environment.

Moreover, several factors beyond size or scale influence the choice between milli- and microfluidic systems; for instance, Berger *et al.* opted for millifluidic systems over microfluidic ones due to their relatively high flow rates with larger volumes, which ensure adequate nutrient and oxygen supply while reducing shear forces on hMOs [152]. This is particularly important because dense organoids have a high metabolic rate, consuming significantly more oxygen and nutrients as they grow. Additionally, millifluidic systems, with their high volume-to-surface ratio, do not require frequent media changes, thereby minimizing the stress and potential damage to organoids caused by frequent handling and media changes [152].



Millifluidic systems utilize simple peristaltic pumps that are low-cost and compatible with standard cell culture incubators; these pumps create a gentle, pulsatile flow of media by compressing and releasing flexible tubing, making the method both cost-effective and well-suited to the limited space and conditions of standard incubators [154]. Furthermore, the construction of millifluidic chambers has become simpler with the advent of 3D printing technology. With modern 3D printers, researchers can produce precise and customized millifluidic components, allowing them to easily design and fabricate these systems in-house. This accessibility and ease of production have significantly advanced the development and application of millifluidic systems in various biological research fields [155].

In conclusion, while significant advancements have been made in developing bioprinted dECM-based in vitro models for liver and intestinal tissues, challenges remain, particularly in accurately replicating the native extracellular environments and dynamic mechanical forces. The integration of millifluidic systems and advanced biofabrication techniques, such as 3D bioprinting, holds promise for creating more physiologically relevant models with higher throughput. These innovations not only enhance our understanding of organ functions and interactions under normal and pathological conditions but also pave the way for more effective therapeutic interventions.

### 3. OBJECTIVES

This thesis, through a series of interconnected studies, explores advanced strategies for utilizing dECM in (bio)printing and for tissue modeling, focusing on dECM enzymatic solubilization methods, establishing bioresin formulations, and demonstrating the utility of these materials in creating dynamic in vitro models, particularly for mimicking the terminal-ileum in the gastrointestinal (GI) tract.

Current methods for digesting dECM while preserving its capacity for subsequent thermally induced physical gelation are limited, primarily relying on animal-derived pepsin that poses zoonotic risks, making it suboptimal for human dECM applications. Alternative enzymes could offer safer, animal-free solutions while maintaining the integrity and bioactive properties of dECM pre-gels. We propose that non-animal-based enzymes, including plant-derived papain and bacterial-derived collagenase and  $\alpha$ -amylase, are promising candidates for dECM digestion, not only due to their animal-free nature but also due to their cost-effectiveness compared to pepsin. Our approach involves exploring these enzymes for digesting porcine liver dECM, determining the most effective one based on their digestion efficiency, maximum preservation of the original dECM properties, and subsequent thermo-gel formation of the pre-gels. The performance of each enzyme will be thoroughly evaluated through comprehensive chemical, physical, and biological characterization.

Building on the solubilized porcine liver dECM from the first study, our focus shifts to developing functionalized, photocrosslinkable dECM bioresins for vat photopolymerization. There is currently a scarcity of bioresins formulated specifically for vat bioprinting, particularly those based solely on dECM biomaterials. Our work leverages the inherent bioactive properties of dECM and the high-resolution capabilities of vat bioprinters and posits that grafting-specific photocrosslinkable groups onto the dECM could enhance resin properties, thereby improving their application in 3D bioprinting. We hypothesize that functionalizing dECM with glycidyl methacrylate (GMA) instead of conventional methacrylic anhydride (MA) will enhance the physicochemical properties and performance of the dECM bioresins in vat bioprinting because of the additional hydroxyl groups that have capacity to increase the material hydrophilicity. Our strategy involves a systematic and comprehensive side-by-side comparison of the two chemically distinct methacryloylated dECM bioresins starting from their synthesis and ending to the final (bio)printed acellular and cellular

hydrogels. This includes a thorough evaluation of resin structural integrity, photocrosslinking characteristics, and the performance of 3D (bio)printed constructs, focusing on stiffness, swelling, cell compatibility, degradation kinetics, and long-term cell culture performance.

Finally, building on the findings from the development of photocrosslinkable dECM bioresins, we aim to explore the integration of the photocrosslinked dECM hydrogels into a millifluidic system for advanced in vitro intestinal tissue modeling. Unlike conventional intestinal models that rely on the static culture of organoid-derived ISC monolayers seeded on Matrigel<sup>TM</sup>-coated synthetic membranes, we propose developing advanced mucus-producing ISC-based models using 3D-printed biomimetic hydrogel scaffolds, with the application of dynamic medium flow in the cell culture. Instead of chemically-triggered differentiation of ISCs, we focus on studying the influence of the applied shear stress on cell differentiation and mucus production, given that the mucus is essential for the intestinal barrier and plays a critical role in gut homeostasis and defense. We designed an easy-to-make and cost-effective 3D-printed tissue chamber to host cell-seeded hydrogels synthesized from bioactive, methacrylated small intestinal submucosa (dSIS-MA) enabling their exposure to adjustable apical laminar shear stress. We will first evaluate the chamber's performance with HT29-MTX cells, then investigate the shear stress-induced multi-lineage differentiation of human ISCs, focusing on mucus production. This assessment will include biochemical and biophysical characterization of the biomaterials and chamber, along with biological characterization of the ISC differentiation under shear stress, including evaluation of mucus production and cell functionality.

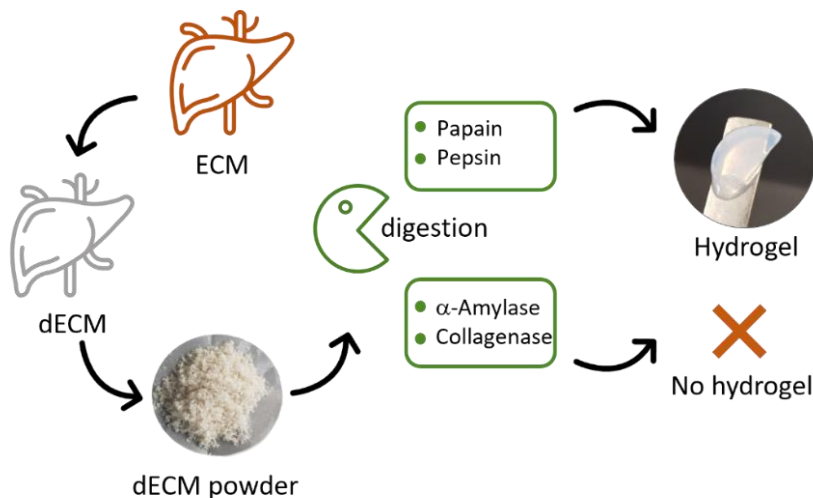
Through these objectives, this thesis seeks to significantly enhance the efficiency and functionality of engineered tissues via developing and optimizing digested thermo-gelling dECM, photocrosslinkable dECM biomaterial resins and bioresins, and the application of dynamic mechanical stimuli to create advanced in vitro models. The research presented in this thesis will provide a robust foundation for future applications in (bio)printing of hydrogels and scaffolds for regenerative medicine and tissue engineering, ultimately aiming to develop advanced solutions for complex biomedical challenges.

## 4. PUBLICATIONS AND MANUSCRIPTS

### 4.1. Papain-Based Solubilization of Decellularized Extracellular Matrix for the Preparation of Bioactive, Thermosensitive Pre-Gels

Almalla, A.; Elomaa, L.; Bechtella, L.; Daneshgar, A.; Yavvari, P.; Mahfouz, Z.; Tang, P.; Kokschi, B.; Sauer, I.; Pagel, K.; Hillebrandt, K. H.; Weinhart, M.

*Biomacromolecules* 2023, 24 (12), 5620-5637. <https://doi.org/10.1021/acs.biomac.3c00602>



This study identifies papain as a cost-effective and plant-based enzyme alternative to animal-derived pepsin for solubilizing liver dECM. Unlike other investigated enzymes, papain preserved both a substantial amount of bioactive components of dECM and maintained gelation properties of the collagen protein fragments, making it highly suitable for creating bioactive hydrogels. The resulting papain-digested hydrogels demonstrated comparable gelation properties and biological activity to conventional pepsin-treated dECM, promoting HepaRG liver cell growth and proliferation. Papain's cost-effectiveness and animal-free nature make it suitable for large-scale production and human dECM digestion, eliminating zoonotic disease risks.

#### Contributions of authors

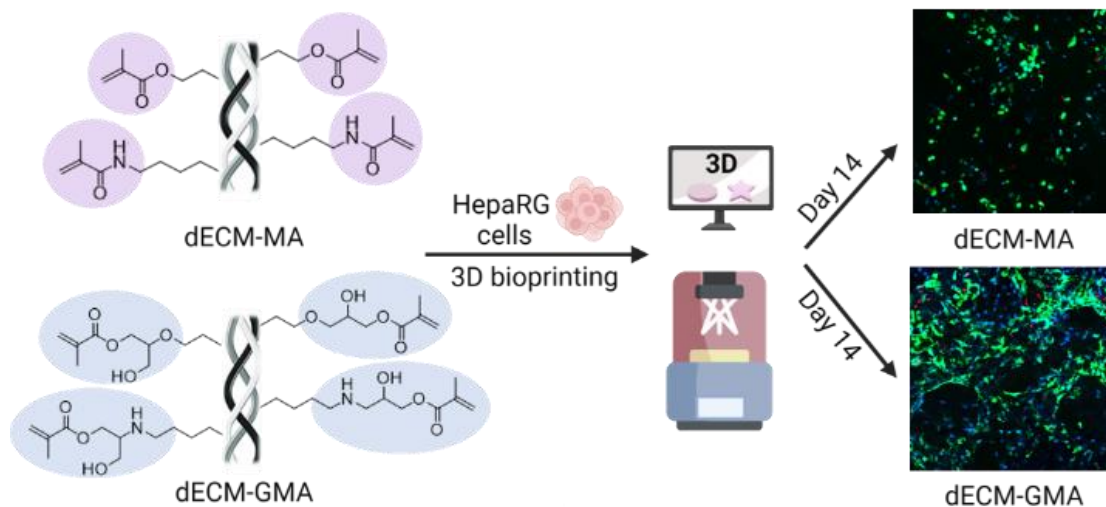
Conceptualization: A.A., L.E., M.W. Methodology: A.A., L.E., L.B., A.D., P.Y., Z.M., P.T., M.W. Writing – original draft: A.A. Writing – review & editing: A.A., L.E., B.K., I.M.S., H.K.H., K.P., L.B., A.D., P.Y., Z.M., M.W. Visualization: A.A., L.E., L.B., A.D., P.Y., Z.M. Validation: A.A. Investigation: A.A., L.E., L.B., A.D., P.Y., Z.M. Formal analysis: A.A., L.E., L.B., A.D., P.Y., Z.M. M.W. Data curation: A.A., L.E. Supervision: L.E., M.W. Funding acquisition: K.P., B.K., I.M.S., H.K.H., M.W. Resources: M.W. Project administration: M.W.

## 4.2. Chemistry Matters: A Side-by-Side Comparison of Two Chemically Distinct Methacryloylated dECM Bioresins for Vat Photopolymerization

Almalla, A.; Elomaa, L.; Fribiczner, N.; Landes, T.; Tang, P.; Mahfouz, Z.; Kokschi, B.; Hillebrandt, K.H.; Sauer, I.M.; Heinemann, D.

*Biomaterials Advances* 2024, 160, 213850. <https://doi.org/10.1016/j.bioadv.2024.213850>

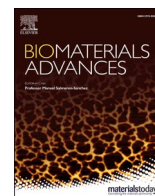
This article is licensed under a [Creative Commons Attribution 4.0](https://creativecommons.org/licenses/by/4.0/) license



This research systematically compares two methacryloyl-functionalized dECM bioresins prepared with glycidyl methacrylate (GMA) and methacrylic anhydride (MA) as the methacryloylation agent. The study reveals how these different chemical modifications impact the photocrosslinking characteristics of the biomaterial resins, structural integrity, swelling, cell compatibility, and degradation kinetics of the photocrosslinked hydrogels. The results show that dECM-GMA hydrogels exhibit superior hydrophilicity, cell compatibility, and faster biodegradation compared to dECM-MA hydrogels. These insights are important for optimizing bioresins used in vat bioprinting, enabling the development of tailored biomaterials for various tissue engineering applications with rational molecular design.

### Contributions of authors

Conceptualization: A.A., K.H.H., I.M.S., M.W. Methodology: L.E., B.K., K.H.H., I.M.S., D.H., S.S., M.W. Writing – original draft: A.A. Writing – review & editing: L.E., B.K., I.M.S., D.H., M.W. Visualization: A.A., N.F., T.L. Validation: A.A. Investigation: A.A., N.F., T.L., P.T., Z.M. Formal analysis: A.A., L.E., N.F., T.L., P.T., Z.M., K.H.H., M.W. Data curation: A.A., N.F., T.L., P.T., Z.M. Supervision: L.E., D.H., S.S., M.W. Funding acquisition: B.K., I.M.S., S.S., M.W. Resources: M.W. Project administration: M.W.



## Chemistry matters: A side-by-side comparison of two chemically distinct methacryloylated dECM bioresins for vat photopolymerization

Ahed Almalla<sup>a</sup>, Laura Elomaa<sup>a</sup>, Nora Fribiczler<sup>b</sup>, Timm Landes<sup>c,d,e</sup>, Peng Tang<sup>a</sup>,  
Zeinab Mahfouz<sup>a</sup>, Beate Kokschi<sup>a</sup>, Karl Herbert Hillebrandt<sup>f,g,h</sup>, Igor Maximilian Sauer<sup>f,h</sup>,  
Dag Heinemann<sup>c,d,e</sup>, Sebastian Seiffert<sup>b</sup>, Marie Weinhart<sup>a,h,i,\*</sup>

<sup>a</sup> Institute of Chemistry and Biochemistry, Freie Universität Berlin, Takustr. 3, 14195 Berlin, Germany

<sup>b</sup> Department of Chemistry, Johannes Gutenberg Universität Mainz, Duesbergweg 10-14, 55128 Mainz, Germany

<sup>c</sup> HOT – Hanover Centre for Optical Technologies, Leibniz Universität Hannover, Nienburger Straße 17, 30167 Hannover, Germany

<sup>d</sup> Institute of Horticultural Productions Systems, Leibniz Universität Hannover, Herrenhäuser Straße 2, 30419 Hannover, Germany

<sup>e</sup> Cluster of Excellence PhoenixD, Leibniz University Hannover, Welfengarten 1a, 30167 Hannover, Germany

<sup>f</sup> Experimental Surgery, Department of Surgery, CCM|CVK, Charité – Universitätsmedizin Berlin, Augustenburger Platz 1, 13353 Berlin, Germany

<sup>g</sup> Berlin Institute of Health at Charité – Universitätsmedizin Berlin, BIH Biomedical Innovation Academy, BIH Charité Clinician Scientist Program, Charitéplatz 1, 10117 Berlin, Germany

<sup>h</sup> Cluster of Excellence Matters of Activity, Image Space Material funded by the Deutsche Forschungsgemeinschaft (DFG, German Research Foundation) under Germany's Excellence Strategy – EXC 2025, Germany

<sup>i</sup> Institute of Physical Chemistry and Electrochemistry, Leibniz Universität Hannover, Callinstr. 3A, 30167 Hannover, Germany

### ARTICLE INFO

#### Keywords:

Biopolymer resin  
Digital light processing  
Photorheology  
Methacrylation  
Liver matrix  
Bioink

### ABSTRACT

Decellularized extracellular matrix (dECM) is an excellent natural source for 3D bioprinting materials due to its inherent cell compatibility. In vat photopolymerization, the use of dECM-based bioresins is just emerging, and extensive research is needed to fully exploit their potential. In this study, two distinct methacryloyl-functionalized, photocrosslinkable dECM-based bioresins were prepared from digested porcine liver dECM through functionalization with glycidyl methacrylate (GMA) or conventional methacrylic anhydride (MA) under mild conditions for systematic comparison. Although the chemical modifications did not significantly affect the structural integrity of the dECM proteins, mammalian cells encapsulated in the respective hydrogels performed differently in long-term culture. In either case, photocrosslinking during 3D (bio)printing resulted in transparent, highly swollen, and soft hydrogels with good shape fidelity, excellent biomimetic properties and tunable mechanical properties (~ 0.2–2.5 kPa). Interestingly, at a similar degree of functionalization (DOF ~ 81.5–83.5 %), the dECM-GMA resin showed faster photocrosslinking kinetics in photorheology resulting in lower final stiffness and faster enzymatic biodegradation compared to the dECM-MA gels, yet comparable network homogeneity as assessed via Brillouin imaging. While human hepatic HepaRG cells exhibited comparable cell viability directly after 3D bioprinting within both materials, cell proliferation and spreading were clearly enhanced in the softer dECM-GMA hydrogels at a comparable degree of crosslinking. These differences were attributed to the additional hydrophilicity introduced to dECM via methacryloylation through GMA compared to MA. Due to its excellent printability and cytocompatibility, the functional porcine liver dECM-GMA biomaterial enables the advanced biofabrication of soft 3D tissue analogs using vat photopolymerization-based bioprinting.

### 1. Introduction

Three-dimensional (3D) bioprinting is widely used to create in vitro tissue models replicating their natural in vivo counterparts. In clinical applications, it holds the potential for customized fabrication of

implantable cell-laden scaffolds to regenerate various human organs and tissues [1]. Ideally, these 3D-bioprinted structures provide encapsulated cells with natural tissue-like environments [2]. To achieve this, the bioprinting materials (i.e., bioinks and bioresins) must be selected carefully to create tissue-specific microenvironments that guide the

\* Corresponding author at: Institute of Physical Chemistry and Electrochemistry, Leibniz Universität Hannover, Callinstr. 3A, 30167 Hannover, Germany.  
E-mail addresses: [marie.weinhart@fu-berlin.de](mailto:marie.weinhart@fu-berlin.de), [marie.weinhart@pci.uni-hannover.de](mailto:marie.weinhart@pci.uni-hannover.de) (M. Weinhart).

<https://doi.org/10.1016/j.bioadv.2024.213850>

Received 7 February 2024; Received in revised form 25 March 2024; Accepted 5 April 2024

Available online 7 April 2024

2772-9508/© 2024 The Authors. Published by Elsevier B.V. This is an open access article under the CC BY license (<http://creativecommons.org/licenses/by/4.0/>).

growth and motility of embedded cells, ultimately leading to functional tissue formation [3–5]. Printing techniques are mostly classified into inkjet, extrusion and light-based 3D bioprinting. Despite their contributions, each method faces limitations. Inkjet bioprinters cannot process high-viscosity materials and high cell density due to nozzle clogging [6]. Extrusion bioprinters are generally more versatile in the selection of bioinks but often face resolution challenges [7]. Vat photopolymerization is a potent light-based 3D printing technique that facilitates layer-by-layer photopolymerization of a photoreactive resin in the presence of a suitable photoinitiator by projecting light onto the material according to a predefined computer-aided design (CAD) model [8]. Major technical advancements within the last decade have made vat photopolymerization printers more affordable and user-friendly. Compared to inkjet- or extrusion-based bioprinters, the vat photopolymerization enables faster and higher-resolution tissue replication down to the micrometer scale [9]. However, the use of photosensitive or reactive bioresins is required, limiting the choice of biomaterials and often necessitating chemical modifications to make them photocrosslinkable [10]. Thus, a major challenge in vat photopolymerization is the identification of proper bioresin formulations that meet the physicochemical requirements for printing while still providing a desirable environment for encapsulated cells [11].

Despite the development of various photo-curable bioresins derived from natural (e.g., collagen [12], hyaluronic acid [13], or gelatin [14]) or synthetic (e.g., polyethylene glycol [15]) sources, no single biomaterial fully replaces the diverse functions and complex composition of native extracellular matrix (ECM). The native ECM provides cells with mechanical support and biochemical signals that promote cell proliferation and differentiation in tissues [16]. Organ- and tissue-specific hydrogels created from decellularized ECM (dECM) are increasingly used in tissue engineering and, more recently, in clinical applications due to their preserved bio-instructiveness and inherent cell adhesive moieties [17]. Given the global prevalence of liver diseases, there's a pressing need for advanced biofabrication techniques. The required advancements include functional liver tissue hydrogels that mimic the tissue's complex microenvironment and liver models for disease modeling, drug screening, and transplantation therapies [18]. To enable the use of dECM in vat photopolymerization, it can be blended with other photocrosslinkable polymers, typically gelatin-methacryloyl (GelMA) [19]. In recent years, a few studies have reported on the formulation of photocrosslinkable dECM resins by mixing unmodified [20,21] or chemically modified dECM [22] with photoinitiators. To render dECM photocrosslinkable, it is typically modified by grafting photo-functional groups primarily onto the free amine or hydroxyl groups of (hydroxy)lysine or other nucleophilic amino acid residues present in collagen's  $\alpha$ -chains. dECM from different tissue sources, such as tendon, cartilage, kidney, and liver, has been functionalized with methacrylic anhydride (MA) and mixed with other components to create materials for extrusion 3D (bio)printing [23–25] or hydrogel production without 3D printing. [26,27] Recently, we have used MA to methacrylate liver dECM [28] and small intestinal submucosa (dSIS) [29] for the multi-layer vat photopolymerization. Even though the MA modification effectively makes dECM photocrosslinkable, it introduces additional hydrophobicity and stiffness to the resulting covalent hydrogels, potentially impairing their cell compatibility [30]. Alternatively, photoreactive methacryloyl groups can be grafted on complex mixtures of ECM proteins via reaction with glycidyl methacrylate (GMA) as recently shown for solubilized and devitalized cartilage hydrogels [31]. So far, high-viscosity pastes of GMA- and MA-modified cartilage-derived matrix proteins have been successfully employed in acellular extrusion 3D printing. These modifications have shown promise in enhancing the printability and structural integrity of the printed constructs. Additionally, (G)MA-functionalized dECMs have demonstrated superior mechanical properties, closely resembling the stiffness of native cartilage tissue after crosslinking. However, despite these advancements, the performance and application of GMA-modified dECM in vat

photopolymerization, particularly in the context of 3D bioprinting, remains unexplored. Understanding the behavior and characteristics of GMA-modified dECM in vat photopolymerization could offer valuable insights into its suitability for biofabrication applications, contributing to the advancement of tissue engineering and regenerative medicine.

We hypothesize that photocrosslinkable dECM-GMA generates gels with enhanced swelling and thus better cell compatibility in soft tissue biofabrication when compared to dECM-MA due to the hydrophilicity of the additional hydroxyl group formed during epoxide ring opening under appropriate reaction conditions (Scheme 1).

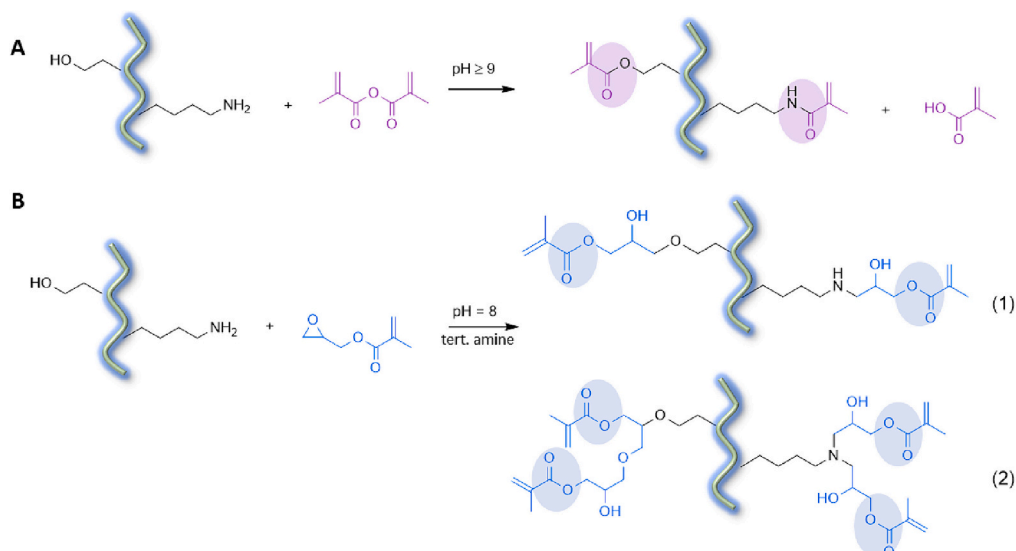
During methacryloylation of protein-based biopolymers with MA under basic aqueous conditions ( $\text{pH} \geq 9$ ), nucleophilic attacks can occur at either of the two carbonyl groups of the anhydride, yielding functional methacrylamide or methacrylate groups on the biopolymer in addition to methacrylic acid as a side product (Scheme 1A) [32]. GMA, on the other hand, adds to biopolymers' free amino or hydroxyl groups under aqueous basic conditions through epoxide ring opening. At moderate reaction conditions ( $\text{pH} = 8$ , RT) amino groups react preferentially at the sterically less hindered site of the epoxide (route [1]) in an irreversible reaction, as schematically illustrated in Scheme 1B. The ring opening is often catalyzed by tertiary amines added to maintain the pH of the aqueous solution [33]. Despite the low reaction temperature, the concomitant ring opening reaction through the biopolymer's hydroxyl groups cannot be fully ruled out in the presence of catalytic tertiary amines as recently demonstrated for glycidol at RT [34]. In general, various amino acid residues within the dECM may serve as nucleophiles, including -SH and -COOH groups, although their reactivity strongly relies on their prevalence within the tissue, their accessibility, as well as the pH and nature of the solvent. Carboxylic groups generally require acidic conditions [35], and thiol groups require more basic conditions ( $\text{pH} > 10$ ) [36] to open the epoxide ring efficiently at RT. Alternative reversible transesterification and corresponding amidation reactions with GMA (not shown in Scheme 1B) under the formation of glycidol as a byproduct typically require higher pH ( $\text{pH} \geq 10.5$ ) and are unlikely to occur at room temperature in protic solvents [37]. Therefore, under the stated mild conditions commonly methacrylate groups are obtained in GMA functionalization instead of methacrylamides. It is worth mentioning that the secondary amines and presumably also the hydroxyl groups generated in route (1) hold the potential for further reaction with additional GMA units as illustrated in route (2) of Scheme 1B and previously reported in the case of Gelatin-GMA [38,39]. To maintain clarity, we have depicted only the most prevalent reactions in Scheme 1 under the stated mild conditions restricted to nucleophilic amino and hydroxyl groups.

To test our hypothesis, we functionalized papain-digested porcine liver dECM with GMA and MA under aqueous conditions for a side-by-side comparison of their material characteristics and performance in vat-based (bio)printing. Acellular and cellular hydrogels were 3D-printed from both dECM variants using a simple liquid crystal display (LCD) 3D printer to evaluate their shape-fidelity and cell compatibility in the context of their biochemical, mechanical, and biophysical properties. This fundamental study is primarily dedicated to developing dECM-MA and dECM-GMA bioresins, serving as an initial step in exploring their potential in 3D printing and cell culture.

## 2. Materials and methods

### 2.1. Materials, buffers, and reagents

All chemicals, buffers, and reagents used in this study were ordered and prepared according to our prior study [40] and are comprehensively listed in the SI section for reference.



**Scheme 1.** Potential reactions in the methacryloylation of protein-based biopolymers under basic aqueous conditions at room temperature (RT), resulting in distinct photoreactive groups. (A) Functionalization with MA solution yields the methacrylated and methacrylamidated biopolymer as well as methacrylic acid as a byproduct. (B) The ring-opening reaction of amine and hydroxyl groups with GMA catalyzed by tertiary amines predominantly occurs at the sterically less hindered site of the epoxide (route 1) with the potential to further react (route 2) on the newly formed secondary amine or less likely the hydroxyl group yielding exclusively methacrylate groups on the biopolymer and no byproducts.

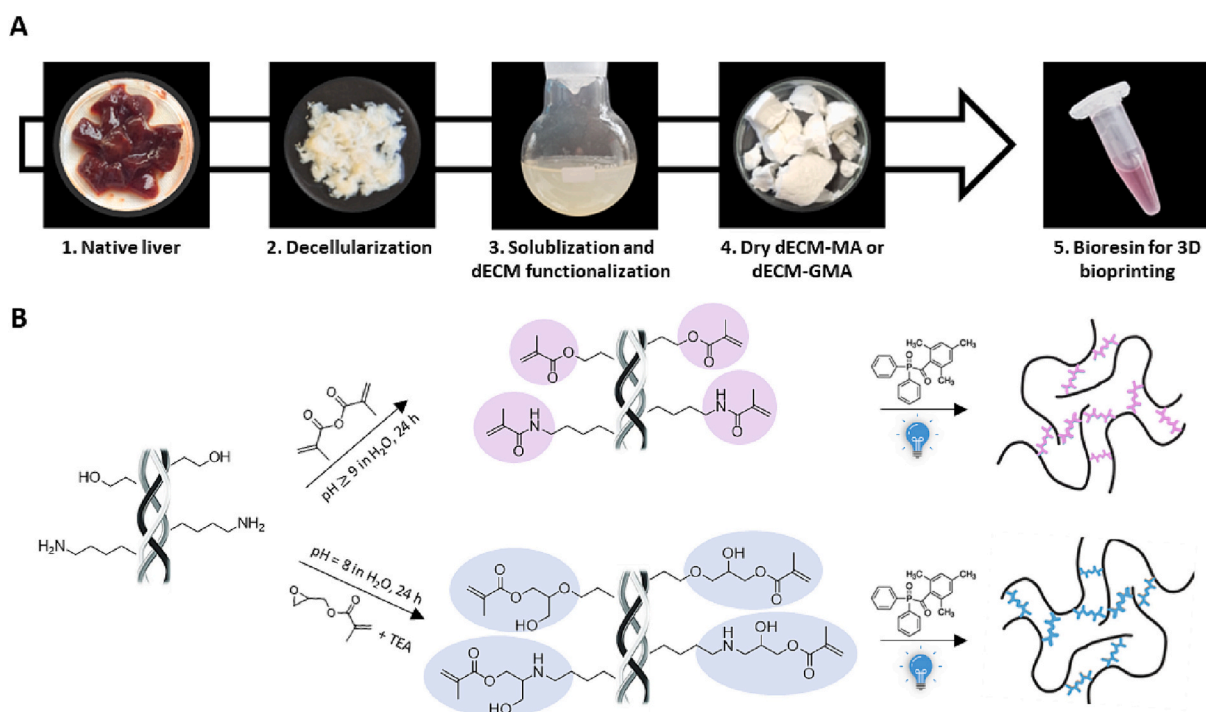


**Fig. 1.** (A) Illustrative workflow of dECM-based (bio)resin preparation, starting with the decellularization of native porcine livers, followed by papain-based solubilization, and subsequent chemical functionalization using either MA or GMA as the methacryloylation agent. The resulting resins are formulated with mammalian cells to create bioresins. (B) Schematic illustration of the main reactions during dECM functionalization using either MA at  $\text{pH} \geq 9$  or GMA at  $\text{pH} = 8$ . Both dECM-MA and dECM-GMA crosslink covalently when exposed to visible light (405 nm) in the presence of lithium phenyl (2,4,6-trimethylbenzoyl) phosphite (LAP) as the photoinitiator.

## 2.2. Decellularization, solubilization, and methacryloylation of liver dECM

Three porcine livers were freshly harvested after an experiment approved by the State Office of Health and Local Affairs (LAGESo, Berlin, Germany), pooled, decellularized, and solubilized according to our

previous protocol described in the SI [40]. Organ pooling reduces batch-to-batch variability, thereby enhancing the reproducibility and consistency of the resulting material properties. The preparative steps towards dECM-based bioresins are illustrated in Fig. 1, including their chemical modification with photocrosslinkable MA and GMA groups, which has been performed under the exclusion of light. The dry dECM-digest (1 g)



was solubilized in 0.01 M HCl (100 mL) until a homogenous viscous solution was formed. The pH was adjusted to 9 with 10 M NaOH for MA functionalization or to pH 8 with triethyl amine (TEA) for GMA functionalization, inducing the formation of a transparent and low viscous solution in both cases. dECM-MA was obtained by dropwise addition of MA under vigorous stirring (3 mL per 1 g dECM) into the dECM gel for 30 min at RT while maintaining the pH  $\geq$  9 for 24 h. Similarly, dECM-GMA was obtained by dropwise GMA addition (3 mL per 1 g dECM) to the stirred dECM gel at RT for 30 min while maintaining the pH at 8 with TEA for 24 h. Both functionalized dECM samples were dialyzed (SpectraPor® dialysis tubing, molecular weight cut-off 1 kDa, Carl Roth GmbH + Co. KG (Karlsruhe)) against distilled water which was then replaced with dilute aqueous HCl (pH = 4–5) at 4 °C for a week with 1–2 acid changes a day. After dialysis, the dECM-MA and dECM-GMA solutions were centrifuged gently at 140 xg for 5 min to remove residual particles, if present. Supernatants were snap-frozen with liquid nitrogen and lyophilized (alpha 2–4 LDplus, Martin Christ Gefrier-trocknungsanlagen GmbH, Osterode am Harz, Germany). The resulting dry foam-like biomaterials were stored at –20 °C until further use. A minimum of three functionalization processes were independently carried out and considered for further characterization and analysis.

### 2.3. Compositional characterization of processed dECM

Isolation and quantification of genomic double-stranded deoxyribonucleic acid (dsDNA), sulfated glycosaminoglycans (sGAGs), and hydroxyproline from native ECM, dECM, digested-dECM, and functionalized dECM-(G)MA was carried out according to a published protocol with slight modifications [40]. Full details can be found in the Supplementary Information (SI) section. Sample preparation and measurements for circular dichroism spectroscopy (CD) and sodium dodecyl sulfate-polyacrylamide gel electrophoresis (SDS-PAGE) were performed as reported previously and are documented in the SI for reference [40].

### 2.4. Determination of the degree of functionalization (DOF)

<sup>1</sup>H nuclear magnetic resonance (NMR) spectra were recorded from digested dECM and dECM-(G)MA biopolymers (5–7 mg) with 3-(trimethylsilyl)propionic-2,2,3,3-d<sub>4</sub> acid sodium salt (TMSP, 1.5 mg) as an internal standard in 0.7 mL D<sub>2</sub>O in 5 mm diameter NMR tubes at 40 °C with a Bruker Avance III 700 MHz NMR spectrometer. Prior to measurement, the sample tubes were immersed in a sonication bath for 10 min at 40 °C to ensure completely solubilized, uniform polymer solutions. The degree of functionalization was calculated by integrating the methacryloyl signals (5.4–6.2 ppm, nominally integrating for 2 protons) and normalizing them to the TMSP integral (0 ppm, integrating for 9 protons), similar to previous reports [31,41], see Eq. (1). The integral of the signal at a chemical shift of 6.1–6.2 ppm provided the methacrylate content in dECM-(G)MA, while the integral of the signal between 5.6 and 5.7 ppm represented the total methacryloyl groups in dECM-(G)MA. The signal at the chemical shift at 5.4 ppm in dECM-MA was not used for quantification due to superimposed proton signals of the methacrylamide and the methine group next to the oxygen of methacrylated hydroxyproline [41]. Subtracting the determined methacrylate group content from the total methacryloyl group amount yielded the quantity of methacrylamide groups.

$$\text{mmol methacryloyl} / \text{g dECM(G)MA} = \left( \frac{\int_{\text{methacryloyl}} 9H_{\text{TMSP}} [\text{mmol}]}{\int_{\text{TMSP}} 1H_{\text{dECM-(G)MA}} [\text{g}]} \right) \quad (1)$$

All spectra were processed and analyzed with the MestReNova software (v.14.1.1, Mestrelab Research, Santiago de Compostela, Spain) and referenced to the deuterated solvent peak.

The conversion of primary amine groups into methacryloyl groups was quantified with a colorimetric 2,4,6-trinitrobenzenesulphonic acid

(TNBS) assay according to the manufacturer's instructions with slight modifications. Briefly, dECM and dECM-(G)MA samples (2 mg) were added to 0.1 M sodium bicarbonate buffer (1 mL, pH 8.5) and heated to 90 °C for 5 min until fully dissolved. The homogeneous sample solution (100  $\mu$ L) was transferred to a 48 well-plate in triplicate, followed by the addition of TNBS reagent (200  $\mu$ L of 0.01 v/v% in 0.1 M sodium bicarbonate buffer) and incubation at 37 °C for 2 h, after which 12 M HCl (100  $\mu$ L) was added to stop the reaction. Blanks of the samples were prepared similarly, except that the HCl was added before incubation with TNBS. The absorbance of the samples was measured at 346 nm using a microplate reader (Infinite® M200 Pro, Tecan, Switzerland). After subtracting the absorbance (A) of blanks from their respective samples, the DOF was calculated using Eq. (2)

$$\text{DOF} = \left( 1 - \frac{A_{\text{dECM-(G)MA}}}{A_{\text{dECM}}} \right) \cdot 100 \quad (2)$$

For TNBS measurements, triplicates of three independent functionalization processes were taken into consideration for the final DOF values.

### 2.5. Determination of the viscosity of the formulated resins

The shear viscosity of the 3D printing resins was analyzed under protection from light using a rotational rheometer (Kinexus pro+, Malvern Panalytical) equipped with a 20 mm/1° upper cone plate geometry with a solvent trap and Peltier system as a temperature controller for the plate. dECM-(G)MA resins were formulated at different concentrations of 1, 1.5, and 2 wt% in cell culture medium (pH = 7.4 after adjustment with 1 M NaOH, if needed) and kept at 4 °C overnight before the measurements. The stability of the resins at the printing temperature of 25 °C was studied by measuring the viscosity at the shear rate of 1 Hz for 12 min. Temperature-dependent shear viscosities were measured at a constant shear rate of 1 Hz while the resin temperature increased from 20 to 40 °C with a heating rate of 1 °C/min. A gap of 0.37 mm was used for all measurements performed in triplicate.

### 2.6. Photorheology of the formulated resins

Acellular resins for photorheological measurements were prepared in cell culture medium at 2 wt% concentration of the dry dECM-(G)MA as a stock and then diluted to 1.5 and 1 wt% for concentration-dependent measurements. When needed, 0.1 M NaOH was added to the resins to ensure a pH of around 7.4 (the slightly pinkish color from the phenol red in the cell culture medium was used as an indicator). Neutralized gels were left at 4 °C overnight to ensure the formation of homogeneous pregels before adding the photoinitiator lithium phenyl-2,4,6-trimethylbenzoylphosphinate (LAP) at different concentrations (0.1, 0.25, and 0.5 wt%) directly before the light-induced measurements. Gelation kinetics of the resins under light exposure were measured with an Anton Paar modular compact rheometer (MCR 302, Anton Paar, Graz, Austria) equipped with a 25 mm plate-to-plate geometry and a UV light curing system. A Peltier plate was used to control the temperature and a solvent trap was used to prevent the evaporation of the solvent. The storage and loss moduli were determined at 20 °C with an angular frequency of 1 rad/s, a shear strain of 1 %, and a gap of 0.5 mm. The strain was determined from the linear viscoelastic (LVE) regime in amplitude sweeps. The UV-lamp (OmniCure® Series 1500, Excelitas Technologies) with an intensity of 100 mW/cm<sup>2</sup> and a band-pass filter of 320–500 nm was turned on at minute 2 of the measurement, which was recorded for 15 min at RT.

### 2.7. Formulation of dECM-(G)MA resins, 3D printing of acellular constructs, and chromogenic assessment of their endotoxin levels

To formulate the methacryloyl-functionalized dECMs into a 3D

printing resin, dry dECM-(G)MA (1.5 wt%) was dissolved either directly at pH 7.4 in cell culture medium or in acidified cell culture medium (pH ~ 5 adjusted with 1 M HCl), with subsequent adjustment of the pH to 7.4 with 1 M NaOH depending on its intrinsic solubility. The formulated resins were left overnight at 4 °C to ensure a fully homogeneous mixture. LAP, as the photoinitiator, was mixed with the homogeneous resin formulations directly before LCD printing. To remove air bubbles introduced during mixing, the resins were gently centrifuged for a few seconds using a mini centrifuge (mini star, VWR International GmbH, Darmstadt, Germany). Various 3D models were prepared with the software Blender (Blender Foundation, version 3.4.1, Amsterdam, Netherlands), sliced with the software LongerWare (version 1.35, LONGER, China), and printed under varying conditions for visual/photographic shape-fidelity assessment and material characterization with a visible light LCD printer (Orange 30 from LONGER, China) at 405 nm with a fixed light intensity of ~ 1 mW/cm<sup>2</sup> and 50 s crosslinking time per 100 μm layer.

Star-shaped samples ( $h = 0.5$  mm and  $d = 5$  mm) were 3D-printed in cell culture medium at neutral conditions (by adjusting the pH when necessary) with varying LAP concentrations (0.5, 0.25, and 0.1 wt%) to study their influence on the printing resolution. The resulting physico-chemical and biological properties of the photocrosslinked dECM-(G)MA hydrogels, were characterized using different printed disc-shaped samples via rheology ( $d = 8$  mm,  $h = 1$  mm), swelling, sol fraction, and degradation measurements as well as scanning electron microscopy (SEM) image analysis ( $d = 6$  mm,  $h = 2$  mm), Brillouin imaging and cell culture studies ( $d = 5$  mm,  $h = 1$  mm).

The potential presence of endotoxins in 3D-printed dECM-(G)MA-based scaffolds was tested using a Pierce™LAL chromogenic endotoxin quantitation kit (Thermo Fisher) according to the manufacturer's instruction and reported in the SI for reference.

## 2.8. Physical characterization of acellular 3D-printed gel structures

After 3D printing, the residual non-crosslinked resin was removed from the samples by immersing them in Milli-Q water for 24 h at 4 °C with repeated water changes. The final mechanical properties of the 3D-printed hydrogels were studied with an oscillating rheometer (Kinexus pro+, Malvern Panalytical) equipped with a solvent trap and Peltier temperature controller using an 8 mm parallel plate geometry (Anton Paar Physica, Ostfildern, Germany). First, the LVE regime of wet samples was determined with an amplitude sweep from a strain of 0.1 to 10 % at 1 Hz, after which the frequency sweep was measured from 0.1 to 10 Hz at 1 % strain. For the final measurements, an optimal strain of 1 % and a frequency of 1 Hz were chosen to record the storage and loss modulus for 10 min at 25 °C. The measurements were repeated under the same parameters at 37 °C with a new set of sample equilibrated in phosphate-buffered saline (PBS -/-) for 24 h. Finally, temperature-dependent rheological properties were measured while ramping the temperature between 20 and 37 °C with a heating rate of 1 °C/min. Measurements were repeated using independent samples ( $n = 3-4$ ).

The degree of crosslinking (DOC) of the 3D-printed structures was estimated using the permanganate ion reduction method following a recent protocol. [42] Briefly, dry uncrosslinked dECM-(G)MA (2 mg) and freshly 3D-printed, unwashed, and lyophilized dECM-(G)MA samples (2 mg) were mixed with 1 mL freshly prepared aqueous 0.025 wt% KMnO<sub>4</sub> solution and centrifuged (10,000 xg for 5 min). The separated supernatants (100 μL) were transferred to a transparent 96 well-plate where the absorbance  $A$  at 525 nm was recorded using a microplate reader (Infinite® M200 Pro, Tecan, Switzerland). Samples were run in triplicate and the DOC was calculated according to Eq. (3)

$$\text{DOC}\% = \left(1 - \frac{A_{3D \text{ printed dECM-(G)MA}}}{A_{\text{uncrosslinked dECM-(G)MA}}}\right) \cdot 100 \quad (3)$$

To measure the swelling ratio and the enzymatic degradation of the

photocrosslinked hydrogels, 3D-printed samples were immersed in Milli-Q water at RT for 24 h with several water changes until all non-crosslinked resin was removed. For swelling studies, the crosslinked samples ( $n = 3$ ) were immersed in Milli-Q water for an additional 24 h at 37 °C to reach the swelling equilibrium, after which the samples were weighed, lyophilized, and weighed again. The swelling ratio was obtained by dividing the wet weight of a sample by its dry weight. For degradation studies, the extracted crosslinked materials ( $n = 3$ ) were immersed in collagenase II solution (1 U/mL in aqueous 50 mM CaCl<sub>2</sub> and 5 mM MES buffer; pH = 7.4) at 37 °C on an orbital shaker (30 rpm), and their wet weight was recorded at different predetermined time points. The remaining mass percentage was calculated by dividing their wet weight ( $w_{\text{time point}}$ ) at the predetermined time points by their initial wet weight ( $w_{\text{initial}}$ ) following Eq. (4)

$$\text{Remaining mass}\% = \frac{w_{\text{time point}}}{w_{\text{initial}}} \cdot 100 \quad (4)$$

The internal micro-architecture of the 3D-printed hydrogels was visualized by SEM imaging of the inner part of the lyophilized samples. Acellular dECM-(G)MA discs were prepared as mentioned above at physiological conditions in cell culture medium. Any excess of uncrosslinked resins, unreacted LAP, and residual salts from the cell culture medium was washed by water changes at 37 °C for 24 h. The 3D-printed scaffolds were blade-cut in two halves after lyophilization, and the inner surface was sputtered with a thin gold layer for subsequent imaging via SEM (Hitachi SU8030) at 15 kV.

## 2.9. 3D bioprinting and cell studies

HepaRG cells (P15–17) were cultured and maintained in William's E medium (WEM) supplemented with 10 % fetal bovine serum (FBS), 1 % L-glutamine, 5 μg/mL insulin, 50 μM hydrocortisone-hemisuccinate, and 1 % penicillin/streptomycin antibiotic solution, hereafter referred to as WEM, under standard conditions (5 % CO<sub>2</sub>, 37 °C, 95 % humidity). dECM-(G)MA resins were prepared as mentioned above under sterile conditions (2 wt% at physiological conditions in WEM) and kept overnight under the exclusion of light at 4 °C before 3D bioprinting. A sterile-filtered and light-protected LAP stock solution (4 wt%) was mixed with the resins (at final concentrations of 0.1, 0.25, and 0.5 wt%) at RT directly before adding the cells as a suspension in WEM at a final cell density of  $1.4 \times 10^6$  cells/mL, and the volume of the cell-laden bioresins was adjusted to a final concentration of 1.5 wt% dECM-(G)MA. The CAD models and printing parameters were applied as described in Section 2.7 and the full 3D bioprinting process occurred in a sterile environment. After 3D bioprinting, scaffolds were immersed immediately in warm culture medium, and the solution was exchanged 2 times during the first 10 min to remove excess uncrosslinked resin and unreacted LAP. Afterward, the bioprinted constructs were cultured statically in an incubator (5 % CO<sub>2</sub>, 37 °C, 95 % humidity), and the culture medium was exchanged every 2–3 days. On days 1, 3, 7, and 14 of cell culture, the cell viability was assessed by fluorescent live/dead staining with fluorescein diacetate (FDA) and propidium iodide (PI). For that, the hydrogels were removed from the culture medium, rinsed with PBS, and treated with FDA/PI and nuclei (Hoechst) staining solution (100 μL per printed hydrogel composed of 0.46 μM FDA/16 μM PI/9 μM Hoechst in PBS) and incubated for 10 min at RT. The stained cells were imaged via confocal fluorescence microscopy (LSM800, Carl Zeiss, Jena, Germany) with either 5× or 10× objectives using tiles and z-stack tools. The metabolic cell activity was detected with a colorimetric PrestoBlue® assay according to the manufacturer's instructions. Briefly, PrestoBlue® solution (200 μL of 10 v/v% of PrestoBlue® reagent diluted with cell culture medium) was added to the cell-laden 3D-printed gels and left to react for 1 h in an incubator (5 % CO<sub>2</sub>, 37 °C, 95 % humidity). The supernatants (100 μL) were pipetted into fresh wells of a 96-well plate and the optical density (OD) was measured with the microplate reader (Infinite® M200 Pro, Tecan, Switzerland) at 570 nm with a reference wavelength of 650

nm at RT. Measurements were repeated with independent samples ( $n = 3$ ).

### 2.10. Statistical analysis

The statistical significance of the gathered data was determined either by the Kruskal-Wallis test followed by Dunn's multiple comparisons post hoc test or the Mann-Whitney  $U$  test using OriginPro software (Version 2021b, OriginLab Corporation, Northampton, MA, USA).  $p$ -values  $p < 0.05$  were considered statistically significant and indicated by \* or otherwise non-significant (n.s.).

## 3. Results and discussion

### 3.1. Solubilization, methacryloylation, and biochemical characterization of dECM

To create dECM-based resins for vat photopolymerization-based 3D printing, the porcine liver tissue was decellularized, solubilized, and methacryloylated. As shown in Fig. 1A, decellularization with SDS and Triton X-100 solutions yielded liver segments with a whitish appearance. Subsequent enzymatic digestion using papain and further homogenization resulted in a semi-transparent and viscous dECM solution. The beneficial use of papain for porcine liver tissue digestion has been extensively investigated in our previous work [40].

The dECM was functionalized at a basic pH to facilitate the reaction of free amino residues of lysine and hydroxylysine with MA or GMA, along with the free hydroxyl groups of serine, tyrosine, threonine, and hydroxyproline (Fig. 1B) [40]. The methacryloylation reagent was added dropwise under vigorous stirring to ensure homogeneous mixing, particularly in the case of water-insoluble GMA, which reacted under heterogeneous-phase conditions. The functionalized dECM was purified from unreacted residues by dialysis at pH 5–6 at 4 °C to prevent hydrolysis of the formed methacrylate groups. The ensuing sections will provide an in-depth characterization of the resulting products to assess the effective functionalization of digested dECM.

To evaluate the structural integrity of the dECM samples after the chemical modification, they were analyzed using SDS-PAGE, FTIR and far-UV CD spectroscopy. The SDS-PAGE image (Fig. 2A) revealed the presence of all collagen type I-specific chains ( $\alpha$ ,  $\beta$ , and  $\gamma$ ) in both dECM-MA and dECM-GMA within the molecular weight range from 120 kDa to 300 kDa, demonstrating that the methacryloylation did not lead to chain scission. According to the far-UV CD analysis (Fig. 2B), functionalization either with MA or GMA did not have a significant impact on the collagen triple-helical structure, as indicated by the positive band around 220 nm, nor on its random coil structure, indicated by the negative band around 200 nm. Corresponding FTIR spectra confirmed consistent characteristic collagen bands across undigested, digested, and dECM-(G)

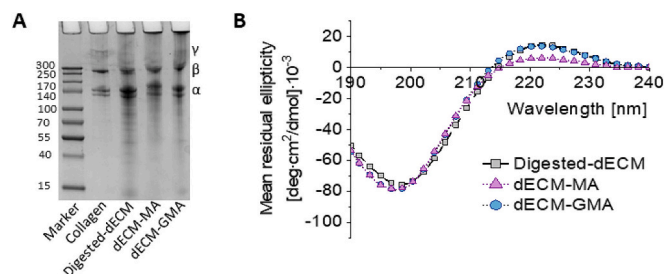


**Fig. 2.** Biomolecular analysis of digested dECM and functionalized dECM-MA and dECM-GMA: (A) Protein molecular mass analysis via SDS-PAGE of digested dECM and dECM-(G)MA resins (2 mg/mL) compared to commercial collagen type I from rat tail (1 mg/mL) as a reference. (B) Representative far-UV CD spectra of the digested dECM and dECM-(G)MA solutions (0.1 mg/mL in 0.1 M phosphate buffer at pH 7.4) to reveal the secondary structure of the proteins.

MA samples (Fig. S1A and B). Therefore, both methacryloylations did not cause substantial alterations to the secondary structure of collagen within the dECM. These results align well with previous reports on collagen-MA [43,44], collagen-GMA [45,46], and dECM-MA [29,47]. Further biochemical characterization, including dsDNA, sGAGs, and hydroxyproline quantification (Fig. S1C, D & E) of the functionalized dECM bioresins, are summarized in the SI section. In brief, the residual dsDNA content indicated efficient decellularization of the liver tissue while largely conserving the native sGAG content. Furthermore, the hydroxyproline content indicative of collagen was enriched in the dECM compared to the native tissue.

### 3.2. Determination of the DOF and crosslinking test of dECM-(G)MA

The DOF is an important adjustable characteristic of the dECM-(G) MA macromer, as it determines the attainable degree of covalent crosslinking and, therefore, directly influences the mechanical properties and stability of the resulting hydrogel. The DOF, measured in relation to the initial amount of primary amino groups, was estimated using a colorimetric TNBS assay and complemented by quantitative  $^1\text{H}$  NMR spectroscopy. Therefore, the relative amount of primary amines from lysine and hydroxylysine groups in the dECM sample before and after functionalization (Fig. 3A) was detected at 346 nm via their chromogenic reaction with TNBS [48]. After functionalization, the amount of chromogenic product generated drastically decreased, indicating a high DOF of the amino groups in a similar range of  $81 \pm 9\%$  and  $84 \pm 7\%$  for dECM-MA and dECM-GMA, respectively (Fig. 3B). This finding aligns with previous studies on MA functionalization of dECM. Ali et al. modified kidney-derived dECM under similar conditions (2.5 mL MA per 1 g of tissue for 48 h) and obtained a DOF of  $80 \pm 3\%$  as determined via TNBS and  $74 \pm 2\%$  via NMR [23]. Other studies have also reported similar DOF values of 80% when using lower amounts of MA for dECM derived from porcine skeletal muscles (1 mL MA per 1 g of tissue for 48 h) [24]. Slightly lower DOF values of around 72% were reported for porcine liver with an even lower MA to dECM ratio (0.6 mL MA per 1 g of tissue for 24 h) [49]. In the  $^1\text{H}$  NMR spectra of both dECM-MA and dECM-GMA (Fig. 3C), the peak at 2.9 ppm (a) assigned to the protons of the terminal methylene group of the lysine side chains in unfunctionalized dECM nearly disappeared, while a new peak at 1.9 ppm (b and e) and multiple peaks between 5.3 and 6.3 ppm (c, d, f and g) assigned to the protons of methacrylamide and methacrylate groups emerged. Their quantitative assessment (Fig. S2A, B) following established methods [31,41] revealed a similar total number of methacryloyl moieties (0.31–0.33 mmol/g) for both dECM-GMA and dECM-MA samples (Fig. S2C) matching the chromogenic results. This low millimolar range of detectable methacryloyl moieties per gram ECM-derived proteins agrees well with literature reports and was shown to be slightly tunable via the equivalents of added MA and GMA reagent [31,32].

A comprehensive structural characterization of GelMA via  $^1\text{H} - ^{13}\text{C}$ -heteronuclear single quantum coherence (HSQC) NMR spectroscopy revealed that methacrylamide- and methacrylate-derived double-bond protons can be clearly distinguished. The peaks around 5.3 and 5.6 ppm were assigned as methacrylamide and those around 5.7 and 6.1 ppm as methacrylate signals [41]. According to this assignment, the GMA-functionalized dECM contained exclusively methacrylate groups as expected, while MA functionalization yielded mainly methacryl amide groups with a minor methacrylate share of up to 5% (Fig. S2C).

To visually confirm the photoreactive modification of our dECM, a simple photocrosslinking test was conducted. Fig. 3D shows the sol-gel conversion of a 1 wt% dECM-MA and dECM-GMA solution in cell culture medium upon irradiation at 405 nm with a 6 W lamp for 5 s in the presence of 0.5 wt% of LAP photoinitiator. Although the DOF of both samples was similar, the dECM-GMA hydrogels appeared haptically softer compared to the dECM-MA ones in this initial photocrosslinking test.

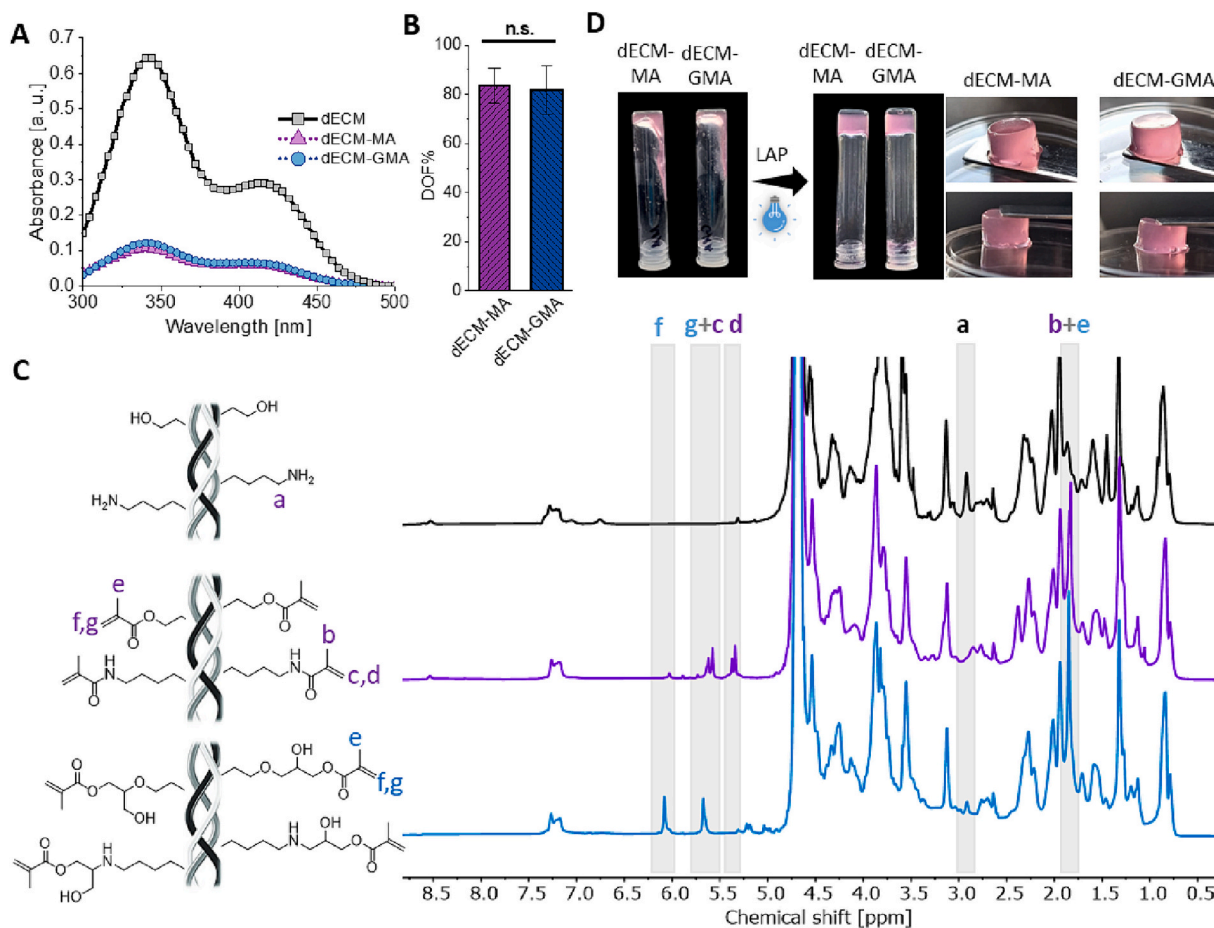


**Fig. 3.** (A) Representative UV-vis spectra of the colorimetric TNBS assay and (B) respective calculated DOF values. Data are presented as mean  $\pm$  SD for  $n = 3-4$ , where n.s. indicates no statistical significance ( $p > 0.05$ ) between samples according to the Mann-Whitney  $U$  test. (C) Representative <sup>1</sup>H NMR spectra of dECM and dECM-(G)MA in D<sub>2</sub>O and their simplified chemical structures. (D) Photographs of the covalently crosslinked dECM-(G)MA (1 wt%) hydrogels in cell culture medium at pH = 7.4 in the presence of 0.5 wt% of LAP as photoinitiator when irradiated at 405 nm for 5 s.

### 3.3. Stability of the formulated dECM-(G)MA resins and its viscosity

To prepare dECM-MA and dECM-GMA for vat photopolymerization, they were directly formulated into aqueous photocrosslinkable resins with cell culture medium at various concentrations (1, 1.5, and 2 wt%). Visual observations of the resins revealed a better solubility of dECM-GMA than dECM-MA at physiological conditions (pH = 7.4 at RT). This observation was further quantitatively assessed by determining the protein concentration in the supernatants of the initially fully

solubilized resins, formulated at 10 mg/mL in PBS (pH = 7.4) at 4 °C to prevent thermally triggered gelation. A bicinchoninic acid (BCA) assay after 2 weeks of cold storage revealed a reduced protein content of 50 and 20 % of the original in dECM-GMA and dECM-MA supernatants, respectively, in agreement with the visually observed fluffy precipitates (Fig. S3). These results confirm a higher solubility of the dECM-GMA resin in neutral buffer, which can be attributed to the generated hydroxyl groups during GMA grafting. The improved biopolymer solubility in aqueous medium after GMA modification is highly advantageous for

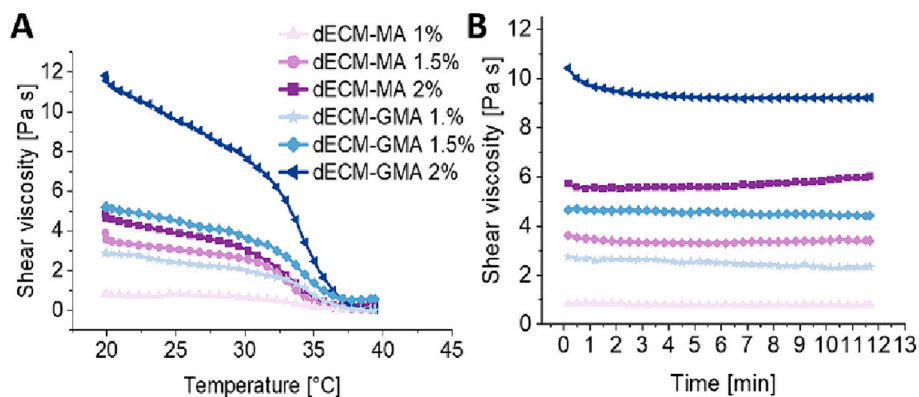


**Fig. 4.** (A) Representative curves of the temperature-dependent viscosity of the resins at different concentrations measured with a rotational rheometer at a shear rate of 1 Hz and (B) the stability of the formulated resins' viscosity at 25 °C ( $n = 3$ ).

(bio)resin formulations and has also been reported for silk fibroin polymeric chains [50,51]. In the case of MA functionalization, positively charged lysine or hydroxylysine residues are mainly converted into uncharged methacrylamide groups, leading to a reduced overall charge density of the macromer and an increased hydrophobicity compared to dECM-GMA and unmodified dECM. As a result, the solubility and stability of the dECM-GMA resin are significantly enhanced compared to the dECM-MA resin or the unmodified dECM (Fig. S3B).

The viscosity of the dissolved dECM resins in cell culture medium was measured using a rotational rheometer, with a temperature ramp from 20 to 40 °C at pH 7.4 (Fig. 4A). For all the samples, viscosity first decreased steadily with rising temperature. The higher the resin concentration, the more pronounced the viscosity decreased with increasing temperature until it started to drop drastically around 30 °C. At this point, visual inspection of the samples revealed the collapse of the gelled resins on the rheometer plate, leading to the separation of the polymer phase from its aqueous medium. Thus, the temperature in the vat should be maintained below 30 °C during 3D printing to ensure a uniform viscosity of the resin formulations in their non-gelled state. Generally, within the temperature range of 20–30 °C, dECM-GMA resins at all concentrations exhibited higher viscosities compared to dECM-MA resins, which can be attributed to hydrogen bonding in the dECM-GMA resins, which became particularly pronounced at high concentrations of 2 wt%. The stability of the resin formulation at 25 °C was evaluated for 12 min (Fig. 4B), revealing that all formulated resins maintained a consistent viscosity at this temperature. Consistent viscosity is vital for vat photopolymerization, ensuring even polymerization and curing, and enabling homogeneous resin flow under the stage for layer printing, yielding 3D constructs with uniform mechanical properties and dimensional accuracy [52].

### 3.4. In-situ photorheology of dECM-(G)MA resins

The photopolymerization kinetics of the formulated resins at pH 7.4

containing 0.25 wt% LAP were evaluated by monitoring changes in their storage ( $G'$ ) and loss modulus ( $G''$ ) during UV-light exposure at 20 °C for a period of 13 min. The graphs in Fig. 5A and B obtained via real-time photorheology revealed high reactivity of the resins at all tested concentrations (2, 1.5, and 1 wt%), as evidenced by the rapid initiation of covalent gel formation within a few seconds after starting the irradiation. For the crosslinked hydrogels, the final  $G'$  values increased with the dECM concentration. Although the  $G'$  values of dECM-GMA hydrogels were significantly lower than those of dECM-MA hydrogels after 8 min of light irradiation, as shown in Fig. 5C, their photoreactivities (i.e., the slope in the linear region of the  $G'$  curves) were similar within the bio-resin group and the delay times  $t_d$  (i.e., the time needed to observe the increase in  $G'$  after switching on the light) were similar for both groups (Fig. S4A, B and C). Within the tested concentration range, all resins exhibited a similar  $t_d$  of around 15 s. Similar gelation rates with delay times of 12 s have been reported for photocrosslinkable collagen-MA [53].

Based on these results, a dECM concentration of 1.5 wt% was chosen for subsequent 3D printing. Higher concentrations increase viscosity, hindering resin mobility within the vat, while lower concentrations result in insufficient crosslinking during the printing process. Varying the photoinitiator concentration (0.1, 0.25, and 0.5 wt%) resulted in similar final stiffness for all hydrogels made with the same resin type and concentration (1.5 wt%) (Fig. 5D). The photorheology studies when irradiating samples for 13 min, indicated that the amount of LAP did not affect the final crosslinking density but only influenced the crosslinking kinetics and, thus, photoreactivity. Lower LAP concentration resulted in a prolonged  $t_d$  of the photopolymerization and a lower curing rate, as evidenced by the decreased slopes ( $\Delta G'/\Delta t$ ) of the linear region of  $G'$  curves in Fig. S4D & E for both dECM-MA and dECM-GMA. The lower photoreactivity can be attributed to the reduced number of radicals present, resulting in delayed and slowed-down photopolymerization. In particular,  $t_d$  increased from around 15 s up to 30–35 s for both resins when the LAP concentration was decreased from 0.5 to 0.1 wt%

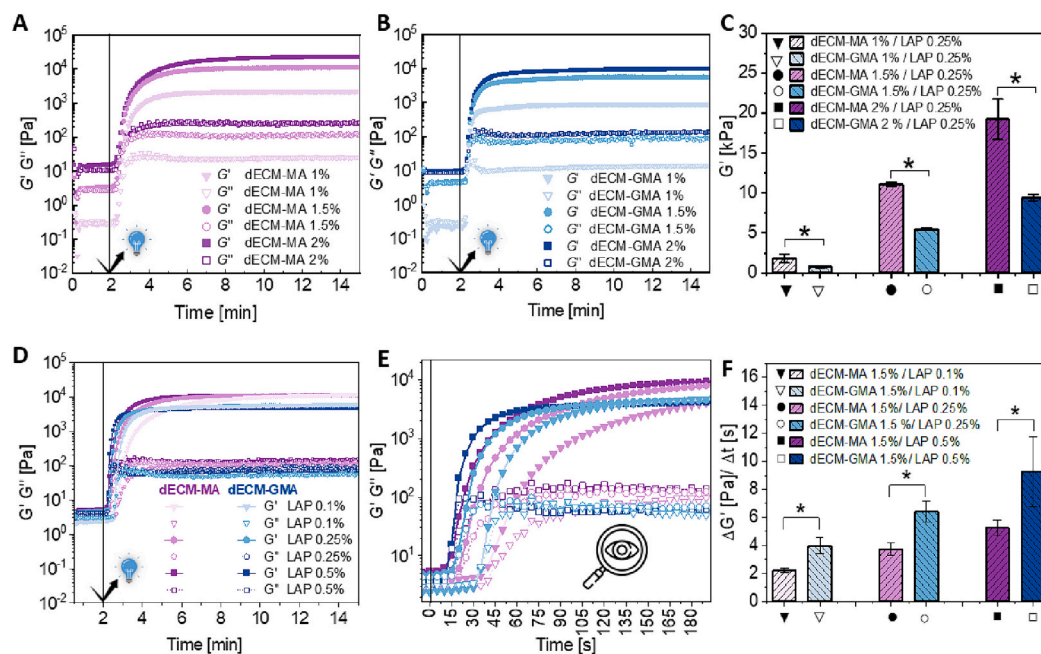


**Fig. 5.** Real-time photorheology of dECM-MA and dECM-GMA resins at 20 °C while irradiating with a light band 320–500 nm for 13 min. Representative curves of storage ( $G'$ ) and loss ( $G''$ ) modulus of both (A) dECM-MA and (B) dECM-GMA at different concentrations (1, 1.5, and 2 wt%) prepared in cell culture medium and mixed with 0.25 wt% LAP right before the measurements. (C) Storage modulus ( $G'$ ) values were extracted after 8 min of UV irradiation. (D) Representative  $G'$  and  $G''$  curves of dECM-(G)MA at 1.5 wt% mixed with different LAP concentrations (0.1, 0.25, and 0.5 wt%) right before the measurements. (E) Enlargement of the first 3 min of curves plotted in D showing both the linear regions of  $G'$  and the beginning convergence times. (F) Index for the photoreactivity  $\Delta G'/\Delta t$  extracted from the slope in the linear region of the  $G'$  curves in E between the onset and the beginning of the convergence period. Data in C and F are presented as mean  $\pm$  SD for  $n = 3$ , where \* indicates statistical significance ( $p < 0.05$ ) between samples according to the Mann-Whitney  $U$  test.

(Fig. S4D). Optimizing the photoinitiator concentration is critical for vat photopolymerization bioprinting, as the curing time and curing rate of photoactive polymers play a major role in both cell viability and printability [54].

The  $\Delta G'/\Delta t$  values, which serve as an index for the photoreactivity of the resins, were extracted from the first three minutes of the photo-rheology curves (Fig. 5E) and are presented in Fig. 5F. Significant differences were observed between dECM-MA and dECM-GMA resins with similar dECM and photoinitiator concentrations. Generally, the dECM-GMA resins exhibited a faster curing rate compared to the dECM-MA resins but resulted in softer hydrogels. Previous studies have shown that the final stages of photoinitiated polymerization are influenced by mobility restrictions due to increased system viscosity with conversion

[55]. A comparative analysis of alginate-GMA and alginate-MA by Araiza-Verduzco et al. involving additional density functional theory (DFT) simulations further revealed that changes in the mechanical properties can be attributed to the different molecular conformation and electron density of the reactive methacrylate groups [30]. The GMA-modified system had a higher number of spacing atoms and electro-negative heteroatoms compared to the MA-functionalized macromer, resulting in a higher electron density of the MA-derived double bond. The presence of intramolecular hydrogen bonds between the carbonyl and the hydroxyl group in GMA-modified macromers further contributed to the rigidity of the grafted double bond, limiting intermolecular reactions and, thereby, the final crosslinking density [30].

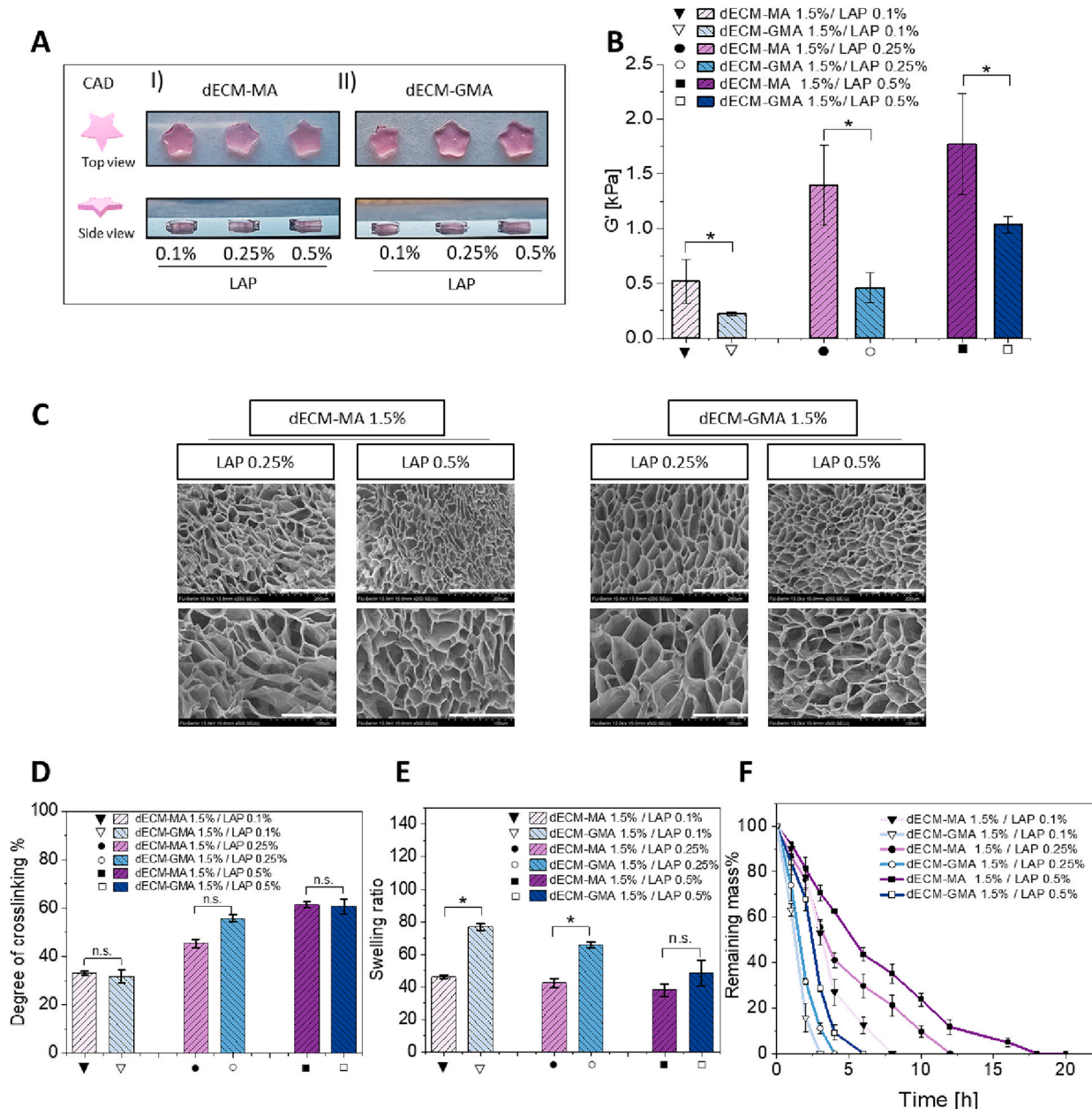


**Fig. 6.** Influence of LAP concentration on 3D-printed acellular liver dECM(G)MA hydrogels (1.5 wt%) and their physical and chemical properties. (A) Photographs of 3D-printed star-shaped hydrogels ( $d = 5$  mm,  $h = 0.5$  mm), (B) average storage modulus of hydrogels at  $37$  °C after equilibration in PBS, and (C–F) physical and chemical properties of the hydrogels: (C) SEM images of the lyophilized hydrogels showing the inner porosity of the samples at various LAP concentrations. Scale bars represent  $200$   $\mu$ m in the upper and  $100$   $\mu$ m in the lower panel of images. (D) DOC determined via the potassium permanganate method, (E) swelling ratio of the bulk hydrogels, and (F) enzymatic biodegradation of the wet hydrogels at  $37$  °C in collagenase II solution ( $1$  U/mL). Data in B, D and E are presented as mean  $\pm$  SD for  $n = 3$ –4, where \* indicates statistical significance ( $p < 0.05$ ) according to the Mann-Whitney  $U$  test.

### 3.5. 3D printing of acellular structures and their physicochemical characterization

After evaluating the photoreactivity of the resins, the printability of all formulations was confirmed using a simple, commercially available LCD printer. The first structures were printed based on a CAD model depicting a simple geometric star shape, as shown in Fig. 6A. Under neutral conditions, both dECM resins formulated with 0.1, 0.25, and 0.5 wt% of LAP resulted in good shape fidelity, although the resolution decreased with decreasing LAP concentration. The disc-shaped 3D-printed structures with 1.5 wt% dECM(G)MA bioresins and 0.5 wt% LAP appeared transparent when placed on a printed "@" symbol (Fig. S5A). Overall, the use of vat photopolymerization-based 3D printing enabled an enhanced shape fidelity of our ECM-based printed 3D structures compared to extrusion-printed devitalized cartilage ECM-MA [47] and ECM-GMA scaffolds [31] elsewhere. It is worth mentioning, that the used printing setup operates at a low light intensity of  $1 \text{ mW/cm}^2$ , which is crucial for maintaining the viability and integrity of cells and DNA within the constructs. However, this configuration necessitates a layer curing time of 50 s, consequently limiting our ability to produce structures higher than 1 mm within a reasonable timeframe of around 10 min when cells are encapsulated. Given these technical constraints, our initial efforts were directed towards simple geometric forms, such as stars and discs. Moving forward, we aim to investigate the printing of more intricate, liver-mimic structures in future projects, leveraging printers with advanced capabilities to overcome the current limitations.

The rheological properties of the 3D-printed hydrogels were measured at  $37^\circ\text{C}$  after equilibrating incubation in PBS for 24 h (Figs. 6B and S5B). The storage modulus  $G'$  of all dECM-GMA samples was lower compared to the respective dECM-MA samples, which was in good agreement with the real-time photorheology measurements above (Fig. 5D and E). The crosslinked hydrogels displayed a similar trend in rheology compared to the real-time photorheology data, though the values were ten times lower. This discrepancy can be attributed to differences in the two crosslinking setups, i.e. photorheometry vs. 3D printing, including light intensity ( $100$  vs.  $1 \text{ mW/cm}^2$ ), light exposure (10 min vs. 50 s), number of layers (1 vs. 10 layers), and layer thickness (0.5 vs. 0.1 mm), respectively. In general, all our 3D-printed hydrogels became slightly softer after equilibration in PBS at  $37^\circ\text{C}$  for 24 h (data not shown). The final storage modulus of the 1.5 wt-% dECM-GMA hydrogels increased with the LAP concentration from 0.2 to 1.2 kPa, making them softer than the corresponding dECM-MA hydrogels ( $\sim 0.5$  to 2 kPa). The stiffness matched the range of healthy native human liver ( $\sim 0.15$ – $5.9$  kPa) [56,57]. Importantly, compared to physically crosslinked liver dECM [58,59], our covalently crosslinked gels were stiffer but markedly softer than extruded photocrosslinked cartilage dECM-MA, dECM-GMA [31] and di-tyrosine crosslinked dECM hydrogels [21] reported elsewhere. Despite the differences in the bulk stiffness of both 3D-printed dECM-(G)MA hydrogels, the crosslinked networks are structurally homogeneous on the mesoscale, as detected by Brillouin imaging spectroscopy (Fig. S6). Generally, the local and bulk mechanical properties determined via Brillouin spectroscopy non-invasively and shear rheology invasively correlate [60]. However, due to minor variations in refractive index and the low mass density in hydrogels, the measured Brillouin shifts are typically small [61] and thus, almost negligible changes in local stiffness between two samples translate into significantly different bulk stiffnesses as observed with our dECM-(G)MA-based hydrogels.

The lyophilized, 3D-printed dECM hydrogels were highly porous, as shown in Fig. 6C. While porosity characteristics of the 3D-printed hydrogels containing 0.1 wt% LAP could not be imaged due to their fragility during sample preparation, a reduction in pore size in the  $\mu\text{m}$  range was observed in both dECM-MA and dECM-GMA when increasing the LAP concentration from 0.25 to 0.5 wt%. This reduction was attributed to the degree of photoinduced crosslinking of dECM

polymers, which strongly influenced the porosity and mechanical properties of the resulting dECM scaffolds. To evaluate the DOC based on the amount of available double bonds, a spectrophotometric assay was employed using potassium permanganate as the colorimetric agent consumed during double bond oxidation [42]. This enables a quantitative estimation of olefinic moieties in both the photocrosslinked and non-crosslinked polymers. Fig. 6D illustrates the effect of LAP concentration on the DOC while maintaining constant polymer concentration and exposure time. A decrease in LAP concentration resulted in an increase in the number of unreacted double bonds in the hydrogel, leading to a decreased DOC and, consequently, an increase in the swelling ratio of the hydrogels. Although the DOC was similar for both polymers with the same LAP content and located between 30 and 60 %, the dECM-GMA scaffolds exhibited higher swelling ratios compared to the dECM-MA hydrogels (Fig. 6E), indicating enhanced hydrophilicity due to the additional hydroxyl groups in the dECM-GMA. The swelling ratio of our samples in the range of 40 to 80 was comparable to previously published data on devitalized cartilage ECM-MA-based hydrogels of similar concentration and stiffness [22]. Static water contact angle measurements further validated the improved increased hydrophilicity of dSIS-GMA hydrogels with a significantly lower contact angle of  $29 \pm 3^\circ$  for dECM-GMA hydrogel surfaces compared to  $36 \pm 2^\circ$  for dECM-MA surfaces (Fig. S5C). As cell-induced enzymatic remodeling of the matrix is essential for tissue development, the enzymatic degradation of the crosslinked dECM hydrogels in collagenase II solution was investigated. As depicted in Fig. 6F, the degradation slowed down with increasing DOC %. Notably, the dECM-GMA hydrogels exhibited faster biodegradation across all crosslinking densities when compared to the dECM-MA hydrogels. This difference can be attributed to the higher hydrophilicity and swelling of dECM-GMA. With the exclusive presence of hydrolytically labile methacrylate in contrast to methacrylamide bonds in dECM-GMA, it is further conceivable that autocatalytic ester hydrolysis also contributes to the observed systematically faster degradation rate compared to dECM-MA. Overall, chemical modification of dECM-derived biomaterials can enhance the enzymatic stability of dECM gels, as the covalent crosslinks formed between protein molecules can make them less susceptible to collagenases and influence the accessibility of triple-helical segments recognized by these enzymes [45,53]. Overall, our findings confirmed that methacryloylation and covalent photocrosslinking do not hinder enzymatic degradation prospectively allowing matrix remodeling.

Finally, the endotoxin levels in dECM-MA and dECM-GMA hydrogels were measured to be  $0.018 \pm 0.002$  and  $0.01 \pm 0.003$  EU/mL, respectively. These levels are significantly below FDA standards (0.5 EU/mL for biologic scaffold eluates), suggesting that these materials are well-suited for use in tissue engineering and regenerative medicine applications [62]. However, further comprehensive safety evaluation is necessary, considering the potential adverse immune responses of in vivo applications of these materials [63].

### 3.6. Cytocompatibility of dECM-(G)MA-based bioresins in 3D bioprinting

We evaluated the cell compatibility of the liver dECM-based materials with human HepaRG cells in 3D bioprinted liver tissue mimics. Just before bioprinting, cells were incorporated into the dECM-based resins (1.5 wt%) at a density of  $1.4 \times 10^6$  cells/mL with varying concentrations of the photoinitiator. In general, the cells were uniformly distributed throughout the entire volume of all 3D bioprinted, 1 mm thick discs, with both formulated bioresins regardless of the LAP concentration. Furthermore, both photocrosslinked resins supported the survival and growth of HepaRG cells throughout our 14-day experiments. There was no evidence of acute material toxicity in the form of drastically reduced cell numbers in the fluorescent microscopy images taken 24 h after bioprinting (Fig. 7A) and the cells were homogeneously distributed inside the hydrogels as shown in the z-stacks (Fig. S7). However, fluorescent live/dead staining indicated a higher proportion of dead cells in

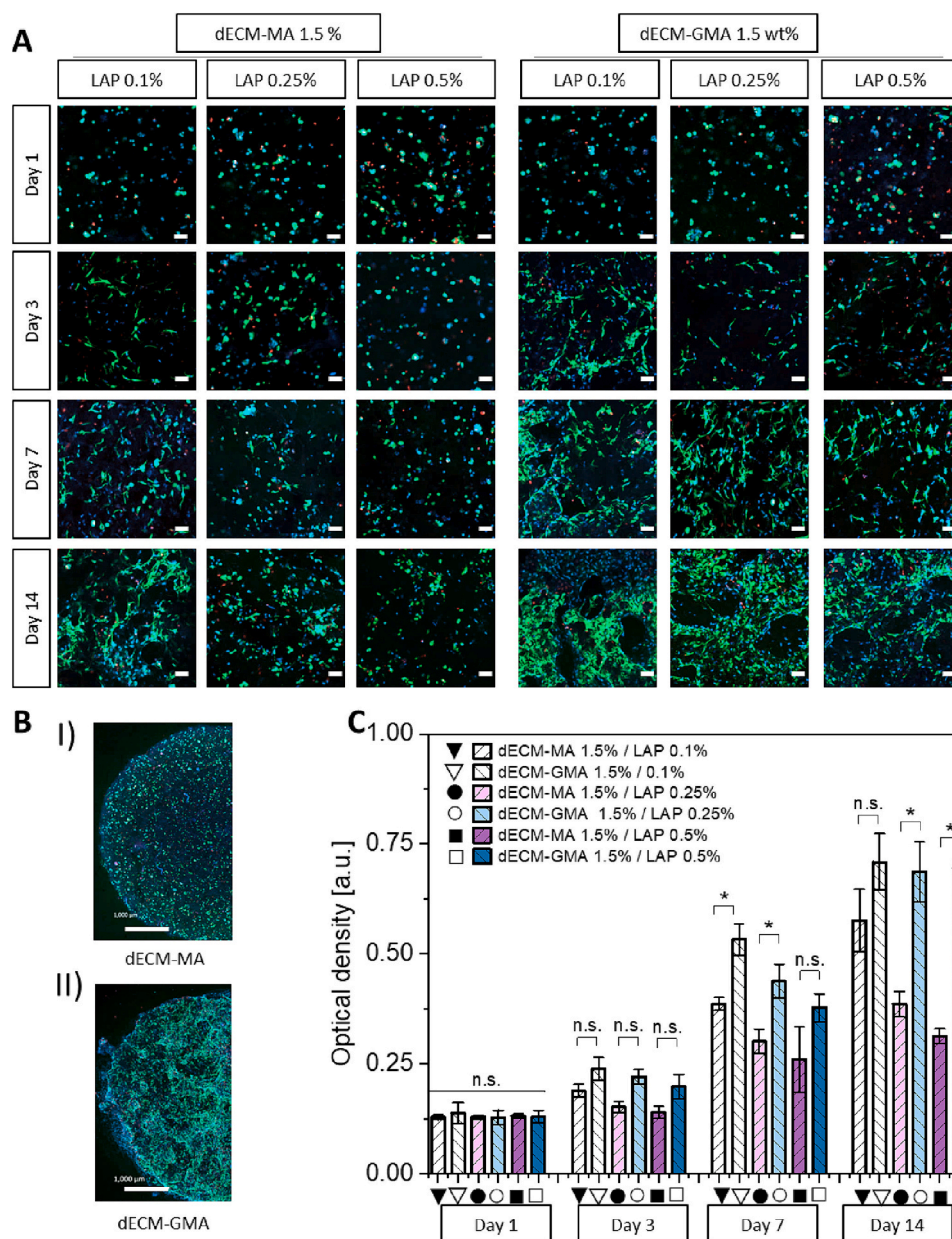


**Fig. 7.** Cytocompatibility assessment of HepaRG cells ( $1.4 \times 10^6$  cells/mL) bioprinted within dECM-(G)MA bioresins (1.5 wt%) at different LAP concentrations. (A) Representative confocal fluorescent microscopy images of the 3D bioprinted structures on days 1, 3, 7, and 14. Cells were fluorescently stained with Hoechst (blue) for nuclei, FDA (green) for live cells, and PI (red) for dead cells; scale bar represents 50  $\mu$ m. (B) Respective tile images of dECM-(G)MA hydrogels prepared with 0.5 % LAP on day 14 (scale bar 1 mm). (C) Time-dependent metabolic activity of human HepaRG cells accessed via a Presto Blue assay. Data are presented as mean  $\pm$  SD for  $n = 3-4$ , where \* indicates statistical significance ( $p < 0.05$ ) of all samples performed by the Kruskal-Wallis test followed by Dunn's test.

both bioresins with increasing LAP concentration, attributable to the higher radical concentration during bioprinting. The softest gels in both formulations showed notably enhanced cell spreading on day 3 of culture when compared to the stiffer gels composed of the same dECM-resin. This effect was more pronounced in dECM-GMA gels compared to dECM-MA gels. Time-dependent live/dead imaging further revealed enhanced proliferation rates and faster spreading starting from day 3 in all dECM-GMA scaffolds compared to the dECM-MA hydrogels with similar stiffnesses (i.e. dECM-GMA with 0.5 wt% LAP vs dECM-MA with 0.25 wt% LAP). Importantly during the 14-day culture period, the 3D bioprinted discs retained their shape (Fig. 7B). The metabolic activity of the printed liver cells, as assessed with a colorimetric PrestoBlue™ assay (Fig. 7C), continuously increased over the 14-day period in all hydrogels. A significantly higher metabolic activity was detected in the dECM-GMA hydrogels on days 7 and 14 compared to the dECM-MA gels,

indicating that the dECM-GMA facilitated superior proliferation of HepaRG cells. Qualitatively similar results of improved cell compatibility with encapsulated immortalized liver carcinoma cells (Huh-7.5) have been reported in a recent comparative study of gelatin-(G)MA [64]. While rheological measurements showed that the photocrosslinked gelatin-GMA was slightly softer than gelatin-MA, the observed difference in cell compatibility was attributed to a better supply of the encapsulated cells in gelatin-GMA gels. The authors explained this by minor differences in gel pore sizes calculated from the elastic modulus of the respective gels by applying the rubber-elasticity theory. While hydrophilicity differences between the two gelatin-(G)MA gels were not considered to rationalize the cell culture observations, our data on the dECM-(G)MA gels strongly supports this explanation. The results of the comparative solubility, rheology, swelling, and biodegradation measurements sustain our initial working hypothesis.



It has been reported that the effect of ECM stiffness on primary hepatocyte morphology and function is most pronounced within a relatively narrow range of 150–1 kPa, which falls within the range of all dECM-GMA and the softest dECM-MA bioprinted scaffolds [56]. Similar to primary human hepatocytes, the HepaRG cell line, derived from a hepatocellular carcinoma, can express a large panel of liver-specific enzymes, specifically carboxylesterase, which are responsible for the hydrolysis of various esters and amides, as well as some thioesters [65–67]. As esters are typically enzymatically hydrolyzed faster than amides [68,69], the predominance of ester linkages within the dECM-GMA scaffolds could contribute to their faster structural remodeling, leading to increased cell proliferation and organization in long-term cultures compared to dECM-MA scaffolds.

#### 4. Conclusion

In this study, we compared the use of two methacryloylation reagents, GMA and MA, under mild reaction conditions for rendering solubilized porcine liver dECM photocrosslinkable and suitable for bioprinting via vat photopolymerization. Both chemical modifications introduced photocrosslinkable groups at comparable DOF for efficient on-demand crosslinking. While the structural integrity of the dECM proteins was preserved for both modifications, dECM-GMA exhibited higher solubility in aqueous medium compared to dECM-MA due to the generated free hydroxyl groups. Both resins reached similar DOCs and network homogeneity within seconds by visible light irradiation with a simple and cost-effective LCD printer in the presence of an appropriate photoinitiator. The transparent dECM hydrogels supported 14-day culture of encapsulated human liver cells while maintaining shape fidelity. At comparable DOF and DOC, dECM-GMA hydrogels generally outperformed the dECM-MA ones in terms of cell compatibility (cell proliferation and viability) attributable to their more hydrophilic and consequently more swollen and softer nature, conceivably supported by a faster proteolytic degradation. Thus, we believe that tissue models developed using dECM-GMA hold potential as *in vitro* liver mimetic platforms in static or dynamic culture for drug testing and fundamental research on organ regeneration and disease development. With this material, we can perform hypothesis-driven investigations with regard to cell-ECM interactions, mechanical tissue properties, and their influence on the development of disease, e.g., related to chronic inflammation or tumors. In future work, we will delve deeper into the printing process and the functionality and behavior of cells within such bioprinted hydrogels, focusing especially on their potential for matrix-induced cell differentiation.

#### CRedit authorship contribution statement

**Ahed Almalla:** Writing – original draft, Visualization, Validation, Investigation, Formal analysis, Data curation, Conceptualization. **Laura Elomaa:** Writing – review & editing, Supervision, Methodology, Formal analysis. **Nora Fribicz:** Visualization, Investigation, Formal analysis, Data curation. **Timm Landes:** Visualization, Investigation, Formal analysis, Data curation. **Peng Tang:** Investigation, Formal analysis, Data curation. **Zeinab Mahfouz:** Investigation, Formal analysis, Data curation. **Beate Koksich:** Writing – review & editing, Methodology, Funding acquisition. **Karl Herbert Hillebrandt:** Methodology, Formal analysis, Conceptualization. **Igor Maximilian Sauer:** Writing – review & editing, Methodology, Funding acquisition, Conceptualization. **Dag Heine-mann:** Writing – review & editing, Supervision, Methodology. **Sebastian Seiffert:** Supervision, Methodology, Funding acquisition. **Marie Weinhart:** Writing – review & editing, Supervision, Resources, Project administration, Methodology, Funding acquisition, Formal analysis, Conceptualization.

#### Declaration of competing interest

The authors declare the following financial interests/personal relationships which may be considered as potential competing interests: Marie Weinhart reports financial support was provided by German Research Foundation. Sebastian Seiffert reports financial support was provided by German Research Foundation. Beate Koksich reports financial support was provided by German Research Foundation. Igor Maximilian Sauer reports financial support was provided by German Research Foundation. If there are other authors, they declare that they have no known competing financial interests or personal relationships that could have appeared to influence the work reported in this paper.

#### Data availability

Data will be made available on request.

#### Acknowledgment

Financial support is kindly acknowledged from the Deutsche Forschungsgemeinschaft (DFG, German Research Foundation) for CRC 1449 (Project ID 431232613, M.W., B.K.), the Research Unit FOR 2811 (S.S., M.W.) (Project ID 397384169 and 423791428), and the Cluster of Excellence Matters of Activity, Image Space Material (M.W., I.M.S.) under Germany's Excellence Strategy – EXC 2025. A.A. warmly thanks Helmholtz Graduate School Macromolecular Bioscience and Dahlem Research School of Freie Universität Berlin for their support. The authors extend their sincere gratitude for the support provided by the Core Facility BioSupraMol, generously funded by the DFG. Special appreciation is also expressed to Johanna Scholz for her assistance in cell culture. Some icons in the TOC Figure and Fig. 5 were used from [flaticon.com](https://www.flaticon.com) or [Biorender.com](https://www.biorender.com).

#### Appendix A. Supplementary data

Additional experimental details of materials and methods. Supplementary figures on material characterization, including, FTIR spectra, biochemical characterization, chemical shifts and integrals of representative  $^1\text{H}$  NMR spectra, solubility tests, and protein quantification via a BCA assay, more detailed real-time photorheology curves, macroscopic photographic images of 3D-printed gels for transparency assessment, representative time-dependent rheology curves, contact angles and Brillouin imaging maps of dECM-(G)MA gels. Representative z-stack confocal fluorescent images of the 3D bioprinted structures from bio-resins composed of dECM-(G)MA and HepaRG stained with Hoechst (blue, nuclei), FDA (green, live cells), and PI (red, dead cells) taken after 24 h of culture. Supplementary data to this article can be found online at <https://doi.org/10.1016/j.bioadv.2024.213850>.

#### References

- [1] D. Kim, M. Kim, J. Lee, J. Jang, Review on multicomponent hydrogel bioinks based on natural biomaterials for bioprinting 3D liver tissues, *Front. Bioeng. Biotechnol.* 10 (2022) 764682.
- [2] F. Pati, J. Jang, D.H. Ha, S. Won Kim, J.W. Rhie, J.H. Shim, D.H. Kim, D.W. Cho, Printing three-dimensional tissue analogues with decellularized extracellular matrix bioink, *Nat. Commun.* 5 (2014) 3935.
- [3] J.H. Park, J. Jang, J.S. Lee, D.W. Cho, Current advances in three-dimensional tissue/organ printing, *Tissue Eng Regen Med* 13 (6) (2016) 612–621.
- [4] J. Jang, J.Y. Park, G. Gao, D.W. Cho, Biomaterials-based 3D cell printing for next-generation therapeutics and diagnostics, *Biomaterials* 156 (2018) 88–106.
- [5] X. Cui, J. Li, Y. Hartanto, M. Durham, J. Tang, H. Zhang, G. Hooper, K. Lim, T. Woodfield, Advances in extrusion 3D bioprinting: a focus on multicomponent hydrogel-based bioinks, *Adv. Healthc. Mater.* 9 (15) (2020) e1901648.
- [6] X. Li, B. Liu, B. Pei, J. Chen, D. Zhou, J. Peng, X. Zhang, W. Jia, T. Xu, Inkjet bioprinting of biomaterials, *Chem. Rev.* 120 (19) (2020) 10793–10833.
- [7] B.S. Kim, S. Das, J. Jang, D.W. Cho, Decellularized extracellular matrix-based bioinks for engineering tissue- and organ-specific microenvironments, *Chem. Rev.* 120 (19) (2020) 10608–10661.

- [8] W. Zhu, X. Ma, M. Gou, D. Mei, K. Zhang, S. Chen, 3D printing of functional biomaterials for tissue engineering, *Curr. Opin. Biotechnol.* 40 (2016) 103–112.
- [9] I. Dondervinkel, J.C.M. van Hest, N.R. Cameron, Bio-inks for 3D bioprinting: recent advances and future prospects, *Polym. Chem.* 8 (31) (2017) 4451–4471.
- [10] C.A. Murphy, K.S. Lim, T.B.F. Woodfield, Next evolution in organ-scale biofabrication: bioresin design for rapid high-resolution vat polymerization, *Adv. Mater.* 34 (20) (2022) e2107759.
- [11] L. Ouyang, J.P.K. Armstrong, Y. Lin, J.P. Wojciechowski, C. Lee-Reeves, D. Hachim, K. Zhou, J.A. Burdick, M.M. Stevens, Expanding and optimizing 3D bioprinting capabilities using complementary network bioinks, *Sci. Adv.* 6 (38) (2020) eabc5529.
- [12] L. Tytgat, A. Dobos, M. Markovic, L. Van Damme, J. Van Hoorick, F. Bray, H. Thienpont, H. Ottevaere, P. Dubruel, A. Ovsianikov, S. Van Vlierberghe, High-resolution 3D bioprinting of photo-cross-linkable recombinant collagen to serve tissue engineering applications, *Biomacromolecules* 21 (10) (2020) 3997–4007.
- [13] A.V. Sochilina, A.G. Savelyev, R.A. Akasov, V.P. Zubov, E.V. Khaydukov, A. N. Generalova, Preparing modified hyaluronic acid with tunable content of vinyl groups for use in fabrication of scaffolds by photoinduced crosslinking, *Russ. J. Bioorg. Chem.* 47 (4) (2021) 828–836.
- [14] M. Cuvellier, F. Ezan, H. Oliveira, S. Rose, J.C. Fricain, S. Langouet, V. Legagneux, G. Baffet, 3D culture of HepaRG cells in GelMa and its application to bioprinting of a multicellular hepatic model, *Biomaterials* 269 (2021) 120611.
- [15] B.F. Pierce, G. Tronci, M. Rössle, A.T. Neffe, F. Jung, A. Lendlein, Photocrosslinked co-networks from glycidylmethacrylated gelatin and poly(ethylene glycol) methacrylates, *Macromol. Biosci.* 12 (4) (2012) 484–493.
- [16] F. Gattazzo, A. Urciuolo, P. Bonaldo, Extracellular matrix: a dynamic microenvironment for stem cell niche, *Biochim. Biophys. Acta* 1840 (8) (2014) 2506–2519.
- [17] J.H. Traverse, T.D. Henry, N. Dib, A.N. Patel, C. Pepine, G.L. Schaar, J.A. DeQuach, A.M. Kinsey, P. Chamberlin, K.L. Christman, First-in-man study of a cardiac extracellular matrix hydrogel in early and late myocardial infarction patients, *JACC Basic Transl Sci* 4 (6) (2019) 659–669.
- [18] S. Cheemerla, M. Balakrishnan, Global epidemiology of chronic liver disease, *Clin. Liver Dis.* 17 (2021) 365–370.
- [19] X. Ma, C. Yu, P. Wang, W. Xu, X. Wan, C.S.E. Lai, J. Liu, A. Koroleva-Maharajh, S. Chen, Rapid 3D bioprinting of decellularized extracellular matrix with regionally varied mechanical properties and biomimetic microarchitecture, *Biomaterials* 185 (2018) 310–321.
- [20] M. Ahearne, A. Coyle, Application of UVA-riboflavin crosslinking to enhance the mechanical properties of extracellular matrix derived hydrogels, *J. Mech. Behav. Biomed. Mater.* 54 (2016) 259–267.
- [21] H. Kim, B. Kang, X. Cui, S.H. Lee, K. Lee, D.W. Cho, W. Hwang, T.B.F. Woodfield, K. S. Lim, J. Jang, Light-activated decellularized extracellular matrix-based bioinks for volumetric tissue analogs at the centimeter scale, *Adv. Funct. Mater.* 31 (32) (2021) 2011252.
- [22] D.O. Visscher, H. Lee, P.P.M. van Zuijlen, M.N. Helder, A. Atala, J.J. Yoo, S.J. Lee, A photo-crosslinkable cartilage-derived extracellular matrix bioink for auricular cartilage tissue engineering, *Acta Biomater.* 121 (2021) 193–203.
- [23] M. Ali, A.K. Pr, J.J. Yoo, F. Zahran, A. Atala, S.J. Lee, A photo-crosslinkable kidney ECM-derived bioink accelerates renal tissue formation, *Adv. Healthc. Mater.* 8 (7) (2019) e1800992.
- [24] W. Kim, H. Lee, J. Lee, A. Atala, J.J. Yoo, S.J. Lee, G.H. Kim, Efficient myotube formation in 3D bioprinted tissue construct by biochemical and topographical cues, *Biomaterials* 230 (2020) 119632.
- [25] L. Elomaa, A. Almalla, E. Keshi, K.H. Hillebrandt, I.M. Sauer, M. Weinhart, Rise of tissue- and species-specific 3D bioprinting based on decellularized extracellular matrix-derived bioinks and bioresins, *Biomater Biosyst* 12 (2023) 100084.
- [26] J. Visser, P.A. Levett, N.C. to Moller, J. Besems, K.W. Boere, M.H. van Rijen, J.C. de Grauw, W.J. Dhert, P.R. van Weeren, J. Malda, Crosslinkable hydrogels derived from cartilage, meniscus, and tendon tissue, *Tissue Eng. Part A* 21 (7–8) (2015) 1195–1206.
- [27] B.B. Rothrauff, L. Coluccino, R. Gottardi, L. Ceseracciu, S. Scaglione, L. Goldoni, R. S. Tuan, Efficacy of thermoresponsive, photocrosslinkable hydrogels derived from decellularized tendon and cartilage extracellular matrix for cartilage tissue engineering, *J. Tissue Eng. Regen. Med.* 12 (1) (2018) e159–e170.
- [28] L. Elomaa, E. Keshi, I.M. Sauer, M. Weinhart, Development of GelMA/PCL and dECM/PCL resins for 3D printing of acellular in vitro tissue scaffolds by stereolithography, *Mater. Sci. Eng. C* 112 (2020) 110958.
- [29] L. Elomaa, L. Gerbeth, A. Almalla, N. Fribicz, A. Daneshgar, P. Tang, K. H. Hillebrandt, S. Seiffert, M.I. Sauer, B. Siegmund, M. Weinhart, Bioactive photocrosslinkable resin solely based on refined decellularized small intestine submucosa for vat photopolymerization of in vitro tissue mimics, *Addit. Manuf.* 64 (2023) 103439.
- [30] F. Araiza-Verduzco, E. Rodriguez-Velazquez, H. Cruz, I.A. Rivero, D.R. Acosta-Martinez, G. Pina-Luis, M. Alatorre-Meda, Photocrosslinked alginate-methacrylate hydrogels with modulable mechanical properties: effect of the molecular conformation and electron density of the methacrylate reactive group, *Materials (Basel)* 13 (3) (2020) 534.
- [31] E.A. Kiyotake, M.E. Cheng, E.E. Thomas, M.S. Detamore, The rheology and printability of cartilage matrix-only biomaterials, *Biomolecules* 12 (6) (2022) 846.
- [32] K. Yue, X. Li, K. Schrobback, A. Sheikhi, N. Annabi, J. Leijten, W. Zhang, Y. S. Zhang, D.W. Huttmacher, T.J. Klein, A. Khademhosseini, Structural analysis of photocrosslinkable methacryloyl-modified protein derivatives, *Biomaterials* 139 (2017) 163–171.
- [33] J. Wu, H.-G. Xia, Tertiary amines as highly efficient catalysts in the ring-opening reactions of epoxides with amines or thiols in H<sub>2</sub>O: expeditious approach to β-amino alcohols and β-aminothioethers, *Green Chem.* 7 (10) (2005) 708–710.
- [34] Y. Du, X. Xue, Q. Jiang, W. Huang, H. Yang, L. Jiang, B. Jiang, S. Komarneni, Ring-opening mechanism of epoxides with alcohol and tertiary amines, *Polym. Chem.* 14 (32) (2023) 3679–3685.
- [35] S. Bakhtin, E. Shved, Y. Bespalko, T. Tyurina, V. Palchykov, Detailing the elementary stages in the oxirane ring opening reactions with carboxylic acids catalyzed by tertiary amines, *J. Phys. Org. Chem.* 33 (9) (2020) e4071.
- [36] I. Gadwal, M.C. Stuparu, A. Khan, Homopolymer bifunctionalization through sequential thiol-epoxy and esterification reactions: an optimization, quantification, and structural elucidation study, *Polym. Chem.* 6 (8) (2015) 1393–1404.
- [37] A.V. Reis, A.R. Fajardo, I.T. Schuquel, M.R. Guilherme, G.J. Vidotti, A.F. Rubira, E. C. Muniz, Reaction of glycidyl methacrylate at the hydroxyl and carboxylic groups of poly(vinyl alcohol) and poly(acrylic acid): is this reaction mechanism still unclear? *J. Org. Chem.* 74 (10) (2009) 3750–3757.
- [38] S. Sharifi, M.M. Islam, H. Sharifi, R. Islam, D. Koza, F. Reyes-Ortega, D. Alba-Molina, P.H. Nilsson, C.H. Dohlman, T.E. Mollnes, J. Chodosh, M. Gonzalez-Andrades, Tuning gelatin-based hydrogel towards bioadhesive ocular tissue engineering applications, *Bioact Mater* 6 (11) (2021) 3947–3961.
- [39] Ezzah M. Muzammil, A. Khan, M.C. Stuparu, Post-polymerization modification reactions of poly(glycidyl methacrylate)s, *RSC Adv.* 7 (88) (2017) 55874–55884.
- [40] A. Almalla, L. Elomaa, L. Bechtella, A. Daneshgar, P. Yavvari, Z. Mahfouz, P. Tang, B. Kokschi, I. Sauer, K. Pagel, K.H. Hillebrandt, M. Weinhart, Papain-based solubilization of decellularized extracellular matrix for the preparation of bioactive, thermosensitive pre-gels, *Biomacromolecules* 24 (12) (2023) 5620–5637.
- [41] C. Claassen, M.H. Claassen, V. Truffault, L. Sewald, G.E.M. Tovar, K. Borchers, A. Southan, Quantification of substitution of gelatin methacryloyl: best practice and current pitfalls, *Biomacromolecules* 19 (1) (2018) 42–52.
- [42] A.V. Sochilina, A.G. Savelyev, P.A. Demina, S.V. Sizova, V.P. Zubov, E. V. Khaydukov, A.N. Generalova, Quantitative detection of double bonds in hyaluronic acid derivative via permanganate ion reduction, *Meas. Sci. Technol.* 30 (7) (2019) 075102.
- [43] R. Ravichandran, M.M. Islam, E.I. Alarcon, A. Samanta, S. Wang, P. Lundstrom, J. Hilborn, M. Griffith, J. Phopase, Functionalised type-I collagen as a hydrogel building block for bio-orthogonal tissue engineering applications, *J. Mater. Chem. B* 4 (2) (2016) 318–326.
- [44] I.D. Gaudet, D.I. Shreiber, Characterization of methacrylated type-I collagen as a dynamic, photoactive hydrogel, *Biointerphases* 7 (1–4) (2012) 25.
- [45] G. Tronci, S.J. Russell, D.J. Wood, Photo-active collagen systems with controlled triple helix architecture, *J. Mater. Chem. B* 1 (30) (2013) 3705–3715.
- [46] W. Li, X. Fan, Y. Wang, J. Wang, M. Li, X. Li, K. Tang, G. Wan, A glycidyl methacrylate modified collagen/polyethylene glycol diacrylate hydrogel: a mechanically strong hydrogel for loading levofloxacin, *New J. Chem.* 44 (39) (2020) 17027–17032.
- [47] K. Behan, A. Dufour, O. Garcia, D. Kelly, Methacrylated cartilage ECM-based hydrogels as injectables and bioinks for cartilage tissue engineering, *Biomolecules* 12 (2) (2022) 216.
- [48] C.M. H., J.Q. Coentro, V. Graceffa, Z. Wu, D.I. Zeugolis, An experimental toolbox for characterization of mammalian collagen type I in biological specimens, *Nat. Protoc.* 13 (3) (2018) 507–529.
- [49] A. Ravichandran, B. Murekatete, D. Moedder, C. Meinert, L.J. Bray, Photocrosslinkable liver extracellular matrix hydrogels for the generation of 3D liver microenvironment models, *Sci. Rep.* 11 (1) (2021) 15566.
- [50] E. Kim, J.M. Seok, S.B. Bae, S.A. Park, W.H. Park, Silk fibroin enhances cytocompatibility and dimensional stability of alginate hydrogels for light-based three-dimensional bioprinting, *Biomacromolecules* 22 (5) (2021) 1921–1931.
- [51] S.B. Bae, M.H. Kim, W.H. Park, Electrospinning and dual crosslinking of water-soluble silk fibroin modified with glycidyl methacrylate, *Polym. Degrad. Stab.* 179 (2020) 109304.
- [52] C. Yu, J. Schimelman, P. Wang, K.L. Miller, X. Ma, S. You, J. Guan, B. Sun, W. Zhu, S. Chen, Photopolymerizable biomaterials and light-based 3D printing strategies for biomedical applications, *Chem. Rev.* 120 (19) (2020) 10695–10743.
- [53] H. Liang, S.J. Russell, D.J. Wood, G. Tronci, Monomer-induced customization of UV-cured atelocollagen hydrogel networks, *Front. Chem.* 6 (2018) 626.
- [54] R. Levato, T. Jungst, R.G. Scheuring, T. Blunk, J. Groll, J. Malda, From shape to function: the next step in bioprinting, *Adv. Mater.* 32 (12) (2020) e1906423.
- [55] C. Decker, Kinetic study and new applications of UV radiation curing, *Macromol. Rapid Commun.* 23 (18) (2002) 1067–1093.
- [56] S. Ye, J.W.B. Boeter, L.C. Penning, B. Spee, K. Schneeberger, Hydrogels for liver tissue engineering, *Bioengineering (Basel)* 6 (3) (2019) 59.
- [57] S. Mueller, L. Sandrin, Liver stiffness: a novel parameter for the diagnosis of liver disease, *Hepat. Med.* 2 (2010) 49–67.
- [58] R.P. Bual, H. Ijima, Intact extracellular matrix component promotes maintenance of liver-specific functions and larger aggregates formation of primary rat hepatocytes, *Regen Ther* 11 (2019) 258–268.
- [59] H. Ijima, S. Nakamura, R. Bual, N. Shirakigawa, S. Tanoue, Physical properties of the extracellular matrix of decellularized porcine liver, *Gels* 4 (2) (2018) 39.
- [60] Z. Meng, T. Thakur, C. Chitrakar, M.K. Jaiswal, A.K. Gaharwar, V.V. Yakovlev, Assessment of local heterogeneity in mechanical properties of nanostructured hydrogel networks, *ACS Nano* 11 (8) (2017) 7690–7696.
- [61] S.V. Adichtchev, Y.A. Karpegina, K.A. Okotrub, M.A. Surovtseva, V.A. Zykova, N. V. Surovtsev, Brillouin spectroscopy of biorelevant fluids in relation to viscosity and solute concentration, *Phys. Rev. E* 99 (6–1) (2019) 062410.

- [62] Z. Wang, X. Jin, R. Dai, J.F. Holzman, K. Kim, An ultrafast hydrogel photocrosslinking method for direct laser bioprinting, *RSC Adv.* 6 (25) (2016) 21099–21104.
- [63] M. Kasravi, A. Ahmadi, A. Babajani, R. Mazloomnejad, M.R. Hatamnejad, S. Shariatzadeh, S. Bahrami, H. Niknejad, Immunogenicity of decellularized extracellular matrix scaffolds: a bottleneck in tissue engineering and regenerative medicine, *Biomater Res* 27 (1) (2023) 10.
- [64] M.M. Sk, P. Das, A. Panwar, L.P. Tan, Synthesis and characterization of site selective photo-crosslinkable glycidyl methacrylate functionalized gelatin-based 3D hydrogel scaffold for liver tissue engineering, *Mater. Sci. Eng. C Mater. Biol. Appl.* 123 (2021) 111694.
- [65] K.P. Kanebratt, T.B. Andersson, Evaluation of HepaRG cells as an in vitro model for human drug metabolism studies, *Drug Metab. Dispos.* 36 (7) (2008) 1444–1452.
- [66] C. Aninat, A. Piton, D. Glaise, T. Le Charpentier, S. Langouet, F. Morel, C. Guguen-Guillouzo, A. Guillouzo, Expression of cytochromes P450, conjugating enzymes and nuclear receptors in human hepatoma HepaRG cells, *Drug Metab. Dispos.* 34 (1) (2006) 75–83.
- [67] Z. Sun, Y. Wu, S. Liu, S. Hu, B. Zhao, P. Li, S. Du, Effects of Panax notoginseng saponins on esterases responsible for aspirin hydrolysis in vitro, *Int. J. Mol. Sci.* 19 (10) (2018) 3144.
- [68] R.F. Michael, Phase I Biotransformation Reactions-Esterases, and Amidases in xPharm: The Comprehensive Pharmacology Reference, Elsevier Science, 2008.
- [69] H.E. Mentlein R, Hydrolysis of ester- and amide-type drugs by the purified isoenzymes of nonspecific carboxylesterase from rat liver, *Biochem. Pharmacol.* 8 (1984) 15–33.

# Chemistry matters: A side-by-side comparison of two chemically distinct methacryloylated dECM bioresins for vat photopolymerization

Ahed Almalla,<sup>1</sup> Laura Elomaa,<sup>1</sup> Nora Fribiczner,<sup>2</sup> Timm Landes,<sup>3,4,5</sup> Peng Tang,<sup>1</sup> Zeinab Mahfouz,<sup>1</sup> Beate Kokschi,<sup>1</sup> Karl Herbert Hillebrandt,<sup>6,7,8</sup> Igor Maximilian Sauer,<sup>6,7,8</sup> Dag Heinemann,<sup>3,4,5</sup> Sebastian Seiffert,<sup>2</sup> Marie Weinhart<sup>1,8,9,\*</sup>

<sup>1</sup>*Institute of Chemistry and Biochemistry, Freie Universität Berlin, Takustr. 3, 14195 Berlin, Germany*

<sup>2</sup>*Department of Chemistry, Johannes Gutenberg Universität Mainz, Duesbergweg 10-14, 55128 Mainz, Germany*

<sup>3</sup>*HOT – Hanover Centre for Optical Technologies, Leibniz Universität Hannover, Nienburger Straße 17, 30167 Hannover, Germany*

<sup>4</sup>*Institute of Horticultural Productions Systems, Leibniz Universität Hannover, Herrenhäuser Straße 2, 30419 Hannover, Germany*

<sup>5</sup>*Cluster of Excellence PhoenixD, Leibniz University Hannover, Welfengarten 1a, 30167 Hannover, Germany*

<sup>6</sup>*Experimental Surgery, Department of Surgery, CCM|CVK, Charité – Universitätsmedizin Berlin, Augustenburger Platz 1, 13353 Berlin, Germany*

<sup>7</sup>*Berlin Institute of Health at Charité – Universitätsmedizin Berlin, BIH Biomedical Innovation Academy, BIH Charité Clinician Scientist Program, Charitéplatz 1, 10117 Berlin, Germany*

<sup>8</sup>*Cluster of Excellence Matters of Activity. Image Space Material funded by the Deutsche Forschungsgemeinschaft (DFG, German Research Foundation) under Germany's Excellence Strategy – EXC 2025*

<sup>9</sup>*Institute of Physical Chemistry and Electrochemistry, Leibniz Universität Hannover, Callinstr. 3A, 30167 Hannover, Germany*

\* Corresponding author: marie.weinhart@fu-berlin.de and marie.weinhart@pci.uni-hannover.de

## 1. Materials and Methods

### 1.1 Materials, buffers, reagents and devices

Papain from *Carica papaya* (#1.07144, 30000 U/mg), sodium dodecyl sulfate (SDS), triton™ X-100, methacrylic anhydride (MA), 2,4,6-trinitrobenzene sulfonic acid (TNBS), collagenase type II from *Clostridium histolyticum*(#C2-22-BIOC,  $\geq 200$  U/mg), 1,9-dimethyl-methylene blue (DMMB), glycine, chondroitin sulfate (CS), chloramine T trihydrate (98%), perchloric acid (70 %), trans-4-hydroxy-L-proline, peracetic acid (38-40%),  $\beta$ -mercaptoethanol, bromophenol blue, coomassie brilliant blue, dithiothreitol, 2-chloroacetamide, hydrocortison-21-hemisuccinat (#H2270), insulin 5 (#I9278), penicillin/streptomycin (p/s) and L-glutamineSolution 100X (#TMS-002), phosphate-buffered saline (PBS) tablets (#4417), 2-(*N*-morpholino)ethanesulfonic acid (MES),3-(trimethylsilyl)propionic-2,2,3,3-d4 acid sodium salt (TMSP,#269913-1), ethylenediamine tetra acetic acid disodium salt (EDTA- $\text{Na}_2$ ), L-cysteine (#168149), tris-base (#T1503), and ammonium bicarbonate (#A6141) were purchased from Sigma-Aldrich (St. Louis, MO, United States) and used as received. Glycidyl methacrylate (GMA, #M0590) and triethylamine (TEA, #T0424) were purchased from TCI Deutschland GmbH (Eschborn, Germany).Precision Plus Protein unstained standard and PROTEAN® TGX™ precasted polyacrylamide gels with a concentration gradient of 4–20% were purchased Bio-Rad and (Feldkirchen, Germany).*p*-Dimethyl aminobenzaldehyde (DMAB), toluene ( $\geq 99.8$  %), propan-2-ol ( $\geq 99.8$  %), glacial acetic acid ( $\geq 99\%$ ), William's E cell culture medium (WEM) with and without phenol red, prestoBlue™ reagent, Pierce BCA™ kit,Pierce™LAL chromogenic endotoxin quantitation kit as well as fluorescein diacetate (FDA, #F7378), propidium iodide (PI, #P4170) and Hoechst (#33342) were purchased from Thermo Fisher Scientific (Waltham, MA, United States). Collagen type I

from rat tail was purchased from (Bio-Techne, R&D Systems, Minnesota, USA). Human HepaRG 101 cells were purchased from Biopredic International (Saint-Grégoire, France). Fetal bovine serum (FBS) was obtained from PAN Biotech (Wimborne, UK). Fine-meshed nylon filters were purchased from Oriental riverkit (Wuhan, China).

Ehrlich's reagent was freshly prepared as 1.1 M DMAB in a 70:30 v/v% mixture of *n*-propanol and 70% perchloric acid. Chloramine-T working solution was prepared as 80:10:10 % v/v of citric acetate buffer, *n*-propanol, and H<sub>2</sub>O, respectively, and stored at RT. Citric acetate buffer for chloramine-T working solution contained 5% citric acid, 7.24% sodium acetate, and 1.2% glacial acetic acid in H<sub>2</sub>O and was adjusted to pH 6.0 with NaOH. The DMMB dye solution was prepared by adding the dye (0.038 mM) to a mixture of glycine (40.5 mM), sodium chloride (40.5 mM), and tris-HCl (0.2 M) in MilliQ water and adjusting the pH to 3 with 1 M HCl. The solution was then filtrated using 0.22 µm syringe filters (PTFE syringe filter, qpore®, neolabMigge GmbH, Heidelberg, Germany). SDS protein lysis buffer (pH 6.8) was prepared from 50 mM tris-HCl, 2% SDS, 10% glycerol, 1% β-mercaptoethanol, 12.5 mM EDTA, and 0.02% bromophenol blue. SDS-PAGE staining solution was prepared as 1% (w/v) coomassie brilliant blue in 5% (v/v) methanol and 10% (v/v) acetic acid in H<sub>2</sub>O. Destaining solution was prepared as 5% (v/v) methanol and 10% (v/v) acetic acid in H<sub>2</sub>O, while SDS running buffer consisted of tris-base (250 mM), glycine (1.92 M), and SDS (1%) in water at pH= 8.3. Lithium phenyl-2,4,6-trimethylbenzoylphosphinate (LAP) photoinitiator was synthesized as described in the literature[1].

## **1.2 Decellularization and solubilization of liver dECM**

The decellularization of liver ECM was conducted in accordance with our previously published protocol[2] without any alterations. Subsequently, the enzymatic solubilization of the dry dECM was performed using papain, following our established protocol with minor

adjustments[2]. Briefly, dry dECM (10 mg) was added to a papain solution (1 mg of papain in 1 mL of aqueous 20 mM EDTA and 5 mM L-cysteine, pH 5.5) at RT for 48 hours with periodic homogenization (T 10 basic Ultra-Turrax, IKA®-Werke GmbH & Co. KG). The papain digestion was then stopped by adjusting the pH to 9.5-10 with 10 M NaOH solution on ice for 1 h. Afterward, the digested dECM was centrifuged gently at 140 x g for 5 minutes to remove any undigested particles. Supernatants were purified via dialysis (SpectraPor® with molecular weight cut-off of 1 kDa, Carl Roth GmbH + Co. KG (Karlsruhe)) first in distilled water and then in 0.01 M HCl for 2-3 days with 2-3 acid changes. The final dECM digests were snap-frozen with liquid nitrogen and lyophilized (alpha 2-4 LDplus, Martin Christ Gefriertrocknungsanlagen GmbH, Osterode am Harz, Germany). Dry dECM foam-like digests were stored at -20 °C until further use.

### **1.3 Biochemical and protein structural characterization**

#### *dsDNA, sGAGs, and hydroxyproline quantification*

In an effort to streamline our prior protocols[2, 3] we employed the same papain-treated sample for the simultaneous assessment of all tissue components, including dsDNA, and sGAGs and hydroxyproline, in a single run. Minor refinements were incorporated with guidance from a recently published protocol[4].

Briefly, dry samples (10 mg) were mixed with 1 mg papain in lysis solution (aqueous 10 mM L-cysteine and 40 mM EDTA; pH=5.5) and incubated at 60 °C for 24 h under strong shaking. Next, digested samples were either centrifuged (1000 x g for 5 min) and the supernatants were transferred into a new vial, mixed, and used for dsDNA and sGAG analysis or used without further purification for hydroxyproline analysis.

The dsDNA content was determined with a DNA-quantitation kit (AccuBlue® Broad Range, Biotium, USA) according to the manufacturer's instructions.

For sGAG quantification, the 1,9-dimethylmethylene blue dye (DMMB) assay was applied. Briefly, 10  $\mu$ L of sGAG standards (chondroitin sulfate) or unknown samples were mixed with filtered DMMB dye solution (200  $\mu$ L) in a 96-well microplate and the absorbance at 525 nm was measured immediately at RT.

To quantify the hydroxyproline content, 250  $\mu$ L of uncentrifuged sample was added to an equal amount of 12 M HCl (250  $\mu$ L) in a screw-cap tube (Eppendorf, Germany) and incubated for 16 h at 120 °C under continuous shaking. After complete hydrolysis and dryness, PBS (1 mL) was added to the dried samples and mixed for a few minutes followed by centrifugation (2,500 x g for 10 min). The supernatant was collected and used to chromogenically quantify the hydroxyproline content. Briefly, 10  $\mu$ L of both standards (trans-4-hydroxy-L-proline) and unknown samples were added in triplicates into the 96-well plate and then oxidized with freshly prepared 0.05 M chloramine-T (50  $\mu$ L) in chloramine-T working solution for 20 min at RT. Finally, freshly prepared Ehrlich's reagent (50  $\mu$ L) was added to each well, mixed, protected from light, and incubated for 30 min at 65 °C. The plate was cooled to RT and absorbance was measured at 540 nm. Blanks of the samples treated in the same conditions without chloramine-T-solution and Ehrlich's reagent served as blanks.

#### *SDS polyacrylamide gel electrophoresis (SDS-PAGE)*

For SDS-PAGE, dry digested dECM, dECM-(G)MA (2 mg/mL), and rat tail collagen (1 mg/mL) as a control were solubilized in 0.01 M HCl, and 10  $\mu$ L of samples were mixed with SDS protein lysis buffer at a 1:1 ratio, heated to 90 °C for 10 min, and then cooled to RT. Subsequent steps were carried out as per our previously established protocol[2].



*Circular dichroism (CD) and Fourier-transform infrared (FTIR) spectroscopy*

For circular dichroism spectroscopy, the digested dECM and dECM-(G)MA samples (2 mg) were dissolved in 0.1 M sodium phosphate (1 mL, pH 7.4) and stirred overnight at 4 °C. Samples were centrifuged gently to remove any insoluble particles and the supernatant was used for CD measurements. The final protein concentration was adjusted to 0.1 mg/mL after concentration determination via UV-vis spectroscopy (Agilent Cary 8454, Agilent technologies, USA) using a standard curve from rat tail collagen type I. Further details on sample measurements can be found in our previous protocol[2]. ATR-FTIR was carried out on lyophilized and ground dECM powders (dECM, digested-dECM, and dECM-(G)MA) using a Nicolet iS10 equipped with a smart diamond ATR accessory. 32 scans were recorded from 4000 to 600  $\text{cm}^{-1}$  and averaged for each spectrum. The resolution and the interval scanning were set to 4 and 2  $\text{cm}^{-1}$ , respectively.

**1.4 Quantification of the cold stability of soluble protein**

To quantify the cold stability of soluble proteins present in digested dECM and dECM-(G)MA suspensions, 10 mg of the dry samples were dissolved in PBS (1 mL), adjusted to a pH of 7.4, if necessary, then homogenized (T 10 basic Ultra-Turrax, IKA®-Werke GmbH & Co. KG) and left for 2 weeks on a shaker at 4 °C. Afterwards, all samples were centrifuged (45000xg for 10 min at 4 °C) and a photograph was taken directly. Soluble proteins in the supernatants were then quantified via a bicinchoninic acid (BCA) assay following the manufacturer's instructions. Therefore, 5  $\mu\text{L}$  of the supernatant was diluted 5-fold by PBS addition (20  $\mu\text{L}$ ) and mixed with the kit-derived working reagent (200  $\mu\text{L}$ ) in a 96 well-plate at 37 °C for 30 minutes. The absorbance was measured at 562 nm at RT using a microplate reader (Infinite® M200 Pro, Tecan, Switzerland). Samples were run in triplicate and compared to the kit-derived BSA standard curve.

### 1.5 Pierce™ LAL chromogenic endotoxin quantitation

The potential presence of endotoxins in dECM-(G)MA 3D-printed scaffolds was tested using a Pierce™ LAL chromogenic endotoxin quantitation kit according to the manufacturer's instructions. Briefly, the 3D-printed scaffolds (d= 5 mm, h= 1 mm) at dECM-(G)MA concentration of 1.5wt% and LAP of 0.5wt% were treated with 70% ethanol (30 min) and subsequently washed with sterile PBS (3 x 10 min) and left overnight in sterile PBS (200 μL), after which 50 μL of the incubated PBS sample was warmed (5 min, 37 °C), mixed with 50 μL of provided Limulus ameocyte lysate reagent (LAL) and incubated under exclusion of light (10 min, 37 °C). Next, chromogenic substrate (100 μL) was added and incubated for an additional 6 min under the exclusion of light. The reaction was stopped with 50 μL of 25% (v/v) acetic acid and the absorbance was read at 405 nm using the microplate reader. The endotoxin content was determined using a provided *E.coli* liposaccharide standard.

### 1.6 Brillouin microscopy mapping

In Brillouin light scattering spectroscopy, the incident laser light scatters on thermally induced density waves, which travel within the sample at the speed of sound. Thus, the incident laser light gets Doppler-shifted by the frequency shift  $\omega_B$ . Accordingly, the frequency shift  $\omega_B$  can be linked to the acoustic velocity by[5]

$$\omega_B = v_A \vec{q},$$

in which  $v_A$  denotes the sound velocity in the sample and  $\vec{q}$  the exchange vector given by:

$$\vec{q} = \frac{2n}{\lambda_0} \sin \frac{\theta}{2}.$$

Here,  $n$  denotes the refractive index of the matrix,  $\lambda_0$  the incident laser wavelength, and  $\theta$  the scattering angle between incident light and collected scattered light. By changing the angle of incidence, the scattering probe intensity can be altered, allowing the measurement of the

material's band structure. Here, we settled on the back-scattering geometry eliminating the trigonometric function.

To access the homogeneity of the crosslinked 1.5 wt% dECM-(G)MA-based gels ( $d = 5\text{mm}$ ,  $h = 1\text{ mm}$ ) via the microelasticity of the equilibrated samples ( $n = 2, 3$  technical replicates each) in PBS at  $20^\circ\text{C}$ , a narrow linewidth single longitudinal mode laser with a wavelength of  $532\text{ nm}$  (Samba; Cobolt AB, Solna, Sweden) coupled into a custom automated microscope was used. The laser spot was focused by a long working distance  $20\times$  objective with a numerical aperture of  $0.42$  (M Plan Apo; Mitutoyo, Takatsuku, Japan) to a diffraction-limited spot ( $1/e^2$ ) of approximately  $770\text{ nm}$  laterally.

The back-scattered light was collected with the same objective. Using a  $\lambda/4$  plate upstream of the objective, the sample was illuminated with circularly polarized light. The scattered light was sent through the polarized beam splitter to the Brillouin spectrometer. The Brillouin-scattered light was analyzed with a 3+3-pass Tandem Fabry-Pérot (TFP) interferometer (TFP-2 HC; The Table Stable Ltd., Mettmenstetten, Switzerland). The spectrometer was actively stabilized in each scan to the wavelength of the laser allowing prolonged acquisition without the loss of frequency locking.

For the experiments conducted, the laser power was set to  $1\text{ mW}$ , in order to prevent heating and additional crosslinking within the sample. As the Brillouin scattering process is linear to the incident laser power, we choose the input pinhole of the Brillouin spectrometer as large as possible. The output pinhole was set to  $450\text{ }\mu\text{m}$ , resulting in a Finesse of the TFP of approximately  $80$  for the chosen mirror spacing of  $3\text{ mm}$ .

For data acquisition on the different samples, a randomly chosen central region of  $25\text{ }\mu\text{m} \times 25\text{ }\mu\text{m}$  per sample was scanned with  $1\text{ }\mu\text{m}$  step width. This allowed for (1) homogeneity

assessments within the sample and (2) averaging the Brillouin frequency shift on two independently printed samples with 3 technical replicates each.

The obtained spectral data was fitted using a custom Python script. First, the data was zero-padded, then deconvoluted, using the automatically detected instrumental spectral response function. The resulting spectrum was fitted using the function of the damped harmonic oscillator:

$$I_{\text{DHO}}(\omega, I_0, \omega_B, \Delta_B, B) = \frac{1}{\pi} \frac{I_0 4\omega_B^2 \Delta_B}{(\omega^2 - \omega_B^2)^2 + 4\omega_B^2 \Delta_B^2} + B,$$

in which  $I_0$  denotes the Brillouin scattering intensity,  $\Delta_B$  the Brillouin scattering line width and  $B$  the baseline of the signal, mainly caused by the detector's dark count.

### **1.7. Contact angle (CA) measurements**

Contact angle measurements on 3D-printed hydrogels (5 mm diameter, 1 mm height) comprising 1.5 wt% dECM-(G)MAbioresins and 0.5 wt% LAP were carried out using the sessile drop method with a DataPhysics Instruments system (Filderstadt, Germany) and the SCA202 software (version 3.12.11). Before measurement, hydrogels were thoroughly rinsed with Milli-Q water, placed on plastic cover slips, and dried by lightly dabbing with dry tissue paper to remove surface water without applying any pressure. A droplet of Milli-Q water (2  $\mu\text{L}$ ) was precisely applied to the hydrogel at 1  $\mu\text{L/s}$  using a precision syringe, and contact angles (CAs) were immediately measured using the Young-Laplace model. Each hydrogel underwent three independent measurements.

## **2. Additional figures and discussion**

Biochemical properties of decellularized, solubilized, and functionalized ECM samples were characterized to evaluate the impact of these processing steps on the dECM macromolecules.

Comparative FTIR spectra of native, digested, and (G)MA-functionalized dECM, as shown in **Figure S1A**, along with their band assignments detailed in **Figure S1B**, revealed consistent collagen-specific bands across all stages. This indicates the protein structural integrity of collagen is maintained from native raw material to final bioresin, demonstrating the effectiveness of the processing steps in preserving key extracellular matrix components.

The dsDNA content of the digested, lyophilized dECM was  $40 \pm 8$  ng/mg, locating below the generally accepted threshold limit of 50 ng/mg established by Crapo *et al.* (**Figure S1C**)[6]. The sGAGs content in the dry tissues remained unchanged after decellularization, digestion, and methacryloylation. Meanwhile, the hydroxyproline content increased in the tissue after removal of the cells and remained unchanged after digestion and methacryloylation (**Figure S1D and S1E**). The retention of sGAGs after decellularization is crucial as they provide structural integrity and mechanical support and regulate cellular processes in the ECM, thereby maintaining tissue bioactivity and functionality[7-9]. The increased hydroxyproline content can be assigned to the enrichment of collagen in dECM after cell removal, as reported in previous studies[10, 11].

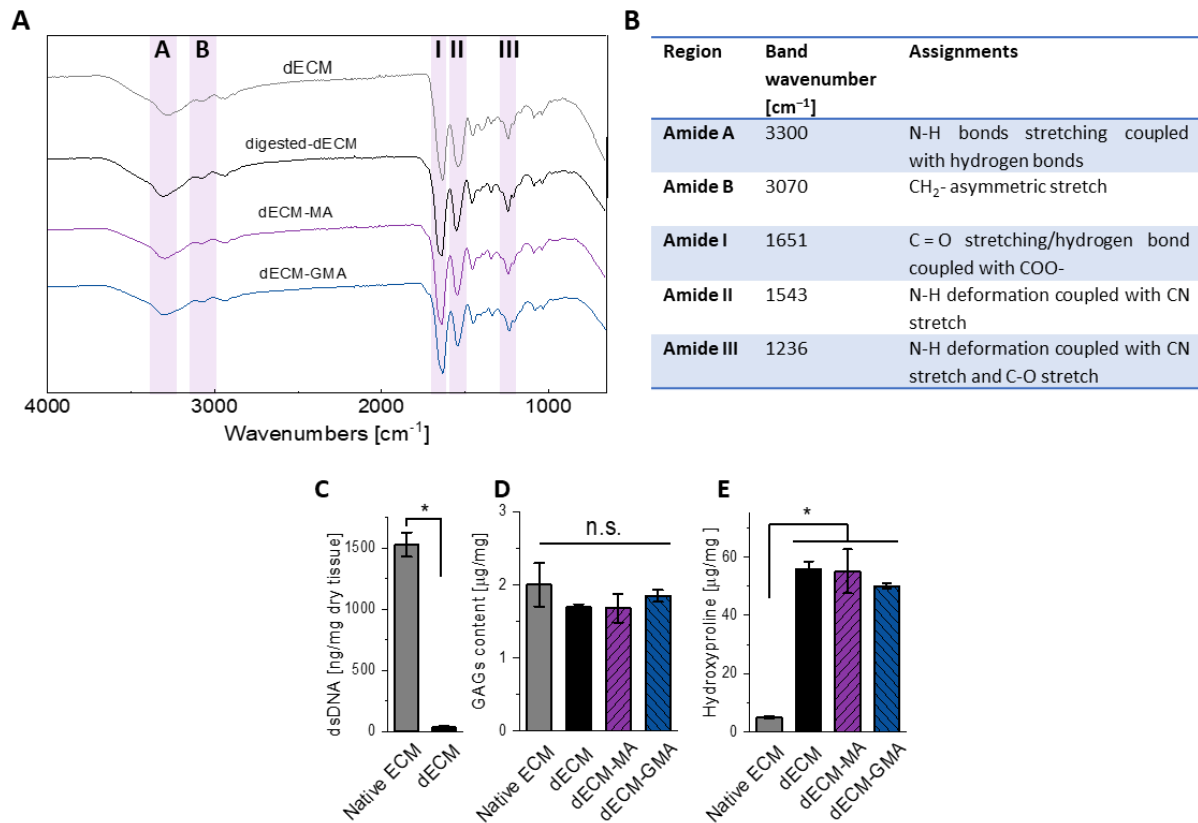


**Figure S1.** Structural and biomolecular analysis of native ECM, digested dECM and functionalized dECM-MA and dECM-GMA. **(A)** FTIR spectra of dry dECM-(G)MA showing the presence of collagen characteristic amide bands A, B, I, II and III in comparison to dECM and digested dECM and **(B)** assignments of the characteristic bands. **(C)** The dsDNA, **(D)** sGAGs, and **(E)** hydroxyproline content. All data were normalized to mg of dry weight of dECM. Data are presented as mean  $\pm$  SD for  $n = 3$ , where \* indicates statistical significance ( $p < 0.05$ ) between samples according to Mann-Whitney U test.

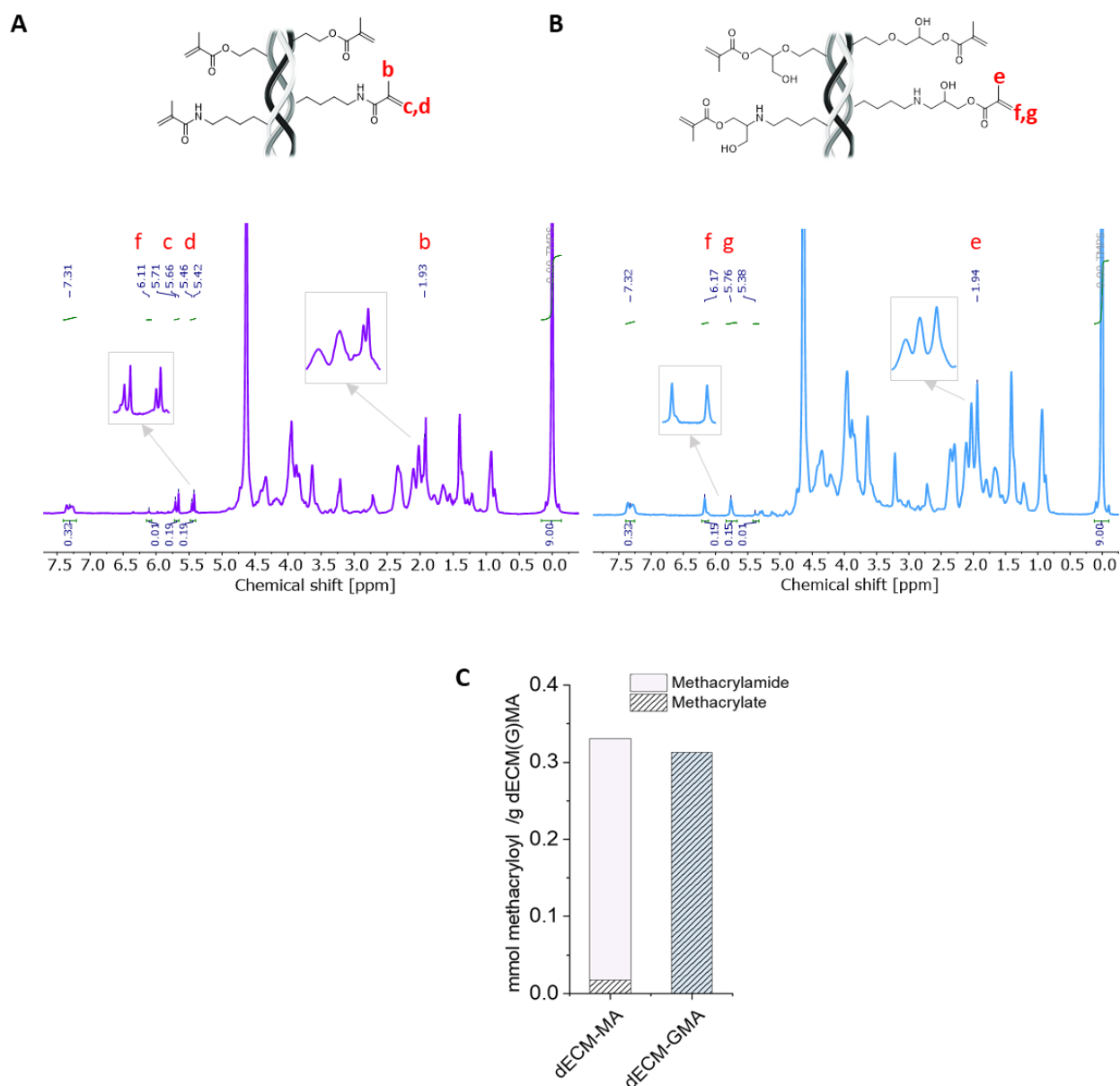


**Figure S2.** Representative  $^1\text{H}$  NMR spectra of (A) dECM-MA and (B) dECM-GMA in  $\text{D}_2\text{O}$ . Signals of the double bond protons in methacrylamide (5.4 & 5.7 ppm, c & d) and methacrylate (5.7 & 6.1 ppm, f & g) groups as well as the methacrylic methyl groups (1.9 ppm) are enlarged and their integrals indicated and compared to TMS at 0 ppm as an internal standard. (C) The methacrylamide and methacrylate content in both dECM-(G)MA biopolymers calculated according to equation (1) stated in the main article.

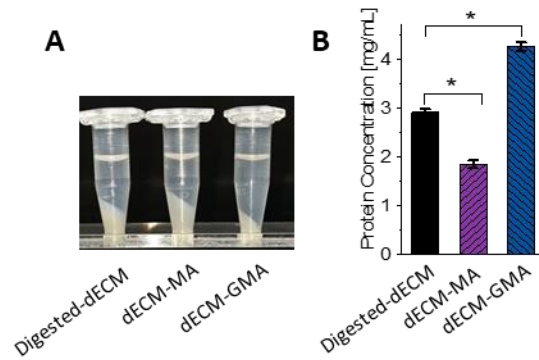


**Figure S3.** (A) Representative photographs of digested dECM and dECM-(G)MA samples after a solubility and stability test of the lyophilized samples (10 mg/mL) in PBS (pH=7.4), which included an extensive two-week solvation period at 4 °C on a rotational shaker followed by centrifugation of the insoluble fraction to quantify the soluble protein fraction in the supernatants. (B) Protein quantification via aBCA assay. Data are presented as mean  $\pm$  SD for  $n = 3$ , where \* indicates statistical significance ( $p < 0.05$ ) between samples according to Mann-Whitney U test.



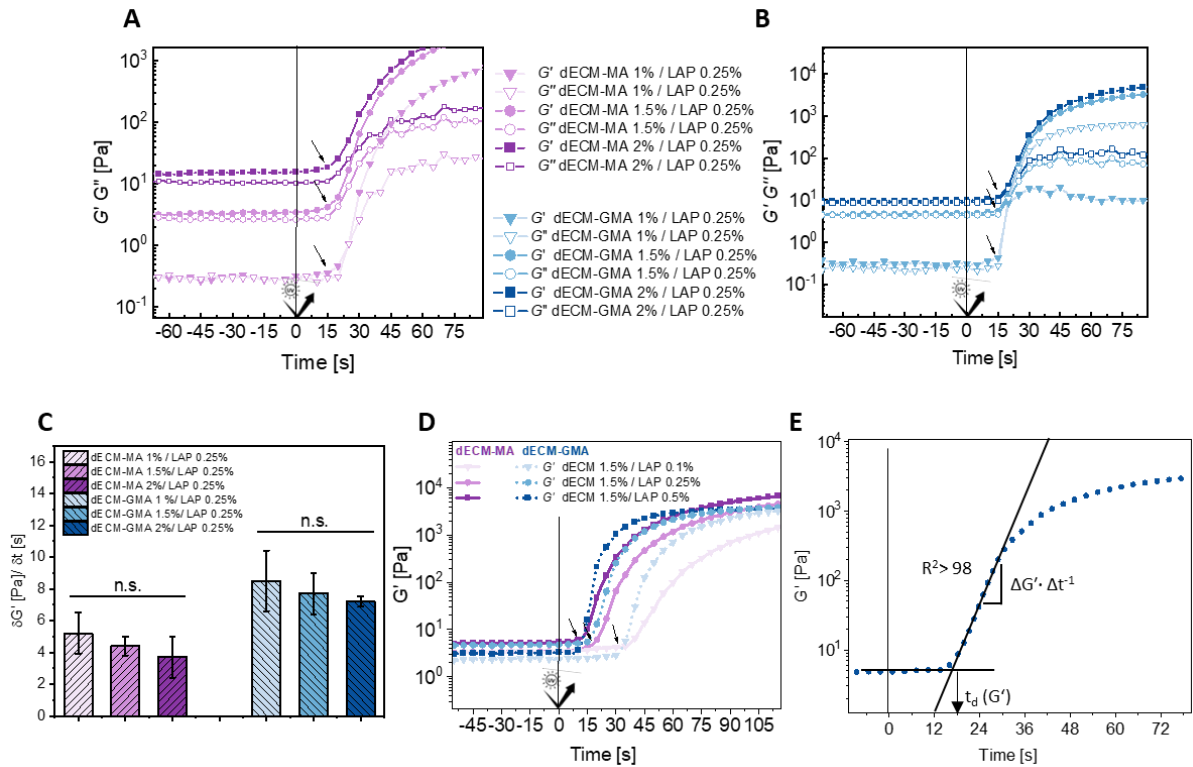


**Figure S4.** Real-time photorheology of dECM-(G)MA resins. Representative curves of storage ( $G'$ ) and loss ( $G''$ ) modulus of both (A) dECM-MA and (B) dECM-GMA at different concentrations (1, 1.5, and 2wt%) prepared in cell culture media at physiological conditions and mixed with 0.25% LAP directly before the measurements with arrows indicating the time needed to observe the increase in the  $G'$  modulus after switching on the light (delay time). (C) Index for the photoreactivity  $\Delta G'/\Delta t$  extracted from the slope in the linear region of the  $G'$  curves in A and B between the onset and the beginning of the convergence period. (D) Representative  $G'$  curves of dECM-(G)MA at 1.5 wt% prepared in cell culture media and mixed with different concentrations of LAP (0.1, 0.25, and 0.5wt%) directly before the measurements with arrows indicating the different delay times for the onset of the  $G'$  modulus increase after switching on the light. (E) Representative model for the determination of the slope ( $\Delta G'/\Delta t$ ) and the delay time ( $t_d(G')$ ) from the obtained photorheology curves. Data in

Care presented as mean  $\pm$  SD for  $n = 3$ , where \* indicates statistical significance ( $p < 0.05$ ) between samples according to Kruskal-Wallis test followed by Dunn's test.

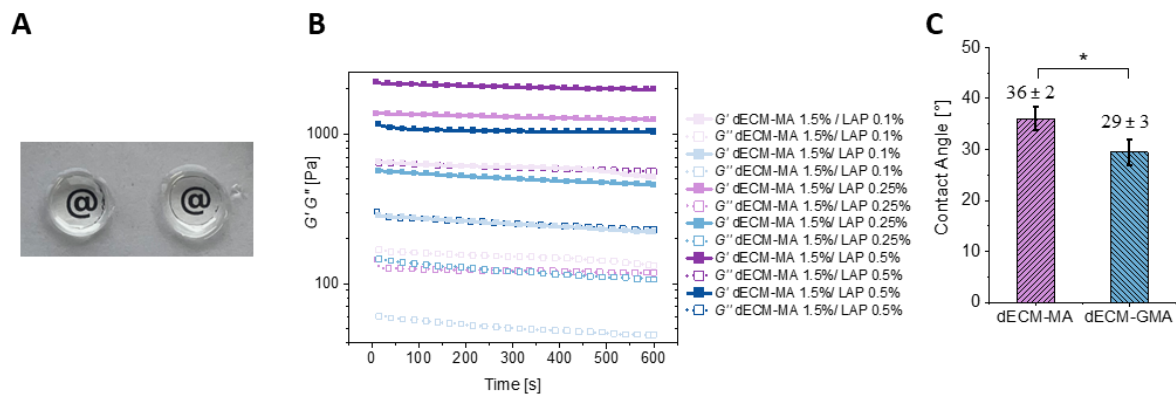


**Figure S5.** (A) Representative image of 3D-printed discs ( $d = 5$  mm and  $h = 1$  mm) from 1.5 wt% dECM-(G)MA bioresins and 0.5 wt% LAP in cell culture medium, subsequently rinsed extensively with Milli-Q water to demonstrate the hydrogel's transparency. (B) Representative time-dependent curves of the storage  $G'$  and the loss modulus  $G''$  of 3D-printed discs ( $d = 8$  mm and  $h = 1$  mm) from dECM-(G)MA resins formulated at 1.5 wt% in cell culture medium with different concentrations of LAP (0.1, 0.25, and 0.5 wt%) at 37 °C. (C) Contact angle analysis on the 3D-printed hydrogels from 1.5 wt% dECM-(G)MA bioresins and 0.5 wt% LAP. Data in Care presented as mean  $\pm$  SD for  $n = 3$ , where \* indicates statistical significance ( $p < 0.05$ ) between samples according to Kruskal-Wallis test followed by Dunn's test.

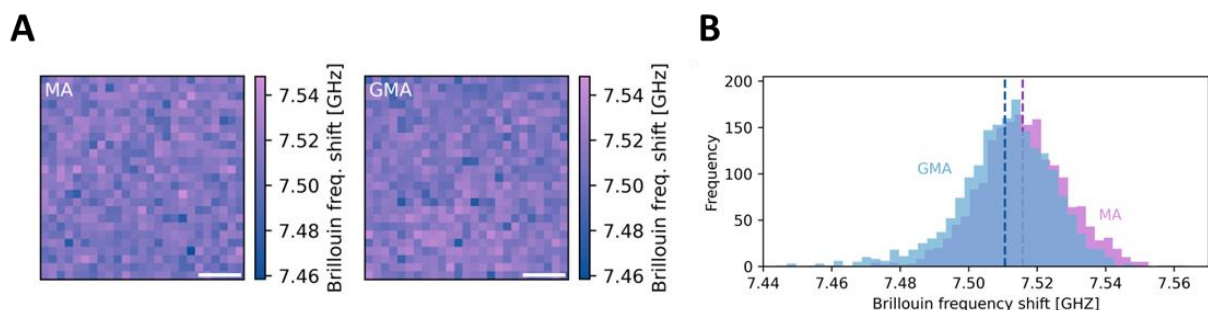


**Figure S6.** Representative Brillouin frequency shift maps (A) and histograms of the Brillouin frequency shift (B) of 25 x 25  $\mu\text{m}^2$  cross sections of dECM-(G)MA-based (1.5 wt% resin, 0.5 wt% LAP) 3D-printed acellular gel discs ( $d = 5 \text{ mm}$ ,  $h = 1 \text{ mm}$ ) which were raster-scanned in 1  $\mu\text{m}$  steps at random positions at 20 °C. Dotted line indicates the average of the distributions. Gels were equilibrated in PBS at 20 °C. Scale bar: 5  $\mu\text{m}$  ( $n = 2, 3$  technical replicates each).

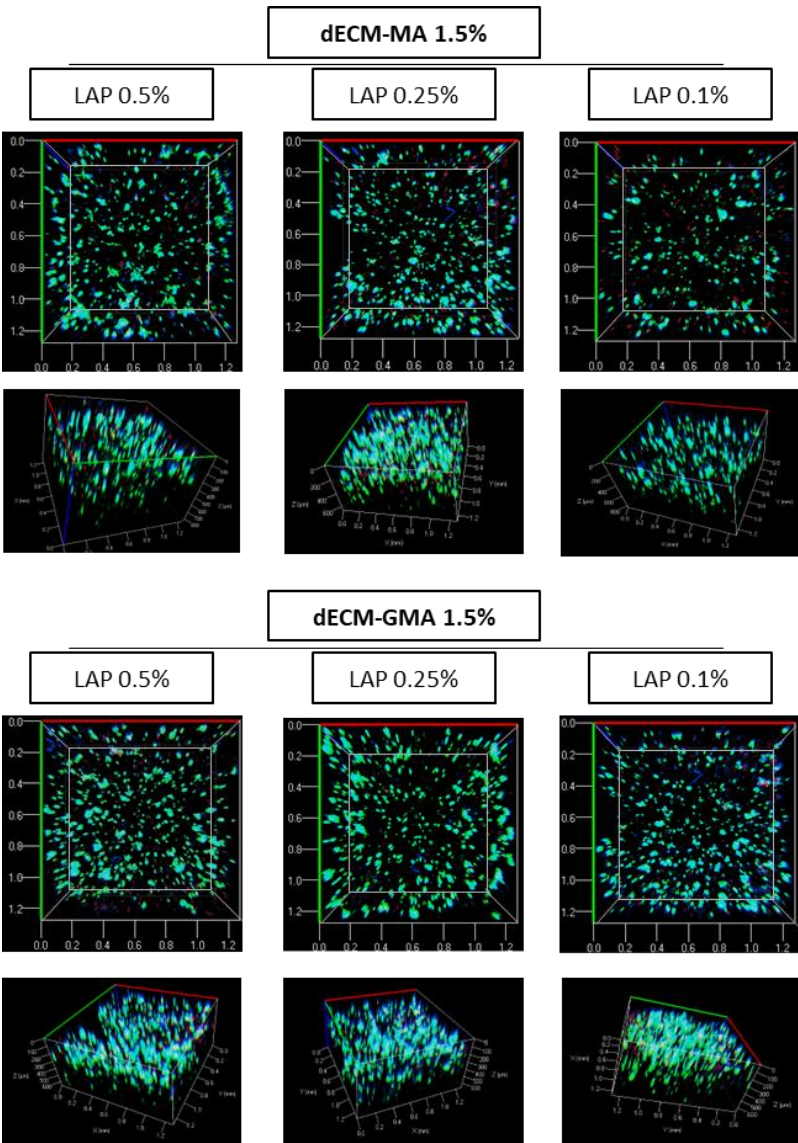


**Figure S7.** *Representative confocal fluorescence images of the 3D-bioprinted structures from bioresins composed of dECM-(G)MA(1.5 wt%) in cell culture medium and mixed directly before printing with different concentrations of LAP (0.1, 0.25, and 0.5wt%) and  $1.4 \times 10^6$  HepaRG cells/mL. Scaffolds were fluorescently stained with Hoechst (blue, nuclei), FDA (green, live cells), and PI (red, dead cells). Images were taken 24 hours after 3D bioprinting, and the thickness of the z-stack was between 600-800  $\mu$ m where the homogeneous distribution within the scaffold is shown.*

## References

- [1] B.D. Fairbanks, M.P. Schwartz, C.N. Bowman, K.S. Anseth, Photoinitiated polymerization of PEG-diacrylate with lithium phenyl-2,4,6-trimethylbenzoylphosphinate: polymerization rate and cytocompatibility, *Biomaterials* 30(35) (2009) 6702-7.
- [2] A. Almalla, L. Elomaa, L. Bechtella, A. Daneshgar, P. Yavvari, Z. Mahfouz, P. Tang, B. Kokschi, I. Sauer, K. Pagel, K.H. Hillebrandt, M. Weinhart, Papain-Based Solubilization of Decellularized Extracellular Matrix for the Preparation of Bioactive, Thermosensitive Pre-Gels, *Biomacromolecules* 24(12) (2023) 5620-5637.
- [3] L. Elomaa, L. Gerbeth, A. Almalla, N. Fribicz, A. Daneshgar, P. Tang, K.H. Hillebrandt, S. Seiffert, M.I. Sauer, B. Siegmund, M. Weinhart, Bioactive photocrosslinkable resin solely based on refined decellularized small intestine submucosa for vat photopolymerization of in vitro tissue mimics, *Addit Manuf* 64 (2023) 103439.
- [4] K.M. Kim J, Hwang DG, Shim IK, Kim SC, Jang J. , Pancreatic Tissue-Derived Extracellular Matrix Bioink for Printing 3D Cell-Laden Pancreatic Tissue Constructs, *J Vis Exp* 13(154) (2019) 1.
- [5] R. Prevedel, A. Diz-Munoz, G. Ruocco, G. Antonacci, Brillouin microscopy: an emerging tool for mechanobiology, *Nat Methods* 16(10) (2019) 969-977.
- [6] P.M. Crapo, T.W. Gilbert, S.F. Badylak, An overview of tissue and whole organ decellularization processes, *Biomaterials* 32(12) (2011) 3233-43.
- [7] F.E. Uhl, F. Zhang, R.A. Pouliot, J.J. Uriarte, S. Rolandsson Enes, X. Han, Y. Ouyang, K. Xia, G. Westergren-Thorsson, A. Malmstrom, O. Hallgren, R.J. Linhardt, D.J. Weiss, Functional role of glycosaminoglycans in decellularized lung extracellular matrix, *Acta Biomater* 102 (2020) 231-246.
- [8] H. Yu, Y. Chen, H. Kong, Q. He, H. Sun, P.A. Bhugul, Q. Zhang, B. Chen, M. Zhou, The rat pancreatic body tail as a source of a novel extracellular matrix scaffold for endocrine pancreas bioengineering, *J Biol Eng* 12 (2018) 6.
- [9] M. Song, Y. Liu, L. Hui, Preparation and characterization of acellular adipose tissue matrix using a combination of physical and chemical treatments, *Mol Med Rep* 17(1) (2018) 138-146.
- [10] R.E. Coronado, M. Somaraki-Cormier, S. Natesan, R.J. Christy, J.L. Ong, G.A. Halff, Decellularization and Solubilization of Porcine Liver for Use as a Substrate for Porcine

Hepatocyte Culture: Method Optimization and Comparison, *Cell Transplant* 26(12) (2017) 1840-1854.

[11] P.L. Lewis, J. Su, M. Yan, F. Meng, S.S. Glaser, G.D. Alpini, R.M. Green, B. Sosa-Pineda, R.N. Shah, Complex bile duct network formation within liver decellularized extracellular matrix hydrogels, *Sci Rep* 8(1) (2018) 12220.

[12] K. Chrabaszcz, K. Kaminska, K. Augustyniak, M. Kujdowicz, M. Smeda, A. Jaształ, M. Stojak, K.M. Marzec, K. Malek, Tracking Extracellular Matrix Remodeling in Lungs Induced by Breast Cancer Metastasis. Fourier Transform Infrared Spectroscopic Studies, *Molecules* 25(1) (2020) 236.

[13] R. Cheheltani, C.M. McGoverin, J. Rao, D.A. Vorp, M.F. Kiani, N. Pleshko, Fourier transform infrared spectroscopy to quantify collagen and elastin in an in vitro model of extracellular matrix degradation in aorta, *Analyst* 139(12) (2014) 3039-47.

[14] J. Habermehl, J. Skopinska, F. Boccafoschi, A. Sionkowska, H. Kaczmarek, G. Laroche, D. Mantovani, Preparation of ready-to-use, stockable and reconstituted collagen, *Macromol Biosci* 5(9) (2005) 821-8.

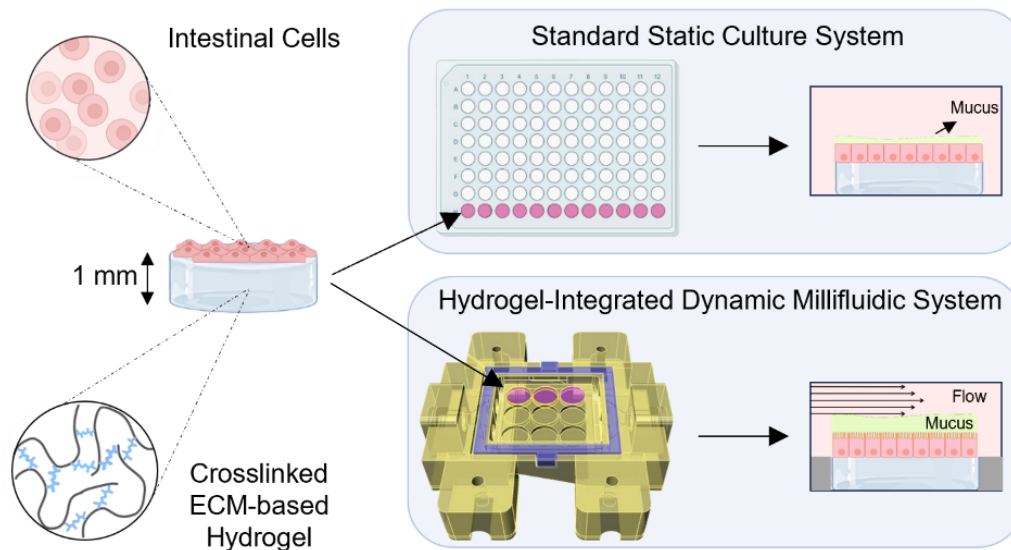
[15] G. Ahn, K.H. Min, C. Kim, J.S. Lee, D. Kang, J.Y. Won, D.W. Cho, J.Y. Kim, S. Jin, W.S. Yun, J.H. Shim, Precise stacking of decellularized extracellular matrix based 3D cell-laden constructs by a 3D cell printing system equipped with heating modules, *Sci Rep* 7(1) (2017) 8624.

### 4.3. Hydrogel-Integrated Millifluidic Systems: Advancing the Fabrication of Mucus-producing Human Intestinal Models

Almalla, A.; Alzain, N., Elomaa, L.; Richter, F.; Scholz, J.; Lindner, M.; Siegmund, B.; Weinhart, M.

*Cells* 2024, 13, 1080. <https://doi.org/10.3390/cells13131080>

This article is licensed under a [Creative Commons Attribution 4.0](https://creativecommons.org/licenses/by/4.0/) license





This study presents a millifluidic system designed to create advanced *in vitro* intestinal models. It hosts hydrogel scaffolds synthesized from bioactive, methacrylated small intestinal submucosa (dSIS-MA) seeded with HT29-MTX cells and human adult intestinal stem cells (ISCs) under apical fluid shear stress stimulus. The functionality of the fluidic system was validated by promoting cell differentiation and tissue maturation, inducing 3D reorganization of intestinal cell monolayers and mucus production. This 3D-printed tissue chamber hosting the dSIS-MA hydrogel shows significant promise for disease modeling and studying intestinal physiology through the modulation of both shear stress and scaffold mechanical properties.

#### Contributions of authors

Conceptualization, A.A., L.E., B.S., M.W. Methodology, A.A., N.A., F.R., J.S., M.L., M.W. Formal analysis, A.A., N.A. Investigation, A.A., N.A. Writing – original draft, A.A., M.W. Writing – review & editing, A.A., N.A., L.E., B.S., M.W. Supervision, B.S., M.W. Project administration, B.S., M.W. Funding acquisition, B.S., M.W.

## Article

# Hydrogel-Integrated Millifluidic Systems: Advancing the Fabrication of Mucus-Producing Human Intestinal Models

Ahed Almalla <sup>1</sup>, Nadra Alzain <sup>1,2</sup>, Laura Elomaa <sup>1</sup>, Fiona Richter <sup>1</sup>, Johanna Scholz <sup>1</sup>, Marcus Lindner <sup>1</sup>, Britta Siegmund <sup>2</sup> and Marie Weinhart <sup>1,3,\*</sup>

<sup>1</sup> Institute of Chemistry and Biochemistry, Freie Universität Berlin, Takustr. 3, 14195 Berlin, Germany; ahed.almalla@fu-berlin.de (A.A.); nadra.alzain@charite.de (N.A.); laura.elomaa@fu-berlin.de (L.E.); fior98@zedat.fu-berlin.de (F.R.); johascholz@zedat.fu-berlin.de (J.S.); m.lindner@fu-berlin.de (M.L.)

<sup>2</sup> Department of Gastroenterology, Infectious Diseases and Rheumatology (Including Nutrition Medicine), Charité—Universitätsmedizin Berlin, Hindenburgdamm 30, 12203 Berlin, Germany; britta.siegmund@charite.de

<sup>3</sup> Institute of Physical Chemistry and Electrochemistry, Leibniz Universität Hannover, Callinstr. 3A, 30167 Hannover, Germany

\* Correspondence: marie.weinhart@fu-berlin.de or marie.weinhart@pci.uni-hannover.de

**Abstract:** The luminal surface of the intestinal epithelium is protected by a vital mucus layer, which is essential for lubrication, hydration, and fostering symbiotic bacterial relationships. Replicating and studying this complex mucus structure *in vitro* presents considerable challenges. To address this, we developed a hydrogel-integrated millifluidic tissue chamber capable of applying precise apical shear stress to intestinal models cultured on flat or 3D structured hydrogel scaffolds with adjustable stiffness. The chamber is designed to accommodate nine hydrogel scaffolds, 3D-printed as flat disks with a storage modulus matching the physiological range of intestinal tissue stiffness (~3.7 kPa) from bioactive decellularized and methacrylated small intestinal submucosa (dSIS-MA). Computational fluid dynamics simulations were conducted to confirm a laminar flow profile for both flat and 3D villi-comprising scaffolds in the physiologically relevant regime. The system was initially validated with HT29-MTX seeded hydrogel scaffolds, demonstrating accelerated differentiation, increased mucus production, and enhanced 3D organization under shear stress. These characteristic intestinal tissue features are essential for advanced *in vitro* models as they critically contribute to a functional barrier. Subsequently, the chamber was challenged with human intestinal stem cells (ISCs) from the terminal ileum. Our findings indicate that biomimicking hydrogel scaffolds, in combination with physiological shear stress, promote multi-lineage differentiation, as evidenced by a gene and protein expression analysis of basic markers and the 3D structural organization of ISCs in the absence of chemical differentiation triggers. The quantitative analysis of the alkaline phosphatase (ALP) activity and secreted mucus demonstrates the functional differentiation of the cells into enterocyte and goblet cell lineages. The millifluidic system, which has been developed and optimized for performance and cost efficiency, enables the creation and modulation of advanced intestinal models under biomimicking conditions, including tunable matrix stiffness and varying fluid shear stresses. Moreover, the readily accessible and scalable mucus-producing cellular tissue models permit comprehensive mucus analysis and the investigation of pathogen interactions and penetration, thereby offering the potential to advance our understanding of intestinal mucus in health and disease.

**Keywords:** intestinal organoid; human terminal ileum; cell-based mucus model; physiological shear stress; CFD; dynamic cell culture; extracellular matrix; 3D printing; vat photopolymerization



**Citation:** Almalla, A.; Alzain, N.; Elomaa, L.; Richter, F.; Scholz, J.; Lindner, M.; Siegmund, B.; Weinhart, M. Hydrogel-Integrated Millifluidic Systems: Advancing the Fabrication of Mucus-Producing Human Intestinal Models. *Cells* **2024**, *13*, 1080. <https://doi.org/10.3390/cells13131080>

Received: 29 May 2024  
Revised: 14 June 2024  
Accepted: 18 June 2024  
Published: 21 June 2024



**Copyright:** © 2024 by the authors. Licensee MDPI, Basel, Switzerland. This article is an open access article distributed under the terms and conditions of the Creative Commons Attribution (CC BY) license (<https://creativecommons.org/licenses/by/4.0/>).

## 1. Introduction

The luminal surface of the intestinal epithelium is protected by a dynamic mucus layer that is essential for lubrication, water retention, and fostering symbiotic relationships with

commensal bacteria [1]. The gel-like layer comprises water (98%) and mucins (2%), with minor constituents, including proteins, lipids, salts, DNA, and cellular debris. Mucins are high-molecular-weight glycoproteins with branched oligomeric carbohydrate side chains on an elongated protein backbone. Gel-forming mucins, including MUC2, MUC5B, and MUC5AC, assemble into a highly swollen hydrogel. MUC2 is the predominant gel-forming mucin in the gut, reaching several hundred micrometers on the human intestinal surface [2]. Membrane-associated mucins, including MUC1, MUC3A, MUC3B, and MUC4, serve to tether the gel to the epithelial cell surface [3].

Despite critically contributing to the first line of defense in the intestinal lumen, the precise functions of the mucus layer in health and disease are not yet fully understood [4]. The challenges of accessing [5,6], processing, and preserving intestinal mucus [7], along with the variability between and within organs [8], impede systematic investigation and controlled modulation. In vitro intestinal models offer a promising avenue for addressing these challenges, provided they accurately replicate the composition and properties of human intestinal mucus, particularly health- and disease-specific features.

Current state-of-the-art models utilize human intestinal stem and progenitor cells (ISCs) isolated from crypts, capable of differentiating into a variety of intestinal epithelial cell types, including mucus-producing goblet cells. In contrast to intestinal cell lines, such as HT29-MTX, which exhibit a mixed absorptive goblet cell phenotype after differentiation and primarily secrete the gastric-specific mucin MUC5AC [9], ISC-derived goblet cells mainly secrete the intestine-specific mucin MUC2 [10]. When cultured in Matrigel™, ISCs assemble into proliferative organoid structures that resemble the intestinal lumen in their interior. These structures serve as models and tools for basic research and personalized medicine [11–13]. Nevertheless, 3D-cultured organoids exhibit limited mucus accessibility, as the secreted mucus lining the lumen appears entrapped within the organoid, impeding further manipulation [14,15]. To address this, apical-out repolarized intestinal organoids, which currently do not qualify for maintenance culture [16], and more practical 2D monolayers obtained from reseeded organoid-derived ISC fragments or single cells have been developed [17]. As substrates for two-dimensional (2D) models, various synthetic materials are employed, including non-porous tissue culture-treated polystyrene (TCPS) [18] and porous membranes derived from polycarbonate, polyethylene terephthalate (PET) [19], or polydimethylsiloxane (PDMS) [14]. The substrates are typically coated with a biomimetic thin layer of extracellular matrix (ECM)-derived proteins, such as growth factor-reduced Matrigel™, collagen, or laminin, to support ISC adhesion and growth. These substrates offer essential mechanical support, yet they do not fully recapitulate the biochemical and biophysical features of the compartmentalized intestinal microenvironments. Consequently, human ISCs seeded on 2D substrates frequently form fractured monolayers with a limited lifespan. These monolayers lack the critical self-sustainment necessary for long-term culture following a transition from an expansion to a differentiation medium [19]. The loss of stemness during the formation of a 2D monolayer or the differentiation of ISCs in vitro can be attributed to unphysiological substrate stiffness and inappropriate regulatory signaling [20,21]. Soft, bulk hydrogel substrates (Young's modulus: <1 kPa) made from natural ECM components, such as collagen or Matrigel™ [22], more closely replicate the composition and stiffness of the basal membrane of the intestinal stem cell niche, thereby supporting the development and proliferation of ISC-based self-sustained monolayers [21,23]. Despite their benefits, such physically crosslinked hydrogels hardly support long-term cultures due to their rapid enzymatic degradation and mechanical instability. To provide enhanced structural and mechanical support, such biopolymer-based gels require additional chemical/covalent crosslinking, particularly when 3D structuring of the bulk hydrogel scaffolds is desired [24]. Consequently, many laboratories currently rely on organoid-derived ISC monolayers cultured on Matrigel™-coated synthetic membranes due to the convenient and straightforward preparation process.

Chemical differentiation protocols are commonly used to induce ISC differentiation [11,12,19]. Recently, alternative mechanical stimulation through peristalsis or fluid shear stress has emerged



as an effective and more physiological alternative to differentiating ISCs [14,25] and cell lines into multiple intestinal cell types [26,27], often accompanied by 3D reorganization of the monolayer. Piezo1, a mechanical sensor expressed on epithelial cells [28], plays a pivotal role in this process by regulating stem cell proliferation and differentiation [29], tight junction protein expression [30], and MUC2 production and secretion of goblet cells [31].

In light of the current opportunities in biofabrication, we propose the development of advanced mucus-producing ISC-based models utilizing 3D-printed biomimetic hydrogel scaffolds with adjustable stiffness and the application of shear stress for the purpose of tissue maturation and mucus modulation. In order to facilitate dynamic culture, a tissue chamber was designed that hosts multiple cell-seeded hydrogels for exposure to adjustable apical shear stress. The chamber's performance was validated with HT29-MTX cells, and its efficacy in the solely shear stress-triggered multi-lineage differentiation of human ISCs from the terminal ileum was demonstrated, thereby highlighting the beneficial mucus-related effects achievable in a dynamic culture environment.

## 2. Materials and Methods

### 2.1. Materials

All chemicals, buffers, and reagents utilized in this investigation were acquired and prepared as previously published [26,32,33]. The Supplementary Materials (SM) section provides a comprehensive listing of these materials.

### 2.2. Decellularized and Methacrylated Small Intestinal Submucosa (dSIS-MA): Preparation, Printing, and Characterization

The preparation of dSIS-MA as a biomaterial resin for vat photopolymerization involved the decellularization, solubilization, and methacrylation of small intestinal submucosa (SIS) for subsequent 3D printing into hydrogels 6 mm in diameter ( $d$ ) and 1 mm in height ( $h$ ). The diameter of the scaffolds was chosen to align with the dimensions of standard 96-well plates ( $d = 6.4$  mm per well) for static culture controls and the cavities of the tissue chamber for dynamic culture following cell seeding. Their precise geometry enabled them to occupy the surface area of a well or tissue chamber's cavity seamlessly while still allowing for easy sample handling within a small margin of space. The preparative procedures, along with a comprehensive characterization of the resulting resin and the printed dSIS-MA-based hydrogels, were performed in accordance with our established protocols and are briefly outlined in the SM [32,33]. The characterization of materials was achieved through a number of different methods, including nuclear magnetic resonance spectroscopy ( $^1\text{H}$  NMR), circular dichroism spectroscopy (CD), rheology, atomic force microscopy (AFM), scanning electron microscopy (SEM), and chromogenic assays.

### 2.3. Flow Chamber Design, Fabrication, and Computational Fluid Dynamics (CFD)

The body of the dynamic tissue culture chambers was designed using the 3D computer-aided design (CAD) software, Rhinoceros (Version 5.0, Robert McNeel & Associates, Seattle, WA, USA), and fabricated with a vat digital light projection (DLP) 3D printer (Anycubic Photon D2 from Anycubic Technology Co., Shenzhen, China). The STL files of the CAD models are provided as Supplementary Data. We utilized a biocompatible, autoclavable resin (BioMed Amber, Formlabs, Somerville, MA, USA) for printing, with an 8 s curing time for each 100  $\mu\text{m}$  layer. Post-printing, the chamber bodies were thoroughly washed in isopropanol to remove uncross-linked resin and then post-cured under a 405 nm blue light lamp for 2.5 min on each side (Figure 1A). The printed chamber body dimensions were set at 5.4 cm  $\times$  5.4 cm  $\times$  1.3 cm ( $l \times w \times h$ ) (Figure 1A–C). The chamber was designed with a centered, broad flow channel ( $l \times w = 2.4$  cm  $\times$  2.0 cm) 2.5 mm in height (Figure 1D). Located just below the flow channel were nine disk-like cavities ( $d = 6$  mm,  $h = 1$  mm) designed to accommodate the intestinal tissue models, which are intended to be exposed to fluid flow shear stress (Figure 1D). The flow channel is formed between the chamber body and a lid when closing the tissue chamber. A transparent polycarbonate (Makroclear<sup>®</sup>

from Arla Plast, Motala, Sweden) lid ( $l \times w = 3.5 \text{ cm} \times 5.4 \text{ cm}$ ) with a height of 4 mm was precisely manufactured via computer numerical control (CNC) machining featuring four threads (M3,  $d = 3 \text{ mm}$ ), allowing it to be securely fastened to the chamber body with stainless-steel knurled thumb or socket head cap screws (M3, 1.2 mm, DIN 646, ERIKS, Halle (Westfalen), Germany) (Figure 1E,F). Detailed dimensions of the lid can be found in the SM. Tight sealing between the lid and chamber was accomplished through a silicone gasket custom-molded from a blue medical-grade two-component silicone kit (REPLISIL 22 N, SILCONIC<sup>®</sup>, Lonsee, Germany) (Figure 1E,F). After fabrication, additional hand-screwed threads (M5 screws) were created on the two sides of the chamber body where the fluid flow enters and exits the chamber to allow for the mounting of adapters (#40101, threaded connector, female luer lock, Qosina, Ronkonkoma, NY, USA) for tubing. The established flow chamber assembly was reusable and maintained structural integrity for up to 10 autoclaving cycles.

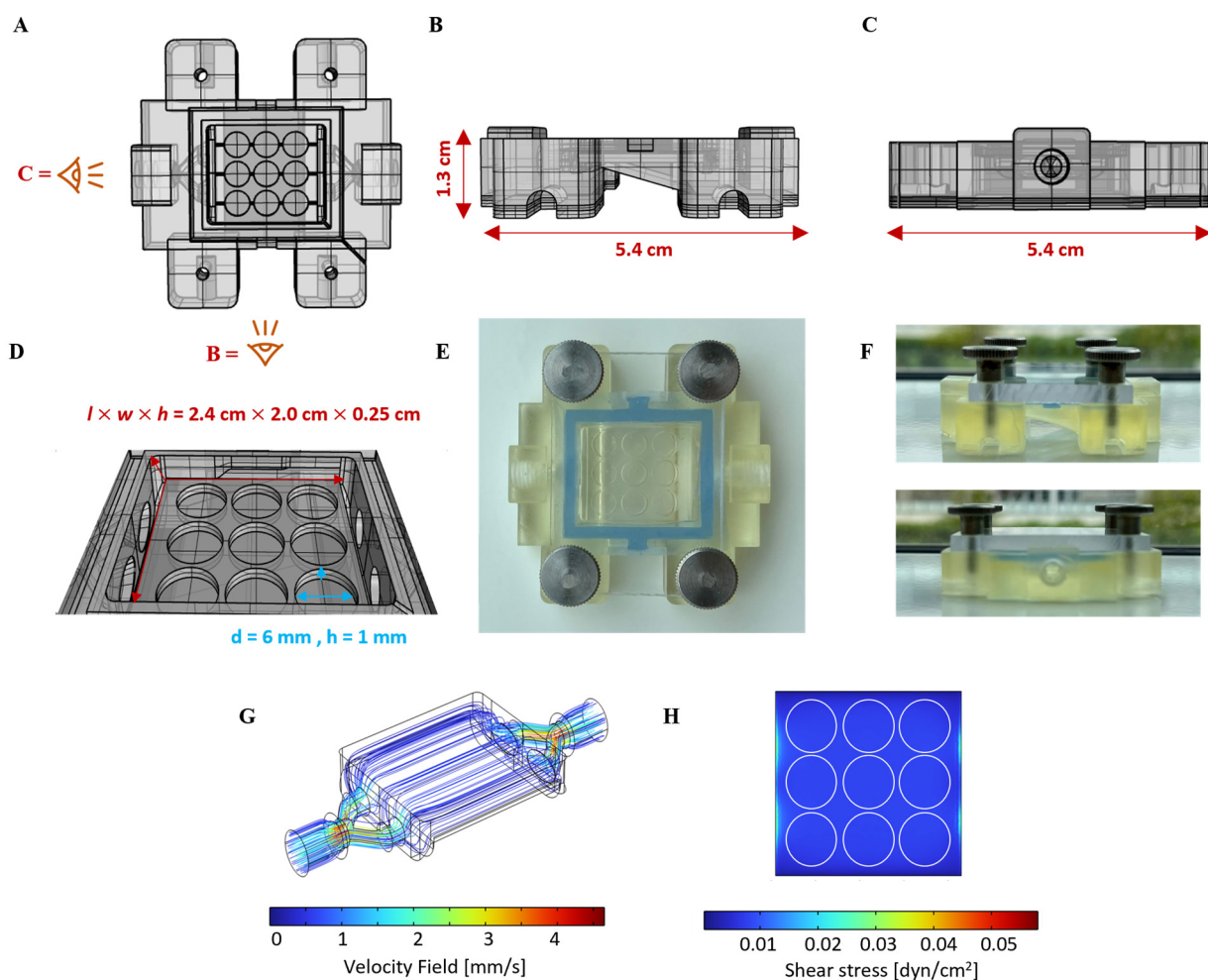


**Figure 1.** Illustration of flow chamber design to hold multiple surface-cellularized, dSIS-MA hydrogel scaffolds and apply defined, physiological surface shear stress under dynamic cell culture conditions. (A) Computer-aided design (CAD) model of the flow chamber body configured to accommodate nine scaffolds ( $d = 6 \text{ mm}$  and  $h = 1 \text{ mm}$ ). (B,C) Side views of the chamber body with its dimensions. (D) Flow channel dimensions in the CAD model. (E) Photographic image of the fully assembled chamber body, including transparent lid, blue silicon sealing, and four M3 screws. (F) Side views of the assembled chamber in (E). (G,H) CFD simulation of surface shear stress within the flow channel, with color gradients representing uniform low flow velocity at a defined medium flow rate of  $1.42 \text{ mL/min}$  and consistent laminar shear stress distribution of around  $0.01 \text{ dyne/cm}^2$ , indicating a homogenous environment for low fluid shear stress-assisted cell culture.

CFD analysis to simulate flow conditions, encompassing velocity fields and shear stress (Figure 1G,H), was conducted using COMSOL Multiphysics (v5.5, CFD module, COMSOL, Stockholm, Sweden). The laminar flow physics was selected, including gravity, and water was chosen as the fluid material. The inlet flow properties were set to  $1.42 \text{ mL}\cdot\text{min}^{-1}$ , with zero static pressure defined as the outlet condition. The default mesh setting was a “physics-controlled” mesh with a “normal” element size, and the mesh quality was judged based on COMSOL’s minimum element quality.

Wall shear stress ( $\tau$ ) within the chamber’s flow channel was estimated using Equation (1), as follows:

$$\tau = 6\mu Qh^{-2}w^{-1} \quad (1)$$

where  $\mu$  denotes dynamic viscosity ( $\mu = 0.93 \text{ mPa}\cdot\text{s}$  [34]),  $Q$  is the volume flow rate [ $\text{cm}^3\text{s}^{-1}$ ], and  $w$  and  $h$  denote the width [mm] and height [mm] of the fluidic channel, respectively.

## 2.4. Static Cell Culture

### 2.4.1. Culture and Seeding of HT29-MTX Cells

Human HT29-MTX cells (European Collection of Authenticated Cell Cultures via Sigma Aldrich, Darmstadt, Germany) were cultured in high glucose Dulbecco’s Modified Eagle Medium (DMEM) enriched with 10% fetal bovine serum (FBS), 1% non-essential amino acid solution (MEM-NEAA), and 1% penicillin/streptomycin (p/s) antibiotic mixture with medium change every 2–3 days. Cultivation was carried out in an incubator at  $37^\circ\text{C}$  with 5%  $\text{CO}_2$  and 95% humidity. To prepare 3D-printed dSIS-MA hydrogels ( $d = 6 \text{ mm}$ ,  $h = 1 \text{ mm}$ ) for cell seeding, they were disinfected with 70% ethanol for an hour and then washed three times in sterile phosphate buffered saline without calcium and magnesium ions (PBS –/–) with  $1 \times \text{p/s}$ , with each wash lasting an hour. The disinfected hydrogels were placed in a 96-well plate (Sarstedt AG & Co., Nümbrecht, Germany) and stored in sterile PBS (–/–) at  $4^\circ\text{C}$  until cell seeding. Before seeding, the PBS was carefully removed, and the hydrogels were allowed to equilibrate to room temperature for 10 min to prevent floating when the cell suspension was added. Next, HT29-MTX cells (passage numbers 10–13) were seeded at a density of  $6 \times 10^4$  cells per hydrogel ( $1.8 \times 10^5$  cells/ $\text{cm}^2$ ) by carefully adding  $100 \mu\text{L}$  of cell medium suspension dropwise directly to the center of each hydrogel to promote even cell distribution across the hydrogel surface. This setup was maintained for 5 days with medium changes every 2–3 days under static conditions to achieve a confluency between 80 and 100%. After reaching confluency, cellularized dSIS-MA hydrogels were transferred to the cavities of the flow chambers with the monolayers facing upward, marking the beginning of the experimental period (Day 0).

### 2.4.2. Crypt Isolation and Organoid Formation and Expansion

The basal medium for crypt isolation and Matrigel™ dilution is composed of Gibco™ advanced Dulbecco’s Modified Eagle Medium (DMEM/12) supplemented with 2 mM Corning™ cellgro™ L-glutamine (Corning Incorporated, Kaiserslautern, Germany),  $1 \times \text{p/s}$ , and 10 mM Gibco™ HEPES (Thermo Fisher Scientific, Darmstadt, Germany). Human primary epithelial cells were obtained from a biopsy of the terminal ileum of an adult healthy donor (sex: male; age: 20; approved by the ethical committee of the Charité—Universitätsmedizin Berlin). L-WRN cells (CRL-3276™, ATCC®) were cultured to generate a conditioned medium containing the growth factors Wnt3a (W), R-spondin-3 (R), and Noggin (N) essential for the culture of human intestinal organoids, following the protocol established by Miyoshi and Stappenbeck [35]. The pooled WRN-conditioned medium was mixed in a 1:1  $v/v$  ratio with PCM medium (Gibco™ advanced DMEM/F12 supplemented with Corning™ cellgro™ L-glutamine,  $1 \times \text{p/s}$ , and 20% FCS). For undifferentiated organoid formation/expansion and ISC culture, the 1:1 medium mixture was further supplemented with recombinant human epidermal growth factor (EGF, 50 ng/mL), nicotinamide (10 mM), A83-01 (0.5  $\mu\text{M}$ ), SB202190 (10  $\mu\text{M}$ ), and human gastrin I (10 nM) to the specified final concentrations and is henceforth referred to as expansion media. Crypt isolation from biopsies and subsequent formation and expansion of intestinal organoids were performed

as described earlier [33] and stated in the SM for reference. Passage numbers between 7 and 12 were used for the experiments.

#### 2.4.3. Culture of Organoid-Derived ISCs on dSIS-MA Hydrogels

For monolayer culture of organoid-derived ISCs, undifferentiated organoids from the human terminal ileum were isolated from Matrigel™ and enzymatically dissociated with TrypLE™ supplemented with rock inhibitor (RI) Y-27632 (10 µM; #M1817, AbMole Bioscience, Houston, TX, USA) for 5 min at 37 °C, as detailed in the SM for passaging, and subsequently subjected to mechanical disruption by expelling the solution through a blunt 18G needle (8–12 times). The washed and isolated (400 × g; 5 min; 4 °C) small ISC clusters containing around 10 cells per cluster and singularized cells were resuspended in expansion media supplemented with Y-27632 (10 µM) and shortly kept on ice until seeding. PBS was removed from disinfected dSIS-MA hydrogels (cf Section 2.4.1), and the hydrogels were equilibrated using a 20 min incubation in expansion media (50 µL) at 37 °C. After removing the cell media, hydrogels were left at 37 °C for 10 min before ISC seeding ( $1 \times 10^5$  cells per hydrogel or  $\sim 3 \times 10^5$  cells/cm<sup>2</sup>) to prevent scaffold floating.

Control experiments on conventional porous polyethylene terephthalate (PET) insert membranes (Falcon® #353095,  $d = 6.5$  mm, 0.4 µm pore size, Corning Inc., Kaiserslautern, Germany) were prepared in 24-well plates. The membranes were coated with Matrigel™ (100 µL, diluted 1:100 in basal medium, cf Section 2.4.2), which was solidified at 37 °C for 1 h prior to cell seeding. Alternatively, the dilute Matrigel™ solution was left on the membrane overnight at 4 °C and incubated at 37 °C for 20 min before seeding. After removing the residual solution, ISCs were seeded at the same density as described for the dSIS-MA hydrogel scaffolds.

For both substrates, the expansion media was replaced every 2–3 days, with the RI supplement excluded from the media after the initial seeding. Monolayers were cultivated for 2–3 days until reaching a confluency of 80–100%, after which they were subjected to fluid flow shear stress or maintained statically, indicated as “Day 0” in the experimental timeline.

#### 2.5. Dynamic Cell Culture

The dynamic cell culture setup includes a peristaltic pump (9QS, Boxer GmbH, Ot-tobeuren, Germany) connected to a medium reservoir containing inlet, outlet, and gas exchange adapters (15 mL, #10454631, PPCO, Nalgene™, Thermo Fisher Scientific, Langensfeld, Germany) and two customized 3D-printed chambers (Figure 2). For detailed fabrication of the media reservoir, see the SM. The system is connected via transparent silicone tubing (TYGON® 3350, Platinum-Cured Silicone, France) with an inner diameter (ID) and wall thickness (WT) of 1.6 mm and 0.8, respectively, along with pump tubing made of a polypropylene-based thermoplastic elastomer (#P60, Innovaprene®, Suzhou Innovapure Co., Leyu Zhen, Suzhou, China) with ID = 2 mm and WT = 1 mm, linking the three components of the circuit. The pump is controlled via an Arduino-based open-source hardware platform. Step-by-step instructions for assembling the Arduino-controlled pump system and its operation, including all supplier specifications, can be found in the SM. The free Arduino IDE software (v 1.8.9) was employed to program the microcontroller via a customized script (see SM and additional INO file as Supplementary Data). For sterilization, the culture circuit (excluding the pump) is packaged in sterilization Steriking® pouches (Wipak, Walsrode, Germany), sealed, and autoclaved at 120 °C. Medium exchange (12 mL) is performed every seven days with the dual-chamber setup (18 hydrogels in total, equivalent to a cell-seeded surface area of 5.09 cm<sup>2</sup>). The peristaltic pumps are calibrated to maintain a constant perfusion rate of 1.42 mL/min at 12 RPM through tubes while operating inside a cell culture incubator at 37 °C, 5% CO<sub>2</sub>, and 95% humidity. This setup yields a physiological surface shear stress of 0.01 dyne/cm<sup>2</sup> on the cellularized hydrogels, referred to as “dynamic culture conditions” in the following sections.

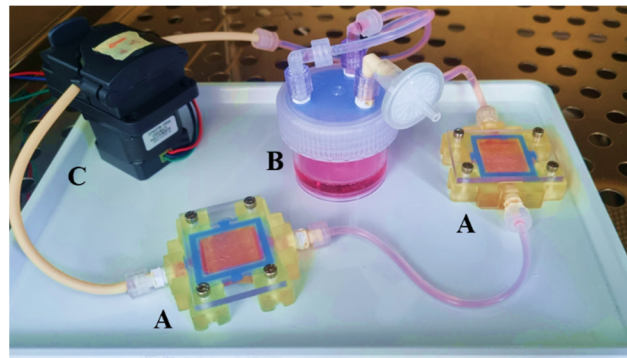


**Figure 2.** Photograph of the fully assembled dynamic cell culture circuit, including (A) two 3D-printed tissue chambers, (B) a medium reservoir filled with cell culture media and equipped with a sterile air filter for gas exchange, and (C) a peristaltic pump.

### 2.6. Immunofluorescence Staining

Sample preparation and conditions for immunofluorescence staining can be found in the SM.

### 2.7. Alkaline Phosphatase (ALP) Activity Assay

Alkaline phosphatase (ALP) activity was measured at days 0, 3, 5, and 7 of a static and dynamic culture using an alkaline phosphatase assay fluorometric kit (#ab83371, Abcam, Regensburg, Germany), according to the manufacturer's protocol. In static culture, the supernatants of twelve cellularized hydrogel or membrane samples were collected and combined for each group just before the scheduled media change on the specified days. In the dynamic culture, the cell medium (1 mL per 18 hydrogel samples) was collected from the media reservoir. All samples were snap-frozen in liquid nitrogen and stored at  $-80^{\circ}\text{C}$  until further analysis.

For the assay, samples (1 mL) were thawed on ice and transferred to a black 96-well plate (130  $\mu\text{L}$ , Corning<sup>TM</sup>, Merck KGaA, Darmstadt, Germany). The results were normalized to account for the number of samples in each condition (12 in static vs. 18 in dynamic), the actual seeding area per sample (28.27  $\text{mm}^2$  for hydrogels and 33.18  $\text{mm}^2$  for membranes), and the initial medium volume (1.2 mL for static and 12 mL for dynamic conditions). The assay was performed with supernatants from three individual runs and reported as mU/mL ALP activity  $\pm$  standard deviation (SD) following normalization and referred to an overall culture area of 3.4  $\text{cm}^2$  per ISC monolayer, assuming similar cell density and size independent of the culture conditions and the substrate.

### 2.8. Mucus Quantification

#### 2.8.1. Sample Preparation for Quantification of Mucins in Supernatants

Cell medium (1 mL) was collected collectively per sample group and stored as described in Section 2.7 from supernatants under static conditions and from the medium reservoir under dynamic conditions on days 0, 3, 5, and 7 of culture. Grouped samples were collected from three individual runs and normalized for each run on the respective sample size, seeding area, and initial medium volume as described in Section 2.7 and reported as mg mucin per mL supernatant  $\pm$  SD produced by a monolayer of ISCs on an overall culture area of 3.4  $\text{cm}^2$ .

#### 2.8.2. Sample Preparation for Quantification of Cell-Bound Mucins

First, culture media was removed, and the cells were washed with PBS (–/–) for both cultures on hydrogels and membranes at the specified time points. Cells grown on membranes were gently scraped off with a spatula, and the harvest of two membranes was collected in PBS (–/–) (200  $\mu\text{L}$ ). In contrast, cells grown on scaffolds were collected

together with the hydrogel scaffold in PBS (–/–) (200  $\mu$ L). All samples were immediately snap-frozen in liquid nitrogen and stored at  $-80^{\circ}\text{C}$  for further analysis.

On the day of the assay, adherent cells on hydrogels were detached through a series of freeze–thaw cycles alternating between  $-80$  and  $37^{\circ}\text{C}$  for 5 min each with three repetitions. After this, TrypLE™ (200  $\mu$ L, Thermo Fisher Scientific, Darmstadt, Germany) express enzyme was added, and samples were incubated for 5 min at  $37^{\circ}\text{C}$  to ensure the complete detachment of the cells. Hydrogels were then carefully removed with tweezers, and the resulting cell suspensions were kept on ice for further analysis. An analogous TrypLE™ treatment was administered to cells harvested from membranes, ensuring methodological uniformity across samples. Additionally, non-seeded hydrogels in PBS (–/–) underwent TrypLE™ treatment, serving as blank controls. The latter was essential to confirm the enzymatic stability of the scaffold under the applied conditions since solubilized dSIS-MA components could falsify the mucin content. Normalization of the collected data was performed with respect to the seeding area and the DNA content (cf SM) of each sample, ensuring the accurate quantification of cell-bound mucins.

### 2.8.3. Mucin Quantification via Periodic Acid–Schiff Base (PAS) Reaction and Alcian Blue (AB) Staining

Soluble mucins in the collected supernatants and cell-bound mucins in cell suspensions were quantified similarly according to the following procedure.

**Quantification of Neutral Mucins (PAS Staining):** Following our previous protocol, ref. [26] a mixture was prepared from 2% *w/v* CHAPS (20  $\mu$ L) and either the sampled mucin-containing cell suspensions (30  $\mu$ L) or supernatants (30  $\mu$ L), which was further diluted with PBS (–/– 50  $\mu$ L). This mixture was then sequentially incubated with periodic acid (20  $\mu$ L) for 2 h and Schiff's reagent (100  $\mu$ L) for 1 h at  $37^{\circ}\text{C}$  in a 96-well plate. The development of a pink-colored solution indicated the presence of neutral mucins. The absorbance was measured at 555 nm.

**Quantification of Acidic Mucins (AB Staining):** Adapted with modifications from Zamora et al. [36], either the sampled mucin-containing cell suspensions (30  $\mu$ L) or supernatants (30  $\mu$ L) and 2% *w/v* CHAPS (20  $\mu$ L) were mixed and diluted with 1 M HEPES buffer (50  $\mu$ L). The suspension was incubated for 2 h with a solution of 1 *w/v*% AB in 3% *v/v* acetic acid (100  $\mu$ L), which was filtered (0.2  $\mu\text{m}$ ) before use. Following incubation, the mucin–alcian blue complex was centrifuged at  $2500\times g$  for 15 min at RT, leaving a pellet of blue gel. Wash and spin cycles using 40% ethanol/60% 0.1 M sodium acetate buffer with 25 mM  $\text{MgCl}_2$  at pH 5.8 were performed to purify the pellets, which were finally fully dissolved in 10% SDS solution for absorbance measurement at 620 nm.

Mucins from bovine submaxillary glands served to prepare a standard calibration curve. Known concentrations of mucins were prepared and analyzed identically and in parallel with experimental samples. To fall within the assay's linear range, samples were diluted accordingly with PBS (–/–) for PAS or HEPES for AB stains.

## 2.9. Statistical Analysis

The statistical significance of the gathered data was determined using the non-parametric Kruskal–Wallis test, followed by Dunn's multiple comparisons test using OriginPro software (Version 2021b. OriginLab Corporation, Northampton, MA, USA). *p*-values  $p < 0.05$  were considered statistically significant and indicated by \* or otherwise non-significant (n.s.).

## 3. Results and Discussion

### 3.1. Design of Hydrogel-Integrated Millifluidic Tissue Chamber and Flow Circuit

With the emergence of organ-on-a-chip technology, microfluidic systems have evolved as a great tool to apply fluid shear stress on cells and tissue models. The field of organoid-derived ISC research has thus far concentrated on the colon, with comparatively less attention being paid to the small intestine, especially the terminal ileum [14,37]. A limiting factor for ISC-derived small intestinal models is the challenging and sustained culture

of fully confluent 2D monolayers derived from human small intestinal organoids [38,39]. The development of hydrogel-integrated microfluidic systems has facilitated the creation of a homeostatic ISC-derived mini-gut model [40]. Although microfluidic devices are highly versatile, their manufacture is not easily scalable and involves a time-consuming, multi-step process associated with substantial expenses, requiring clean room facilities. Moreover, the generated tissue inside a microfluidic channel is not easily accessible for direct manipulation or analysis via SEM or AFM.

To address these challenges, we developed a scalable and cost-efficient, 3D-printed millifluidic tissue chamber setup [26]. Initially tailored for HT29-MTX cell cultivation, we redesigned our setup to securely accommodate multiple 3D-printed hydrogel scaffolds without the risk of buoyancy. The chamber design ensures uniform laminar fluid flow, which is crucial for the application of homogenous apical shear stress in order to study ISC and epithelial cell differentiation following scaffold cellularization. The surface area for cell seeding and the medium volume within the chamber were significantly reduced in order to facilitate economic cell culture, including that of human organoid-derived ISCs. Figure 1A–D illustrate the CAD of the chamber securing nine scaffolds within size-matched cavities to apply surface shear stresses within the physiological range of the intestine (0.002–0.08 dyne/cm<sup>2</sup> [41]) at defined flow rates. The fully assembled chamber, tightly sealed with a transparent lid, is shown in Figure 1E,F. CFD simulations confirmed a homogeneous laminar flow through the wide but flat flow channel. This was evidenced by the observation of uniform velocity streamlines and homogeneous shear stress on the surface of flat objects within the chamber cavities at a set flow rate of 1.42 mL/min (Figure 1G,H). CFD simulation under identical conditions, but with 3D villi-structured instead of flat objects, revealed a surprisingly homogenous flow profile with a low shear stress gradient that increased from the base to the tip of the villi, closely emulating the physiological situation (Figure S1). The chamber was 3D-printed using a simple DLP printer with an autoclavable, biocompatible, and cost-effective commercial resin, ensuring usability and affordability. The manufacturing process, which takes 45 min, requires 40 mL of resin, resulting in consumable costs of EUR 5.93 per chamber [42].

The interlinking of two chambers, a medium reservoir with gas exchange, and a peristaltic pump within a single circuit enabled continuous media circulation, resulting in the generation of a defined physiological shear stress of 0.01 dyne/cm<sup>2</sup> at a set flow rate of 1.42 mL/min. The implementation of an Arduino-based pump control system enables the precise adjustment of shear stress levels within this setup from 0.005 to 0.1 dyne/cm<sup>2</sup>. This range can be further expanded by altering the flow channel height. The setup offers the potential for flexible experimental throughput, similar to that observed in our previously reported flow chambers [26], and therefore has utility for diverse research applications.

### 3.2. dSIS-MA-Based Hydrogel Scaffolds for Advanced Small Intestinal Models

We prepared biomimetic hydrogels mimicking the stiffness range of the intestinal extracellular matrix. This was achieved by using 1.5 wt% dSIS-MA, in accordance with our previously established procedure, with only minor adjustments [33]. First, porcine small intestinal submucosa (SIS) was decellularized, enzymatically solubilized, and functionalized with photoreactive methacrylic groups to yield dSIS-MA as a biomaterial resin for 3D printing via vat photopolymerization (Figure S2A,B). In contrast to our previous protocol [33], the enzymatic solubilization of dSIS was achieved using papain instead of pepsin, resulting in comparable material properties at a lower cost [32]. The degree of functionalization with photoreactive groups was approximately 82%, as confirmed by <sup>1</sup>H NMR (Figure S2B) and a chromogenic TNBS assay (Figure S2C). Furthermore, the analysis of CD demonstrated the maintenance of protein structural integrity in the dSIS-MA biomaterial resin following chemical functionalization (Figure S2D). Standardized quality control measurements are imperative for each new dSIS-MA batch, as this ensures the consistency and reliability of the resulting material properties [43].

The fabrication of flat disk-shaped hydrogel scaffolds ( $d = 6$  mm and  $h = 1$  mm) was achieved via layer-by-layer 3D printing from a 1.5 wt% dSIS-MA resin formulation containing 1 wt% photoinitiator, as previously reported [33], ensuring scalability and precision (Figure S3A,B). Although our printing process allows for customization into various 3D shapes relevant to the intestine [33,44,45], we opted for flat surfaces to ensure high cell seeding efficiency and facilitate convenient downstream microscopic readout. The optimal height of 1 mm for scaffolds with a diameter of 6 mm was determined to prevent floating under flow conditions, thereby minimizing sample loss. By optimizing the curing time during printing, the stiffness range of healthy human small intestinal tissue (Young's modulus: 1.3–4.0 kPa) [46] was matched at the given biopolymer and photoinitiator concentrations. The targeted surface stiffness was approximately 15 kPa, which has previously been demonstrated to support efficient ISC adhesion and proliferation [33]. Rheological and AFM nanoindentation analyses confirmed the reproducibility of bulk stiffness ( $3.7 \pm 0.2$  kPa) (Figure S3C) and surface stiffness ( $14.3 \pm 8.8$  kPa) (Figure S3D) across various batches, meeting the mechanical criteria for advanced intestinal tissue models. Notably, even moderate variations in the mechanical properties of synthetic hydrogels within the low kPa range (soft = 0.6 kPa, medium = 2.4 kPa, and stiff = 9.6 kPa) have been demonstrated to significantly impact the stemness and differentiation pathways of ISCs [21].

Furthermore, the scaffold's porous microarchitecture [33] was confirmed as essential for nutrient and biochemical signal exchange during cell culture. While the wet hydrogels indicate a pore size of up to 5  $\mu\text{m}$  according to the widths of the darker areas and surface cross-section in AFM topography measurements in quantitative imaging mode (Figure S3D), SEM images of the lyophilized dry samples (Figure S3E) indicate a porous interior with pore sizes up to 100–150  $\mu\text{m}$  and collapsed pores on the gel surface.

### 3.3. Validation of the Millifluidic System with Mucus-Producing HT29-MTX Cells

The newly designed millifluidic system was empirically validated using intestinal cell-seeded hydrogels. Given our previous findings regarding the impact of shear stress on mucus-producing HT29-MTX cells cultured on TCPS substrates [26], we utilized these cells and anticipated enhanced differentiation, mucus formation, and 3D organization of the cell monolayer under physiological shear stress. Control experiments were conducted under static conditions to isolate the effects attributable to the hydrogel scaffolds alone. The experimental setup, outlined in Figure 3A, served to validate the functionality of the millifluidic system and elucidate the influence of dSIS-MA hydrogels on cellular behavior, particularly mucus production.

Initially, HT29-MTX cells were seeded on hydrogel scaffolds and cultured statically in 96-well plates until reaching confluency. Subsequently, they were transferred to the tissue chamber for dynamic culture or maintained statically for 7 and 14 days. Phase-contrast imaging revealed distinct dark areas on day 14 under static conditions and on days 7 and 14 under dynamic conditions (Figure 3B; top row), indicating the accumulation of secreted mucus [10,14] and a 3D reorganized cellular monolayer [26]. The multilayered structure was more pronounced under dynamic culture conditions, presenting challenges for focusing. Immunofluorescence staining of the tight junction marker ZO-1 on days 7 and 14 indicated comparable epithelial barrier development on the hydrogels, regardless of shear stress (Figure 3B, bottom row).

To further investigate cellular differentiation and confirm augmented mucus formation under dynamic conditions, we conducted immunofluorescence staining. Static culture controls exhibited robust proliferation on both days 7 (Figure S4A) and 14 (Figure 4A), as evidenced by the high prevalence of KI-67<sup>+</sup> cells across the cell layer. Additionally, mucin detection, specifically MUC2 and MUC5AC, hardly increased from days 7 (Figure S4A) to 14 (Figure 4A), indicating no evident cellular maturation and differentiation over time under static conditions.



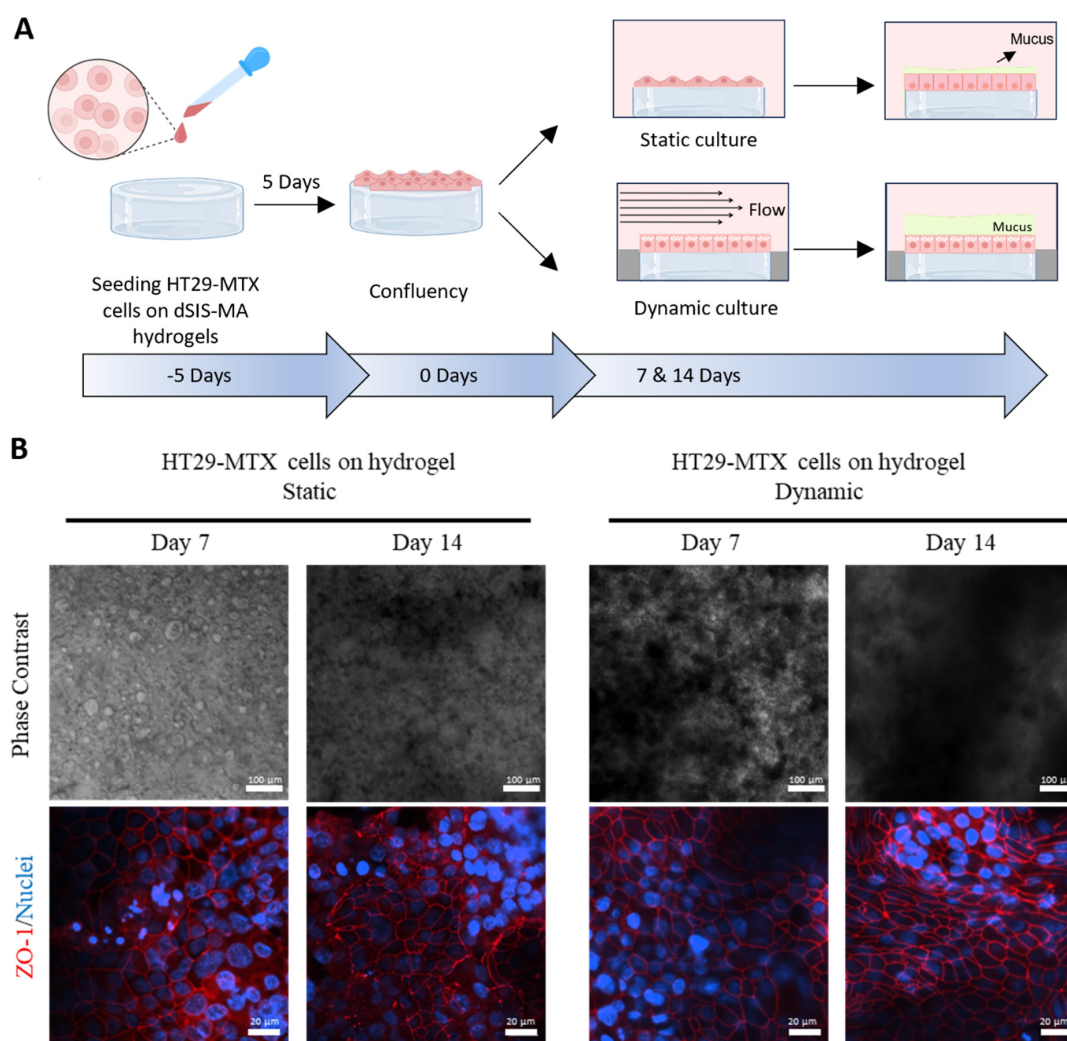


**Figure 3.** Validation of the newly designed, hydrogel-integrated flow chamber with HT29-MTX cells seeded on dSIS-MA (1.5 wt%) hydrogels under static and dynamic (shear stress:  $0.01 \text{ dyne/cm}^2$ ) culture conditions on days 7 and 14. (A) Illustration of the experimental workflow. (B) Representative phase-contrast (top) and confocal fluorescence images (bottom, in one plane) stained for the tight junction protein zonula occludens-1 (ZO-1, red) with cell nuclei counterstain (blue).

Remarkably, under fluid flow conditions, there was a notable reduction in proliferative KI-67<sup>+</sup> cells on both days 7 (Figure S4B) and 14 (Figure 4B). This suggests that cellular differentiation into mature tissue occurred more rapidly than in static conditions. Similar observations, but on a slower timescale, were reported with HT29-MTX on hard substrates under dynamic culture, showing increased proliferation within the first two weeks of culture [10,26]. However, this proliferation becomes markedly reduced until week 3 [26]. The biomimetic properties of the dSIS-MA scaffold [33] are likely to create a microenvironment that, in conjunction with shear stress, significantly promotes cellular maturation and differentiation. This results in a notable decrease in cell proliferation as early as day 7. Consequently, there was a notable elevation in both mucin MUC2 and MUC5AC expression as early as day 7 (Figure S4B) under dynamic conditions, exceeding levels observed in statically cultured cells by day 14 (Figure 4A). This elevated mucin expression was further intensified by day 14 under dynamic conditions (Figure 4B), which is in full agreement with the phase-contrast images. Notably, hydrogels subjected to flow exhibited distinctive 3D organization of cellular layers, which was in stark contrast to their counterparts in static culture (Figure 4C and Figure S4C).

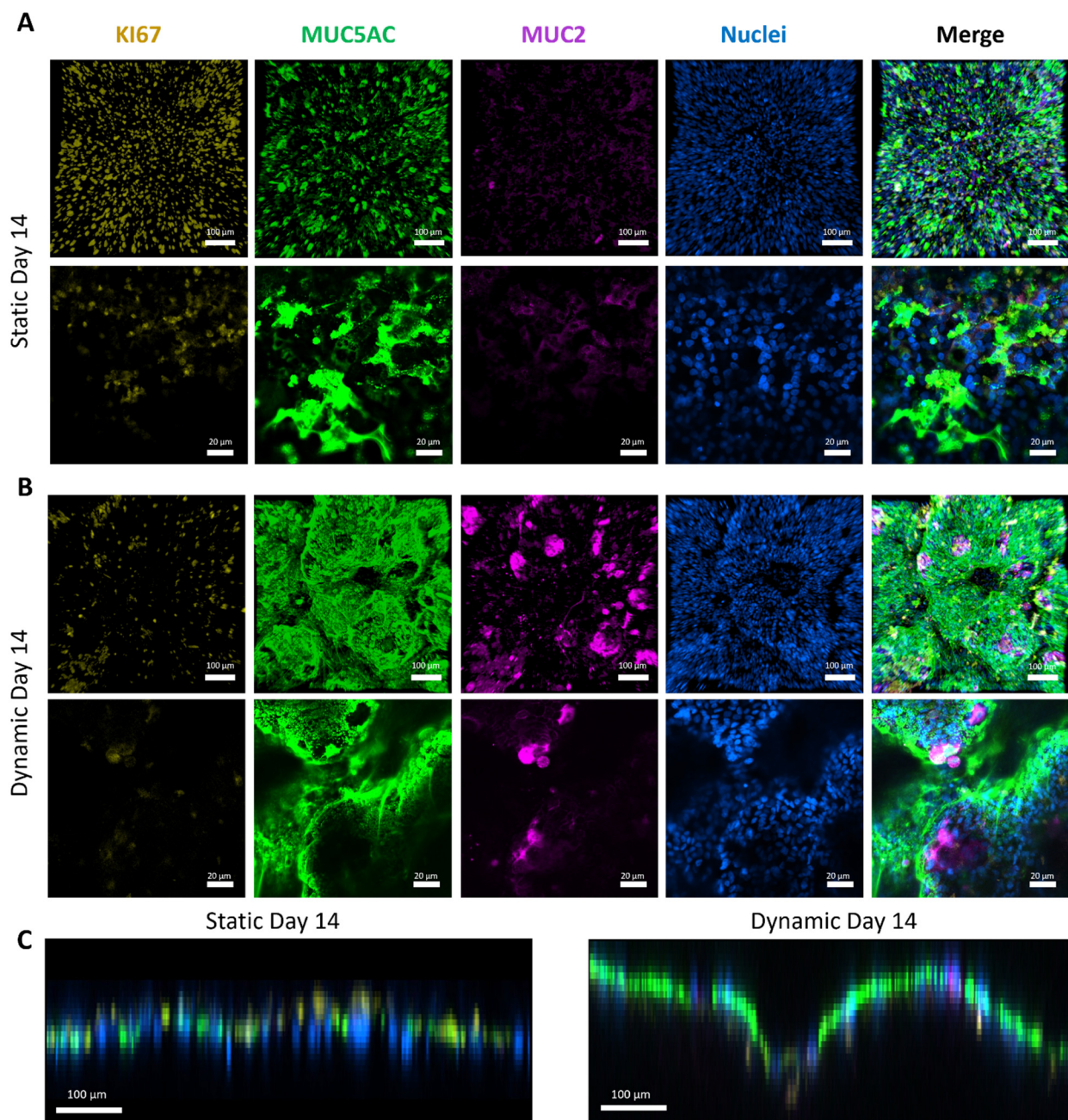


**Figure 4.** (A) Representative fluorescent confocal microscopy images of HT29-MTX cells cultured statically on dSIS-MA (1.5 wt%) hydrogels on day 14, stained via IF for KI-67 (yellow) to indicate proliferation and MUC5AC (green) and MUC2 (purple) as mucin markers, with nuclei counterstain (blue). Top: xy projection of z-stack images; Bottom: higher-magnification 2D images. (B) Representative fluorescent confocal microscopy images of HT29-MTX cells cultured under dynamic conditions (shear stress: 0.01 dyne/cm<sup>2</sup>), stained and imaged with identical settings to (A). (C) Side projections (xz/yz) of z-stacks from (A,B). Samples are collected from three independent runs (n = 3).

Importantly, matured tissue models under dynamic conditions showed no differences in scaffold-hosting cavity location within the chamber or chamber position within the circuit assembly. This confirms the functionality and validity of the newly developed tissue chamber for the controlled and scalable application of shear stress to cell-seeded hydrogel scaffolds.

Surprisingly, our current tissue model cultured on hydrogels demonstrated a significant enhancement in mucin MUC2 and MUC5AC expression compared to identical

conditions on TCPS [26]. This underscores the synergistic effect of dynamic culture's shear stress with dSIS-MA hydrogels' bioactive properties, driving cell differentiation toward a goblet cell-like phenotype with increased mucus production.

### 3.4. Culture of Organoid-Derived ISCs on Scaffolds under Static and Dynamic Conditions

Next, the validated millifluidic system was challenged with human organoid-derived ISCs from the terminal ileum cultured exclusively in WRN-containing expansion media. The ISC growth and differentiation on dSIS-MA scaffolds (without transitioning to differentiation medium) under both static and dynamic conditions were examined, comparing them to conventional static cultures on Matrigel<sup>TM</sup>-coated insert membranes. A similar experimental design was employed for the ISC monolayers on scaffolds, as previously described for the HT29-MTX cells. The monolayers were either subjected to flow in tissue chambers or maintained statically in well plates for a duration of 5–7 days. Monolayers cultured statically on insert membranes served as controls. RNA isolation for RT-qPCR analysis was conducted after 3 days of culture, while samples were fixed for immunofluorescence (IF) staining directly after reaching confluence or on days 5–7. A time-dependent assessment of ALP activity and mucus quantification, both in the culture medium and attached to the tissue, was conducted on days 0, 3, 5, and 7.

#### 3.4.1. Formation and Culture of ISC-Based Monolayers on Scaffolds

The ISCs were cultured on hydrogels and membranes for 2–3 days following their dissociation into single cells and small cell clusters of approximately ten cells. The seeding of ISCs at a high cell density under these conditions facilitated the rapid formation of intact and confluent cell monolayers on the scaffolds, exhibiting minimal irregularities similar to those observed on Matrigel<sup>TM</sup>-coated membranes (Figure S5A). IF analysis of successfully generated flat monolayers after reaching confluency (day 0) revealed the presence of highly proliferative KI-67<sup>+</sup> cells distributed randomly throughout the layers both on membranes and hydrogels (Figure 5A).

A markedly higher expression of the progenitor cell marker olfactomedin 4 (OLFM4) compared to the stem cell marker leucine-rich repeat-containing G protein-coupled receptor 5 (LGR5) suggests a confluency-triggered shift from stem cells toward more mature epithelial progenitor cells. However, the relatively low IF staining efficiency of the LGR5 antibody needs to be considered. This is due to the fact that the LGR5 protein is expressed at low levels in native intestinal tissue and ISC-based models [47]. Following a period of 5–7 days in static conditions (Figure 5B), a moderate decrease in KI-67<sup>+</sup> and OLFM4<sup>+</sup> cells was observed on both substrates in comparison to day 0, indicating a continual process of maturation. This observation is consistent with the findings of Van Dussen et al., who reported a pronounced decrease in *MKI67* and *OLFM4* mRNA expression levels in human ileal organoids following chemically induced differentiation (removal of WRN from the medium) [19].

Under dynamic conditions, a notable decrease in KI-67 and an increase in OLFM4 expression were observed in comparison to day 0, with stable LGR5 levels across all conditions (Figure 5B). This finding was corroborated by an RT-qPCR analysis of cells on hydrogels three days post-confluency, which revealed a moderate 2.5-fold increase in *LGR5* and a pronounced, nearly 20-fold increase in *OLFM4* under dynamic compared to static conditions (Figure S6A). Furthermore, an increase in *OLFM4* mRNA levels was observed in colon-derived ISCs cultured on-chip for eight days under dynamic conditions [15]. Interestingly, OLFM4 protein expression in ISCs was accompanied by a decrease in LGR5 when the substrate stiffness was increased from 0.6 to 2.4 kPa in static culture [21], a stiffness comparable to that of the hydrogels used in this study (3.7 kPa). The precise roles of OLFM4 in ISC differentiation in health and disease remain incompletely understood [48]. Following a period of 5–7 days in expansion media, ISCs subjected to shear stress organized into 3D villi-like protrusions (Figure 5B and Figure S7A), as observed with HT29-MTX cells on hydrogels (Figure 4C and Figure S4C) and TCPS substrates [26], resulting in zoned

areas with high OLFM4 expression at their boundaries in the case of the ISC culture. Similar 3D protrusions have been observed with ISCs from the human colon and duodenum when cultured on-chip under physiological shear stress [14,39]. Despite the provision of essential stem cell niche factors (WRN) in our expansion media, a decline in active ISC proliferation during 2D culture was noted, particularly under dynamic conditions. This is likely due to the progression of cellular differentiation induced by mechanical stimulation, as observed in ISC-based colon-on-chip [14] and jejunum-on-chip models [49].

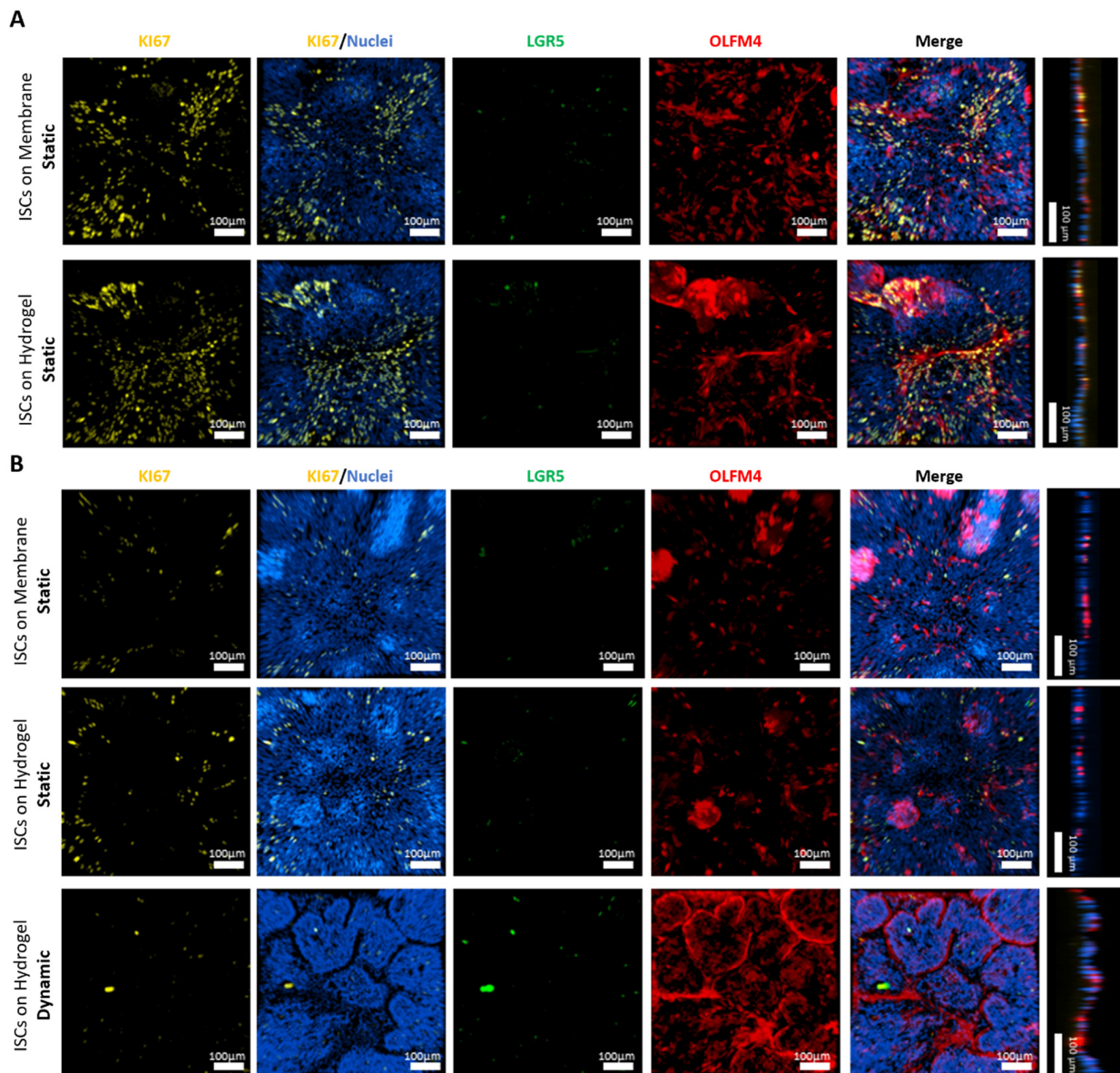


**Figure 5.** Transfer of the experimental approach to undifferentiated organoid-derived ISCs from the human terminal ileum cultured in expansion media. **(A)** Representative confocal fluorescent images of ISC monolayers cultured in static conditions on Matrigel<sup>TM</sup>-coated insert membranes and hydrogels at the onset of confluency (Day 0). IF staining for proliferative marker KI-67 (yellow), stem cell marker LGR5 (green), and progenitor cell marker OLFM4 (red) with nuclei counterstain (blue). For fluorescent staining, samples are collected from three independent runs ( $n = 3$ ) and presented as xy projections of their z-stacks, along with their xz/yz projections. **(B)** Representative IF images of ISCs on days 5–7 cultured in expansion media under static and dynamic conditions, stained for the same markers used in **(A)**. For fluorescent staining, samples are collected from three independent runs ( $n = 3$ ) and presented as xy projections of their z-stacks, along with their xz/yz projections.

It is important to note that throughout the course of this study, numerous unsuccessful cell seeding attempts were conducted, resulting in the formation of holes in the monolayers. These instances constituted approximately 40% of all trials and were therefore excluded from further analysis (Figure S5B). Similar failure rates (approximately 60%) have been reported with human small intestine-derived stem cells, which were improved using fragmented organoids instead of single cells [39]. The challenges in reproducing fully confluent, intact monolayers of human ISCs derived from the terminal ileum are currently being addressed in ongoing research.

Additionally, under physiological shear stress, three morphological categories of monolayers were observed, with the majority featuring intact villus-like structures adhering tightly to the scaffold (Figure S7A and Figure 5B). However, starting on day 7, monolayers exhibited villi displacement, likely due to flow dynamics and rapid *in vivo*-like intestinal cell turnover (Figure S7B). Consequently, by day 14 of dynamic culture, only a few dispersed cells remained on the scaffolds, as similarly described in the literature [21] and attributed to insufficient stem cell preservation, currently limiting the experimentation time of our model to around 5 days. Some cases revealed flatter monolayers devoid of protrusions with pore-like patterns upon ZO-1 staining (Figure S7C). This observation might be a result of shear stress-induced noncanonical autophagy, evident by the formation of 10–20  $\mu\text{m}$  vacuoles in intestinal monolayers, as reported previously [50], and requires further investigation. The observed morphological variability suggests varying degrees of cellular differentiation between samples, with some potentially shedding previously formed 3D protrusions in response to shear forces. For future studies, it is recommended that dynamically cultured samples are collected on day 5 rather than day 7 and that interval exposure to shear stress is employed to better mimic the physiological situation in the human intestine, allowing for tissue regeneration during static resting phases.

#### 3.4.2. Differentiation of ISC-Based Monolayers and Tissue Formation

Expanding on the transformative impact of shear stress from stemness toward differentiation, we examined structural, functional, and differentiation markers of ileal ISC monolayers. Following 5–7 days of culture in expansion media, immunofluorescence (IF) staining of F-actin, E-cadherin (E-cad), and zonula occludens (ZO-1) protein markers revealed an intact cytoskeletal architecture and the presence of adherens and tight junctions across all samples and conditions (Figure S8). These confirmed epithelial features are essential for epithelial integrity and barrier function.

Next, we investigated the potential for the multi-lineage differentiation of ISCs cultured under dynamic conditions to generate cells characteristic of enterocytic, enteroendocrine, Paneth, and goblet cell lineages. Shear stress augmented ISC differentiation into the enterocyte lineage compared to static cultures, as evidenced by the increased mRNA expression of alkaline phosphatase (*ALPI*, ~30-fold) and sucrase-isomaltase (*SI*, ~18-fold) on day 3 of culture (Figure S6B). This was further supported by a significant rise in extracellular alkaline phosphatase (ALP) activity in supernatants on days 3, 5, and 7 of dynamic compared to static cultures, irrespective of the culture substrate (Figure 6A). Additional immunofluorescence staining of the enterocyte protein marker villin on samples collected after 5–7 days of culture confirmed the findings from RT-qPCR and ALP activity assays (Figure 6B), as well as cell polarization. Intriguingly, in the absence of chemical differentiation inducers, shear stress alone can mechanically stimulate functional ISC differentiation into the absorptive enterocyte lineage, which is shown here for the first time on the enzymatic activity level. Functionally differentiated and matured enterocytes play a crucial role in intestinal models, emulating primary functions such as nutrient absorption and barrier maintenance.

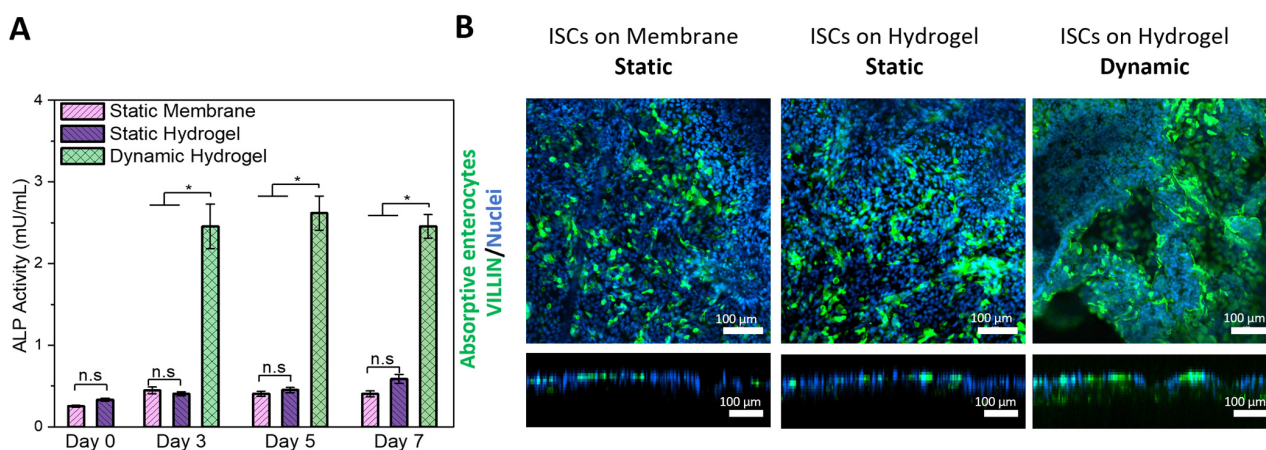


**Figure 6.** Mechanically stimulated differentiation of human terminal ileum-derived ISCs into functional enterocytes by physiological shear stress exposure. ISCs were cultured on insert membranes and dSIS-MA hydrogels (1.5 wt%) statically or dynamically in expansion media for 5–7 days after reaching confluency. (A) ALP activity was assessed on days 0, 3, 5, and 7 post-confluency from supernatants of ISC monolayers on a culture area of around 3.4 cm<sup>2</sup>. Data are presented as mean  $\pm$  SD for  $n = 3$ , where “\*” indicates statistical significance ( $p < 0.05$ ) and “n.s.” indicates non-significance according to the Kruskal–Wallis test, followed by Dunn’s test. (B) Representative confocal images in xy projections and their xz/yz projections of acquired z-stacks after IF staining of villin (green), indicating absorptive enterocyte with counterstained nuclei (blue), on days 5–7 cultured statically or dynamically on insert membranes and hydrogels in expansion media.

Further RT-qPCR analysis assessed on day 3 revealed that shear stress resulted in a four- and fivefold upregulation of chromogranin A (*CHRA*) and lysosome (*LYZ*) expression in ISCs, respectively, in comparison to static culture on dSIS-MA hydrogels (Figure S6C). The results indicate that the ISC can be effectively differentiated into the enteroendocrine and Paneth cell lineages. This is further substantiated by IF staining of the expressed protein markers (Figure 7A,B). Particularly under dynamic conditions, enteroendocrine-like cells localize at positions of the generated 3D protrusions, while Paneth-like cells, at least under shear stress, appear at the bottom of the cellular layer. This is similar to what is observed in vivo, where they are located in close proximity to the crypts. Enteroendocrine and Paneth cells are integral components of the ISC niche, and their presence is crucial for maintaining a functional niche and ISC homeostasis.

Our findings are consistent with previous research on human small intestinal stem cells subjected to flow conditions, particularly regarding increased markers for absorptive enterocytes and enteroendocrine cells. However, discrepancies arise concerning Paneth cells. Kasendra et al. observed enhanced differentiation of human duodenum-derived ISCs after switching to a differentiation medium lacking WRN within a microfluidic environment. This was accompanied by increased transcriptional levels of markers for absorptive enterocytes and enteroendocrine cells, alongside decreased Paneth cell markers [39,51]. The precise mechanism by which these changes occur remains unclear. It is possible that they result solely from mechanical stimulation, the transition to differentiation medium, or a combination of both. Yin et al. found that shear stress on-chip alone induced the differentiation of human jejunum-derived ISCs into absorptive enterocytes and enteroendocrine cells when cultured in expansion media, which is consistent with the findings of our study [49]. However, Paneth cell markers were not assessed for the jejunal model, while none of the above studies confirmed functional absorptive enterocyte differentiation as demonstrated by ALP production and secretion in our study. Our results suggest a unique synergistic effect of shear stress and the dSIS hydrogel environment on ISC differentiation toward the Paneth cell lineage requiring more in-depth investigations. A comprehensive gene sequencing study on ISCs cultured on our hydrogel scaffolds comparing static and dynamic conditions is currently in progress.

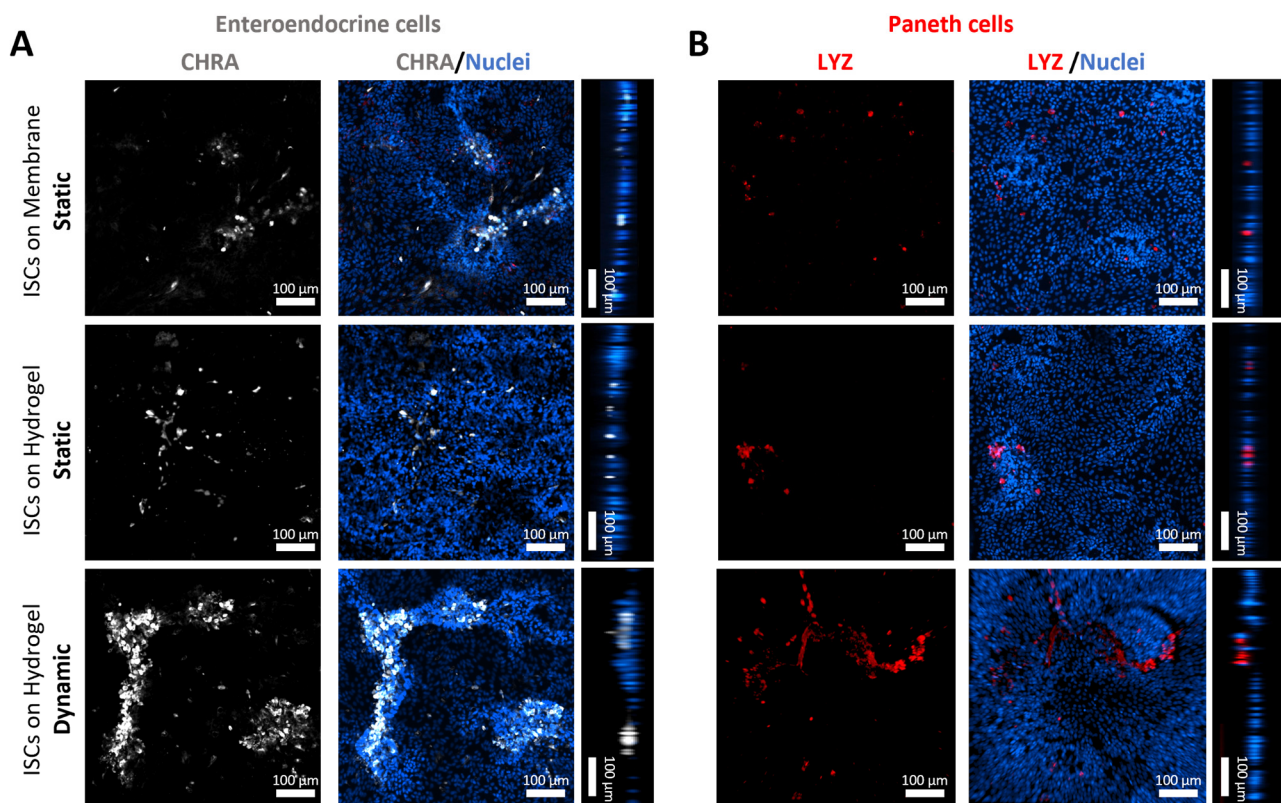


**Figure 7.** Representative z-stacks of confocal fluorescence microscopy images presented as xy projections and their xz/yz projections. Protein expression of (A) chromogranin A (white) and (B) lysozyme (red) in ISC-based monolayers with counterstained nuclei (blue) on days 5–7 cultured statically or dynamically on insert membranes and hydrogels in expansion media. Samples are collected from three independent runs ( $n = 3$ ).

#### 3.4.3. Mucus Production and Secretion of ISC-Based Monolayers on Scaffolds

Goblet cells play a crucial role in the intestinal epithelium by producing mucins, particularly MUC2. Quantitative RT-PCR analysis on day 3 revealed the strong upregulation of gel-forming mucins *MUC2*, *MUC5AC*, and *MUC5B*, as well as the moderate upregulation of *MUC17* and trefoil factor 3 (*TFF3*) in ISCs cultured on dSIS-MA (1.5 wt%) hydrogels under shear stress conditions, compared to static culture (Figure S6D). IF staining on days 5–7 confirmed a markedly increased production and secretion of MUC2 and MUC5AC in cells cultured dynamically on hydrogels, compared to basement levels through spontaneous cell differentiation observed in static controls, all maintained in expansion media (Figure 8). Notably, MUC2 protein expression levels surpass MUC5AC levels, while the opposite is observed for their transcriptional levels.

Similarly to a duodenum-on-chip study, in which increased *MUC2* and *MUC5AC* mRNA levels were detected upon chemically induced differentiation [39], our findings show the same effect solely via mechanical stimulation without chemical differentiation. Conversely, in a colon-on-chip setup, *MUC2* mRNA levels increased while *MUC5AC* decreased after eight days of culture under flow in expansion media, compared to static conditions [15]. The discrepancy in *MUC5AC* expression highlights the complex relationship between mucin expression and intestinal health. Increased *MUC5AC* expression, typically associated with the gastric and respiratory tracts, may indicate a protective or adaptive response to stress or injury in the small intestine [52]. This suggests further investigation into the mechanisms and implications of this response for disease progression or healing.

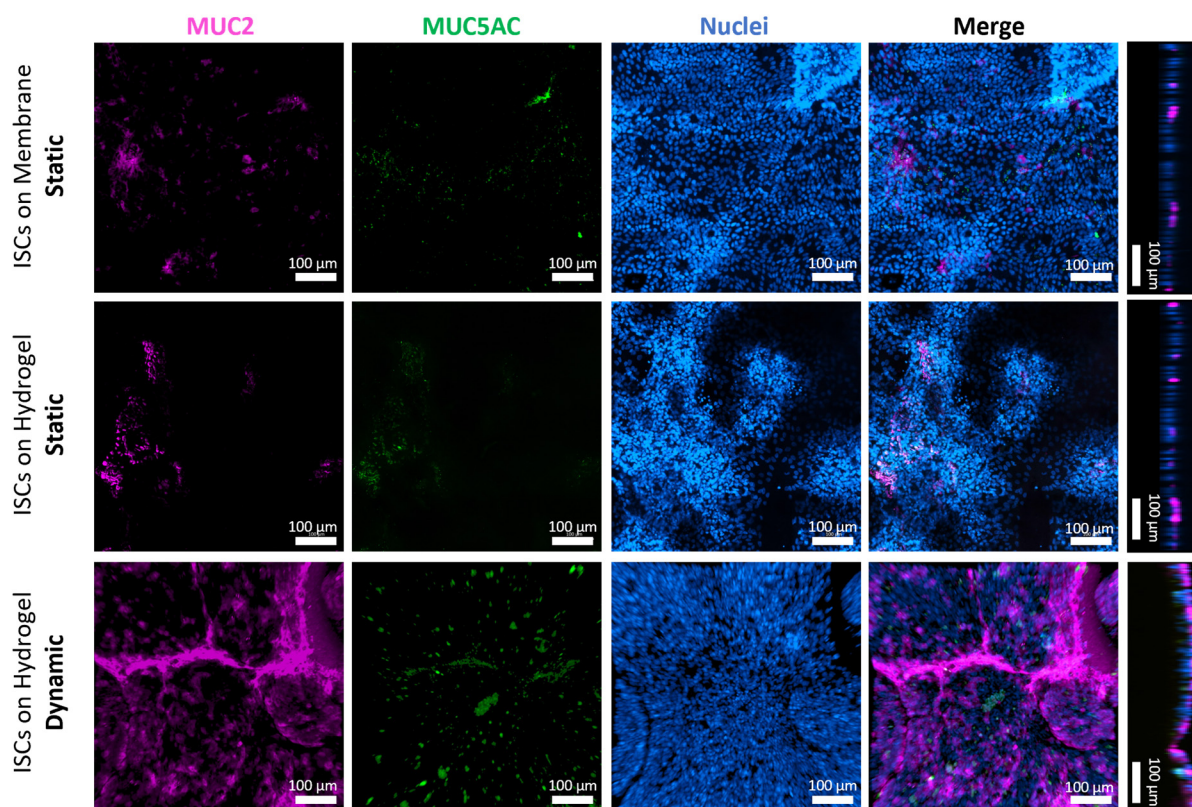


**Figure 8.** Representative confocal z-stack images in xy projection, along with their xz/yz projections, of ISCs stained for the MUC2 (purple) and MUC5AC (green) and counterstained with nuclei (blue) after static culture on insert membranes and hydrogels or dynamic culture on hydrogels on days 5–7 in expansion media. Samples are collected from three independent runs ( $n = 3$ ).

To further characterize the secreted mucus within our experimental setup, quantitative assays employing alcian blue (AB) staining for an acidic and periodic acid–Schiff base reaction (PAS) for neutral mucins were utilized. However, the direct staining of acidic and neutral mucins is not possible when dSIS-based hydrogels are used as a culture substrate due to significant background staining of the gels' ECM components (Figure S9). Therefore, a modified protocol was developed, in which the cellular layer is first removed from the scaffolds before assessing acidic and neutral mucins.

Our assessment of the loose shed mucus both in the apical medium compartment of static cultures and in the medium reservoir of dynamic cultures (Figure 9A), as well as the cell-attached mucus (Figure 9B) of both conditions on specified days, revealed a distinct pattern. Significantly larger amounts of mucus were secreted under dynamic compared to static conditions, which is in line with enhanced ISC differentiation into functional, mucin-producing goblet cells under shear stress (Figure 8). A general correlation between AB/PAS staining and mucin protein expression levels has been demonstrated in the literature [53]. The shedding of mucins from the polarized epithelial monolayers emulates the dynamic nature of the intestinal mucus layer *in vivo*. This layer undergoes continuous replenishment by goblet cell secretions and dispersion through peristalsis and intestinal flow, ensuring the removal of pathogens and debris while maintaining a protective barrier and facilitating nutrient uptake.

The shedding and accumulation of mucus in cell culture medium, particularly under flow conditions, was also reported with an ISC-derived ileum-on-chip model, reaching levels of around 400 µg/mL of secreted mucus in the medium after seven days of dynamic flow in expansion media, as determined using an AB assay [54]. Unfortunately, the absolute mucin concentrations are not comparable in such studies due to the varying setups affecting the cell number, medium volume in the circuit, and the exact flow rate. It is important to



note that PBS (–/–) destabilizes the forming AB–mucin complex, resulting in significant complex precipitation during a quantitative AB assay. Replacing PBS with HEPES buffer resolves this issue by enhancing the stability and solubility of the AB dye and facilitating its interaction with mucins in an entropy-driven process, resulting in a more stable and soluble mucin–AB complex for subsequent absorbance-based quantification.

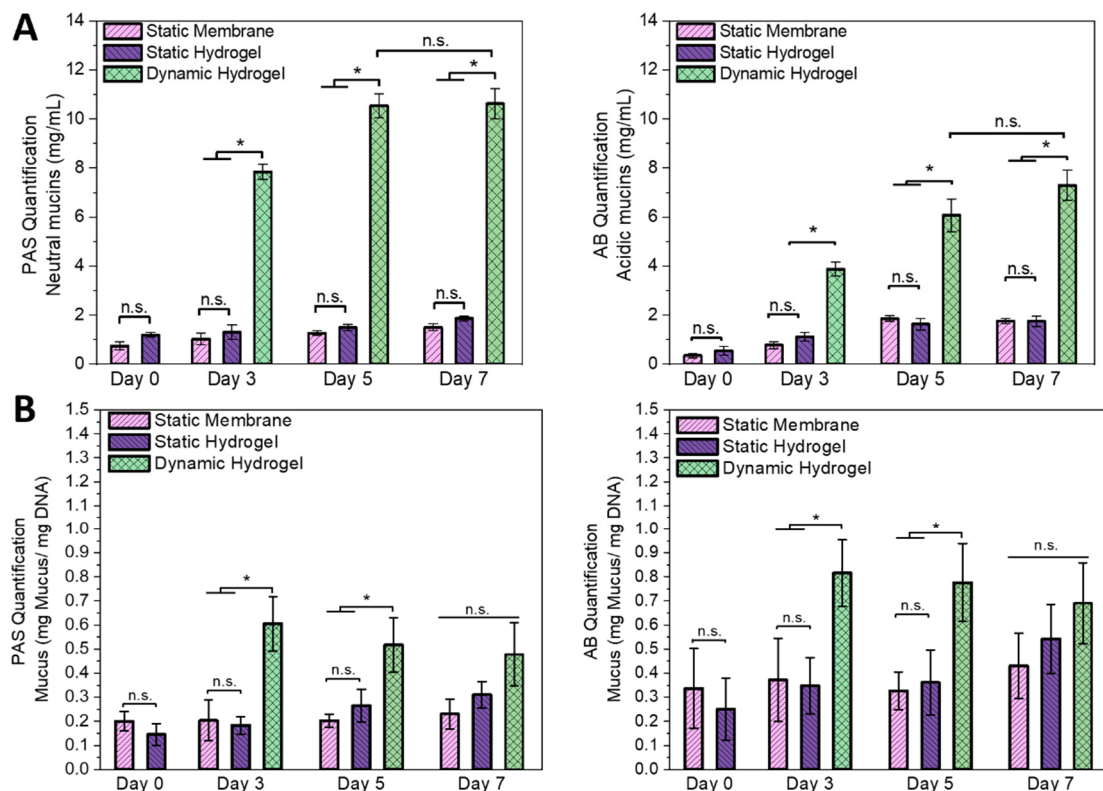


**Figure 9.** Time-dependent quantification of neutral (PAS assay) and acidic (AB assay) mucins produced by ISCs during static and dynamic culture on Matrigel™-coated insert membranes and dSIS-MA (1.5 wt%) hydrogels for estimation of the amount of secreted mucus via a standard calibration curve using bovine submaxillary gland mucins. **(A)** Amount of mucins shed to the culture media by intestinal monolayers on a substrate area of approximately 3.4 cm<sup>2</sup>. Samples were taken from the apical supernatant in static cultures and the media reservoir in dynamic cultures and normalized accordingly. **(B)** Amount of cell- or membrane-bound mucins normalized to the DNA content of the monolayer. Data are presented as mean ± SD for independent runs n = 3, where “\*” indicates statistical significance ( $p < 0.05$ ) and “n.s.” indicates non-significance of all samples performed by the Kruskal–Wallis test, followed by Dunn’s test.

Technical limitations concerning the working distance in our microscopy setup did not allow for the direct assessment of mucus thickness in the unfixed state via fluorescent beads [26] due to the hydrogels’ thickness (1 mm). We are currently developing solutions to overcome these obstacles in future investigations by reducing the thickness of the hydrogels while increasing their weight through fixation on glass coverslips to prevent floating.

#### 4. Conclusions

The objective of this study was to develop a hydrogel-integrated millifluidic system for the application of defined shear stress to diverse tissue models, with a particular focus on intestinal models. The designed tissue chamber is capable of accommodating nine flat or 3D-structured hydrogel scaffolds while maintaining a laminar flow profile. The chamber’s performance was initially validated with HT29-MTX cells and then challenged during the culture of human ISCs derived from the terminal ileum. Our findings demonstrate

the beneficial mucus-related effects achievable during the multi-lineage differentiation and 3D structural organization of human ISCs when cultured on biomimicking hydrogel scaffolds under physiological shear stress without distinct chemical differentiation triggers. Functional differentiation into enterocyte and goblet cell lineages was confirmed via quantitative ALP activity and mucus measurements. No marked differences were observed at the protein level between Matrigel<sup>TM</sup>-coated and dSIS-MA hydrogel controls when culturing ISCs statically in expansion media, clearly assigning the observed cellular effects to shear stress and flow conditions. However, distinct differences were noted in HT29-MTX cells cultured dynamically on TCPS and hydrogels, highlighting the bioinstructive properties of the scaffold. Future investigations will explore the impact of the mechanical properties of culture scaffolds/substrates, accompanied by a comprehensive mRNA gene expression analysis, to reveal intricate interactions between hydrogel and ISCs. We propose that dSIS-MA hydrogels, with tunable stiffness and bioactive composition, could offer biomimetic alternatives to synthetic scaffolds [21] for modeling diseased states, such as inflammatory bowel disease [55]. Additionally, variations in medium composition will be explored to understand their influence on ISC differentiation, cellular responses, and mucus properties.

While colon-on-chip systems have achieved notable success in creating *in vitro* mucosal models featuring physiological mucus properties [14], analogous models of the small intestine are rare. A unique feature of our dynamic small intestinal model is the fact that it does not require co-cultured endothelial cells for proper tissue maturation, as frequently observed with gut-on-chip systems [39,51,54], allowing the investigation of isolated epithelial cell-derived effects.

The printed millifluidic chamber presents a cost-effective alternative to fluidic chip systems, enabling flexible design modifications to suit diverse experimental requirements and boost sample throughput. This work opens avenues for elucidating complex interactions within the intestinal epithelium under dynamic conditions, with the resulting tissue models providing promising avenues for advanced disease modeling, drug discovery, and pathogen studies. Future work will address challenges such as the limited self-sustainment of ISC-based tissue models under shear stress by including more physiologically relevant features, such as crypts, which will protect ISCs regionally from shear stress exposure.

**Supplementary Materials:** The following supporting information can be downloaded at: <https://www.mdpi.com/article/10.3390/cells13131080/s1>, Table S1: Antibodies used in IF staining; Table S2: Primers used in RT-qPCR analysis; Figure S1: CFD simulation of 3D villi-structured hydrogels in the millifluidic tissue chamber showing shear stress gradient along the villi. Figure S2: Processing, modification, and characterization of dSIS-MA biomaterial resins; Figure S3: Characterization of printed dSIS-MA hydrogels; Figure S4: Confocal images of HT29-MTX under static and dynamic conditions on day 7 showing KI-67, MUC2, and MUC5AC expression; Figure S5: Phase-contrast images of human organoid-derived ISC monolayers under static conditions on day 0 post-confluency; Figure S6: Quantitative RT-qPCR analysis of ISCs on hydrogels on day 3 post-confluency; Figure S7: Confocal images of ISC monolayers under dynamic conditions on days 5–7 post-confluency; Figure S8: Confocal images of ISCs under static or dynamic conditions showing F-actin, E-cadherin, and ZO-1; Figure S9: 3D-printed hydrogel scaffolds showing background staining of AB and PAS after water washes; Table S3: Jumper pins configuration of the X,Y,Z, and A axes for the step motors; Figure S10: settings for different configuration modes of standard micro-stepping and a photograph of the operational quarter step mode set on Arduino board; Figure S11: Step-by-step assembly of the Arduino-controlled pump system. References [32,33,43,56] are cited in the Supplementary Materials.

**Author Contributions:** Conceptualization, A.A., L.E., B.S. and M.W.; Methodology, A.A., N.A., F.R., J.S., M.L. and M.W.; Formal analysis, A.A.; Investigation, A.A.; Writing—original draft, A.A. and M.W.; Writing—review & editing, A.A., N.A., L.E., B.S. and M.W.; Supervision, B.S. and M.W.; Project administration, B.S. and M.W.; Funding acquisition, B.S. and M.W. All authors have read and agreed to the published version of the manuscript.

**Funding:** Financial support is kindly acknowledged from the Deutsche Forschungsgemeinschaft (DFG, German Research Foundation) for CRC 1449 (project ID 431232613, M.W, B.S.) and CRC-TRR 241-B01 and Z02 (project number 375876048 to B.S.); CRU 5023 (project number 50474582 to B.S.); and CRC 1340-B06 (project number 372486779 to B.S.). The authors express their gratitude for the support provided by the Core Facility BioSupraMol, generously funded by the DFG.

**Institutional Review Board Statement:** The study was conducted in accordance with the Declaration of Helsinki, and approved by the Institutional Review Board (Ethics Committee) of Charité University Medicine Berlin (EA4/120/20).

**Informed Consent Statement:** Informed and written consent was obtained from all subjects involved in the study.

**Data Availability Statement:** Data are reported within the article and in the Supplementary Materials. Further data will be made available through the corresponding author upon reasonable request.

**Acknowledgments:** Special appreciation is also expressed to Z. Mahfouz for assisting in CD spectroscopy and P. Tang for SEM imaging. Some icons in the figures were used with a license from [Biorender.com](https://www.biorender.com) (accessed on 16 June 2024) or [flaticon.com](https://www.flaticon.com) (accessed on 30 May 2024).

**Conflicts of Interest:** The authors declare no conflicts of interest.

## References

1. Wright, L.; Joyce, P.; Barnes, T.J.; Prestidge, C.A. Mimicking the Gastrointestinal Mucus Barrier: Laboratory-Based Approaches to Facilitate an Enhanced Understanding of Mucus Permeation. *ACS Biomater. Sci. Eng.* **2023**, *9*, 2819–2837. [[CrossRef](#)]
2. Izadifar, Z.; Sontheimer-Phelps, A.; Lubamba, B.A.; Bai, H.; Fadel, C.; Stejskalova, A.; Ozkan, A.; Dasgupta, Q.; Bein, A.; Junaid, A.; et al. Modeling Mucus Physiology and Pathophysiology in Human Organs-on-Chips. *Adv. Drug Deliv. Rev.* **2022**, *191*, 114542. [[CrossRef](#)]
3. Song, C.; Chai, Z.; Chen, S.; Zhang, H.; Zhang, X.; Zhou, Y. Intestinal Mucus Components and Secretion Mechanisms: What We Do and Do Not Know. *Exp. Mol. Med.* **2023**, *55*, 681–691. [[CrossRef](#)]
4. Atreya, R.; Siegmund, B. Location Is Important: Differentiation between Ileal and Colonic Crohn’s Disease. *Nat. Rev. Gastroenterol. Hepatol.* **2021**, *18*, 544–558. [[CrossRef](#)]
5. Martinez-Medina, J.N.; Ghazisaeedi, F.; Kramer, C.; Ziegler, J.F.; McParland, V.; Siegmund, B.; Jarquín-Díaz, V.H.; Fulde, M.; Forslund, S.K. Mucosal Washes Are Useful for Sampling Intestinal Mucus-Associated Microbiota Despite Low Biomass. *bioRxiv* **2023**, 12.12.571228. [[CrossRef](#)]
6. Nakamura, M.; Maeda, K.; Yamamoto, K.; Yamamura, T.; Sawada, T.; Ishikawa, E.; Kakushima, N.; Furukawa, K.; Iida, T.; Mizutani, Y.; et al. Preliminary Comparison of Endoscopic Brush and Net Catheters as the Sampling Tool to Analyze the Intestinal Mucus in the Rectum with Ulcerative Colitis Patients. *Digestion* **2022**, *103*, 232–243. [[CrossRef](#)]
7. Kramer, C.; Rulff, H.; Ziegler, J.F.; Alzain, N.; Addante, A.; Kuppe, A.; Timm, S.; Schrade, P.; Bischoff, P.; Glauben, R.; et al. Ileal Mucus Viscoelastic Properties Differ in Crohn’s Disease. *Mucosal Immunol.* **2024**. *accepted*. [[CrossRef](#)]
8. Macierzanka, A.; Mackie, A.R.; Krupa, L. Permeability of the Small Intestinal Mucus for Physiologically Relevant Studies: Impact of Mucus Location and Ex Vivo Treatment. *Sci. Rep.* **2019**, *9*, 17516. [[CrossRef](#)]
9. Martinez-Maqueda, D.; Miralles, B.; Recio, I. Ht29 Cell Line. In *The Impact of Food Bioactives on Health: In Vitro and Ex Vivo Models*; Verhoeckx, K., Cotter, P., Lopez-Exposito, I., Kleiveland, C., Lea, T., Mackie, A., Requena, T., Swiatecka, D., Wichers, H., Eds.; Springer: Cham, Switzerland, 2015; pp. 113–124.
10. Elzinga, J.; van der Lugt, B.; Belzer, C.; Steegenga, W.T. Characterization of Increased Mucus Production of Ht29-Mtx-E12 Cells Grown under Semi-Wet Interface with Mechanical Stimulation. *PLoS ONE* **2021**, *16*, e0261191. [[CrossRef](#)] [[PubMed](#)]
11. Pauzuolis, M.; Samperio Ventayol, P.; Neyazi, M.; Bartfeld, S. Organoids as a Tool to Study the Impact of Heterogeneity in Gastrointestinal Epithelium on Host-Pathogen Interactions. *Clin. Exp. Immunol.* **2024**, uxae002. [[CrossRef](#)]
12. Sato, T.; Stange, D.E.; Ferrante, M.; Vries, R.G.; Van Es, J.H.; Van den Brink, S.; Van Houdt, W.J.; Pronk, A.; Van Gorp, J.; Siersema, P.D.; et al. Long-Term Expansion of Epithelial Organoids from Human Colon, Adenoma, Adenocarcinoma, and Barrett’s Epithelium. *Gastroenterology* **2011**, *141*, 1762–1772. [[CrossRef](#)]
13. Taelman, J.; Diaz, M.; Guiu, J. Human Intestinal Organoids: Promise and Challenge. *Front. Cell Dev. Biol.* **2022**, *10*, 854740. [[CrossRef](#)]
14. Sontheimer-Phelps, A.; Chou, D.B.; Tovaglieri, A.; Ferrante, T.C.; Duckworth, T.; Fadel, C.; Frimantas, V.; Sutherland, A.D.; Jalili-Firoozinezhad, S.; Kasendra, M.; et al. Human Colon-on-a-Chip Enables Continuous in Vitro Analysis of Colon Mucus Layer Accumulation and Physiology. *Cell Mol. Gastroenterol. Hepatol.* **2020**, *9*, 507–526. [[CrossRef](#)]
15. Beaurivage, C.; Kanapeckaitė, A.; Loomans, C.; Erdmann, K.S.; Stallen, J.; Janssen, R.A.J. Development of a Human Primary Gut-on-a-Chip to Model Inflammatory Processes. *Sci. Rep.* **2020**, *10*, 21475. [[CrossRef](#)]
16. Co, J.Y.; Margalef-Catala, M.; Monack, D.M.; Amieva, M.R. Controlling the Polarity of Human Gastrointestinal Organoids to Investigate Epithelial Biology and Infectious Diseases. *Nat. Protoc.* **2021**, *16*, 5171–5192. [[CrossRef](#)]

17. Dutton, J.S.; Hinman, S.S.; Kim, R.; Wang, Y.; Allbritton, N.L. Primary Cell-Derived Intestinal Models: Recapitulating Physiology. *Trends Biotechnol.* **2019**, *37*, 744–760. [CrossRef]
18. Thorne, C.A.; Chen, I.W.; Sanman, L.E.; Cobb, M.H.; Wu, L.F.; Altschuler, S.J. Enteroid Monolayers Reveal an Autonomous Wnt and Bmp Circuit Controlling Intestinal Epithelial Growth and Organization. *Dev. Cell* **2018**, *44*, 624–633.e4. [CrossRef]
19. VanDussen, K.L.; Marinshaw, J.M.; Shaikh, N.; Miyoshi, H.; Moon, C.; Tarr, P.I.; Ciorba, M.A.; Stappenbeck, T.S. Development of an Enhanced Human Gastrointestinal Epithelial Culture System to Facilitate Patient-Based Assays. *Gut* **2015**, *64*, 911–920. [CrossRef]
20. Costa, J.; Ahluwalia, A. Advances and Current Challenges in Intestinal in Vitro Model Engineering: A Digest. *Front. Bioeng. Biotechnol.* **2019**, *7*, 144. [CrossRef]
21. He, S.; Lei, P.; Kang, W.; Cheung, P.; Xu, T.; Mana, M.; Park, C.Y.; Wang, H.; Imada, S.; Russell, J.O.; et al. Stiffness Restricts the Stemness of the Intestinal Stem Cells and Skews Their Differentiation toward Goblet Cells. *Gastroenterology* **2023**, *164*, 1137–1151.e15. [CrossRef]
22. Soofi, S.S.; Last, J.A.; Liliensiek, S.J.; Nealey, P.F.; Murphy, C.J. The Elastic Modulus of Matrigel as Determined by Atomic Force Microscopy. *J. Struct. Biol.* **2009**, *167*, 216–219. [CrossRef]
23. Onfroy-Roy, L.; Hamel, D.; Foncy, J.; Malaquin, L.; Ferrand, A. Extracellular Matrix Mechanical Properties and Regulation of the Intestinal Stem Cells: When Mechanics Control Fate. *Cells* **2020**, *9*, 2629. [CrossRef]
24. Wang, Y.; Gunasekara, D.B.; Reed, M.I.; DiSalvo, M.; Bultman, S.J.; Sims, C.E.; Magness, S.T.; Allbritton, N.L. A Microengineered Collagen Scaffold for Generating a Polarized Crypt-Villus Architecture of Human Small Intestinal Epithelium. *Biomaterials* **2017**, *128*, 44–55. [CrossRef]
25. Schweinlin, M.; Wilhelm, S.; Schwedhelm, I.; Hansmann, J.; Rietscher, R.; Jurowich, C.; Walles, H.; Metzger, M. Development of an Advanced Primary Human in Vitro Model of the Small Intestine. *Tissue Eng. Part. C Methods* **2016**, *22*, 873–883. [CrossRef]
26. Lindner, M.; Laporte, A.; Block, S.; Elomaa, L.; Weinhart, M. Physiological Shear Stress Enhances Differentiation, Mucus-Formation and Structural 3d Organization of Intestinal Epithelial Cells in Vitro. *Cells* **2021**, *10*, 2062. [CrossRef]
27. Kim, H.J.; Ingber, D.E. Gut-on-a-Chip Microenvironment Induces Human Intestinal Cells to Undergo Villus Differentiation. *Integr. Biol. (CAMB)* **2013**, *5*, 1130–1140. [CrossRef]
28. He, J.; Xie, X.; Xiao, Z.; Qian, W.; Zhang, L.; Hou, X. Piezo1 in Digestive System Function and Dysfunction. *Int. J. Mol. Sci.* **2023**, *24*, 12953. [CrossRef]
29. He, L.; Si, G.; Huang, J.; Samuel, A.D.T.; Perrimon, N. Mechanical Regulation of Stem-Cell Differentiation by the Stretch-Activated Piezo Channel. *Nature* **2018**, *555*, 103–106. [CrossRef]
30. Jiang, Y.; Song, J.; Xu, Y.; Liu, C.; Qian, W.; Bai, T.; Hou, X. Piezo1 Regulates Intestinal Epithelial Function by Affecting the Tight Junction Protein Claudin-1 Via the Rock Pathway. *Life Sci.* **2021**, *275*, 119254. [CrossRef] [PubMed]
31. Xu, Y.; Bai, T.; Xiong, Y.; Liu, C.; Liu, Y.; Hou, X.; Song, J. Mechanical Stimulation Activates Piezo1 to Promote Mucin2 Expression in Goblet Cells. *J. Gastroenterol. Hepatol.* **2021**, *36*, 3127–3139. [CrossRef] [PubMed]
32. Almalla, A.; Elomaa, L.; Bechtella, L.; Daneshgar, A.; Yavvari, P.; Mahfouz, Z.; Tang, P.; Kokschi, B.; Sauer, I.; Pagel, K.; et al. Papain-Based Solubilization of Decellularized Extracellular Matrix for the Preparation of Bioactive, Thermosensitive Pre-Gels. *Biomacromolecules* **2023**, *24*, 5620–5637. [CrossRef]
33. Elomaa, L.; Gerbeth, L.; Almalla, A.; Fribicz, N.; Daneshgar, A.; Tang, P.; Hillebrandt, K.H.; Seiffert, S.; Sauer, M.I.; Siegmund, B.; et al. Bioactive Photocrosslinkable Resin Solely Based on Refined Decellularized Small Intestine Submucosa for Vat Photopolymerization of in Vitro Tissue Mimics. *Addit. Manuf.* **2023**, *64*, 103439. [CrossRef]
34. Poon, C. Measuring the Density and Viscosity of Culture Media for Optimized Computational Fluid Dynamics Analysis of in Vitro Devices. *J. Mech. Behav. Biomed. Mater.* **2022**, *126*, 105024. [CrossRef]
35. Miyoshi, H.; Stappenbeck, T.S. In Vitro Expansion and Genetic Modification of Gastrointestinal Stem Cells in Spheroid Culture. *Nat. Protoc.* **2013**, *8*, 2471–2482. [CrossRef] [PubMed]
36. Zamora, C.Y.; Ward, E.M.; Kester, J.C.; Chen, W.L.K.; Velazquez, J.G.; Griffith, L.G.; Imperiali, B. Application of a Gut-Immune Co-Culture System for the Study of N-Glycan-Dependent Host-Pathogen Interactions of *Campylobacter Jejuni*. *Glycobiology* **2020**, *30*, 374–381. [CrossRef] [PubMed]
37. Donkers, J.M.; Eslami Amirabadi, H.; van de Steeg, E. Intestine-on-a-Chip: Next Level In vitro Research Model of the Human Intestine. *Curr. Opin. Toxicol.* **2021**, *25*, 6–14. [CrossRef]
38. Altay, G.; Larranaga, E.; Tosi, S.; Barriga, F.M.; Batlle, E.; Fernandez-Majada, V.; Martinez, E. Self-Organized Intestinal Epithelial Monolayers in Crypt and Villus-Like Domains Show Effective Barrier Function. *Sci. Rep.* **2019**, *9*, 10140. [CrossRef] [PubMed]
39. Kasendra, M.; Tovaglieri, A.; Sontheimer-Phelps, A.; Jalili-Firoozinezhad, S.; Bein, A.; Chalkiadaki, A.; Scholl, W.; Zhang, C.; Rickner, H.; Richmond, C.A.; et al. Development of a Primary Human Small Intestine-on-a-Chip Using Biopsy-Derived Organoids. *Sci. Rep.* **2018**, *8*, 2871. [CrossRef]
40. Nikolaev, M.; Mitrofanova, O.; Broguiere, N.; Geraldo, S.; Dutta, D.; Tabata, Y.; Elci, B.; Brandenburg, N.; Kolotuev, I.; Gjorevski, N.; et al. Homeostatic Mini-Intestines through Scaffold-Guided Organoid Morphogenesis. *Nature* **2020**, *585*, 574–578. [CrossRef]
41. Kim, H.J.; Huh, D.; Hamilton, G.; Ingber, D.E. Human Gut-on-a-Chip Inhabited by Microbial Flora That Experiences Intestinal Peristalsis-Like Motions and Flow. *Lab. Chip* **2012**, *12*, 2165–2174. [CrossRef]
42. Available online: <https://formlabs.com/de/shop/materials/biomed-amber-resin/> (accessed on 16 April 2024).

43. Almalla, A.; Elomaa, L.; Fribicz, N.; Landes, T.; Tang, P.; Mahfouz, Z.; Koks, B.; Hillebrandt, K.H.; Sauer, I.M.; Heinemann, D.; et al. Chemistry Matters: A Side-by-Side Comparison of Two Chemically Distinct Methacryloylated Decm Bioresins for Vat Photopolymerization. *Biomater. Adv.* **2024**, *160*, 213850. [[CrossRef](#)] [[PubMed](#)]
44. Elomaa, L.; Almalla, A.; Keshi, E.; Hillebrandt, K.H.; Sauer, I.M.; Weinhart, M. Rise of Tissue- and Species-Specific 3d Bioprinting Based on Decellularized Extracellular Matrix-Derived Bioinks and Bioresins. *Biomater. Biosyst.* **2023**, *12*, 100084. [[CrossRef](#)] [[PubMed](#)]
45. Elomaa, L.; Keshi, E.; Sauer, I.M.; Weinhart, M. Development of Gelma/Pcl and Decm/Pcl Resins for 3d Printing of Acellular in Vitro Tissue Scaffolds by Stereolithography. *Mater. Sci. Eng. C Mater. Biol. Appl.* **2020**, *112*, 110958. [[CrossRef](#)] [[PubMed](#)]
46. Johnson, L.A.; Rodansky, E.S.; Sauder, K.L.; Horowitz, J.C.; Mih, J.D.; Tschumperlin, D.J.; Higgins, P.D. Matrix Stiffness Corresponding to Strictured Bowel Induces a Fibrogenic Response in Human Colonic Fibroblasts. *Inflamm. Bowel Dis.* **2013**, *19*, 891–903. [[CrossRef](#)] [[PubMed](#)]
47. Kemper, K.; Prasetyanti, P.R.; De Lau, W.; Rodermond, H.; Clevers, H.; Medema, J.P. Monoclonal Antibodies against Lgr5 Identify Human Colorectal Cancer Stem Cells. *Stem Cells* **2012**, *30*, 2378–2386. [[CrossRef](#)] [[PubMed](#)]
48. Liu, W.; Rodgers, G.P. Olfactomedin 4 Is Not a Precise Marker for Human Intestinal Stem Cells, but Is Involved in Intestinal Carcinogenesis. *Gastroenterology* **2022**, *162*, 1001–1004. [[CrossRef](#)]
49. Yin, J.; Sunuwar, L.; Kasendra, M.; Yu, H.; Tse, C.M.; Talbot, C.C., Jr.; Boronina, T.; Cole, R.; Karalis, K.; Donowitz, M. Fluid Shear Stress Enhances Differentiation of Jejunal Human Enteroids in Intestine-Chip. *Am. J. Physiol. Gastrointest. Liver Physiol.* **2021**, *320*, G258–G271. [[CrossRef](#)] [[PubMed](#)]
50. Lee, H.; Han, W.; Kim, H.; Ha, D.H.; Jang, J.; Kim, B.S.; Cho, D.W. Development of Liver Decellularized Extracellular Matrix Bioink for Three-Dimensional Cell Printing-Based Liver Tissue Engineering. *Biomacromolecules* **2017**, *18*, 1229–1237. [[CrossRef](#)] [[PubMed](#)]
51. Kasendra, M.; Luc, R.; Yin, J.; Manatakis, D.V.; Kulkarni, G.; Lucchesi, C.; Sliz, J.; Apostolou, A.; Sunuwar, L.; Obrigewitch, J.; et al. Duodenum Intestine-Chip for Preclinical Drug Assessment in a Human Relevant Model. *eLife* **2020**, *9*, 50135. [[CrossRef](#)]
52. Grondin, J.A.; Kwon, Y.H.; Far, P.M.; Haq, S.; Khan, W.I. Mucins in Intestinal Mucosal Defense and Inflammation: Learning from Clinical and Experimental Studies. *Front. Immunol.* **2020**, *11*, 2054. [[CrossRef](#)]
53. Lopes, C.; Pereira-Lima, J.; Hartmann, A. *Correlation between Alcian Blue–Periodic Acid–Schiff Stain and Immunohistochemical Expression of Mucin 2 in Barrett’s Oesophagus*; Blackwell Publishing Ltd.: Oxford, UK, 2004; Volume 45.
54. Jalili-Firoozinezhad, S.; Gazzaniga, F.S.; Calamari, E.L.; Camacho, D.M.; Fadel, C.W.; Bein, A.; Swenor, B.; Nestor, B.; Cnonce, M.J.; Tovaglieri, A.; et al. A Complex Human Gut Microbiome Cultured in an Anaerobic Intestine-on-a-Chip. *Nat. Biomed. Eng.* **2019**, *3*, 520–531. [[CrossRef](#)] [[PubMed](#)]
55. Stewart, D.C.; Berrie, D.; Li, J.; Liu, X.; Rickerson, C.; Mkoji, D.; Iqbal, A.; Tan, S.; Doty, A.L.; Glover, S.C.; et al. Quantitative Assessment of Intestinal Stiffness and Associations with Fibrosis in Human Inflammatory Bowel Disease. *PLoS ONE* **2018**, *13*, e0200377. [[CrossRef](#)]
56. Fairbanks, B.D.; Schwartz, M.P.; Bowman, C.N.; Anseth, K.S. Photoinitiated Polymerization of Peg-Diacrylate with Lithium Phenyl-2,4,6-Trimethylbenzoylphosphinate: Polymerization Rate and Cytocompatibility. *Biomaterials* **2009**, *30*, 6702–6707. [[CrossRef](#)]

**Disclaimer/Publisher’s Note:** The statements, opinions and data contained in all publications are solely those of the individual author(s) and contributor(s) and not of MDPI and/or the editor(s). MDPI and/or the editor(s) disclaim responsibility for any injury to people or property resulting from any ideas, methods, instructions or products referred to in the content.

# Hydrogel-Integrated Millifluidic Systems: Advancing the Fabrication of Mucus-producing Human Intestinal Models

Ahed Almalla,<sup>1</sup> Nadra Alzain,<sup>1,2</sup> Laura Elomaa,<sup>1</sup> Fiona Richter,<sup>1</sup> Johanna Scholz,<sup>1</sup> Marcus Lindner,<sup>1</sup> Britta Siegmund,<sup>2</sup> Marie Weinhart<sup>1,3,\*</sup>

<sup>1</sup>Institute of Chemistry and Biochemistry, Freie Universität Berlin, Takustr. 3, 14195 Berlin, Germany

<sup>2</sup>Department of Gastroenterology, Infectious Diseases and Rheumatology (including Nutrition Medicine), Charité Universitätsmedizin Berlin, corporate member of Freie Universität Berlin and Humboldt-Universität zu Berlin, Hindenburgdamm 30, 12203 Berlin, Germany

<sup>3</sup>Institute of Physical Chemistry and Electrochemistry, Leibniz Universität Hannover, Callinstr. 3A, 30167 Hannover, Germany

\* Corresponding author: marie.weinhart@fu-berlin.de and marie.weinhart@pci.uni-hannover.de

## Table of Contents

1.	Materials and Methods .....	2
1.1.	Materials and Reagents .....	2
1.2.	Decellularization, Solubilization, and Methacrylation of Porcine Small Intestinal Submucosa (SIS) .....	5
1.3.	3D printing of dSIS-MA-based Hydrogels .....	6
1.4.	Tissue Chamber Accessory .....	6
2.	Material Characterization .....	7
2.1.	dSIS-MA Resin Characterization .....	7
2.2.	Rheology of the dSIS-MA-based Hydrogels .....	8
2.3.	Atomic Force Microscopy (AFM) and Scanning Electron Microscopy (SEM) of dSIS-MA-based hydrogels .....	8
2.4.	Human Crypt Isolation and Organoid Culture .....	9
2.5.	Real-time Quantitative Polymerase Chain Reaction (RT-qPCR) Analysis .....	10
2.6.	DNA Content Quantification .....	11
2.7.	Immunofluorescence Staining .....	11
3.	Supplementary Tables and Figures .....	12
4.	Controller-Board Assembly and Pump Programming .....	21
4.1.	Assembly of the Arduino Board to Control the Pump System .....	21
4.2.	Arduino Software and Programming .....	23

## Supporting Information

### 1. Materials and Methods

#### 1.1. Materials and Reagents

*Materials for dSIS-MA preparation, analysis and scaffold printing:* Porcine small intestinal submucosa (SIS) was purchased from a local meat market (Rasch GmbH, Berliner Fleischgroßmarkt, Germany). Papain from *Carica papaya* (#1.07144, 30000 U/mg), sodium dodecyl sulfate (SDS, #8.22050), triton™ X-100 (#X100), methacrylic anhydride (MA, #276685), 2,4,6-trinitrobenzene sulfonic acid (TNBS, #P2297), peracetic acid (PAA; 38-40% #107222), penicillin/streptomycin (p/s, #P4333, 10,000 units penicillin and 10 mg/mL streptomycin; 100x concentrated), phosphate-buffered saline (#P4417, tablets without calcium and magnesium ions (PBS (-/-)), ethylenediamine tetraacetic acid disodium salt (EDTA-Na<sub>2</sub>, #E4884), and L-cysteine (#168149) were purchased from Sigma-Aldrich (Sigma Aldrich/Merck KGaA, Darmstadt, Germany). Hydrochloric acid (HCl, 37%, #10244100), glacial acetic acid (>99.7%, #AA36289AE), and sodium hydroxide (NaOH, ≥ 98%, #11438327) was purchased from Thermo Fisher Scientific (Darmstadt, Germany). Lithium-phenyl-2,4,6-trimethylbenzoylphosphinat as the photoinitiator for dSIS-MA printing was synthesized according to literature [1].

*Materials for tissue chamber fabrication and dynamic cell culture:* Heat-seal sterilization bags (400 mm× 250 mm, SÜDPACK Medica, Baar, Switzerland), syringe filters (Minisart®, PTFE, 0.2 µm, #SRP15, Sartorius, Göttingen, Germany).

*Materials for HT29-MTX culture, cell staining and fixation, and mucin quantification:* Fetal bovine serum (FBS, Superior, #S0615), nonessential amino acids (MEM-NEAA), alcian blue powder (#A5268), sodium acetate (#S-2889), magnesium chloride (#M8266), periodic acid Schiff (PAS) staining kit (#395B), bovine submaxillary glands mucin (#M3895) and phalloidin–Atto® 647N (#65906), Triton X-100 (#X100), and Tween-20 (#P9416) were purchased from Sigma-Aldrich (Sigma Aldrich/Merck KGaA, Darmstadt, Germany). 3-[(3-Cholamidopropyl)-dimethyl-ammonio]-1-propansulfonate (CHAPS, #1.11662.0001) was purchased from VWR International (Darmstadt, Germany). Hoechst dye (#33342) was purchased from Thermo Fisher Scientific (Darmstadt, Germany). Gibco™ Dulbecco's Modified Eagle's Medium (DMEM, high glucose, GlutaMAX™, #35050-061) Gibco™ trypsin-ethylenediamine tetraacetic acid (Trypsin-

EDTA, #15400-054) was purchased from Thermo Fisher Scientific (Darmstadt, Germany). Mounting medium (ProTaq<sup>®</sup> Mount Flour) was purchased from Biocyc (Luckenwalde, Germany). Paraformaldehyde (PFA, ROTI<sup>®</sup>Histofix 4%, #P087.4) and albumin fraction V (BSA, biotin-free, # 0163.4) were ordered from Carl Roth (Karlsruhe, Germany). Primary and secondary antibodies for immunofluorescence staining are listed in Table 1.

*Materials for organoid isolation and culture:* D-sorbitol (#6213.1, Carl Roth, Karlsruhe, Germany), sucrose (#A15583.0C, Thermo Fisher, Darmstadt, Germany), dithiothreitol (DTT) (#6908.2, Carl Roth, Karlsruhe, Germany), ciprofloxacin (#J01MA02, Fresenius Kabi, Bad Homburg vor der Höhe, Germany), fluconazole (#603231, B. Braun SE, Melsungen, Germany), primocin (#ant-pm-05, Invivogen, San Diego, CA, USA), gentamycin (#15750060, Thermo Fisher, Darmstadt, Germany), L-WRN cells (CRL-3276TM, ATCC<sup>®</sup>, Manassas, Virginia, USA), advanced Dulbecco's Modified Eagle Medium (DMEM)/F12 (#12634010, Thermo Fisher Scientific, Darmstadt, Germany), GlutaMAX<sup>™</sup> L-glutamine (#35050-038, ThermoFisher Scientific, Darmstadt, Germany), p/s (#A2213, Merck Biochrom, Darmstadt, Germany), HEPES buffer (#15630-056, Thermo Fisher Scientific, Darmstadt, Germany), FCS (#12604013, Merck, Darmstadt, Germany), recombinant human EGF (#AF-100-15, PeproTech<sup>®</sup>, Thermo Fisher Scientific, Darmstadt, Germany), nicotinamide (#N0636, Sigma-Aldrich/Merck KGaA, Darmstadt, Germany), A 83-01 (#SML0788, Sigma Aldrich/Merck KGaA, Darmstadt, Germany), SB 202190 (#S7067, Sigma Aldrich/Merck KGaA, Darmstadt, Germany), Y-27632 dihydrochloride (#M1817, AbMole Bioscience via Hölzel Diagnostika Handels GmbH, Köln, Germany), [Leu<sup>15</sup>]-Gastrin I human (#G9145, Sigma Aldrich/Merck KGaA, Darmstadt, Germany), Gibco<sup>™</sup> TrypLE<sup>™</sup> Express solution (#12604013: 1x from Thermo Fisher Scientific, Darmstadt, Germany), Falcon<sup>®</sup> permeable support Transwells fitting 24-well plates with a 0.4 µm transparent PET membrane (#353095, Merck KGaA, Darmstadt, Germany), Corning<sup>®</sup> Matrigel<sup>™</sup> growth factor reduced basement membrane matrix (#CLS356231, Merck KGaA, Darmstadt, Germany).

*Chelating buffer composition for crypt isolation:* 54.9 mM D-sorbitol, 43.4 mM sucrose, 10 mM EDTA, 1 mM DTT, 10 µg/ml ciprofloxacin, 1 µg/ml fluconazole, 100 µg/ml primocin, and 50 µg/ml gentamycin.



*Basal medium composition for crypt isolation:* Gibco™ advanced Dulbecco's Modified Eagle Medium supplemented with 2 mM Corning™ cellgro™ L-glutamine, 1x p/s, and 10 mM Gibco™ HEPES.

*Primary culture medium (PCM):* Gibco™ advanced Dulbecco's Modified Eagle Medium supplemented with 2 mM Corning™ cellgro™ L-glutamine, 1x p/s and 20% FCS (#12604013, Merck, Darmstadt, Germany).

*Expansion medium:* WRN-conditioned medium mixed in a 1:1 v/v ratio with PCM supplemented with recombinant human epidermal growth factor (EGF, 50 ng/ml), nicotinamide (10 mM), A83-01 (0.5 μM), SB202190 (10 μM), and human gastrin I (10 nM) to the specified final concentrations.

*Growth factor and small molecule stocks:* recombinant human EGF was prepared at 100 μg/mL in 0.1% BSA/PBS (-/-). Nicotinamide was prepared at 1 M in PBS (-/-). The transforming growth factor and kinase-type-1-receptor inhibitor A 83-01 (3-(6-methyl-2-pyridinyl)-N-phenyl-4-(4-quinolinyl)-1H-pyrazol-1-carbothioamid) was prepared at 5 mM in DMSO. The p38-MAP-kinase inhibitor SB 202190 (4-(4-fluorophenyl)-2-(4-hydroxyphenyl)-5-(4-pyridyl)-1H-imidazole) was prepared at 30 mM in DMSO. Rho kinase inhibitor Y-27632 dihydrochloride was prepared at 10 mM in PBS (-/-). [Leu<sup>15</sup>]-Gastrin I human was prepared at 0.1 mM in 0.1% NaOH.

*Materials for RNA isolation and qPCR:* TRIzol™ reagent (Invitrogen™, Thermo Fisher Scientific, Darmstadt, Germany), Direct-zol RNA Microprep kit (#R2062, Zymo Research, Freiburg, Germany), Amplification Grade DNase I; 100U (1U/μl) (#18068-015, including 25 mM EDTA and 10X DNase I reaction buffer, Invitrogen™, Thermo Fisher Scientific, Darmstadt, Germany), EDTA (Thermo Fisher Scientific, Darmstadt, Germany), oligo(dT)<sub>12-18</sub> primers (Invitrogen™, Thermo Fisher Scientific, Darmstadt, Germany), deoxy nucleoside triphosphates (dNTPs, ROTI®Mix PCR3, Carl Roth, Karlsruhe, Germany), RNaseOUT™ recombinant ribonuclease inhibitor (20 U, Invitrogen™, Thermo Fisher Scientific, Darmstadt, Germany), DTT (Thermo Fisher Scientific, Darmstadt, Germany), and M-MLV reverse transcriptase (250 U, Invitrogen™, Thermo Fisher Scientific, Darmstadt, Germany), Aqua™ RNase-free water (B. Braun, Melsungen, Germany), SYBR™ Green PCR Master Mix (Invitrogen™, Thermo Fisher Scientific, Darmstadt, Germany), MicroAmp™ fast optical 96-well reaction plate (Applied Biosystems, Thermo Fisher Scientific, Darmstadt, Germany), Quant-iT™ PicoGreen™ dsDNA assay kit

(Thermo Fisher Scientific, Darmstadt, Germany). Primers listed in Table 2 were ordered from TIB Molbiol Syntheselabor GmbH (Berlin, Germany).

*Materials for ISC-derived monolayer staining and proliferation:* Alkaline phosphatase assay kit (#ab83371) was ordered from Abcam, Regensburg, Germany. Cell fixation, staining, and mucin quantification reagents are the same as listed for HT29-MTX cultures.

#### 1.2. Decellularization, Solubilization, and Methacrylation of Porcine Small Intestinal Submucosa (SIS)

Porcine small intestinal submucosa (SIS) stored in salt solution was decellularized according to our previously published protocol, [2] with minor modifications. Briefly, SIS was sectioned into pieces (3-4 cm) and placed in 2 L beakers, stirred for 24 hours at 4 °C in deionized water (2-3 water changes) to eliminate residual salts. Subsequently, the tissue was treated with SDS solution (1%) for 2 hours, exchanging the SDS solution once, then with Triton X-100 (1 %) for 24 hours (2-3 triton changes). The decellularized SIS (dSIS) was then extensively rinsed with water for 30 minutes, defatted in pure ethanol for 30 minutes, and sterilized in 0.1% PAA for 20 minutes. Final removal of residual chemicals was achieved through sequential washes in PBS (-/-) and deionized water over 3-5 days with 2-3 daily media changes. Following decellularization, the enzymatic solubilization of dSIS was achieved using papain, adhering to a published protocol with minor adjustments [3]. Briefly, dry and milled dSIS pieces (2 g) were incubated in 200 mL papain solution (200 mg papain in 20 mM EDTA containing 5 mM L-cysteine at pH = 5.5) at RT for 48 hours under periodic homogenization using a T 10 basic Ultra-Turrax (IKA®-Werke GmbH & Co. KG). The solubilization process was halted by adjusting the pH to 9.5-10 with a 10 M NaOH solution on ice for 1 hour to deactivate the enzyme. The solution was again homogenized and centrifuged at 140 x g for 5 minutes to discard any undigested remnants if present, and the supernatant was directly subjected to methacrylation without further processing [2]. In brief, MA (1 mL of MA per 1 g papain-treated dSIS) was incrementally added to the solubilized dSIS-containing supernatant under vigorous stirring and protected from light over a time course of 3 hours, while maintaining the pH  $\geq 9$  with 10 M NaOH. After finishing MA addition, the reaction was allowed to proceed for 24 hours, after which the crude mixture underwent dialysis against distilled water for 2 hours (molecular weight cut-off 1 kDa, Carl Roth GmbH + Co. KG, Karlsruhe). Subsequently, water was replaced with dilute aqueous 0.01 M HCl at 4°C for one week, changing the acidic medium 1-2 times daily while protecting the dSIS-MA

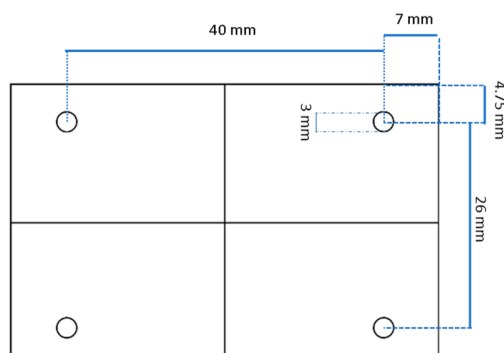
from light. Post-dialysis, the dSIS-MA-containing solution was centrifuged at 1000 x g for 5 minutes to eliminate any residual particles if present. The supernatants were snap-frozen with liquid nitrogen and lyophilized (alpha 2-4 LDplus, Martin Christ Gefriertrocknungsanlagen GmbH, Osterode am Harz, Germany) to yield dry, cotton-like resins, which were stored at -20°C until use.

### 1.3. 3D printing of dSIS-MA-based Hydrogels

3D printing of dSIS-MA-based hydrogel discs was performed according to previously established protocols [4]. In brief, dry dECM-MA (1.5 wt%) was dissolved in 0.1 M NaOH and left to stand overnight at 4°C to achieve a homogeneous resin formulation for 3D printing. Immediately before printing, the photoinitiator LAP (1 wt%) was added to the resin formulation. To eliminate air bubbles from the mixing process, the resin was centrifuged at 140 x g for 5 minutes. The computer-aided design (CAD) models for the 3D discs (6 mm diameter, 1 mm height) were crafted using the 3D builder software (Microsoft Corporation, USA), then processed with the LongerWare software (version 1.35, LONGER, China) for slicing, and finally printed using a visible light liquid crystal display (LCD) printer (Orange 30, LONGER, China) at 405 nm with a light intensity of approximately 1 mW/cm<sup>2</sup> and a crosslinking duration of 50 seconds for each 100 µm layer. After printing, the 3D hydrogels were immersed in distilled water and washed 3 x 30 min to remove any unlinked macromolecules or photoinitiator. The hydrogels were then stored in PBS (-/-) at 4°C and used within two weeks.

### 1.4. Tissue Chamber Accessory

The tissue chamber was printed as described in the main article with the CAD files provided in the SI files. The transparent chamber lid made from a polycarbonate plate (thickness = 4 mm; Makroclear® from Arla Plast, Borensberg, Sweden) was fabricated by CNC milling with the dimensions shown below including four holes.



The medium reservoir is manufactured from a wide-mouthed, straight-walled polypropylene copolymer container (#10454631, PPCO, Nalgene™, Thermo Scientific™, USA) featuring a screw-on lid, available in various volumes to suit different experimental setups. For our experiments, we utilized the 15 mL container. These translucent containers offer superior chemical resistance and can withstand repeated autoclaving. Three 5.5 mm-diameter holes are drilled into the plastic lid using a drill (#2463977, Bosch Professional GSR 120-LI, Abstatt, Germany) and a drill bit (any brand). Threads (Threaded bit with 1/4" 28 UNF, any brand) are created to accommodate three adapters (for inlet, outlet, and gas exchange). The adapters (#40101, Threaded female luer lock connector; Qosina, Ronkonkoma, USA) are then installed and wrapped with poly(tetrafluoroethylene) (PTFE) tape to enhance sealing. A sterile 0.2 μm PTFE syringe filter (Minisart®, PTFE, 0.2 μm, #SRP15, Sartorius, Göttingen, Germany) is placed on the gas exchange adapter. The other two adapters are connected to tubing for integration into the circuit as described in the main article.

## 2. Material Characterization

### 2.1. dSIS-MA Resin Characterization

The presence of photoreactive groups, the degree of functionalization, and the protein's structural integrity of the dSIS-MA were determined via <sup>1</sup>H NMR spectroscopy, a chromogenic TNBS assay, and circular dichroism (CD) spectroscopy, in accordance with protocols reported previously [4].

## 2.2. Rheology of the dSIS-MA-based Hydrogels

Rheological analysis of the 3D-printed hydrogels was conducted following immersion in Milli-Q water for 24 hours at 4°C, with 2-3 water changes. Mechanical characterization was performed using a Kinexus pro+ oscillating rheometer (Malvern Panalytical) with an 8 mm parallel plate setup, a solvent trap, and a Peltier temperature controller (Anton Paar Physica, Ostfildern, Germany). The linear viscoelastic (LVE) regime was established through amplitude sweeps from 0.1 to 10% strain at 1 Hz, followed by frequency sweeps from 0.1 to 10 Hz at 0.5% strain at 37°C using samples pre-equilibrated in PBS (-/-) for 24 hours. Tests were conducted on three independent samples.

## 2.3. Atomic Force Microscopy (AFM) and Scanning Electron Microscopy (SEM) of dSIS-MA-based hydrogels

Morphology and surface stiffness of the 3D-printed hydrogels were characterized with a NanoWizard4® AFM (JPK Instruments, Berlin, Germany) equipped with a PetriDishHeater™ (JPK Instruments, Berlin, Germany) for *in situ* temperature-controlled measurements. The temperature was set to 37°C throughout the measurement.

To assess the morphology and surface Young's modulus  $E$ , a triangular silicon nitride pyramidal tip attached to a cantilever with a nominal spring constant ( $k$ ) of 0.03 N/m and a tip radius of 20 nm (MLCT-D, Bruker, Mannheim, Germany) was used. Tip calibration and estimation of the spring constant were conducted by the thermal fluctuation method using the simple harmonic oscillator model on a bare petri dish and in PBS (-/-). For the nanoindentation experiments, a  $z$ -length of 3  $\mu\text{m}$ , a speed of 2  $\mu\text{m/s}$ , and a set point of 0.5 nN were used to ensure a very gentle indentation. Controlled deformations were applied to the samples and the compressive feedback forces were measured through cantilever deflection. Force-displacement ( $F$ - $z$ ) curves were produced by translating cantilever deflection ( $d$ ) into force ( $F$ ) by means of  $F = \frac{1}{4} kd$ , where  $k$  is the cantilever spring constant. The Young's modulus of the probed material was calculated by fitting the contact part of the measured approach force curves to a standard Sneddon model for a pyramidal indenter (tip) with a Poisson's ratio of 0.5. The measurements were operated in force spectroscopy contact mode, wherein an array  $6 \times 6$  (36 points) of force-distance ( $F$ - $z$ ) curves was collected over the entire scan area of  $40 \times 40 \mu\text{m}$ . Morphological images of the samples were

obtained with the same cantilever in quantitative imaging mode (QI) using a set point of 0.5 V and a z-length between 1-2  $\mu\text{m}$  scanning a 40 x 40  $\mu\text{m}$  area of the hydrogel pixel-per-pixel.

SEM imaging was performed to visualize the inner and outer micro-architecture of 3D-printed hydrogel samples after lyophilization following our published procedure [4].

#### 2.4. Human Crypt Isolation and Organoid Culture

Human intestinal crypts were harvested from the mucosa of the terminal ileum procured from endoscopic biopsies of healthy individual volunteers. The biopsies were repeatedly rinsed in cold PBS (-/-) until the supernatant cleared, then incubated in a chelating buffer (cf section 1.1) for 45 minutes on ice with gentle agitation. After removing the chelating buffer, crypts were liberated by vortexing the biopsies for 30 seconds in 10 ml of a modified chelating buffer without EDTA, DTT, and antibiotics. This vortexing step was repeated with fresh buffer three times to maximize crypt yield, with the resulting crypt-containing supernatants pooled and concentrated by centrifugation at 300 x g, 4°C for 5 minutes. The crypts were then washed thrice through centrifugation (400 x g, 4°C for 5 minutes) in basal medium (see section 1.1), resuspended in Matrigel™ diluted with basal medium (1:1 ratio), and plated in 50  $\mu\text{l}$  droplets into a pre-warmed 24-well plate corresponding to ~100 crypts per well. The plates were first flipped upside-down, followed by a 20-minute Matrigel™ solidification at 37°C. Subsequently, the wells were supplemented with WRN-conditioned medium (expansion medium; see section 1.1) containing an initial supplement of 10  $\mu\text{M}$  Y-27632 (RI) for the first two days. The medium was refreshed every 2-3 days with expansion medium without the RI supplement, and organoids were passaged weekly at a 1:6 ratio. For passaging, organoid-containing Matrigel™ domes were mechanically removed with a pipette tip from 12 wells of a 24-well plate, collectively placed into a 15 ml tube and supplemented with 6 ml cold basal medium (6 mL). Suspended organoids were then concentrated by centrifugation at 300 x g for 5 minutes at 4°C. After supernatant removal, the organoid pellet was enzymatically dissociated with 1.3 mL TrypLE™ supplemented with RI (10  $\mu\text{M}$ ) for 5 minutes at 37°C and subsequently subjected to mechanical disruption by expelling the solution through a blunt 18 G needle (10-20 times). The isolated cell pellet obtained after centrifugation (300 x g; 4°C; 5 min) was rinsed in cold basal medium (1 mL) and centrifuged once more (400 x g; 4°C; 5 min). After centrifugation and removal of the supernatant, the cells were resuspended in cold PCM medium (final density:  $5 \times 10^5$  cells/mL) and mixed with

Matrigel™ at a 1:1 ratio. The suspension was then placed as 50 µL domes per well into a pre-warmed 24-well plate with a flat bottom ( $2.5 \times 10^5$  cells/mL or  $12.5 \times 10^3$  cells per Matrigel™ dome), left for 3 min at 37°C before being flipped upside-down for 20-30 min 37°C to fully solidify the Matrigel™. Next, 500 µL expansion medium is added per well with medium change every 2-3 days. Human terminal ileum-derived organoids of passage numbers 7 to 12 were used for the experiments.

## 2.5. Real-time Quantitative Polymerase Chain Reaction (RT-qPCR) Analysis

*Sample preparation and RNA extraction:* Cell culture medium was aspirated, and cellularized hydrogel scaffolds were gently rinsed with PBS (-/-) without disturbing the monolayer integrity. Subsequently, the cell-seeded scaffolds were placed into 1.5 ml Eppendorf tubes, lysed with TRIzol™ reagent (300 µl) and conserved at -80°C for later RNA extraction. RNA isolation was performed using Direct-zol RNA Microprep kit, according to the manufacturer's instructions. The isolated RNA was reconstituted in RNase-free water and maintained at -80°C. RNA purity and concentration were assessed using a NanoDrop™2000c spectrophotometer (Thermo Scientific™, USA).

*Synthesis of cDNA from RNA and real-time quantitative PCR:* To synthesize cDNA from RNA, 250 ng of RNA was first diluted in RNase-free water (10 µl). The solution underwent DNase I treatment (1 U) for 15 minutes at 22°C, which was subsequently inactivated with EDTA (25 mM) over 10 minutes at 65°C. The addition of Oligo(dT)<sub>12-18</sub> primers (12.5 ng/ml), dNTPs (10 mM), and supplemental water brought the volume to 40 µl, which was then incubated at 65°C for 5 minutes to allow primer annealing. Afterwards, RNaseOUT™ recombinant ribonuclease inhibitor (20 U) and DTT (10 mM) were introduced, followed by the addition of M-MLV reverse transcriptase (250 U) in first-strand buffer, with incubation periods of 50 minutes at 37°C and 15 minutes at 70°C, respectively. Post-reaction, samples were stored at 4°C.

For the qPCR analysis, 1 µl of the resulting cDNA was diluted with nuclease-free water, mixed with specific forward and reverse primers (**Table S2**), and SYBR™ Green PCR Master Mix according to the manufacturer's specifications. This reaction mixture was then placed into a MicroAmp™ fast optical 96-well reaction plate for processing in a StepOnePlus® real-time PCR system (Applied Biosystems, Thermo Fisher Scientific, USA), following these parameters: an initial denaturation at 95°C for 600 seconds, followed by 40 cycles of amplification (denaturation

at 95°C for 15 seconds, and annealing/extension at 62°C for 60 seconds each cycle). The specificity of amplification was confirmed through melting curve analysis. Relative gene expression was quantified using the expression of glyceraldehyde-3-phosphate dehydrogenase (GAPDH) as a reference gene, employing established comparative threshold cycle (Ct) methods.

## 2.6. DNA Content Quantification

To analyze the DNA content, 100 µL of the cell lysate was combined with PicoGreen™ working reagent from the Quant-iT™ PicoGreen™ dsDNA assay kit. Following a 5-minute incubation, the fluorescence was assessed using a microplate reader set to excitation/emission wavelengths of 480/520 nm. These fluorescence readings were then aligned against a standard dsDNA curve, facilitating the quantification of dsDNA content within each sample.

## 2.7. Immunofluorescence Staining

On predetermined days, epithelial cells from dynamic and static cultures were fixed after washing them twice with PBS (-/-) by incubation in 4% paraformaldehyde (PFA) at room temperature (RT) or cold methanol at 4°C for 10 minutes. Fixed cells were washed twice with PBS (-/-) and stored at 4°C until staining. For immunostaining, cells were permeabilized with 0.1% Triton X-100 for 10 minutes, blocked with 1% w/v BSA in 0.05% v/v Tween-20/PBS (-/-) for 1 hour and then incubated with primary antibodies for 1.5 hours. Afterward, secondary antibodies were applied for 30 minutes at RT in the dark. The specific primary and secondary antibodies utilized are listed in Table S1, including their dilutions in antibody buffer (1% w/v BSA in 0.05% v/v Tween-20/PBS (-/-)). Nuclei and actin filaments were stained with Hoechst 33342 (10 µg·mL<sup>-1</sup>) for 10 minutes and phalloidin-Atto®647 for 15 minutes in the dark, respectively. Following staining, samples were mounted and imaged with a confocal microscope (LSM800, Carl Zeiss, Jena, Germany) equipped with the Zen Blue software (v2.6, Carl Zeiss, Jena, Germany). 10x and 25x objectives (#420340-9901-000 EC Plan-Neofluar 10x/0.3 M27 and #420852-9871-000 LD LCI Plan-Apochromat 25x/0.8 Imm Corr DIC M27) were used for confocal imaging in one plane, while z-stacked 3D images were taken with the 10x objective with a slice thickness of 5-6 µm. Cells cultured on membranes were imaged on the membrane, while cells cultured on thick hydrogel samples ( $h = 1$  mm) were flipped upside down for better image quality.



### 3. Supplementary Tables and Figures

**Table S1.** List of antibodies used in immunofluorescence staining.

Primary antibodies						
Antibodies	ID	Company	Clonality	Host	Dilution	Fixation
OLFM-4	AB85046	Abcam	Polyclonal	Rabbit	1:200	4% PFA
LGR5	AB273092	Abcam	Monoclonal	Mouse	1:200	4% PFA
Lysozyme	BS-0816R	Bioss	Polyclonal	Rabbit	1:200	4% PFA
Villin	PA5-29078	Invitrogen	Polyclonal	Rabbit	1:100	4% PFA
Chromogranin A	LK2H10	Invitrogen	Monoclonal	Mouse	1:200	4% PFA
MUC2	ABIN2854828	Antibodies	Polyclonal	Rabbit	1:200	4% PFA
MUC5AC	MA5-12178	Invitrogen	Monoclonal	Mouse	1:200	4% PFA
CD324	14-3249-82/DECMA-1	Invitrogen/e-bioscience	Monoclonal	Rabbit	1:100	4% PFA
KI-67	41-5698-80/SolA15	Invitrogen/e-bioscience	Monoclonal	Rabbit	1:200	4% PFA
ZO-1	40-2200	Invitrogen	Polyclonal	Rabbit	1:250	Cold Methanol
Secondary antibodies						
Goat anti-rabbit Alexa 647	A-21245	Invitrogen	Polyclonal	Rabbit	1:500	--
Goat anti-mouse Alexa 488	A-11001	Invitrogen	Polyclonal	Mouse	1:500	--

**Table S2.** Primers used in RT-qPCR analysis.

Gene		Sequence 5' – 3'
GAPDH	Forward	ACCCACTCCTCCACCTTTGAC
	Reverse	TGTTGCTGTAGCCAAATTCGTT
LGR5	Forward	GCGGGAAACGCTCTGACATA
	Reverse	CATCCAGACGCAGGGATTGA
ALPI	Forward	CATCCAGAAGGTCGCCAAGA
	Reverse	TGCCATTCTTCTGCCCTTT
LYZ	Forward	GCCAAATGGGAGAGTGGTTA
	Reverse	TAACTGCTCCTGGGGTTTTG

MUC2	Forward	CAGAGGGCAGAACCCGAAAC
	Reverse	GAAGTTGTAGTCGCAGGGGC
CHGA	Forward	CTACGCGCCTTGTCTCCTAC
	Reverse	GCTGCCTGTGTTTCAGAGAAG
MUC17	Forward	TGGGAGTGAGGAGATCCCAG
	Reverse	CGGGGCTTGTTCCTGTACT
TFF3	Forward	TCCACCCGAGGACAGTTCTT
	Reverse	AGGGAGTCTTTTCCTGCCCT
MUC5B	Forward	GGCTGTTTCAGCACACACTG
	Reverse	CTTGTAGGTGGCCTCGTTGT
SI	Forward	TTTGGCAGCCTTATCCAAGTC
	Reverse	ACAGCAGGTGTCTTAGTTGCT
OLFM4	Forward	AAATGCTCGAGAGTTGCGGA
	Reverse	CACAGCAATCGTGTTGGTGG
MUC5AC	Forward	TATGTGCTGACCAAGCCCTG
	Reverse	TTGATCACCACCACCGTCTG

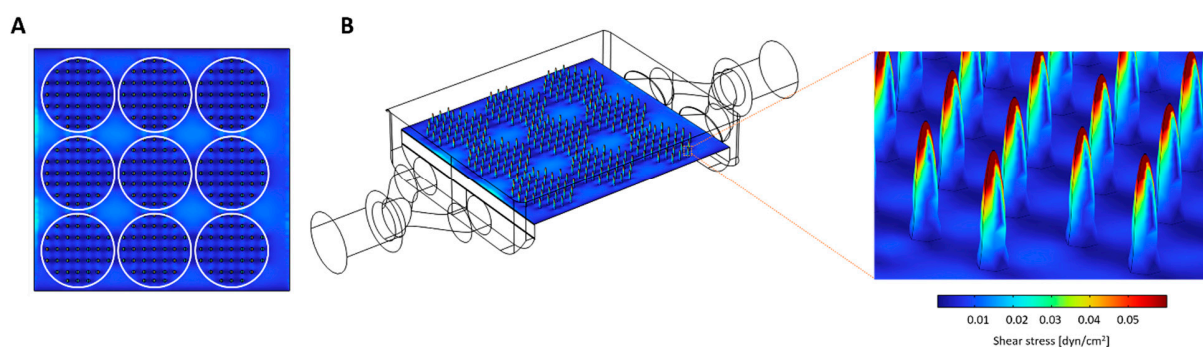


**Figure S1.** CFD simulation of 3D villi-structured hydrogels inserted into the designed hydrogel-integrated millifluidic tissue chamber at a defined medium flow rate of 1.42 mL/min. The color gradient illustrates the shear stress distribution on the 3D structured hydrogel scaffolds made of 1.5% dSIS-MA. The modeled villi have a height of 1 mm and a diameter ranging from 0.28 mm at the base to 0.03 mm at the tip [2]. **(A)** An xy projection of the hydrogel-integrated flow channel shows a consistent laminar shear stress distribution of approximately 0.01 dyne/cm<sup>2</sup> across the surface. **(B)** An xyz projection provides a closer look at the shear stress gradient along the villi, with shear stress values starting from  $\leq 0.01$  dyne/cm<sup>2</sup> at their base and increasing to  $\geq 0.06$  dyne/cm<sup>2</sup> at their tips.

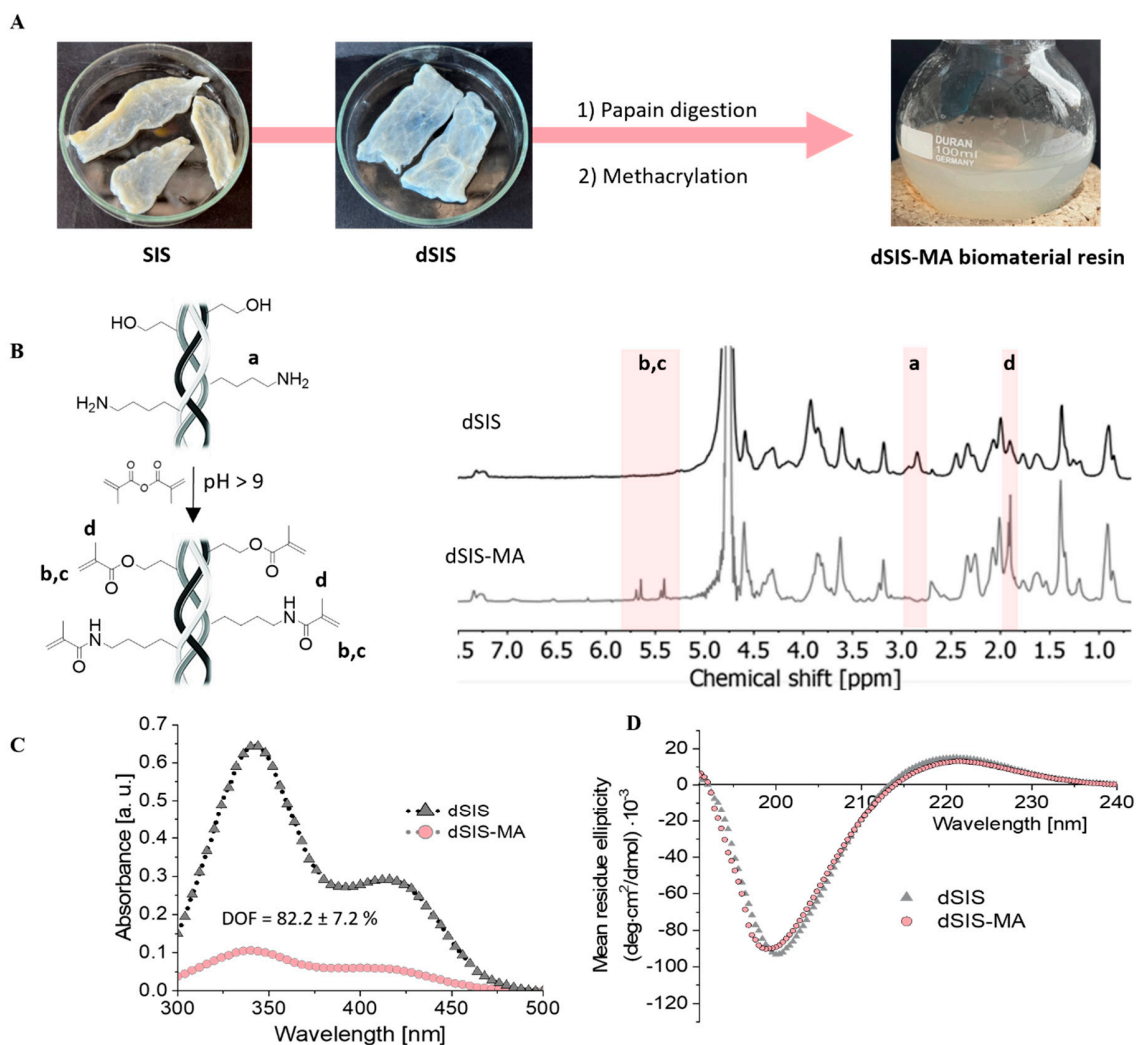


**Figure S2.** Processing, modification, and characterization of dSIS-MA biomaterial resins for vat photopolymerization-based 3D printing of intestinal tissue hydrogels. **(A)** Photographic illustration of the processing of porcine SIS via decellularization to dSIS, enzymatic solubilization with papain, and subsequent chemical modification to obtain dSIS-MA resins. **(B)** Schematic illustration of methacrylation with methacrylic anhydride under aqueous basic conditions and comparative representative <sup>1</sup>H NMR spectra indicating the successful modification via the new signals attributed to the double bond (b,c) and the methyl group (d) as well as the vanishing methylene group signal (a) next to the free amino group. **(C)** Representative UV absorbance spectra of dSIS and dSIS-MA after reaction of their primary amino groups with the chromogenic reagent 2,4,6-trinitrobenzene sulfonic acid (TNBS) indicating a minimum degree of functionalization (DOF) with photocrosslinkable methacryloyl groups in dSIS-MA of around 82%

( $n=3$  of independent samples). **(D)** Representative CD spectra of digested dSIS and dSIS-MA indicating the preserved structural integrity of the proteins in dSIS-MA.

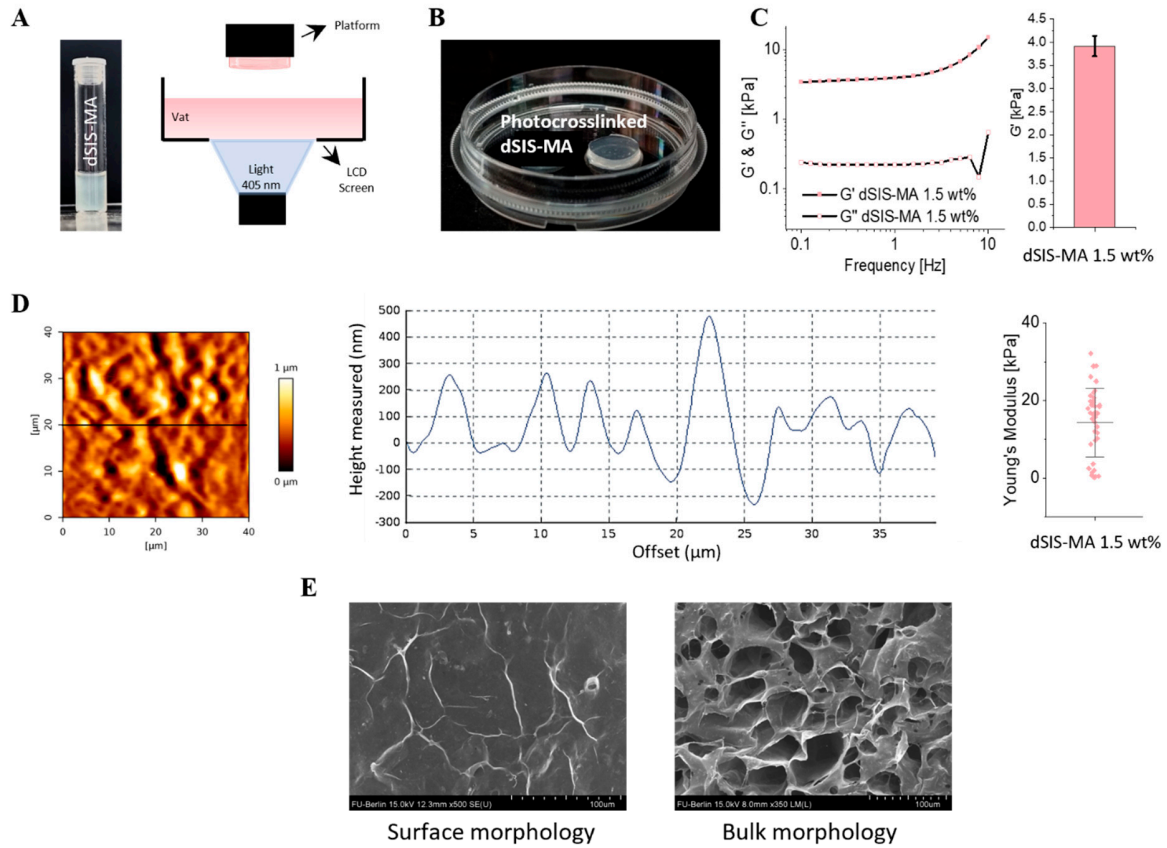


**Figure S3.** Characterization of printed dSIS-MA (1.5 wt%) hydrogels. **(A)** Photograph of the dSIS-MA (1.5 wt%) resin formulation and schematic illustration of the vat photopolymerization-based 3D printing process. **(B)** Photograph of the resulting flat and transparent printed hydrogel scaffold equilibrated in PBS (-/-) ( $d = 6$  mm and  $h = 1$  mm). **(C)** Representative storage and loss moduli  $G'$  and  $G''$  of the printed hydrogel (dSIS-MA 1.5 wt%) as a function of frequency and derived stiffness of the gels at 1 Hz ( $n = 3$ , mean  $\pm$  SD). **(D)** Surface topography, cross-section, and surface stiffness (Young's modulus) of the dSIS-MA (1.5 wt%) hydrogels accessed via AFM imaging in QI mode and nanoindentation, respectively ( $n=2$ , mean  $\pm$  SD). **(E)** Surface and bulk morphology of the printed flat dSIS-MA (1.5 wt%) hydrogels via SEM imaging ( $n=2$ ).

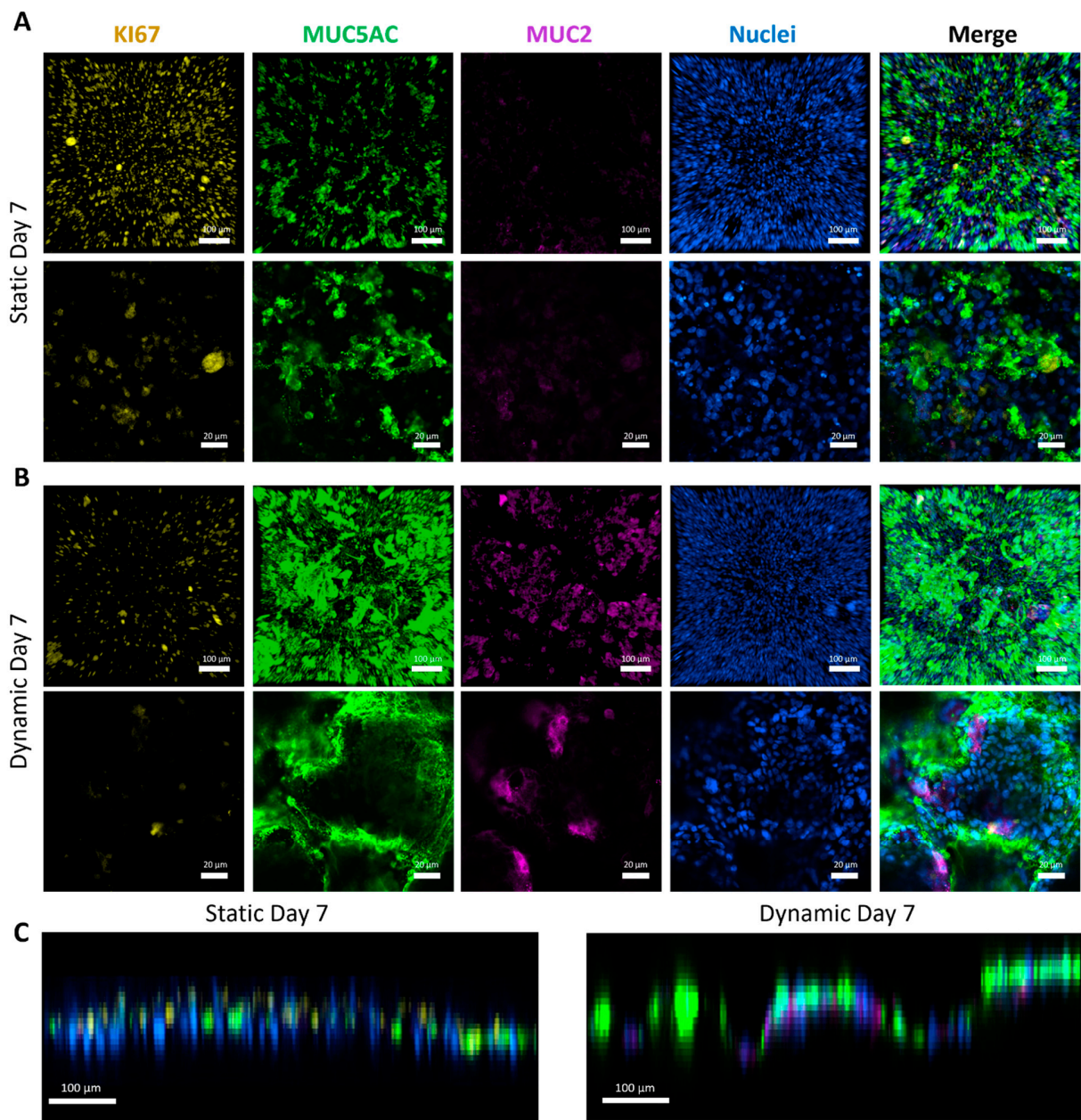


**Figure S4.** (A) Representative confocal fluorescence microscopy images of HT29-MTX cells cultured statically on dSIS-MA (1.5 wt%) hydrogels for 7 days post-confluency. Immunofluorescence staining for KI-67 (yellow) indicates cell proliferation, MUC5AC (green) and MUC2 (purple) indicate mucins, and Hoechst 33342 staining indicates cell nuclei (blue). Top panel: *xy* projection of *z*-stack images; Bottom panel: higher magnification 2D images. (B) Representative confocal fluorescence microscopy images of HT29-MTX cells cultured under dynamic conditions (shear stress: 0.01 dyn/cm<sup>2</sup>), stained and imaged with identical settings as

shown in A. (C) Side projections ( $xz/yz$ ) of  $z$ -stacks from A and B. Representative images of three independent runs ( $n = 3$ ) are shown.

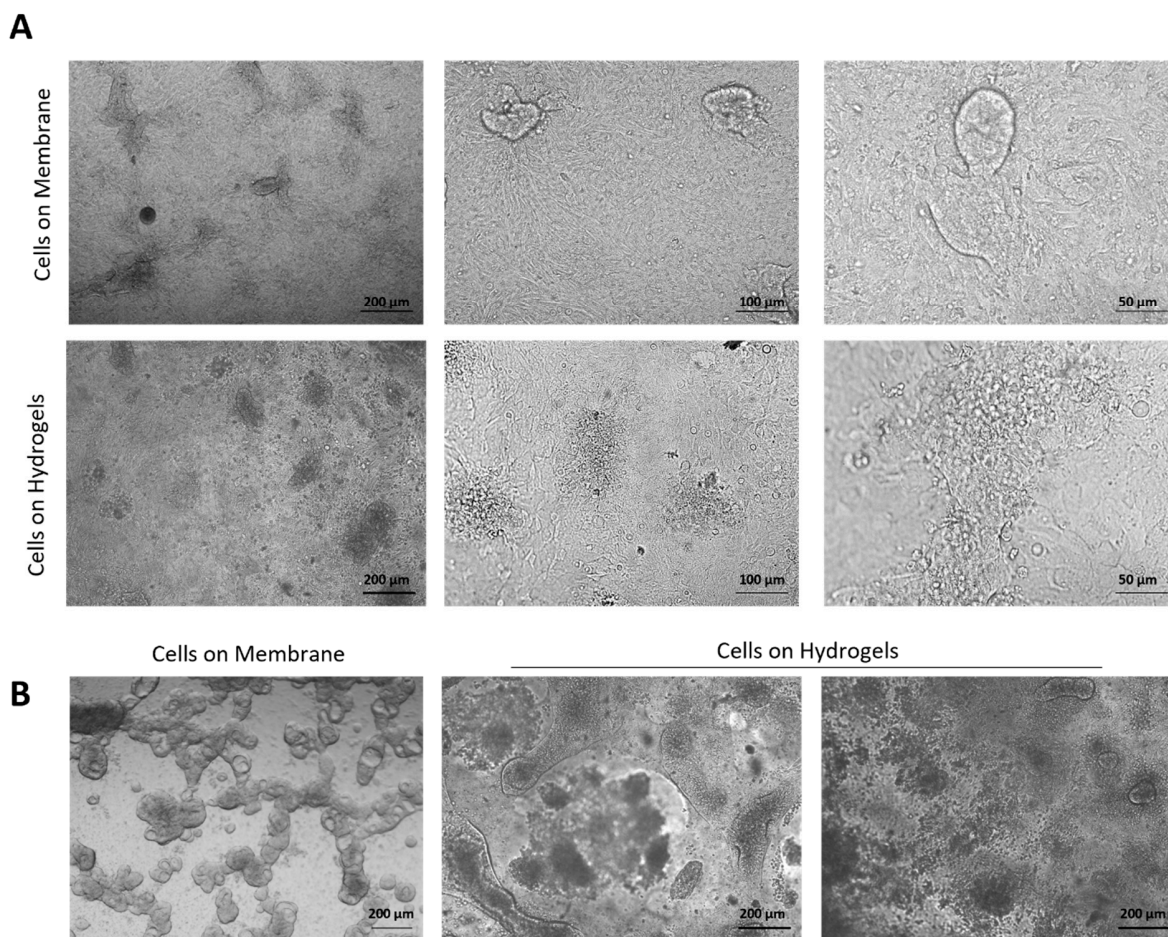


**Figure S5.** Representative phase contrast images of cell monolayers of human organoid-derived ISCs from the terminal ileum cultured statically in expansion medium on insert membranes coated with a thin film of Matrigel<sup>TM</sup> and bulk uncoated dSIS-MA (1.5 wt%) hydrogel scaffolds. (A) Intact ISC monolayers imaged in three magnifications after reaching confluency (Day 0). (B) Exemplary images of culture trials on membrane and hydrogel, which did not yield fully confluent monolayers due to limited ISC proliferation even after extended culture periods, resulting in areas devoid of cells or cell debris. Such unsuccessful seedings in our hands comprise up to 40% of all trials.

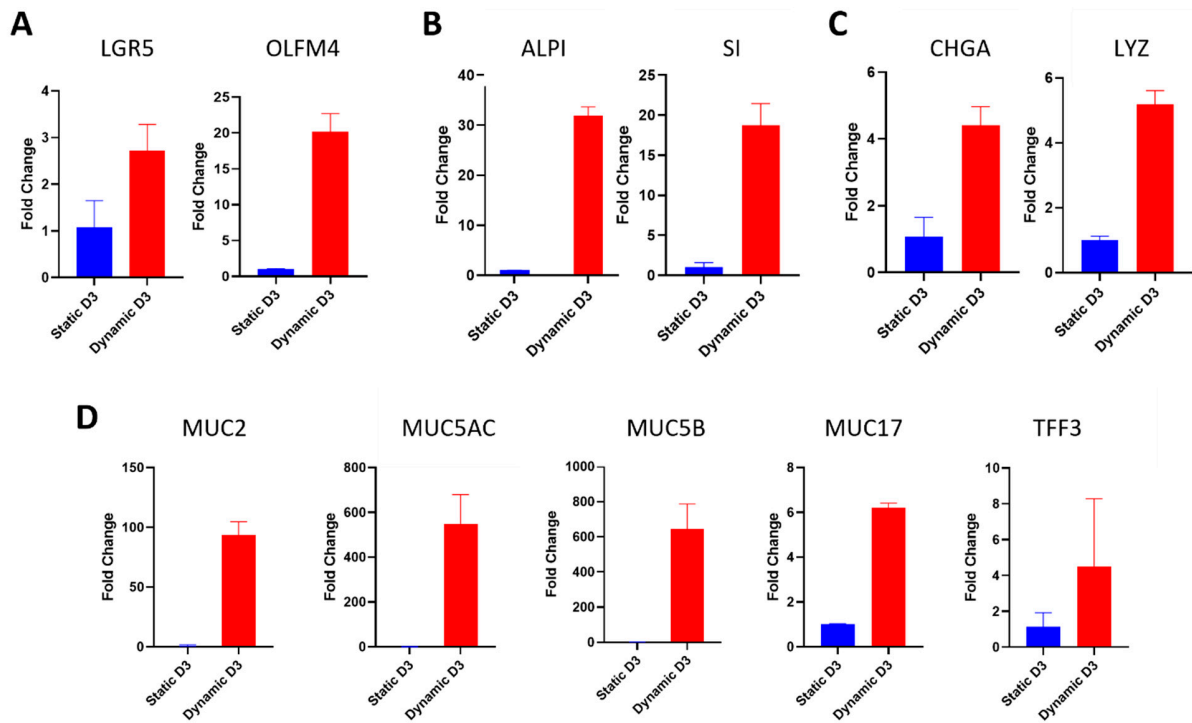


**Figure S6.** Quantitative RT-qPCR analysis of cells cultured on hydrogels in expansion medium under static and dynamic conditions assessed on Day 3 post-confluency showing the fold-change in transcript levels of (A) stem (LGR5) and progenitor (OLFM4) markers; (B) markers specific to enterocytes, namely alkaline phosphatase (ALPI) and sucrose-isomaltase (SI); (C) markers for enteroendocrine and Paneth cells, chromogranin A (CHRA) and lysozyme (LYZ), respectively; and (D) goblet cell markers MUC2, MUC5AC, MUC5B, MUC17, and TFF3. Data are presented as mean  $\pm$  SD for  $n = 2$  independent samples.

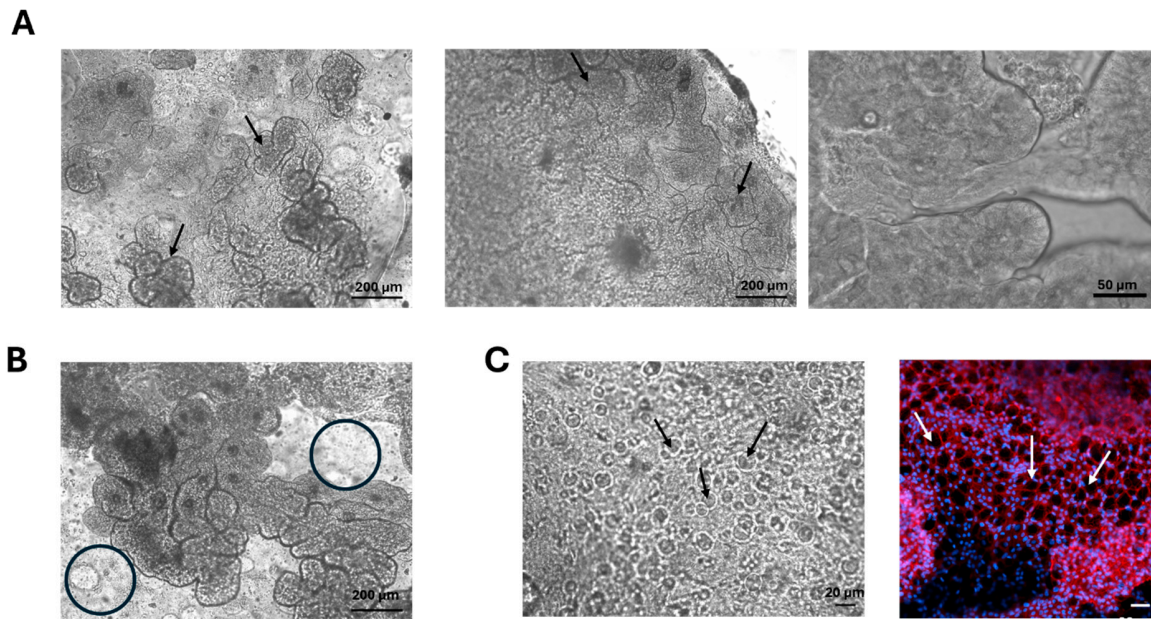


**Figure S7.** Representative images of monolayers of human organoid-derived ISCs from the terminal ileum on dSIS-MA (1.5 wt%) hydrogels cultured in expansion medium and transferred to dynamic conditions for 5-7 days after reaching confluency. (A) Phase contrast images of intact cell layers with 3D villi-like protrusions (indicated by arrows), covering the entire surface of the hydrogel in different magnifications as predominantly observed. (B) Phase contrast images of cell layers with partial villi displacement, likely due to flow dynamics combined with diminished cell-hydrogel adhesion (indicated by circles) as rarely observed. (C) Rarely observed phase contrast and fluorescent images of comparably flat cell layers comprising a pore-like pattern ('pores' indicated by arrows) with representative fluorescent ZO-1 staining of such epithelial layers.



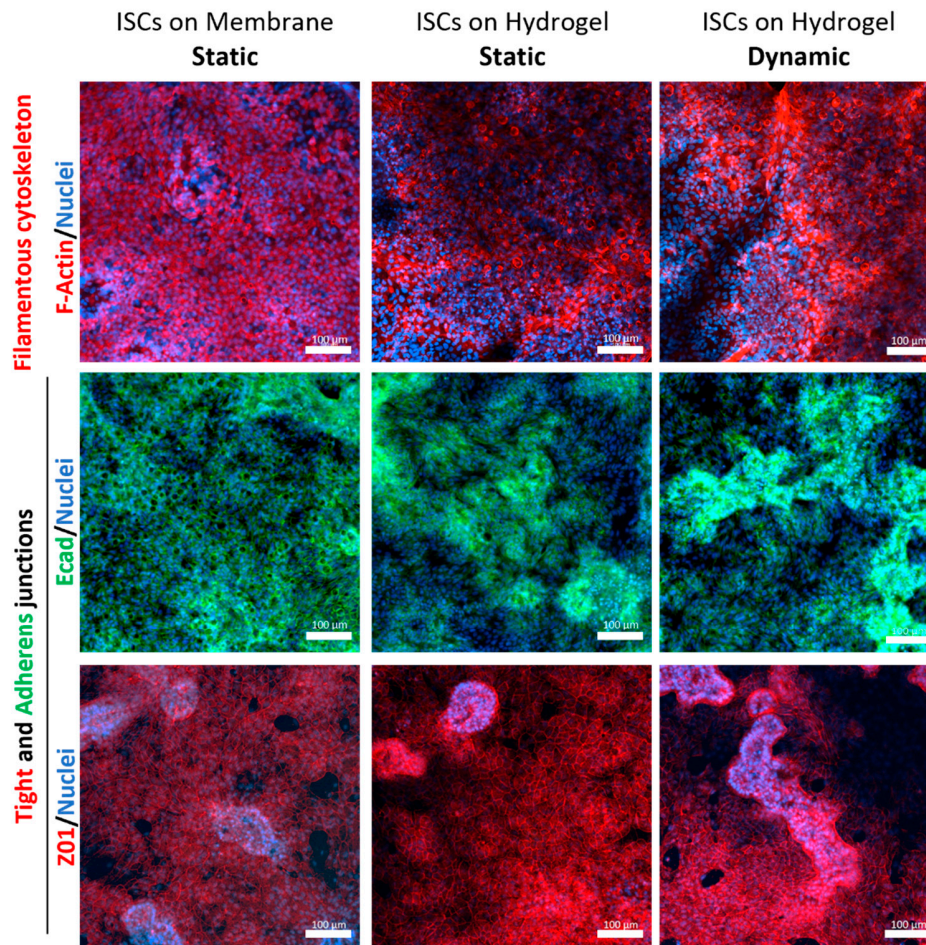


**Figure S8.** Representative z-stacks of confocal fluorescence microscopy images of ISCs cultured on insert membranes and dSIS-MA hydrogels (1.5 wt%) statically or dynamically in expansion medium for 5-7 days after reaching confluency. IF staining of F-Actin (red), E-cadherin (green), and ZO-1 (red) indicates filamentous cytoskeleton as well as adherens and tight junctions with nuclei counterstaining (blue).



**Figure S9.** Photographs of 3D-printed dSIS-MA (1.5 wt%) hydrogel scaffolds before (left side) and after (right side) incubation with alcian blue (AB) and periodic Schiff-base (PAS) reagents

and subsequent water changes illustrating a significant AB and PAS background staining of dECM-based hydrogels.

#### 4. Controller-Board Assembly and Pump Programming

##### 4.1. Assembly of the Arduino Board to Control the Pump System

The following controller board-related pieces are purchased and assembled in the following order as illustrated in **Figure S11**:

- A) First, the Arduino Uno microcontroller board based on the ATmega328P (Arduino Uno Rev 3, Arduino S.r.l, Monza, Italy) is assembled: The CNC shield V3 development board is attached (SIMAC Electronics GmbH, Neukirchen-Vluyn, Germany) for A4988 stepper drivers to control up to four stepper motors.
- B) Next, the jumper pins (RM 2.54, BKL Electronic, Lüdenscheid, Germany) on the CNC shield are inserted to configure the X, Y, Z, and A axes for the pump stepper motors following Table S3.

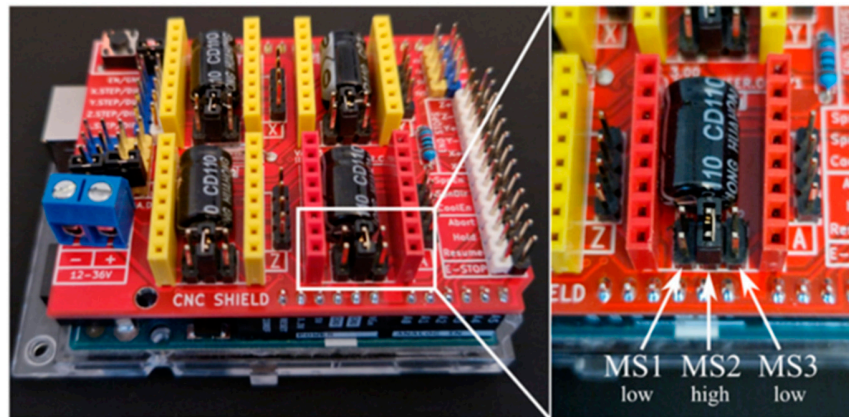
*Table S3. Jumper pins configuration of the X,Y,Z, and A axes for the step motors.*

Axis	Definition (pins)
X	AccelStepper Xaxis(1, 2, 5)
Y	AccelStepper Yaxis(1, 3, 6)
Z	AccelStepper Zaxis(1, 4, 7)
A	AccelStepper Aaxis(1, 12, 13)

The motors are set to operate in quarter-step mode using the jumper pins attached to MS1-MS3 positions, balancing smoothness and torque, as outlined in the Table in **Figure S10** for standard micro-stepping.

**A**

Mode	MS1	MS2	MS3
Full step	Low	Low	Low
Half step	High	Low	Low
Quarter step	Low	High	Low
Eighth step	High	High	Low
Sixteenth step	High	High	High

**B**

**Figure S10.** (A) Table of the settings for different configuration modes of standard microstepping and (B) a photograph of the operational quarter step mode set on our board.

- C) Then, four carriers for A4988 stepper motor drivers are placed onto the CNC Shield (A4988, Pololu Robotics and Electronics, Las Vegas, NV/USA). 4-PIN Dupont cables (any brand) are used to connect the pump to the stepper motor drivers.

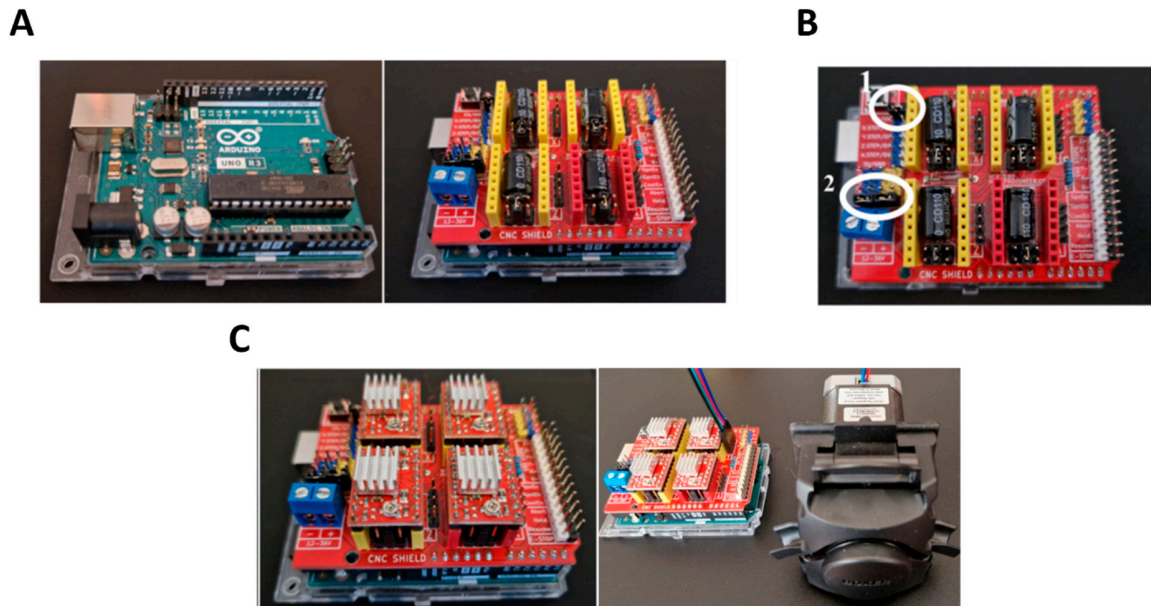


**Figure S11.** Step-by-step assembly of the Arduino-controlled pump system

The microcontroller can be powered via a normal USB cable (connected to a laptop or USB power adapter) or with a universal power supply (7-12 V, 1 A, plug: 5.5 x 2.1 mm).

Finally, before use, the reference voltage ( $V_{ref}$ ) of the motor driver has to be adjusted based on the stepper motor's rated current and the stepper driver's sense resistor to prevent overheating or insufficient torque.

#### 4.2. Arduino Software and Programming

##### A) Software installation and configuration

1. The free version of the Arduino IDE is installed from the official website (<https://www.arduino.cc/>) to write the script (sketch), which is intended to be operated by the microcontroller.
2. Within the IDE software, the AccelStepper library (<https://www.arduino.cc/>) has to be installed to manage the stepper motor control.
3. The provided sketch (see below) has to be loaded into the Arduino programming interface.
4. Finally, the revolutions per minute (RPM) settings must be fine-tuned for each axis to calibrate the desired flow rates.

##### B) Sketch (programming)

```

#include <AccelStepper.h>
// 1 min = 60000
// 5 min = 300000
// 10 min = 600000
// 15 min = 900000
// 30 min = 1800000
// 45 min = 2700000
// 60 min = 3600000
float RPMXaxis = 12.; // speed of Pump connected to X-Axis
float maxStepsX = 1.; // number of steps for pump-speed increase; no
acceleration for a value of 1
unsigned long intervalLengthX = 1000; //in milliseconds, see above

float RPMYaxis = 12.; // speed of Pump connected to Y-Axis
float maxStepsY = 1.; // number of steps for pump-speed increase; no
acceleration for a value of 1; for example with 3 steps and 45 RPM: 1st
intervall runs with 15, 2nd with 30 and 3rd/final with 45 RPM.
unsigned long intervalLengthY = 10000; //in milliseconds, see above

float RPMZaxis = 12.; // speed of Pump connected to Z-Axis
float maxStepsZ = 1.; // number of steps for pump-speed increase; no
acceleration for a value of 1
unsigned long intervalLengthZ = 1000; //in milliseconds, see above

float RPMAaxis = 12.; // speed of Pump connected to A-Axis
float maxStepsA = 1.; // number of steps for pump-speed increase; no
acceleration for a value of 1; for example with 3 steps and 45 RPM: 1st
intervall runs with 15, 2nd with 30 and 3rd/final with 45 RPM.
unsigned long intervalLengthA = 10000; //in milliseconds, see above

//Do not change anything below this!!!

unsigned long delayStart = 0; // the time the delay started
// unsigned long currentStep = 0;

boolean doCalculationX = true;
boolean doCalculationY = true;
boolean doCalculationZ = true;
boolean doCalculationA = true;

//int displayX;
//int displayY;
//int displayZ;
//int displayA = 1;

// int led = 13; // not important for operation

AccelStepper Xaxis(1, 2, 5); // pin 2 = step, pin 5 = direction
AccelStepper Yaxis(1, 3, 6); // pin 3 = step, pin 6 = direction
AccelStepper Zaxis(1, 4, 7); // pin 2 = step, pin 5 = direction
AccelStepper Aaxis(1, 12, 13); // pin 3 = step, pin 6 = direction

```

```

void setup() {
// pinMode(led, OUTPUT); // initialize the digital pin as an output.
// digitalWrite(led, HIGH); // turn led on

delayStart = millis(); // start delay
Xaxis.setMaxSpeed(1000.0);
Yaxis.setMaxSpeed(1000.0);
Zaxis.setMaxSpeed(1000.0);
Aaxis.setMaxSpeed(1000.0);

// Serial.begin(9600);
// pinMode(10, INPUT_PULLUP);
// pinMode(11, INPUT_PULLUP);
}
void loop() {

    if (doCalculationX) {
        unsigned long timeElapsed = millis() - delayStart;
        int intervalCountX = timeElapsed / intervalLengthX;
        if (intervalCountX < (maxStepsX - 1)) {
            Xaxis.setSpeed(RPMXaxis * 4 * (200. / 60.) * (intervalCountX + 1)
/ maxStepsX);
        } else {
            Xaxis.setSpeed(RPMXaxis * 4 * (200. / 60.));
            doCalculationX = false;
        }
    }
    if (doCalculationY) {
        unsigned long timeElapsed = millis() - delayStart;
        int intervalCountY = timeElapsed / intervalLengthY;

        if (intervalCountY < (maxStepsY - 1)) {
            Yaxis.setSpeed(RPMYaxis * 4 * (200. / 60.) * (intervalCountY + 1)
/ maxStepsY);
        } else {
            Yaxis.setSpeed(RPMYaxis * 4 * (200. / 60.));
            doCalculationY = false;
        }
    }
    if (doCalculationZ) {
        unsigned long timeElapsed = millis() - delayStart;
        int intervalCountZ = timeElapsed / intervalLengthZ;
        if (intervalCountZ < (maxStepsZ - 1)) {
            Zaxis.setSpeed(RPMZaxis * 4 * (200. / 60.) * (intervalCountZ + 1)
/ maxStepsZ);
        } else {
            Zaxis.setSpeed(RPMZaxis * 4 * (200. / 60.));
            doCalculationZ = false;
        }
    }
    if (doCalculationA) {
        unsigned long timeElapsed = millis() - delayStart;

```

```

    int intervalCountA = timeElapsed / intervalLengthA;

    if (intervalCountA < (maxStepsA - 1)) {
        Aaxis.setSpeed(RPMAaxis * 4 * (200. / 60.) * (intervalCountA + 1)
/ maxStepsA);
        //displayA = (RPMAaxis * 4 * (intervalCountA + 1) / maxStepsA);

    } else {
        Aaxis.setSpeed(RPMAaxis * 4 * (200. / 60.));
        doCalculationA = false;
    }
}

Xaxis.runSpeed();
Yaxis.runSpeed();
Zaxis.runSpeed();
Aaxis.runSpeed();
}

```

## References

1. Fairbanks, B.D.; Schwartz, M.P.; Bowman, C.N.; Anseth, K.S. Photoinitiated Polymerization of Peg-Diacrylate with Lithium Phenyl-2,4,6-Trimethylbenzoylphosphinate: Polymerization Rate and Cytocompatibility. *Biomaterials* **2009**, *30*, 6702-6707, doi:10.1016/j.biomaterials.2009.08.055.
2. Elomaa, L.; Gerbeth, L.; Almalla, A.; Fribicz, N.; Daneshgar, A.; Tang, P.; Hillebrandt, K.H.; Seiffert, S.; Sauer, M.I.; Siegmund, B.; et al. Bioactive Photocrosslinkable Resin Solely Based on Refined Decellularized Small Intestine Submucosa for Vat Photopolymerization of in Vitro Tissue Mimics. *Addit Manuf* **2023**, *64*, 103439, doi:10.1016/j.addma.2023.103439.
3. Almalla, A.; Elomaa, L.; Bechtella, L.; Daneshgar, A.; Yavvari, P.; Mahfouz, Z.; Tang, P.; Kokschi, B.; Sauer, I.; Pagel, K.; et al. Papain-Based Solubilization of Decellularized Extracellular Matrix for the Preparation of Bioactive, Thermosensitive Pregel. *Biomacromolecules* **2023**, *24*, 5620-5637, doi:10.1021/acs.biomac.3c00602.
4. Almalla, A.; Elomaa, L.; Fribicz, N.; Landes, T.; Tang, P.; Mahfouz, Z.; Kokschi, B.; Hillebrandt, K.H.; Sauer, I.M.; Heinemann, D.; et al. Chemistry Matters: A Side-by-Side Comparison of Two Chemically Distinct Methacryloylated Decm Bioresins for Vat Photopolymerization. *Biomaterials Advances* **2024**, *160*, doi:10.1016/j.bioadv.2024.213850.

## 5. SHORT SUMMARY

This thesis advances the field of bioprinting and tissue modeling by addressing the limitations of current processing protocols for dECM-based bioresins. It explores effective enzymes for thermogelling dECM pre-gels, investigates the grafting of different methacryloylated groups on dECM for vat 3D bioprinting, and uses 3D printing to fabricate advanced dynamic culture systems that apply mechanical shear stress on epithelial cells to develop advanced in vitro tissue models.

Precise control over the physical, mechanical, and biochemical properties of dECM hydrogels after solubilization and gelation is crucial for their application. While animal-derived pepsin is traditionally used for solubilization of dECM, in our first study, we investigated various non-animal-based alternatives, including plant-derived papain, bacterial-based collagenase, and  $\alpha$ -amylase. Although  $\alpha$ -amylase-digested dECM exhibited the highest content of growth factors and cytokines, both  $\alpha$ -amylase and collagenase treatments disrupted collagen self-assembly of dECM digests and compromised the protein structural integrity. Moreover, their insufficient digestion efficiency resulted in significantly reduced yields of dECM digests ( $\sim 7 - 10\%$ ). In contrast, papain preserved the physical gel formation capacity of digested dECM and demonstrated comparable yields ( $\sim 79-86\%$ ), thermo-gelation kinetics, and bulk mechanical properties to pepsin, along with increased amounts of retained growth factors and superior cell adhesion. As a conclusion, papain was found to be a cost-effective and reproducible alternative to pepsin for producing liver-derived dECM hydrogels, eliminating the risk for zoonotic disease transmission.

The second study covered functionalization of papain-digested liver dECM with glycidyl methacrylate (dECM-GMA) and methacrylic anhydride (dECM-MA) into photoactive bioresins for vat photopolymerization. Both chemical modifications yielded a comparable degree of functionalization (DOF  $\sim 81.5 - 83.5\%$ ) without disrupting the dECM structure. Interestingly, dECM-GMA showed enhanced solubility and higher shear viscosity compared to dECM-MA due to the additional hydroxyl groups and the increased hydrogen bonding. When formulated into resins, both modifications yielded a similar degree of photocrosslinking ( $30 - 60\%$ , depending on the condition), enabling efficient on-demand crosslinking and good printing fidelity. The bulk stiffness of 3D printed dECM-GMA hydrogels was slightly softer ( $\sim 0.2 - 1.2$  kPa) compared to dECM-MA ( $\sim 0.5 - 2$  kPa), both being within the range of healthy human liver tissue ( $\sim 0.15 - 5.9$  kPa), making them suitable candidates for bioprinting of HepaRG cells. dECM-GMA hydrogels



exhibited enhanced hydrophilicity and cell compatibility and faster biodegradation compared to dECM-MA gels, highlighting the critical role of chemical functionalization in optimizing bioresins for vat bioprinting.

In the third study, the papain digestion protocol established in the first study was applied to porcine intestinal dSIS, achieving characteristics similar to liver dECM and thereby demonstrating its versatility. Functionalized with methacrylic anhydride (MA) for vat 3D printing, dSIS produced biomimetic dSIS-MA hydrogels with tunable stiffness ( $3.7 \pm 0.2$  kPa), matching healthy human small intestinal tissue ( $\sim 1.3 - 4.0$  kPa). Moreover, the functionalization enhanced biostability of the hydrogels when seeded with intestinal epithelial cells, essential for advanced intestinal in vitro tissue models. To enable dynamic cell culture conditions, a biocompatible 3D-printed millifluidic tissue chamber was designed to host cellular dSIS-MA hydrogel scaffolds while maintaining a laminar flow profile, as confirmed by computational fluid dynamics simulations. The millifluidic system enables advanced intestinal models with tunable stiffness and fluid shear stresses, offering a scalable and cost-effective solution for in vitro tissue modeling. As demonstrated by culturing HT29-MTX monolayers under low physiological shear stress ( $\sim 0.01$  dyne/cm<sup>2</sup>), the system induced 3D tissue reorganization and enhanced differentiation and mucus production, particularly MUC5AC, when compared to static culture conditions as evidenced by immunofluorescent proteins staining. Experiments with human organoid-derived ileum ISCs showed that physiological shear stress combined with biomimetic hydrogel scaffolds decreased proliferation and stemness of the cells while promoting their multi-lineage differentiation. Changes in alkaline phosphatase (ALP) activity and secreted mucus demonstrated functional cell differentiation into enterocyte and goblet cell lineages.

The studies in this thesis covered the critical steps in dECM bioprinting, from enzyme-based solubilization of dECM through their chemical functionalization for vat (bio)printing until the integration of advanced fluidic systems for tissue modeling. Each step advances the understanding and development of biomimical materials and strategies, enhancing the efficiency and functionality of bioengineered tissues. This paves the way for future applications in regenerative medicine and tissue engineering.

## 6. KURZZUSAMMENFASSUNG

Diese Dissertation erweitert das Feld des Bioprintings und der Gewebemodellierung, indem sie die Einschränkungen der aktuellen Verarbeitungsprotokolle für dECM-basierte Bioharze adressiert. Sie untersucht effektive Enzyme für das Thermogelierung von dECM-Vorgelen, erforscht die Verwendung von dECM, die mit verschiedenen methacryloylierten Gruppen funktionalisiert wurde, für das Vat-3D Bioprinting. Weiterhin wird der 3D-Druck zur Entwicklung fortschrittlicher dynamischer Kultursysteme, die mechanischen Scherstress auf Epithelzellen ausüben, um fortschrittliche in vitro-Gewebemodelle zu entwickeln.

Die präzise Kontrolle über die physikalischen, mechanischen und biochemischen Eigenschaften von dECM-Hydrogelen nach Solubilisierung und Gelierung ist entscheidend für ihre Anwendung. Während tierisches Pepsin traditionell zur Solubilisierung von dECM verwendet wird, haben wir in unserer ersten Studie verschiedene nicht-tierische Alternativen untersucht, darunter pflanzliches Papain sowie bakterielle Kollagenase und  $\alpha$ -Amylase. Obwohl dECM, die mit  $\alpha$ -Amylase verdaut wurde, den höchsten Gehalt an Wachstumsfaktoren und Zytokinen aufwies, beeinträchtigten sowohl  $\alpha$ -Amylase- als auch Kollagenase-Behandlungen die Kollagen-Selbstassemblierung der verdauten dECM und beeinflussten auch die Proteinstrukturintegrität. Darüber hinaus führte ihre unzureichende Verdauungseffizienz zu deutlich reduzierten Ausbeuten an verdauter dECM ( $\sim 7 - 10\%$ ). Im Gegensatz dazu bewahrte Papain die physikalische Gelbildungspotenzial der verdauten dECM und zeigte vergleichbare Ausbeuten ( $\sim 79 - 86\%$ ), Thermogelierungskinetiken und mechanische Bulk-Eigenschaften wie Pepsin, zusammen mit erhöhten Mengen an zurückgehaltenen Wachstumsfaktoren und gesteigerter Zelladhäsion. Fazit: Papain erwies sich als reproduzierbare und kostengünstigere Alternative zu Pepsin für die Herstellung von leberbasierten dECM-Hydrogelen, wodurch das Risiko einer zoonotischen Krankheitsübertragung eliminiert wird.

Die zweite Studie untersuchte die Funktionalisierung von papainverdauter Leber-dECM mit Glycidylmethacrylat (dECM-GMA) und Methacrylsäureanhydrid (dECM-MA) zu photoaktiven Bioharzen für die Vat-Photopolymerisation. Beide chemischen Modifikationen führten zu einem vergleichbaren Funktionalisierungsgrad (DOF  $\sim 81,5 - 83,5\%$ ), ohne die dECM-Struktur dabei

zu beeinträchtigen. Interessanterweise zeigte dECM-GMA, aufgrund der zusätzlichen Hydroxylgruppen und der erhöhten Wasserstoffbrückenbindung, eine verbesserte Löslichkeit und höhere Scherviskosität im Vergleich zu dECM-MA. Bei beide Modifikationen konnte während der Herstellung der jeweiligen Harze ein ähnlicher Grad an Vernetzung durch den Photocrosslinking Prozess festgestellt wurden (30 – 60%, abhängig von den Bedingungen), was eine effiziente Vernetzungsgrad bei Bedarf und gute Druckgenauigkeit ermöglichte. Das Bulk-Elastizitätsmodul der 3D-gedruckten dECM-GMA-Hydrogele war etwas niedriger ( $\sim 0,2 - 1,2$  kPa) im Vergleich zu dECM-MA ( $\sim 0,5 - 2$  kPa). Beide lagen jedoch im Bereich eines gesunden menschlichen Lebergewebes ( $\sim 0,15 - 5,9$  kPa), was sie zu geeigneten Kandidaten für das Bioprinting von HepaRG-Zellen macht. dECM-GMA-Hydrogele zeigten eine verbesserte Hydrophilie und Zellkompatibilität, sowie eine schnellere Biodegradation im Vergleich zu dECM-MA-Gelen, wodurch die entscheidende Rolle der chemischen Funktionalisierung bei der Optimierung von Bioharzen für das Vat-Bioprinting hervorgehoben wird.

In der dritten Studie wurde das, in der ersten Studie etablierte Papainverdauungsprotokoll, auf den Dünndarm von Schweinen angewendet, um ähnliche Eigenschaften wie bei Leber-dECM zu erzielen und damit die Vielseitigkeit von Papain zu demonstrieren. Durch die Funktionalisierung mit Methacrylsäureanhydrid (MA) für das Vat-3D-Drucken, wurden dSIS-MA-Hydrogele hergestellt, die eine biomimetische Steifigkeit von  $3,7 \pm 0,2$  kPa aufweisen, ähnlich der gesunden menschlichen Dünndarmgewebesteifigkeit ( $\sim 1,3 - 4,0$  kPa). Zudem verbesserte die Funktionalisierung die Biostabilität der Hydrogele, wenn sie mit Darmepithelzellen besiedelt wurden, was für fortschrittliche intestinale in vitro-Gewebemodelle unerlässlich ist. Zur Schaffung dynamischer Zellkulturbedingungen wurde eine biokompatible, 3D-gedruckte Millifluidik-Gewebekammer entwickelt, die zelluläre dSIS-MA-Hydrogelgerüste aufnimmt und gleichzeitig ein laminares Flussprofil aufrechterhält, was durch Strömungsdynamiksimulationen bestätigt wurde. Das Millifluidik-System ermöglicht die Entwicklung fortschrittlicher, intestinaler Modelle mit anpassbarer Steifigkeit und Flüssigkeitsscherbeanspruchung und bietet eine skalierbare und kosteneffektive Lösung für die in vitro-Gewebemodellierung. Experimente mit HT29-MTX-Monoschicht unter niedrigem physiologischem Scherstress ( $\sim 0,01$  dyne/cm<sup>2</sup>) zeigten, dass das System eine 3D-Gewebeorganisation induzierte und Differenzierung sowie die Schleimproduktion, insbesondere von MUC5AC, im Vergleich zu statischen Kulturbedingungen verbesserte, was durch immunfluoreszierende Proteinfärbungen nachgewiesen wurde. Versuche

mit Ileum-ISCs, die aus menschlichen Organoiden abgeleitet wurden, zeigten dass physiologischer Scherstress in Kombination mit biomimetischen Hydrogelgerüsten die Proliferation und Stammcharakter der Zellen verringerte und gleichzeitig ihre multilineare Differenzierung förderte. Änderungen in der alkalischen Phosphatase (ALP)-Aktivität und der produzierten Schleimmenge zeigten eine funktionelle Zelldifferenzierung in Enterozyten- und Becherzelllinien an.

Die Studien in dieser Dissertation umfassten die kritischen Schritte des dECM-Bioprintings, beginnend von der enzymatischen Solubilisierung der dECM, gefolgt von deren chemische Funktionalisierung für das Vat-(Bio-)Drucken bis hin zur Integration fortschrittlicher Fluidiksysteme für die Gewebemodellierung. Jeder dieser Schritte erweitert das Verständnis für die Entwicklung biomimetischer Materialien und zugehörigen Strategien, verbessert die Effizienz und Funktionalität bioengineerter Gewebe und ebnet den Weg für zukünftige Anwendungen in der regenerativen Medizin und Gewebekonstruktion.

## 7. OUTLOOK

Despite the progress made in this thesis, much remains to be understood. The potential for applying dECM biomaterials in bioprinting and tissue engineering is still emerging, and there is considerable room for improvement and further exploration.

The work in this thesis has demonstrated that plant-derived papain is a highly attractive alternative to animal-derived pepsin for producing liver and intestine dECM hydrogels. Future research can focus on applying the papain digestion protocol to various animal tissue types, expanding their applicability, and refining the solubilization process for a broader range of biological materials. Additionally, thoroughly investigating the exact mechanism of how papain digests ECM components at a molecular level will help optimize digestion protocols, improving the reproducibility and quality of dECM hydrogels. The cost-effectiveness and safety of plant-based papain make it suitable for large-scale production of dECM digests; however, careful attention must be paid to optimizing enzyme concentrations, ensuring consistent quality control, and adhering to regulatory standards to maintain the integrity and efficacy of the final product.

The comparative study of methacryloyl-functionalized dECM bioresins has highlighted the significant impact of chemical functionalization on bioprinting outcomes. Future investigations should focus on enhancing the resolution and complexity of bioprinted constructs using these bioresins, closely mimicking the native tissue environment without compromising cell biocompatibility. Optimizing the degree of functionalization and crosslinking conditions to achieve finer structural details without adversely affecting cellular interactions is crucial. Furthermore, integrating these bioresins with advanced bioprinting techniques can create complex, multi-cellular structures with enhanced biological functionality. The cell-ECM interactions and the potential for matrix-induced cell differentiation within these bioprinted hydrogels warrant further investigation. With tunable stiffness and distinct chemical groups for crosslinking, dECM-(G)MA hydrogels could serve as *in vitro* liver mimetic platforms for fundamental research on organ regeneration and disease development.

Finally, integrating human adult ileum-derived ISCs into the millifluidic system designed for hosting papain-digested dSIS-MA hydrogel scaffolds presented some challenges, necessitating further refinement. Future research should focus on improving the efficiency and reproducibility of ISCs by optimizing seeding protocols, including media compositions, to achieve intact

functional epithelial monolayers suitable for further experimentation and characterization. Additionally, investigating the effects of various fluidic mechanical stimuli, such as shear stresses ranging from 0.001 to 0.1 dyne/cm<sup>2</sup>, or mechanical properties in the scaffold, such as 0.5 to 10 kPa, can provide valuable insights into how these factors impact the stemness and differentiation pathways of ISCs. Furthermore, integrating vascular hydrogels seeded with ISCs within the system can further increase physiological relevance, allowing for a thorough study of their effects on tissue development. Comprehensive mRNA gene expression analysis, supported by advanced RNA-level tools such as qRT-PCR, microarrays, and RNA-Seq, can elucidate gene expression profiles and molecular mechanisms, enhancing the readout of experimental conclusions.

In summary, while progress has been made, much remains to be explored. Continued investigations into dECM biomaterials and ISC integration will further unlock their potential, leading to advancements in regenerative medicine and tissue engineering.

## 8. LIST OF PUBLICATIONS AND CONFERENCE CONTRIBUTIONS

### Peer-reviewed publications and manuscripts

1. **Almalla, A.**; Elomaa, L.; Bechtella, L.; Daneshgar, A.; Yavvari, P.; Mahfouz, Z.; Tang, P.; Kokschi, B.; Sauer, I.; Pagel, K.; Hillebrandt, K. H.; Weinhart, M. Papain-Based Solubilization of Decellularized Extracellular Matrix for the Preparation of Bioactive, Thermosensitive Pre-Gels. *Biomacromolecules* **2023**, 24 (12), 5620-5637. DOI: 10.1021/acs.biomac.3c00602.
2. **Almalla, A.**; Elomaa, L.; Fribicz, N.; Tang, B.; Mahfouz, Z.; Kokschi, B.; Hillebrandt, H. K.; Sauer, M. I.; Seiffert, S.; Weinhart, M. Chemistry matters: A side-by-side comparison of two chemically distinct methacryloylated dECM bioresins for vat photopolymerization. *Biomaterials Advances* **2024**, 160, 213850. DOI: 10.1016/j.bioadv.2024.213850.
3. **Almalla, A.**; Alzain, N., Elomaa, L.; Lindner, M.; Siegmund, B.; Weinhart, M. Hydrogel-Integrated Millifluidic Systems: Advancing Intestinal Epithelial and Mucosal Simulations with small intestine-derived Tissue models. *Cells* **2024**, 13, 1080. DOI:10.3390/cells13131080.
4. **Almalla, A.**; Hertwig, A.; Fischer, D.; Ozcan, O.; Witt, J. Development of Layer-by-Layer Assembled Thin Coatings on Aluminium Alloy Aa2024-T3 for High Resolution Studies of Local Corrosion Processes. *Journal of Applied Polymer Science* **2020**, 137, DOI:10.1002/app.49826.
5. **Almalla, A.**; Ozcan, O.; Witt, J. In Situ Atomic Force Microscopy Analysis of the Corrosion Processes at the Buried Interface of an Epoxy-Like Model Organic Film and Aa2024-T3 Aluminum Alloy. *Advanced Engineering Materials* **2022**, 24, DOI:10.1002/adem.202101342.
6. Elomaa, L.; **Almalla, A.**; Keshi, E.; Hillebrandt, K. H.; Sauer, I. M.; Weinhart, M. Rise of tissue- and species-specific 3D bioprinting based on decellularized extracellular matrix-derived bioinks and bioresins. *Biomaterials and Biosystems* **2023**, 12, 100084. DOI: 10.1016/j.bbiosy.2023.100084.
7. Elomaa, L.; Gerbeth, L.; **Almalla, A.**; Fribicz, N.; Daneshgar, A.; Tang, P.; Hillebrandt, K. H.; Seiffert, S.; Sauer, M. I.; Siegmund, B.; Weinhart, M. Bioactive photocrosslinkable resin solely based on refined decellularized small intestine submucosa for vat photopolymerization of in vitro tissue mimics. *Additive Manufacturing* **2023**, 64, 103439. DOI: 10.1016/j.addma.2023.103439.
8. Schüler, K.; **Almalla, A.**; Seitel, S.; Seiffert, S.; Weinhart, M.; Elomaa, L. Vascularization of covalently crosslinked decellularized extracellular matrix hydrogels bioprinted via vat photopolymerization. *In preparation* **2024**.
9. Veetil, N.; Gransar T.; Liu, S.; **Almalla A.**; Kirchner, M.; Brackin-Helmert, R.; Henning, F.; Yeter, R.; Weinhart, M.; Mertins, P.; Falk, V; Szulcek, R.; Kucherenko, M.; Kuebler, W.; Knosalla, C. Remodeling and stiffening of pulmonary arterial endothelial extracellular matrix promote smooth muscle cell hyperplasia in pulmonary hypertension due to left heart disease. *In preparation* **2024**.

## Presentations and posters

1. **Almalla, A.;** Bechtella, L.; Mahfouz, Z.; Elomaa, L.; and Weinhart, M. Animal-free, cost-effective and simple method for solubilization of decellularized extracellular matrix (dECM), *Deutschen Gesellschaft für Biomaterialien (DGBM)*, **2022**.
2. **Almalla, A;** Elomaa, L.; Alzain, N.; Siegmund, B.; Weinhart, M. Shear stress-induced mucus production and differentiation of primary organoid-derived epithelial cell monolayer seeded on printed dSIS-MA hydrogels. *1st International Symposium des SFB*, **2022**.
3. **Almalla, A;** Alzain, N.; Kramer, C.; Elomaa, L.; Gerbeth, L.; Köhl, A.; Glaubien, R.; Weinhart, M.; Siegmund, B. Mucus properties on intestinal surfaces in health and disease. *2nd Retreat des SFB 1449*, **2023**.
4. **Almalla, A;** ECM liver-based bioinks for 3D bioprinting. *Speed lecture award*, Final list of candidates, oral presentation, **2022**.

## 9. References

1. Bae, M.; Kim, J.J.; Kim, J.; Cho, D.-W. Decellularized Extracellular Matrix for Three-Dimensional Bioprinted in Vitro Disease Modeling. *Int J Bioprinting* **2024**, *10*, 1970, doi:10.36922/ijb.1970.
2. Jovic, T.H.; Combella, E.J.; Jessop, Z.M.; Whitaker, I.S. 3d Bioprinting and the Future of Surgery. *Front Surg* **2020**, *7*, 609836, doi:10.3389/fsurg.2020.609836.
3. Lam, E.H.Y.; Yu, F.; Zhu, S.; Wang, Z. 3d Bioprinting for Next-Generation Personalized Medicine. *Int J Mol Sci* **2023**, *24*, 6357, doi:10.3390/ijms24076357.
4. Golebiowska, A.A.; Intravaia, J.T.; Sathe, V.M.; Kumbar, S.G.; Nukavarapu, S.P. Decellularized Extracellular Matrix Biomaterials for Regenerative Therapies: Advances, Challenges and Clinical Prospects. *Bioact Mater* **2024**, *32*, 98-123, doi:10.1016/j.bioactmat.2023.09.017.
5. Dzobo, K.; Motaung, K.; Adesida, A. Recent Trends in Decellularized Extracellular Matrix Bioinks for 3d Printing: An Updated Review. *Int J Mol Sci* **2019**, *20*, 4628, doi:10.3390/ijms20184628.
6. Gadre, M.; Kasturi, M.; Agarwal, P.; Vasanthan, K.S. Decellularization and Their Significance for Tissue Regeneration in the Era of 3d Bioprinting. *ACS Omega* **2024**, *9*, 7375-7392, doi:10.1021/acsomega.3c08930.
7. Saldin, L.T.; Cramer, M.C.; Velankar, S.S.; White, L.J.; Badylak, S.F. Extracellular Matrix Hydrogels from Decellularized Tissues: Structure and Function. *Acta Biomater* **2017**, *49*, 1-15, doi:10.1016/j.actbio.2016.11.068.
8. Zhang, W.; Du, A.; Liu, S.; Lv, M.; Chen, S. Research Progress in Decellularized Extracellular Matrix-Derived Hydrogels. *Regen Ther* **2021**, *18*, 88-96, doi:10.1016/j.reth.2021.04.002.
9. Khatri, V.; Ramachandraiah, H.; Pati, F.; Svahn, H.A.; Gaudenzi, G.; Russom, A. 3d Bioprinting of Multi-Material Decellularized Liver Matrix Hydrogel at Physiological Temperatures. *Biosensors* **2022**, *12*, 521, doi:10.3390/bios12070521.
10. Traverse, J.H.; Henry, T.D.; Dib, N.; Patel, A.N.; Pepine, C.; Schaer, G.L.; DeQuach, J.A.; Kinsey, A.M.; Chamberlin, P.; Christman, K.L. First-in-Man Study of a Cardiac Extracellular Matrix Hydrogel in Early and Late Myocardial Infarction Patients. *JACC Basic Transl Sci* **2019**, *4*, 659-669, doi:10.1016/j.jacbts.2019.07.012.
11. Han, H.; Park, Y.; Choi, Y.M.; Yong, U.; Kang, B.; Shin, W.; Min, S.; Kim, H.J.; Jang, J. A Bioprinted Tubular Intestine Model Using a Colon-Specific Extracellular Matrix Bioink. *Adv Healthc Mater* **2022**, *11*, e2101768, doi:10.1002/adhm.202101768.



12. Giobbe, G.G.; Crowley, C.; Luni, C.; Campinoti, S.; Khedr, M.; Kretzschmar, K.; De Santis, M.M.; Zambaiti, E.; Michielin, F.; Meran, L.; Hu, Q.; van Son, G.; Urbani, L.; Manfredi, A.; Giomo, M.; Eaton, S.; Cacchiarelli, D.; Li, V.S.W.; Clevers, H.; Bonfanti, P.; Elvassore, N.; De Coppi, P. Extracellular Matrix Hydrogel Derived from Decellularized Tissues Enables Endodermal Organoid Culture. *Nat Commun* **2019**, *10*, 5658, doi:10.1038/s41467-019-13605-4.
13. Abaci, A.; Guvendiren, M. Designing Decellularized Extracellular Matrix-Based Bioinks for 3d Bioprinting. *Adv Healthc Mater* **2020**, *9*, e2000734, doi:10.1002/adhm.202000734.
14. Qiao, S.; Peijie, T.; Nan, J. Crosslinking Strategies of Decellularized Extracellular Matrix in Tissue Regeneration. *J Biomed Mater Res A* **2024**, *112*, 640-667, doi:10.1002/jbm.a.37650.
15. Elomaa, L.; Gerbeth, L.; Almalla, A.; Fribicz, N.; Daneshgar, A.; Tang, P.; Hillebrandt, K.H.; Seiffert, S.; Sauer, M.I.; Siegmund, B.; Weinhart, M. Bioactive Photocrosslinkable Resin Solely Based on Refined Decellularized Small Intestine Submucosa for Vat Photopolymerization of in Vitro Tissue Mimics. *Addit Manuf* **2023**, *64*, 103439, doi:10.1016/j.addma.2023.103439.
16. Sorushanova, A.; Delgado, L.M.; Wu, Z.; Shologu, N.; Kshirsagar, A.; Raghunath, R.; Mullen, A.M.; Bayon, Y.; Pandit, A.; Raghunath, M.; Zeugolis, D.I. The Collagen Suprafamily: From Biosynthesis to Advanced Biomaterial Development. *Adv Mater* **2019**, *31*, e1801651, doi:10.1002/adma.201801651.
17. Leon-Lopez, A.; Morales-Penaloza, A.; Martinez-Juarez, V.M.; Vargas-Torres, A.; Zeugolis, D.I.; Aguirre-Alvarez, G. Hydrolyzed Collagen-Sources and Applications. *Molecules* **2019**, *24*, doi:10.3390/molecules24224031.
18. Trebacz, H.; Barzycka, A. Mechanical Properties and Functions of Elastin: An Overview. *Biomolecules* **2023**, *13*, 574, doi:10.3390/biom13030574.
19. Halper, J.; Kjaer, M. Basic Components of Connective Tissues and Extracellular Matrix: Elastin, Fibrillin, Fibulins, Fibrinogen, Fibronectin, Laminin, Tenascins and Thrombospondins. *Adv Exp Med Biol* **2014**, *802*, 31-47, doi:10.1007/978-94-007-7893-1\_3.
20. Manka, S.W.; Bihan, D.; Farndale, R.W. Structural Studies of the Mmp-3 Interaction with Triple-Helical Collagen Introduce New Roles for the Enzyme in Tissue Remodelling. *Sci Rep* **2019**, *9*, 18785, doi:10.1038/s41598-019-55266-9.
21. Gattazzo, F.; Urciuolo, A.; Bonaldo, P. Extracellular Matrix: A Dynamic Microenvironment for Stem Cell Niche. *Biochim Biophys Acta* **2014**, *1840*, 2506-2519, doi:10.1016/j.bbagen.2014.01.010.
22. Kim, E.J.; Choi, J.S.; Kim, J.S.; Choi, Y.C.; Cho, Y.W. Injectable and Thermosensitive Soluble Extracellular Matrix and Methylcellulose Hydrogels for Stem Cell Delivery in Skin Wounds. *Biomacromolecules* **2016**, *17*, 4-11, doi:10.1021/acs.biomac.5b01566.
23. Bomkamp, C.; Skaalure, S.C.; Fernando, G.F.; Ben-Arye, T.; Swartz, E.W.; Specht, E.A. Scaffolding Biomaterials for 3d Cultivated Meat: Prospects and Challenges. *Adv Sci (Weinh)* **2022**, *9*, e2102908, doi:10.1002/advs.202102908.
24. Murphy, S.V.; Atala, A. 3d Bioprinting of Tissues and Organs. *Nat Biotechnol* **2014**, *32*, 773-785, doi:10.1038/nbt.2958.
25. Hull, C.W.; Arcadia, C. Apparatus for Production of Three-Dimensional Objects by Stereolithography. 1986.
26. Ng, W.L.; Lee, J.M.; Zhou, M.; Chen, Y.W.; Lee, K.A.; Yeong, W.Y.; Shen, Y.F. Vat Polymerization-Based Bioprinting-Process, Materials, Applications and Regulatory Challenges. *Biofabrication* **2020**, *12*, 022001, doi:10.1088/1758-5090/ab6034.
27. Wilson, W.C., Jr.; Boland, T. Cell and Organ Printing 1: Protein and Cell Printers. *Anat Rec A Discov Mol Cell Evol Biol* **2003**, *272*, 491-496, doi:10.1002/ar.a.10057.
28. Groll, J.; Burdick, J.A.; Cho, D.W.; Derby, B.; Gelinsky, M.; Heilshorn, S.C.; Jungst, T.; Malda, J.; Mironov, V.A.; Nakayama, K.; Ovsianikov, A.; Sun, W.; Takeuchi, S.; Yoo, J.J.; Woodfield, T.B.F. A Definition of Bioinks and Their Distinction from Biomaterial Inks. *Biofabrication* **2018**, *11*, 013001, doi:10.1088/1758-5090/aaec52.

29. Lim, K.S.; Galarraga, J.H.; Cui, X.; Lindberg, G.C.J.; Burdick, J.A.; Woodfield, T.B.F. Fundamentals and Applications of Photo-Cross-Linking in Bioprinting. *Chem Rev* **2020**, *120*, 10662–10694, doi:10.1021/acs.chemrev.9b00812.
30. Murphy, C.A.; Lim, K.S.; Woodfield, T.B.F. Next Evolution in Organ-Scale Biofabrication: Bioresin Design for Rapid High-Resolution Vat Polymerization. *Adv Mater* **2022**, *34*, e2107759, doi:10.1002/adma.202107759.
31. Mir, T.A.; Nakamura, M. Three-Dimensional Bioprinting: Toward the Era of Manufacturing Human Organs as Spare Parts for Healthcare and Medicine. *Tissue Eng Part B Rev* **2017**, *23*, 245-256, doi:10.1089/ten.TEB.2016.0398.
32. Kort-Mascort, J.; Flores-Torres, S.; Peza-Chavez, O.; Jang, J.H.; Pardo, L.A.; Tran, S.D.; Kinsella, J. Decellularized Ecm Hydrogels: Prior Use Considerations, Applications, and Opportunities in Tissue Engineering and Biofabrication. *Biomater Sci* **2023**, *11*, 400-431, doi:10.1039/d2bm01273a.
33. Visscher, D.O.; Lee, H.; van Zuijlen, P.P.M.; Helder, M.N.; Atala, A.; Yoo, J.J.; Lee, S.J. A Photo-Crosslinkable Cartilage-Derived Extracellular Matrix Bioink for Auricular Cartilage Tissue Engineering. *Acta Biomater* **2021**, *121*, 193-203, doi:10.1016/j.actbio.2020.11.029.
34. Shin, Y.J.; Shafraneck, R.T.; Tsui, J.H.; Walcott, J.; Nelson, A.; Kim, D.H. 3d Bioprinting of Mechanically Tuned Bioinks Derived from Cardiac Decellularized Extracellular Matrix. *Acta Biomater* **2021**, *119*, 75-88, doi:10.1016/j.actbio.2020.11.006.
35. Pati, F.; Jang, J.; Ha, D.H.; Won Kim, S.; Rhie, J.W.; Shim, J.H.; Kim, D.H.; Cho, D.W. Printing Three-Dimensional Tissue Analogues with Decellularized Extracellular Matrix Bioink. *Nat Commun* **2014**, *5*, 3935, doi:10.1038/ncomms4935.
36. Kim, B.S.; Kwon, Y.W.; Kong, J.S.; Park, G.T.; Gao, G.; Han, W.; Kim, M.B.; Lee, H.; Kim, J.H.; Cho, D.W. 3d Cell Printing of in Vitro Stabilized Skin Model and in Vivo Pre-Vascularized Skin Patch Using Tissue-Specific Extracellular Matrix Bioink: A Step Towards Advanced Skin Tissue Engineering. *Biomaterials* **2018**, *168*, 38-53, doi:10.1016/j.biomaterials.2018.03.040.
37. Kiyotake, E.A.; Cheng, M.E.; Thomas, E.E.; Detamore, M.S. The Rheology and Printability of Cartilage Matrix-Only Biomaterials. *Biomolecules* **2022**, *12*, doi:10.3390/biom12060846.
38. Ali, M.; Pr, A.K.; Yoo, J.J.; Zahran, F.; Atala, A.; Lee, S.J. A Photo-Crosslinkable Kidney Ecm-Derived Bioink Accelerates Renal Tissue Formation. *Adv Healthc Mater* **2019**, *8*, e1800992, doi:10.1002/adhm.201800992.
39. Lee, J.; Hong, J.; Kim, W.; Kim, G.H. Bone-Derived Decm/Alginate Bioink for Fabricating a 3d Cell-Laden Mesh Structure for Bone Tissue Engineering. *Carbohydr Polym* **2020**, *250*, 116914, doi:10.1016/j.carbpol.2020.116914.
40. Kim, W.; Lee, H.; Lee, J.; Atala, A.; Yoo, J.J.; Lee, S.J.; Kim, G.H. Efficient Myotube Formation in 3d Bioprinted Tissue Construct by Biochemical and Topographical Cues. *Biomaterials* **2020**, *230*, 119632, doi:10.1016/j.biomaterials.2019.119632.
41. Townsend, J.M.; Beck, E.C.; Gehrke, S.H.; Berkland, C.J.; Detamore, M.S. Flow Behavior Prior to Crosslinking: The Need for Precursor Rheology for Placement of Hydrogels in Medical Applications and for 3d Bioprinting. *Prog Polym Sci* **2019**, *91*, 126-140, doi:10.1016/j.progpolymsci.2019.01.003.
42. Liu, J.; He, J.; Liu, J.; Ma, X.; Chen, Q.; Lawrence, N.; Zhu, W.; Xu, Y.; Chen, S. Rapid 3d Bioprinting of in Vitro Cardiac Tissue Models Using Human Embryonic Stem Cell-Derived Cardiomyocytes. *Bioprinting* **2019**, *13*, doi:10.1016/j.bprint.2019.e00040.
43. Yu, C.; Ma, X.; Zhu, W.; Wang, P.; Miller, K.L.; Stupin, J.; Koroleva-Maharajh, A.; Hairabedian, A.; Chen, S. Scanningless and Continuous 3d Bioprinting of Human Tissues with Decellularized Extracellular Matrix. *Biomaterials* **2019**, *194*, 1-13, doi:10.1016/j.biomaterials.2018.12.009.
44. Kim, H.; Kang, B.; Cui, X.; Lee, S.H.; Lee, K.; Cho, D.W.; Hwang, W.; Woodfield, T.B.F.; Lim, K.S.; Jang, J. Light-Activated Decellularized Extracellular Matrix-Based Bioinks for Volumetric Tissue Analogs at the Centimeter Scale. *Adv Funct Mater* **2021**, *31*, doi:10.1002/adfm.202011252.

45. Elomaa, L.; Almalla, A.; Keshi, E.; Hillebrandt, K.H.; Sauer, I.M.; Weinhart, M. Rise of Tissue- and Species-Specific 3d Bioprinting Based on Decellularized Extracellular Matrix-Derived Bioinks and Bioresins. *Biomater Biosyst* **2023**, *12*, 100084, doi:10.1016/j.bbiosy.2023.100084.
46. Gilpin, A.; Yang, Y. Decellularization Strategies for Regenerative Medicine: From Processing Techniques to Applications. *Biomed Res Int* **2017**, *2017*, 9831534, doi:10.1155/2017/9831534.
47. Crapo, P.M.; Gilbert, T.W.; Badylak, S.F. An Overview of Tissue and Whole Organ Decellularization Processes. *Biomaterials* **2011**, *32*, 3233-3243, doi:10.1016/j.biomaterials.2011.01.057.
48. Gilpin, S.E.; Guyette, J.P.; Gonzalez, G.; Ren, X.; Asara, J.M.; Mathisen, D.J.; Vacanti, J.P.; Ott, H.C. Perfusion Decellularization of Human and Porcine Lungs: Bringing the Matrix to Clinical Scale. *J Heart Lung Transplant* **2014**, *33*, 298-308, doi:10.1016/j.healun.2013.10.030.
49. Liu, J.; Song, Q.; Yin, W.; Li, C.; An, N.; Le, Y.; Wang, Q.; Feng, Y.; Hu, Y.; Wang, Y. Bioactive Scaffolds for Tissue Engineering: A Review of Decellularized Extracellular Matrix Applications and Innovations. *Exploration* **2024**, doi:10.1002/exp.20230078.
50. Roth, S.P.; Glauche, S.M.; Plenge, A.; Erbe, I.; Heller, S.; Burk, J. Automated Freeze-Thaw Cycles for Decellularization of Tendon Tissue - a Pilot Study. *BMC Biotechnol* **2017**, *17*, 13, doi:10.1186/s12896-017-0329-6.
51. Badylak, S.F.; Taylor, D.; Uygun, K. Whole-Organ Tissue Engineering: Decellularization and Recellularization of Three-Dimensional Matrix Scaffolds. *Annu Rev Biomed Eng* **2011**, *13*, 27-53, doi:10.1146/annurev-bioeng-071910-124743.
52. Bakhtiar, H.; Rajabi, S.; Pezeshki-Modaress, M.; Ellini, M.R.; Panahinia, M.; Alijani, S.; Mazidi, A.; Kamali, A.; Azarpazhooh, A.; Kishen, A. Optimizing Methods for Bovine Dental Pulp Decellularization. *J Endod* **2021**, *47*, 62-68, doi:10.1016/j.joen.2020.08.027.
53. Tao, M.; Ao, T.; Mao, X.; Yan, X.; Javed, R.; Hou, W.; Wang, Y.; Sun, C.; Lin, S.; Yu, T.; Ao, Q. Sterilization and Disinfection Methods for Decellularized Matrix Materials: Review, Consideration and Proposal. *Bioact Mater* **2021**, *6*, 2927-2945, doi:10.1016/j.bioactmat.2021.02.010.
54. Dai, Z.; Ronholm, J.; Tian, Y.; Sethi, B.; Cao, X. Sterilization Techniques for Biodegradable Scaffolds in Tissue Engineering Applications. *J Tissue Eng* **2016**, *7*, 2041731416648810, doi:10.1177/2041731416648810.
55. Yamanaka, H.; Morimoto, N.; Yamaoka, T. Decellularization of Submillimeter-Diameter Vascular Scaffolds Using Peracetic Acid. *J Artif Organs* **2020**, *23*, 156-162, doi:10.1007/s10047-019-01152-0.
56. Song, J.J.; Guyette, J.P.; Gilpin, S.E.; Gonzalez, G.; Vacanti, J.P.; Ott, H.C. Regeneration and Experimental Orthotopic Transplantation of a Bioengineered Kidney. *Nat Med* **2013**, *19*, 646-651, doi:10.1038/nm.3154.
57. Godier-Furnemont, A.F.; Martens, T.P.; Koeckert, M.S.; Wan, L.; Parks, J.; Arai, K.; Zhang, G.; Hudson, B.; Homma, S.; Vunjak-Novakovic, G. Composite Scaffold Provides a Cell Delivery Platform for Cardiovascular Repair. *Proc Natl Acad Sci U S A* **2011**, *108*, 7974-7979, doi:10.1073/pnas.1104619108.
58. Novak, T.; Seelbinder, B.; Twitchell, C.M.; Voytik-Harbin, S.L.P.; Neu, C.P.P. Dissociated and Reconstituted Cartilage Microparticles in Densified Collagen Induce Local Hmsc Differentiation. *Adv Funct Mater* **2016**, *26*, 5427-5436, doi:10.1002/adfm.201601877.
59. Teng, Y.; Li, X.; Chen, Y.; Cai, H.; Cao, W.; Chen, X.; Sun, Y.; Liang, J.; Fan, Y.; Zhang, X. Extracellular Matrix Powder from Cultured Cartilage-Like Tissue as Cell Carrier for Cartilage Repair. *J Mater Chem B* **2017**, *5*, 3283-3292, doi:10.1039/c7tb00640c.
60. Pouliot, R.A.; Young, B.M.; Link, P.A.; Park, H.E.; Kahn, A.R.; Shankar, K.; Schneck, M.B.; Weiss, D.J.; Heise, R.L. Porcine Lung-Derived Extracellular Matrix Hydrogel Properties Are Dependent on Pepsin Digestion Time. *Tissue Eng Part C Methods* **2020**, *26*, 332-346, doi:10.1089/ten.TEC.2020.0042.
61. Zhang, Y.; He, Y.; Bharadwaj, S.; Hammam, N.; Carnagey, K.; Myers, R.; Atala, A.; Van Dyke, M. Tissue-Specific Extracellular Matrix Coatings for the Promotion of Cell Proliferation and

- Maintenance of Cell Phenotype. *Biomaterials* **2009**, *30*, 4021-4028, doi:10.1016/j.biomaterials.2009.04.005.
62. Patience, C.; Switzer, W.M.; Takeuchi, Y.; Griffiths, D.J.; Goward, M.E.; Heneine, W.; Stoye, J.P.; Weiss, R.A. Multiple Groups of Novel Retroviral Genomes in Pigs and Related Species. *J Virol* **2001**, *75*, 2771-2775, doi:10.1128/JVI.75.6.2771-2775.2001.
  63. Takeuchi Y, P.C., Magre S, Weiss RA, Banerjee PT, Le Tissier P, Stoye JP. Host Range and Interference Studies of Three Classes of Pig Endogenous Retrovirus. *J Virol.* **1998**, *12*, 9986–9991, doi:10.1128/JVI.72.12.
  64. Choi, J.S.; Kim, B.S.; Kim, J.Y.; Kim, J.D.; Choi, Y.C.; Yang, H.J.; Park, K.; Lee, H.Y.; Cho, Y.W. Decellularized Extracellular Matrix Derived from Human Adipose Tissue as a Potential Scaffold for Allograft Tissue Engineering. *J Biomed Mater Res A* **2011**, *97*, 292-299, doi:10.1002/jbm.a.33056.
  65. Jabbari, E.; Leijten, J.; Xu, Q.; Khademhosseini, A. The Matrix Reloaded: The Evolution of Regenerative Hydrogels. *MaterToday* **2016**, *19*, 190-196, doi:10.1016/j.mattod.2015.10.005.
  66. Gilbert, T.W.; Stolz, D.B.; Biancaniello, F.; Simmons-Byrd, A.; Badylak, S.F. Production and Characterization of Ecm Powder: Implications for Tissue Engineering Applications. *Biomaterials* **2005**, *26*, 1431-1435, doi:10.1016/j.biomaterials.2004.04.042.
  67. Voytik-Harbin SL; Brightman AO. Small Intestinal Submucosa: A Tissue-Derived Extracellular Matrix That Promotes Tissue-Specific Growth and Differentiation of Cells in Vitro. *Tissue Eng* **1998**, *4*, 157-174, doi:DOI:10.1089/ten.1998.4.157.
  68. Salelles, L.; Floury, J.; Le Feunteun, S. Pepsin Activity as a Function of Ph and Digestion Time on Caseins and Egg White Proteins under Static in Vitro Conditions. *Food Funct* **2021**, *12*, 12468-12478, doi:10.1039/d1fo02453a.
  69. Motyan, J.A.; Toth, F.; Tozser, J. Research Applications of Proteolytic Enzymes in Molecular Biology. *Biomolecules* **2013**, *3*, 923-942, doi:10.3390/biom3040923.
  70. Drake, M.P.; Davison, t.P.F.; Bump, S.; and Schmitt, F. Action of Proteolytic Enzymes on Tropocollagen and Insoluble Collagen. *Biochem* **1966**, *5*, 301-312, doi:DOI: 10.1021/bi00865a039.
  71. Zhu, S.; Yu, X.; You, J.; Yin, T.; Lin, Y.; Chen, W.; Dao, L.; Du, H.; Liu, R.; Xiong, S.; Hu, Y. Study of the Thermodynamics and Conformational Changes of Collagen Molecules Upon Self-Assembly. *Food Hydrocolloids* **2021**, *114*, doi:10.1016/j.foodhyd.2020.106576.
  72. Usha, R.R., T. Influence of Hydrogen Bond, Hydrophobic and Electrovalent Salt Linkages on the Transition Temperature, Enthalpy and Activation Energy in Rat Tail Tendon (Rtt) Collagen. *Thermochim Acta* **1999**, *338*, 17±25.
  73. O'Leary, L.E.; Fallas, J.A.; Bakota, E.L.; Kang, M.K.; Hartgerink, J.D. Multi-Hierarchical Self-Assembly of a Collagen Mimetic Peptide from Triple Helix to Nanofibre and Hydrogel. *Nat Chem* **2011**, *3*, 821-828, doi:10.1038/nchem.1123.
  74. Wu, Y.; Wenger, A.; Golzar, H.; Tang, X.S. 3d Bioprinting of Bicellular Liver Lobule-Mimetic Structures Via Microextrusion of Cellulose Nanocrystal-Incorporated Shear-Thinning Bioink. *Sci Rep* **2020**, *10*, 20648, doi:10.1038/s41598-020-77146-3.
  75. Medberry, C.J.; Crapo, P.M.; Siu, B.F.; Carruthers, C.A.; Wolf, M.T.; Nagarkar, S.P.; Agrawal, V.; Jones, K.E.; Kelly, J.; Johnson, S.A.; Velankar, S.S.; Watkins, S.C.; Modo, M.; Badylak, S.F. Hydrogels Derived from Central Nervous System Extracellular Matrix. *Biomaterials* **2013**, *34*, 1033-1040, doi:10.1016/j.biomaterials.2012.10.062.
  76. Kim, S.; Min, S.; Choi, Y.S.; Jo, S.H.; Jung, J.H.; Han, K.; Kim, J.; An, S.; Ji, Y.W.; Kim, Y.G.; Cho, S.W. Tissue Extracellular Matrix Hydrogels as Alternatives to Matrigel for Culturing Gastrointestinal Organoids. *Nat Commun* **2022**, *13*, 1692, doi:10.1038/s41467-022-29279-4.
  77. Sackett, S.D.; Tremmel, D.M.; Ma, F.; Feeney, A.K.; Maguire, R.M.; Brown, M.E.; Zhou, Y.; Li, X.; O'Brien, C.; Li, L.; Burlingham, W.J.; Odorico, J.S. Extracellular Matrix Scaffold and Hydrogel Derived from Decellularized and Delipidized Human Pancreas. *Sci Rep* **2018**, *8*, 10452, doi:10.1038/s41598-018-28857-1.

78. Jung, K.H.; Choi, Y.C.; Chun, J.Y.; Min, S.G.; Hong, G.P. Effects of Concentration and Reaction Time of Trypsin, Pepsin, and Chymotrypsin on the Hydrolysis Efficiency of Porcine Placenta. *Korean J Food Sci Anim Resour* **2014**, *34*, 151-157, doi:10.5851/kosfa.2014.34.2.151.
79. Miersch, C.; Stange, K.; Rontgen, M. Effects of Trypsinization and of a Combined Trypsin, Collagenase, and Dnase Digestion on Liberation and in Vitro Function of Satellite Cells Isolated from Juvenile Porcine Muscles. *In Vitro Cell Dev Biol Anim* **2018**, *54*, 406-412, doi:10.1007/s11626-018-0263-5.
80. Sato, K.; Ebihara, T.; Adachi, E.; Kawashima, S.; Hattori, S.; Irie, S. Possible Involvement of Aminotelopeptide in Self-Assembly and Thermal Stability of Collagen I as Revealed by Its Removal with Proteases. *J Biol Chem* **2000**, *275*, 25870-25875, doi:10.1074/jbc.M003700200.
81. Steven, F.S. The Nishihara Technique for the Solubilization of Collagen: Application to the Preparation of Soluble Collagens from Normal and Rheumatoid Connective Tissue. *Ann rheum Dis* **1964**, *23*, 300-301, doi:10.1136/ard.23.4.300.
82. Yu, C.; Bianco, J.; Brown, C.; Fuetterer, L.; Watkins, J.F.; Samani, A.; Flynn, L.E. Porous Decellularized Adipose Tissue Foams for Soft Tissue Regeneration. *Biomaterials* **2013**, *34*, 3290-3302, doi:10.1016/j.biomaterials.2013.01.056.
83. Shridhar, A.; Lam, A.Y.L.; Sun, Y.; Simmons, C.A.; Gillies, E.R.; Flynn, L.E. Culture on Tissue-Specific Coatings Derived from Alpha-Amylase-Digested Decellularized Adipose Tissue Enhances the Proliferation and Adipogenic Differentiation of Human Adipose-Derived Stromal Cells. *Biotechnol J* **2020**, *15*, e1900118, doi:10.1002/biot.201900118.
84. Kornmuller, A.; Brown, C.F.C.; Yu, C.; Flynn, L.E. Fabrication of Extracellular Matrix-Derived Foams and Microcarriers as Tissue-Specific Cell Culture and Delivery Platforms. *J Vis Exp* **2017**, *122*, 55436, doi:DOI: 10.3791/55436.
85. Russo, V.; Omid, E.; Samani, A.; Hamilton, A.; Flynn, L.E. Porous, Ventricular Extracellular Matrix-Derived Foams as a Platform for Cardiac Cell Culture. *BioResearch Open Access* **2015**, *4*, 374-388, doi:10.1089/biores.2015.0030.
86. Freytes, D.O.; Martin, J.; Velankar, S.S.; Lee, A.S.; Badylak, S.F. Preparation and Rheological Characterization of a Gel Form of the Porcine Urinary Bladder Matrix. *Biomaterials* **2008**, *29*, 1630-1637, doi:10.1016/j.biomaterials.2007.12.014.
87. Krishtul, S.; Baruch, L.; Machluf, M. Processed Tissue-Derived Extracellular Matrices: Tailored Platforms Empowering Diverse Therapeutic Applications. *Adv Funct Mater* **2019**, *30*, doi:10.1002/adfm.201900386.
88. Shirani, A.; Ganji, F.; Golmohammadi, M.; Hashemi, S.M.; Mozafari, M.; Amoabediny, G.; Karkuki Osguei, N.; Samadikuchaksaraei, A. Cross-Linked Acellular Lung for Application in Tissue Engineering: Effects on Biocompatibility, Mechanical Properties and Immunological Responses. *Mater Sci Eng C Mater Biol Appl* **2021**, *122*, 111938, doi:10.1016/j.msec.2021.111938.
89. Vyborny, K.; Vallova, J.; Koci, Z.; Kekulova, K.; Jirakova, K.; Jendelova, P.; Hodan, J.; Kubinova, S. Genipin and EDC Crosslinking of Extracellular Matrix Hydrogel Derived from Human Umbilical Cord for Neural Tissue Repair. *Sci Rep* **2019**, *9*, 10674, doi:10.1038/s41598-019-47059-x.
90. Singelyn, J.M.; Christman, K.L. Modulation of Material Properties of a Decellularized Myocardial Matrix Scaffold. *Macromol Biosci* **2011**, *11*, 731-738, doi:10.1002/mabi.201000423.
91. Sung, H.-W.; Shih, J.-S.; Hsu, C.-S. Crosslinking Characteristics of Porcine Tendons: Effects of Fixation with Glutaraldehyde or Epoxy. *Journal of Biomedical Materials Research* **1996**, *30*, 361-367, doi:10.1002/(sici)1097-4636(199603)30:3<361::Aid-jbm10>3.0.Co;2-n.
92. Zheng, X.; Chen, Y.; Dan, N.; Dan, W.; Li, Z. Highly Stable Collagen Scaffolds Crosslinked with an Epoxidized Natural Polysaccharide for Wound Healing. *Int J Biol Macromol* **2021**, *182*, 1994-2002, doi:10.1016/j.ijbiomac.2021.05.189.

93. Wang, X.; Chang, J.; Tian, T.; Ma, B. Preparation of Calcium Silicate/Decellularized Porcine Myocardial Matrix Crosslinked by Procyanidins for Cardiac Tissue Engineering. *RSC Advances* **2016**, *6*, 35091-35101, doi:10.1039/c6ra02947g.
94. Basara, G.; Ozcebe, S.G.; Ellis, B.W.; Zorlutuna, P. Tunable Human Myocardium Derived Decellularized Extracellular Matrix for 3d Bioprinting and Cardiac Tissue Engineering. *Gels* **2021**, *7*, doi:10.3390/gels7020070.
95. Tomal, W.; Ortyl, J. Water-Soluble Photoinitiators in Biomedical Applications. *Polymers (Basel)* **2020**, *12*, doi:10.3390/polym12051073.
96. Mao, Q.; Wang, Y.; Li, Y.; Juengpanich, S.; Li, W.; Chen, M.; Yin, J.; Fu, J.; Cai, X. Fabrication of Liver Microtissue with Liver Decellularized Extracellular Matrix (Decm) Bioink by Digital Light Processing (Dlp) Bioprinting. *Mater Sci Eng C* **2020**, *109*, doi:10.1016/j.msec.2020.110625.
97. Ma, X.; Yu, C.; Wang, P.; Xu, W.; Wan, X.; Lai, C.S.E.; Liu, J.; Koroleva-Maharajh, A.; Chen, S. Rapid 3d Bioprinting of Decellularized Extracellular Matrix with Regionally Varied Mechanical Properties and Biomimetic Microarchitecture. *Biomaterials* **2018**, *185*, 310-321, doi:10.1016/j.biomaterials.2018.09.026.
98. Yeleswarapu, S.; Dash, A.; Chameettachal, S.; Pati, F. 3d Bioprinting of Tissue Constructs Employing Dual Crosslinking of Decellularized Extracellular Matrix Hydrogel. *Biomater Adv* **2023**, *152*, 213494, doi:10.1016/j.bioadv.2023.213494.
99. Nizamoglu, M.; de Hilster, R.H.J.; Zhao, F.; Sharma, P.K.; Borghuis, T.; Harmsen, M.C.; Burgess, J.K. An in Vitro Model of Fibrosis Using Crosslinked Native Extracellular Matrix-Derived Hydrogels to Modulate Biomechanics without Changing Composition. *Acta Biomater* **2022**, *147*, 50-62, doi:10.1016/j.actbio.2022.05.031.
100. Fairbanks, B.D.; Schwartz, M.P.; Bowman, C.N.; Anseth, K.S. Photoinitiated Polymerization of Peg-Diacrylate with Lithium Phenyl-2,4,6-Trimethylbenzoylphosphinate: Polymerization Rate and Cytocompatibility. *Biomaterials* **2009**, *30*, 6702-6707, doi:10.1016/j.biomaterials.2009.08.055.
101. Lee, Y.B.; Lim, S.; Lee, Y.; Park, C.H.; Lee, H.J. Green Chemistry for Crosslinking Biopolymers: Recent Advances in Riboflavin-Mediated Photochemistry. *Materials (Basel)* **2023**, *16*, doi:10.3390/ma16031218.
102. Elkhoury, K.; Zuazola, J.; Vijayavenkataraman, S. Bioprinting the Future Using Light: A Review on Photocrosslinking Reactions, Photoreactive Groups, and Photoinitiators. *SLAS Technol* **2023**, *28*, 142-151, doi:10.1016/j.slast.2023.02.003.
103. Rydholm, A.E.R., S. K.; Anseth, K. S.; Bowman, C. N. Controlling Network Structure in Degradable Thiol-Acrylate Biomaterials to Tune Mass Loss Behavior. *Biomacromolecules* **2006**, doi:10.1021/bm0603793.
104. Duong, V.T.; Nguyen, H.D.; Luong, N.H.; Chang, C.Y.; Lin, C.C. Photo-Responsive Decellularized Small Intestine Submucosa Hydrogels. *Adv Funct Mater* **2024**, doi:10.1002/adfm.202401952.
105. Hewawasam, R.S.Š., P.; Blomberg, R.; Magin, C.M. Chemical Modification of Human Decellularized Extracellular Matrix for Incorporation into Phototunable Hybrid-Hydrogel Models of Tissue Fibrosis. *ACS Appl Mater Interfaces* **2023**, *15*, 15071-15083, doi:10.1021/acsami.2c18330.
106. Petrou, C.L.; D'Ovidio, T.J.; Bolukbas, D.A.; Tas, S.; Brown, R.D.; Allawzi, A.; Lindstedt, S.; Nozik-Grayck, E.; Stenmark, K.R.; Wagner, D.E.; Magin, C.M. Clickable Decellularized Extracellular Matrix as a New Tool for Building Hybrid-Hydrogels to Model Chronic Fibrotic Diseases in Vitro. *J Mater Chem B* **2020**, *8*, 6814-6826, doi:10.1039/d0tb00613k.
107. Yu, C.; Miller, K.L.; Schimelman, J.; Wang, P.; Zhu, W.; Ma, X.; Tang, M.; You, S.; Lakshmiathy, D.; He, F.; Chen, S. A Sequential 3d Bioprinting and Orthogonal Bioconjugation Approach for Precision Tissue Engineering. *Biomaterials* **2020**, *258*, 120294, doi:10.1016/j.biomaterials.2020.120294.
108. Pierau, L.; Abbad Andaloussi, S.; Chiappone, A.; Lajnef, S.; Peyrot, F.; Malval, J.-P.; Jockusch, S.; Versace, D.-L. Eosin Y Derivatives for Visible Light-Mediated Free-Radical Polymerization:

- Applications in 3d-Photoprinting and Bacterial Photodynamic Inactivation. *European Polymer Journal* **2024**, *214*, doi:10.1016/j.eurpolymj.2024.113143.
109. Fan, L.; Jung, O.; Herrmann, M.; Shirokikh, M.; Stojanovic, S.; Najman, S.; Körte, F.; Xiong, X.; Schenke-Layland, K.; Barbeck, M. Deciphering Uva/Riboflavin Collagen Crosslinking: A Pathway to Improve Biomedical Materials. *Adv Funct Mater* **2024**, doi:10.1002/adfm.202401742.
  110. Jang, J.; Kim, T.G.; Kim, B.S.; Kim, S.W.; Kwon, S.M.; Cho, D.W. Tailoring Mechanical Properties of Decellularized Extracellular Matrix Bioink by Vitamin B2-Induced Photo-Crosslinking. *Acta Biomater* **2016**, *33*, 88-95, doi:10.1016/j.actbio.2016.01.013.
  111. Hu, W.; Wang, Z.; Xiao, Y.; Zhang, S.; Wang, J. Advances in Crosslinking Strategies of Biomedical Hydrogels. *Biomater Sci* **2019**, *7*, 843-855, doi:10.1039/c8bm01246f.
  112. Yu, C.; Kornmuller, A.; Brown, C.; Hoare, T.; Flynn, L.E. Decellularized Adipose Tissue Microcarriers as a Dynamic Culture Platform for Human Adipose-Derived Stem/Stromal Cell Expansion. *Biomaterials* **2017**, *120*, 66-80, doi:10.1016/j.biomaterials.2016.12.017.
  113. Rothrauff, B.B.; Coluccino, L.; Gottardi, R.; Ceseracciu, L.; Scaglione, S.; Goldoni, L.; Tuan, R.S. Efficacy of Thermo-responsive, Photocrosslinkable Hydrogels Derived from Decellularized Tendon and Cartilage Extracellular Matrix for Cartilage Tissue Engineering. *J Tissue Eng Regen Med* **2018**, *12*, e159-e170, doi:10.1002/term.2465.
  114. Skardal, A.; Devarasetty, M.; Kang, H.W.; Mead, I.; Bishop, C.; Shupe, T.; Lee, S.J.; Jackson, J.; Yoo, J.; Soker, S.; Atala, A. A Hydrogel Bioink Toolkit for Mimicking Native Tissue Biochemical and Mechanical Properties in Bioprinted Tissue Constructs. *Acta Biomater* **2015**, *25*, 24-34, doi:10.1016/j.actbio.2015.07.030.
  115. B, M.M.a.M. Characterization of Gelatine and Acid Soluble Collagen by Size Exclusion Chromatography Coupled with Multi Angle Light Scattering (Sec-Mals). *Biomacromolecules* **2003**, *4*, 1727-1732, doi:10.1021/bm0341531.
  116. Han, W.; Singh, N.K.; Kim, J.J.; Kim, H.; Kim, B.S.; Park, J.Y.; Jang, J.; Cho, D.W. Directed Differential Behaviors of Multipotent Adult Stem Cells from Decellularized Tissue/Organ Extracellular Matrix Bioinks. *Biomaterials* **2019**, *224*, 119496, doi:10.1016/j.biomaterials.2019.119496.
  117. Fernandez-Perez, J.; Ahearne, M. The Impact of Decellularization Methods on Extracellular Matrix Derived Hydrogels. *Sci Rep* **2019**, *9*, 14933, doi:10.1038/s41598-019-49575-2.
  118. Jeong, W.; Kim, M.K.; Kang, H.W. Effect of Detergent Type on the Performance of Liver Decellularized Extracellular Matrix-Based Bio-Inks. *J Tissue Eng* **2021**, *12*, 2041731421997091, doi:10.1177/2041731421997091.
  119. Ravichandran, A.; Murekatete, B.; Moedder, D.; Meinert, C.; Bray, L.J. Photocrosslinkable Liver Extracellular Matrix Hydrogels for the Generation of 3d Liver Microenvironment Models. *Sci Rep* **2021**, *11*, 15566, doi:10.1038/s41598-021-94990-z.
  120. Shenoy, S.L.; Bates, W.D.; Frisch, H.L.; Wnek, G.E. Role of Chain Entanglements on Fiber Formation During Electrospinning of Polymer Solutions: Good Solvent, Non-Specific Polymer-Polymer Interaction Limit. *Polymer* **2005**, *46*, 3372-3384, doi:10.1016/j.polymer.2005.03.011.
  121. Toprakhisar, B.; Nadernezhad, A.; Bakirci, E.; Khani, N.; Skvortsov, G.A.; Koc, B. Development of Bioink from Decellularized Tendon Extracellular Matrix for 3d Bioprinting. *Macromol Biosci* **2018**, *18*, e1800024, doi:10.1002/mabi.201800024.
  122. Claudio-Rizo, J.A.; Delgado, J.; Quintero-Ortega, I.A.; Mata-Mata, J.L.; Mendoza-Novelo, B. Decellularized Ecm-Derived Hydrogels: Modification and Properties. In *Hydrogels*; 2018.
  123. Kular, J.K.; Basu, S.; Sharma, R.I. The Extracellular Matrix: Structure, Composition, Age-Related Differences, Tools for Analysis and Applications for Tissue Engineering. *J Tissue Eng* **2014**, *5*, 2041731414557112, doi:10.1177/2041731414557112.
  124. Tschalkowsky, M.; Neumann, T.; Brander, S.; Haschke, H.; Rolauffs, B.; Balzer, B.N.; Hugel, T. Hybrid Fluorescence-Afm Explores Articular Surface Degeneration in Early Osteoarthritis across Length Scales. *Acta Biomater* **2021**, *126*, 315-325, doi:10.1016/j.actbio.2021.03.034.

125. Meng, Z.; Thakur, T.; Chitrakar, C.; Jaiswal, M.K.; Gaharwar, A.K.; Yakovlev, V.V. Assessment of Local Heterogeneity in Mechanical Properties of Nanostructured Hydrogel Networks. *ACS Nano* **2017**, *11*, 7690-7696, doi:10.1021/acsnano.6b08526.
126. Caliari, S.R.; Burdick, J.A. A Practical Guide to Hydrogels for Cell Culture. *Nat Methods* **2016**, *13*, 405-414, doi:10.1038/nmeth.3839.
127. Guo, K.; Wang, H.; Li, S.; Zhang, H.; Li, S.; Zhu, H.; Yang, Z.; Zhang, L.; Chang, P.; Zheng, X. Collagen-Based Thiol-Norbornene Photoclick Bio-Ink with Excellent Bioactivity and Printability. *ACS Appl Mater Interfaces* **2021**, *13*, 7037-7050, doi:10.1021/acsmi.0c16714.
128. Sochilina, A.V.; Savelyev, A.G.; Demina, P.A.; Sizova, S.V.; Zubov, V.P.; Khaydukov, E.V.; Generalova, A.N. Quantitative Detection of Double Bonds in Hyaluronic Acid Derivative Via Permanganate Ion Reduction. *Meas Sci Technol* **2019**, *30*, doi:10.1088/1361-6501/ab0fb4.
129. Rezaei, T.N.; Kumar, H.; Liu, H.; Rajeev, A.; Natale, G.; Lee, S.S.; Park, S.S.; Kim, K. 3d Bioprinting of Liver Microenvironment Model Using Photocrosslinkable Decellularized Extracellular Matrix Based Hydrogel. *bioRxiv* **2024**, doi:10.1101/2024.04.17.589849.
130. White, L.J.; Keane, T.J.; Smoulder, A.; Zhang, L.; Castleton, A.A.; Reing, J.E.; Turner, N.J.; Dearth, C.L.; Badylak, S.F. The Impact of Sterilization Upon Extracellular Matrix Hydrogel Structure and Function. *Journal of Immunology and Regenerative Medicine* **2018**, *2*, 11-20, doi:10.1016/j.regen.2018.04.001.
131. Palmer, I.; Clarke, S.A.; Nelson, J.; Schatton, W.; Dunne, N.J.; Buchanan, F. Identification of a Suitable Sterilisation Method for Collagen Derived from a Marine Demosponge. *International Journal of Nano and Biomaterials* **2012**, *4*, doi:10.1504/ijnbm.2012.050306.
132. Cutler, T.D.; Zimmerman, J.J. Ultraviolet Irradiation and the Mechanisms Underlying Its Inactivation of Infectious Agents. *Anim Health Res Rev* **2011**, *12*, 15-23, doi:10.1017/S1466252311000016.
133. Coronado, R.E.; Somaraki-Cormier, M.; Natesan, S.; Christy, R.J.; Ong, J.L.; Halff, G.A. Decellularization and Solubilization of Porcine Liver for Use as a Substrate for Porcine Hepatocyte Culture: Method Optimization and Comparison. *Cell Transplant* **2017**, *26*, 1840-1854, doi:10.1177/0963689717742157.
134. Manita, P.G.; Garcia-Orue, I.; Santos-Vizcaino, E.; Hernandez, R.M.; Igartua, M. 3d Bioprinting of Functional Skin Substitutes: From Current Achievements to Future Goals. *Pharmaceuticals (Basel)* **2021**, *14*, doi:10.3390/ph14040362.
135. Das, S.; Basu, B. An Overview of Hydrogel-Based Bioinks for 3d Bioprinting of Soft Tissues. *Journal of the Indian Institute of Science* **2019**, *99*, 405-428, doi:10.1007/s41745-019-00129-5.
136. Issa, R.I.; Engebretson, B.; Rustom, L.; McFetridge, P.S.; Sikavitsas, V.I. The Effect of Cell Seeding Density on the Cellular and Mechanical Properties of a Mechanostimulated Tissue-Engineered Tendon. *Tissue Eng Part A* **2011**, *17*, 1479-1487, doi:10.1089/ten.TEA.2010.0484.
137. Costantini, M.; Idaszek, J.; Szoke, K.; Jaroszewicz, J.; Dentini, M.; Barbetta, A.; Brinckmann, J.E.; Swieszkowski, W. 3d Bioprinting of Bm-Mscs-Loaded Ecm Biomimetic Hydrogels for in Vitro Neocartilage Formation. *Biofabrication* **2016**, *8*, 035002, doi:10.1088/1758-5090/8/3/035002.
138. Kyle, S.; Jessop, Z.M.; Al-Sabah, A.; Whitaker, I.S. 'Printability' of Candidate Biomaterials for Extrusion Based 3d Printing: State-of-the-Art. *Adv Healthc Mater* **2017**, *6*, doi:10.1002/adhm.201700264.
139. Malijauskaite, S.; Connolly, S.; Newport, D.; McGourty, K. Gradients in the in Vivo Intestinal Stem Cell Compartment and Their in Vitro Recapitulation in Mimetic Platforms. *Cytokine Growth Factor Rev* **2021**, *60*, 76-88, doi:10.1016/j.cytogfr.2021.03.002.
140. Li, X.G.; Chen, M.X.; Zhao, S.Q.; Wang, X.Q. Intestinal Models for Personalized Medicine: From Conventional Models to Microfluidic Primary Intestine-on-a-Chip. *Stem Cell Rev Rep* **2022**, *18*, 2137-2151, doi:10.1007/s12015-021-10205-y.



141. Elomaa, L.; Keshi, E.; Sauer, I.M.; Weinhart, M. Development of Gelma/Pcl and Decm/Pcl Resins for 3d Printing of Acellular in Vitro Tissue Scaffolds by Stereolithography. *Mater Sci Eng C* **2020**, *112*, doi:10.1016/j.msec.2020.110958.
142. Dutton, J.S.; Hinman, S.S.; Kim, R.; Wang, Y.; Allbritton, N.L. Primary Cell-Derived Intestinal Models: Recapitulating Physiology. *Trends Biotechnol* **2019**, *37*, 744-760, doi:10.1016/j.tibtech.2018.12.001.
143. Zheng, F.; Xiao, Y.; Liu, H.; Fan, Y.; Dao, M. Patient-Specific Organoid and Organ-on-a-Chip: 3d Cell-Culture Meets 3d Printing and Numerical Simulation. *Adv Biol (Weinh)* **2021**, *5*, e2000024, doi:10.1002/adbi.202000024.
144. Sontheimer-Phelps, A.; Chou, D.B.; Tovaglieri, A.; Ferrante, T.C.; Duckworth, T.; Fadel, C.; Frisimantas, V.; Sutherland, A.D.; Jalili-Firoozinezhad, S.; Kasendra, M.; Stas, E.; Weaver, J.C.; Richmond, C.A.; Levy, O.; Prantil-Baun, R.; Breault, D.T.; Ingber, D.E. Human Colon-on-a-Chip Enables Continuous in Vitro Analysis of Colon Mucus Layer Accumulation and Physiology. *Cell Mol Gastroenterol Hepatol* **2020**, *9*, 507-526, doi:10.1016/j.jcmgh.2019.11.008.
145. Donkers, J.M.; Eslami Amirabadi, H.; van de Steeg, E. Intestine-on-a-Chip: Next Level In vitro Research Model of the Human Intestine. *Current Opinion in Toxicology* **2021**, *25*, 6-14, doi:10.1016/j.cotox.2020.11.002.
146. Shin, W.; Kim, H.J. 3d in Vitro Morphogenesis of Human Intestinal Epithelium in a Gut-on-a-Chip or a Hybrid Chip with a Cell Culture Insert. *Nat Protoc* **2022**, *17*, 910-939, doi:10.1038/s41596-021-00674-3.
147. Shin, W.; Hinojosa, C.D.; Ingber, D.E.; Kim, H.J. Human Intestinal Morphogenesis Controlled by Transepithelial Morphogen Gradient and Flow-Dependent Physical Cues in a Microengineered Gut-on-a-Chip. *iScience* **2019**, *15*, 391-406, doi:10.1016/j.isci.2019.04.037.
148. Kasendra, M.; Tovaglieri, A.; Sontheimer-Phelps, A.; Jalili-Firoozinezhad, S.; Bein, A.; Chalkiadaki, A.; Scholl, W.; Zhang, C.; Rickner, H.; Richmond, C.A.; Li, H.; Breault, D.T.; Ingber, D.E. Development of a Primary Human Small Intestine-on-a-Chip Using Biopsy-Derived Organoids. *Sci Rep* **2018**, *8*, 2871, doi:10.1038/s41598-018-21201-7.
149. Yin, J.; Sunuwar, L.; Kasendra, M.; Yu, H.; Tse, C.M.; Talbot, C.C., Jr.; Boronina, T.; Cole, R.; Karalis, K.; Donowitz, M. Fluid Shear Stress Enhances Differentiation of Jejunal Human Enteroids in Intestine-Chip. *Am J Physiol Gastrointest Liver Physiol* **2021**, *320*, G258-G271, doi:10.1152/ajpgi.00282.2020.
150. An, S.; Han, S.Y.; Cho, S.-W. Hydrogel-Integrated Microfluidic Systems for Advanced Stem Cell Engineering. *BioChip Journal* **2019**, *13*, 306-322, doi:10.1007/s13206-019-3402-5.
151. Goy, C.B.; Chaile, R.E.; Madrid, R.E. Microfluidics and Hydrogel: A Powerful Combination. *Reactive and Functional Polymers* **2019**, *145*, doi:10.1016/j.reactfunctpolym.2019.104314.
152. Berger, E.; Magliaro, C.; Paczia, N.; Monzel, A.S.; Antony, P.; Linster, C.L.; Bolognin, S.; Ahluwalia, A.; Schwamborn, J.C. Millifluidic Culture Improves Human Midbrain Organoid Vitality and Differentiation. *Lab Chip* **2018**, *18*, 3172-3183, doi:10.1039/c8lc00206a.
153. Mastrorocco, A.; Cacopardo, L.; Temerario, L.; Martino, N.A.; Tridente, F.; Rizzo, A.; Lacalandra, G.M.; Robbe, D.; Carluccio, A.; Dell'Aquila, M.E. Investigating and Modelling an Engineered Millifluidic in Vitro Oocyte Maturation System Reproducing the Physiological Ovary Environment in the Sheep Model. *Cells* **2022**, *11*, doi:10.3390/cells11223611.
154. Wilkinson, J.M. A Review of Complex in Vitro Cell Culture Stressing the Importance of Fluid Flow and Illustrated by Organ on a Chip Liver Models. *Front Toxicol* **2023**, *5*, 1170193, doi:10.3389/ftox.2023.1170193.
155. Nielsen, A.V.; Beauchamp, M.J.; Nordin, G.P.; Woolley, A.T. 3d Printed Microfluidics. *Annu Rev Anal Chem (Palo Alto Calif)* **2020**, *13*, 45-65, doi:10.1146/annurev-anchem-091619-102649.